

N° d'ordre: 40767

Année 2012

UNIVERSITÉ LILLE 1 - SCIENCES ET TECHNOLOGIES

**ÉCOLE DOCTORALE SCIENCES DE LA MATIÈRE DU RAYONNEMENT ET DE
L'ENVIRONNEMENT**

THÈSE

pour obtenir le grade de

DOCTEUR DE L'UNIVERSITÉ LILLE 1

Spécialité: Molécules et Matière condensée

Soutenance publique le 31 janvier 2012 par

Mihaela Luciana IORGULESCU

**Oxo-halogénures de cobalt: Compréhension de
l'influence des substitutions cationiques et
anioniques**

Thèse dirigée par :

Mr Olivier MENTRÉ, Mr Pascal ROUSSEL et Mme Nathalie TANCRET

Composition de la commission d'examen:

Jacques DARRIET, Directeur de Recherche Emérite, ICMCB-CNRS, PESSAC

Werner PAULUS, Professeur CM2, Université Montpellier 2, MONTPELLIER

Silviu COLIS, Maître de conférences HDR, IPCMS – DCMI, STRASBOURG

Olivier MENTRE, Directeur de recherche CNRS, LILLE

Pascal ROUSSEL, Chargé de Recherche HDR CNRS, LILLE

Nathalie TANCRET, Maître de conférences, UCCS-ENSCL, LILLE

REMERCIEMENTS

Ce travail de thèse a été effectué au sein de l'Axe Chimie du Solide de l'UCCS dirigée par Madame Rose-Noëlle Vannier que je remercie de m'avoir accueillie au sein du laboratoire. Cette thèse a été dirigée par Monsieur Oliver Mentré, Directeur de Recherches CNRS, Monsieur Pascal Roussel, Chargé de Recherches CNRS et Madame Nathalie Tancret, Maître de conférences à l'ENSCL. Je tiens à les remercier pour avoir dirigé cette thèse. Tout au long de ces trois années, ils ont pu orienter mon travail et m'ont donné leurs conseils d'experts qui ont mené à la finalisation de cette thèse. Pour tout cela, leur patience et leur disponibilité, je les remercie de tout mon cœur.

Je remercie Monsieur Werner Paulus, Professeur à l'Université de Montpellier pour l'honneur qu'il m'a fait d'examiner ce travail et de présider le jury. Que Monsieur Jacques Darriet, Directeur de Recherche Emérite à ICMCB-CNRS, Bordeaux et Monsieur Silviu Colis, Maître de conférences HDR à l'IPCMS –DCMI, Strasbourg trouvent ici toute ma gratitude pour avoir accepté de rapporter mon travail en apportant une analyse détaillée du manuscrit. Je remercie vivement ces trois personnes pour l'intérêt qu'elles ont porté à ce travail et pour le regard critique qu'elles y ont apporté.

Je tiens aussi à remercier toutes les personnes qui ont contribué à la réalisation de cette thèse, aussi bien pour les différentes expériences qu'elles ont réalisées (DRX sur poudre et monocristal, ATG, ATD, MEB, EDX) : Laurence Burylo, Nora Djelal, Frédéric Capet, Maxence Vandewalle que pour les discussions et les conseils éclairés. Je pense en particulier à Madame Sylvie Daviero-Minaud à laquelle j'adresse mes remerciements pour ses conseils avisés, notamment sur la titration iodométrique, Madame Houria Kabbour pour les calculs DFT qui ont contribué à la finalisation de ce travail, Madame Marielle Huvé pour les expériences de TEM, EDX, ainsi que pour leur disponibilité et leur patience.

Cette étude a été le fruit de nombreuses collaborations. Merci aux personnes de la diffraction neutronique, Monsieur Gilles André, responsable G41 (LLB, Saclay), Madame Florence Porcher, responsable 3T2 (LLB, Saclay). J'adresse aussi un grand merci à Monsieur Silviu Colis de l'IPCMS – DCMI à Strasbourg et Monsieur Nicolas Tiercelin de l'IEMN pour toutes les mesures de susceptibilité magnétique sans lesquelles ce travail ne serait pas complet.

Je tiens tout particulièrement à remercier à Nicolas Renault pour toute son aide et sa gentillesse et mes collègues, Mihai et Ionut pour leur soutien et leur amitié. Que trouvent ici l'expression de mon amitié, mes collègues Vincent, Rénaud, Aani, Diana, Ana, Nina, Zhen, Daniel et tous les autres, anciens et futurs, avec lesquels j'ai passé de moments inoubliables dans le laboratoire et à l'extérieur.

J'ai passé des moments mémorables dans l'Equipe de Chimie du Solide et je tiens à remercier toute l'équipe pour son accueil et l'ambiance chaleureuse qu'ils ont fait régner.

Enfin, ces remerciements ne seraient pas complets sans mentionner ma famille qui, par ses encouragements m'a permis de faire cette thèse dans de bonnes conditions. Son amour, son écoute et son soutien ont toujours été sans faille : merci infiniment à vous.

Summary

Introduction	9
Chapter 1. State of the art.....	15
1. 1. Perovskites – Structural aspect	15
1. 2. Anion deficient and oxo-halides layers	18
1.2.1. <i>Disconnected tetrahedra dimers (c'- [BaO₂] layers).....</i>	18
1.2.2. <i>Connected tetrahedral dimers (via [BaO] layers and/or [BaOX] (X = Cl, F) layers).....</i>	19
1.2.3. <i>Other layers, the Br case</i>	21
1. 3. Cubic versus hexagonal layers: the driving force	22
1.3.1. <i>The BaCoO_{3-δ} system</i>	23
1.3.2. <i>The BaMnO_{3-δ} system.....</i>	25
1.3.3. <i>The BaFeO_{3-δ} system.....</i>	27
1.3.4. <i>Mixed Ba(MM')O_{3-δ} compounds.....</i>	28
1.3.5. <i>Cobalt oxo-halides.....</i>	29
1.3.6. <i>Conclusion:.....</i>	31
Chapter 2. Mixed BaMX_{0.2-x}O_{3-δ} systems	35
2. 1. BaMX_{0.2-x}O_{3-δ} (M = Mn, Fe, Co; X = Cl, F) phase diagrams.....	35
Synthesis of the compounds:.....	36
2.1.1.a) Ba(Co,Fe)X _{0.2-x} O _{3-δ}	36
2.1.1.b) Ba(Co,Mn)X _{0.2-x} O _{3-δ}	36
2.1.1.c) Ba(Mn,Fe)X _{0.2-x} O _{3-δ}	37
2.1.1.d) Ba(Co,Mn,Fe)X _{0.2-x} O _{3-δ}	37
2.1.1. <i>Predominant phases in the oxo – chloride phase diagram:</i>	38
2.1.2.a) Line Co – Fe (binary substitutions Ba(Fe,Co)Cl _{0.2-x} O _{3-δ}).....	39
2.1.2.b) Line Co – Mn (binary substitutions Ba(Co,Mn)Cl _{0.2-x} O _{3-δ}).....	39
2.1.2.c) Line Fe – Mn (binary substitutions Ba(Fe,Mn)Cl _{0.2-x} O _{3-δ})	40
2.1.2.d) Ternary substitution Ba(Co,Fe,Mn)Cl _{0.2-x} O _{3-δ}	41
2.1.2. <i>Predominant phases in the oxo-fluoride phase diagram:.....</i>	41
2.1.3.a) The 6H area (oxidized blue zone):	42
2.1.3.b) Fe -rich zone (yellow zone):	43

2.1.3. <i>Predominant polytypes: General conclusions</i>	43
2.2. Structural characterization of the mixed $BaMX_{0.2-x}O_{3-\delta}$ systems	44
2.2.1. $Ba_5(Co,Fe)_5XO_{13-\delta}$ ($X = Cl, F$)	44
2.2.1.a) Room temperature lattice parameters	45
2.2.1.b) Thermal behaviour.....	48
2.2.1.c) Thermo gravimetric analysis:.....	49
2.2.1.d) Thermal induced structural changes.....	52
2.2.1.e) Neutron diffraction	54
2.2.1.f) High temperature in-plane reorganization	58
2.2.1.g) Conclusion in few points.....	60
2.2.2. $Ba_6(Co,Mn)_6XO_{16-\delta}$ ($X = Cl, F$)	60
2.2.2.a) Difficulties and limits	60
2.2.2.b) $Ba_6(Co,Mn)_6ClO_{16-\delta}$ case	62
2.2.2.c) $Ba_6(Co,Mn)_6FO_{16-\delta}$ case.....	67
2.2.2.d) Mn/Co cationic distribution	68
2.2.2.e) Conclusion in few points.....	72
2.2.3. <i>The structure of $Ba_8Co_2Mn_6ClO_{22-\delta}$, a new quasi-1D-hexagonal perovskite polytype containing novel 8H- blocks</i>	73
2.2.3.a) Synthesis.....	73
2.2.3.b) Structural description.....	74
2.2.3.c) Elemental analysis (Microprobe EPMA)	75
2.2.3.d) Cationic distribution by Density Functional Theory (DFT).....	76
2.2.3.e) Powder synthesis	78
2.2.3.f) Magnetic / electric potentialities.....	79
2.2.3.g) Conclusion.....	80
2.2.4. $Ba(Mn,Fe)_1X_{0.2-x}O_{3-\delta}$ ($X = Cl, F$)	81
2.2.4.a) Phases identification for $BaMn_yFe_{1-y}Cl_{0.2-x}O_{3-\delta}$	82
2.2.4.b) Phases identification for $BaMn_yFe_{1-y}F_{0.2-x}O_{3-\delta}$	89
2.2.4.c) Conclusions	90
2.2.5. $BaMX_{0.2-x}O_{3-\delta}$ ($M = Mn + Fe + Co$; $X = Cl, F$) ternary substitutions.....	90
2.3. Magnetic and electrical characterization of mixed $BaMX_{0.2-x}O_{3-\delta}$ systems	93
2.3.1. <i>State of the art on $Ba_5Co_5XO_{13-\delta}$ and $Ba_6Co_6XO_{16-\delta}$ ($X = Cl, F$) properties</i>	93
2.3.1.a) Magnetic structure and proprieties of parent oxo-halides	93

2.3.1.b) Electric properties of parent Co-oxo-halides.....	97
2.3.2. $Ba_5(Co,Fe)_5XO_{13-\delta}$ ($X = Cl, F$).....	98
2.3.2.a) $Ba_5(Co,Fe)_5XO_{13-\delta}$ ($X = F, Cl$) magnetic susceptibility	98
2.3.2.b) $Ba_5(Co,Fe)_5XO_{13-\delta}$ ($X = F, Cl$) magnetic structures.....	102
2.3.2.c) Transport properties of $Ba_5(Co,Fe)_5XO_{13-\delta}$ ($X = F, Cl$).....	105
2.3.3. $Ba_6(Co,Mn)_6XO_{16-\delta}$ ($X = Cl$)	107
2.3.3.a) Magnetic properties	107
2.3.3.b) Low temperature electric proprieties.....	109
2. 4. Supplementary information	113
Chapter 3. Anionic substitution in the 10H and 6H forms.....	119
3. 1. State of the art: importance of the halogen nature on the magnetic and electric properties	119
3.1.1. <i>Connected FM blocks (F and Cl) vs. disconnected FM blocks (O and Br)</i>	119
3.1.2. <i>Magnetocrystalline anisotropy versus X</i>	121
3.1.3. <i>"History" of the proposed charge distribution</i>	122
3. 2. Short chapter presentation.....	122
3. 3. Synthesis of the compounds.....	123
3. 4. Trimer and tetramer Cl – F solid solutions.....	125
3.4.1. <i>10H (trimer) Cl–F solid solution</i>	125
3.4.1.a) Lattice parameters evolution	126
3.4.1.b) Structure investigation by powder neutron diffraction.....	127
3.4.1.c) Single crystals structure investigation.....	132
3.4.1.d) Summary structural investigation $Ba_5Co_5Cl_{1-y}F_yO_{13-\delta}$	134
3.4.1.e) $Ba_5Co_5Cl_{1-y}F_yO_{13-\delta}$ solid solution properties	135
3.4.1.f) Conclusion in few points.....	143
3.4.2. <i>6H (tetramer) Cl – F solid solution</i>	145
3.4.2.a) Powder XRD analysis and lattice parameters evolution	145
3.4.2.b) ^{19}F NMR.....	147
3.4.2.c) Magnetic properties	147
3.4.2.d) Transport properties:	151
3.4.2.e) Conclusion in few points:.....	152

3.4.3. $Ba_5(Co, Pt)_5BrO_{13-\delta}$	152
3.4.3.a) Structural analysis by X – ray diffraction.....	155
3.4.3.b) Conclusion in few points:.....	158
3. 5. Compounds with carbonate groups	159
3.5.1. <i>Case of carbonate groups as inter – block separators</i>	159
3.5.1.a) Carbonate presence investigation by infrared spectroscopy	161
3.5.1.b) Structural analysis by single crystal XRD and MEM.....	161
3.5.1.c) Disorder rationalisation.....	163
3.5.1.d) Compound formulation and Co average charge.....	164
3.5.1.e) Magnetic properties:.....	164
3.5.2. <i>Carbonate insertion possibility in 2H-BaCoO₃ compounds; evidence of a new family of 2H-Ba(Co, CO₃)O₃ compounds</i>	168
3.5.2.a) Evidence of the (CO ₃) ²⁻ entities presence in the hypothetical β - 2H–BaCoO ₃	170
3.5.2.b) Structural models for sample B	173
3.5.2.c) Superstructure investigation by Precession Electron Diffraction (PED).....	176
3. 6. Supplementary information	181
Conclusions	191
Bibliography.....	196
Materials and methods	206

Introduction

Introduction

Ceramics are by far the highest volume and highest tonnage materials made and used by humankind. Yet, there are only a half dozen specific ceramic phases that dominate human use of such materials not only in terms of volume, weight, etc., but also in terms of technological significance. Any list of such materials would contain at least the following:

- Quartz – which as sand is ubiquitous in rocks, beaches, soil, buildings, and roads,
- Mullite – the principal component both of crude and refined pottery of all kinds, bricks, etc.
- Calcium silicates – Ca_3SiO_5 , Ca_2SiO_4 and $\text{Ca}_3\text{Al}_2\text{O}_6$ – and their hydration products, the key constituents of cement and concrete, which at 1500 million tons/year is humankind's largest tonnage manufactured product.
- Al_2O_3 – the key oxide of ceramic technologies, used for hard grinding materials and all kinds of refractory ceramics, laser hosts, gems (rubies and sapphires).
- TiO_2 – the required high refractive index material in a variety of high volume uses, and the key ingredient in electroceramics.

Examination of the list of the existent ceramics reveal that the most used category are the ternary systems (thousands of complex structures, *Bhalla2000*) and, among them, only a dozen or so dominate the entire world of useful ceramics. Among these, the A_2BX_4 structure - spinel and the ABX_3 structure - perovskite, stand out as a wide margin, and perovskite is far ahead of spinel, because, as single structure, with skilled chemical manipulation, can produce an incredibly wide area of phases with totally different functions. The properties of ABX_3 systems are attributed especially to the transitional metal (B) capacity to adopt various oxidation states. In this system, Co has attracted the attention by his capacity to adopt +2, +3 and +4 oxidation states, with more than one spins configurations available for each oxidation degree. Furthermore, structurally, Co atom is capable of adopting different structural arrangements, monodimensional (2H-BaCoO_3 , *Taguchi1977*), bidimensional ($12\text{H-BaCoO}_{3-\delta}$, *Jacobson1980*) or tridimensional (cubic $\text{BaCoO}_{2.23}$, *Strauss1951*). This system dimensionality is of great importance since, for example, the existence of infinite face- sharing polyhedra strings in one structure can lead to privileged magnetic/electronic paths in the structural edifice as observed for $\text{Ca}_3\text{Co}_2\text{O}_6$

(Maignan2004) and 2H-BaCoO₃. The magnetic properties of these compounds were also intensively studied since they exhibit a ferromagnetic (FM) connection along the strings and antiferromagnetic (AFM) between the chains. From this, arises our interest in the study of cobaltites system and into the development of new members exhibiting new structural edifices, a challenging aspect taking into account the number of previous works dedicated to the same goal. More, the objective to modify the characteristic of these compounds by simple methods such as substitutions (at cationic as anionic level) can be well understood.

The structural types existent in the polymorphs (ABX₃) system will be presented in the first chapter, focusing on A = Ba, B = Co, Fe, Mn and X = O or halogen. Here our choice for Ba, Co, Mn and Fe will be debated. The three systems concerned here (BaFeO_{3-δ}, BaMnO_{3-δ} and BaFeO_{3-δ}) will be detailed, and we will try to establish a relationship between the structural polytype and the oxygen content. The mixed Co – Mn, Mn – Fe and Co – Fe systems and the particular case of BaCoX_{0.2-x}O_{3-δ} halogeno-cobaltites (X = Cl, F, Br), which are at the base of my work and are topical of prior works at the laboratory (*Kauffmann2006, 2007, 2007a, 2007c; Ehora2007, 2007a, 2007b; Tancret2004, Mentré2008 and 2010, Toulemonde2010*), will be especially focused on. The two structural polytypes (10H-trimer/6H-tetramer for X = F, Cl and 18R-trimer/14H-tetramer for X = Br with both differences and similarities between F/Cl/Br systems) are analyzed.

The second chapter deals with the cationic substitution in BaMX_{0.2-x}O_{3-δ} (M = Co, Fe, Mn and X = Cl, F) systems. Then the mixed Co/Mn, Fe/Mn and Co/Fe binary and Co/Fe/Mn ternary systems assorted with X = Cl and F have been investigated, with a special attention on the correlations between the redox and structural stable edifices. In the second part of this chapter, investigations by X – ray diffraction, neutrons diffraction, redox titration... will permit us to validate previous observations and to study interesting structural features related on the location of oxygen vacancies as well as the Fe/Mn/Co cationic distribution in different structural polytypes. In addition, the thermal stability of some terms will be studied. In the last part of this chapter, the magnetic and electrical properties of the parent BaCoX_{0.2-x}O_{3-δ} halogeno-cobaltites will be recalled and compared to new results on the mixed Co/Fe and Co/Mn terms, focusing on the effect of the doping.

The last chapter of this manuscript deals with anionic substitutions in the same system of halogeno-cobaltites. Mixed $\text{BaCoX}_{0.2-x}\text{O}_{3-\delta}$ with $X = \text{Cl}+\text{F}$ compounds in the 10H and 6H polytypes were investigated. The particular role of the halide anion on the structural features as well as on the magnetic and electrical properties will be analyzed. A 10H (trimer) Br/Pt compound was synthesized and show a rare example of [BaOBr] layer. In the last part of this chapter, an interesting $\text{Ba}_2\text{Co}_4\text{XO}_7$ compound will be reinvestigated in order to explore the structural disorder reported previously (*Kauffmann2007b*). More important, magnetic investigation on single crystals will be presented. Finally, a new family of 2H – carbonates structures obtained involuntarily will be presented in this part.

Chapter 1

Chapter 1. State of the art

1. 1. Perovskites – Structural aspect

Materials with the perovskite structure have attracted considerable interest, due to the fact that they can exhibit a wide range of technologically important properties, e.g. superconductivity, colossal magnetoresistance, oxide ion conductivity, proton conductivity, ferroelectricity and several other properties. (*Ramirez1997, Raveau1998, Raveau2001*). Nowadays, the development of novel specificities involves new structural edifices, a challenging aspect taking into account the number of previous works dedicated to the prospection for new members, in the field of perovskite related compounds. Taking into account the main goal of this work, mainly dedicated to the prospection for new materials/structures, the main structural characteristics of the perovskite-materials and derivatives deserve attention.

From the structural point of view, the ideal ABX_3 perovskite can be described from the cubic close-packing of AX_3 layers with the B cations occupying the octahedral holes resulting in a three dimensional framework with the sequence $ccc (=3C)$ leading to corner-sharing octahedra (*Katz1964*). In Fig. 1-1(a) are given some examples adopting this structural type: $BaCoO_{2.23}$ (*Strauss1951*), $BaFeO_{3-\delta}$ ($0.35 \leq \delta \leq 0.5$) (*Erchak1946*), $SrTiO_3$ (*Meyer1978*). In opposite, in the ideal ABX_3 hexagonal perovskite the B cations occupy octahedra that are connected by face-sharing to form chains running along the c -axis of the hexagonal unit cell, the stacking sequence of the $[AX_3]$ layers is $hh (=2H)$. In Fig. 1-1 (b) are given some examples: $2H-BaCoO_3$ (*Taguchi1977*), $2H-BaMnO_3$ (*Cussen2000*) and $2H-BaNiO_3$ (*Takeda1976*).

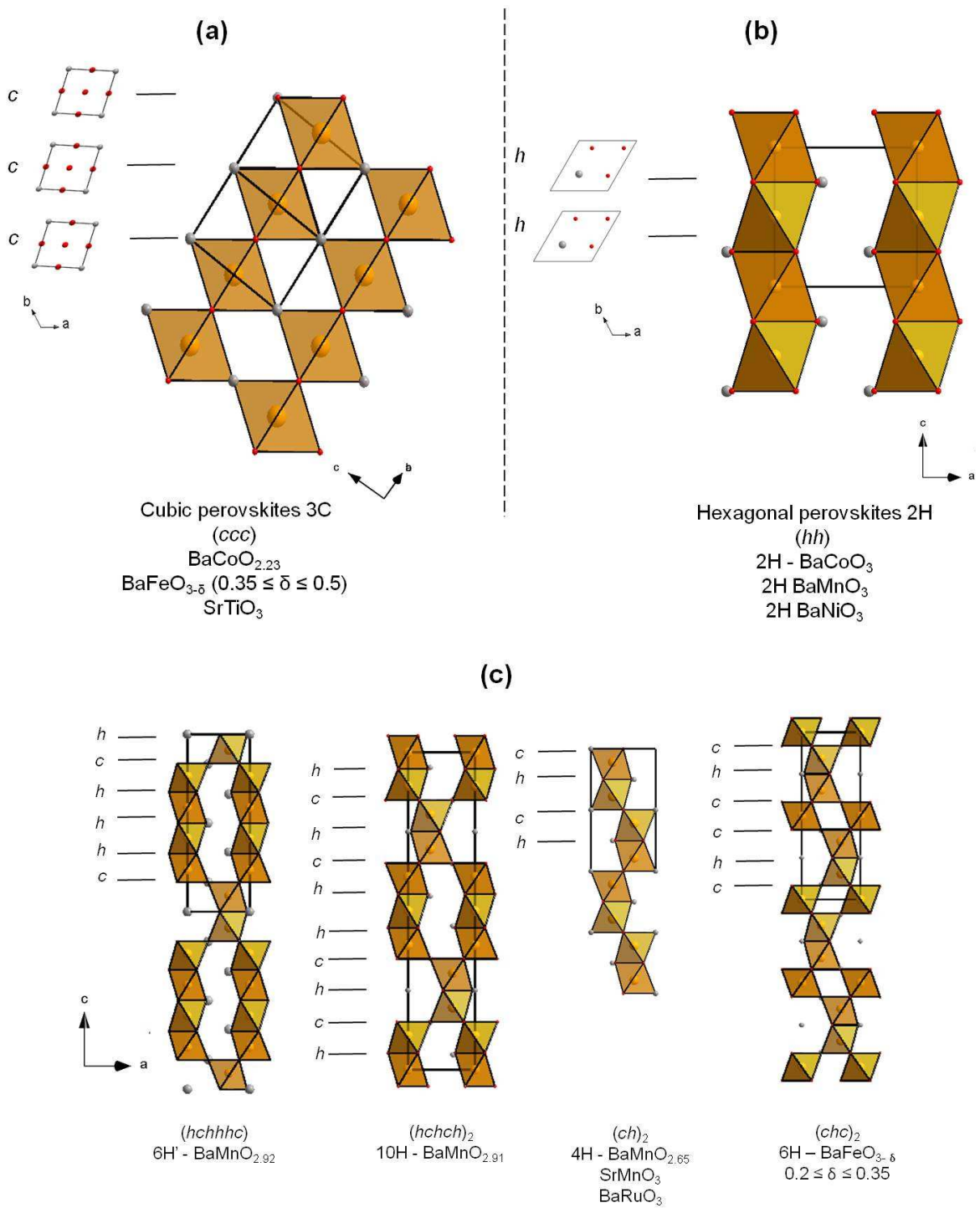


Fig. 1-1: ABX_3 cubic 3C perovskites structure (a), 2H hexagonal perovskites (b) and few examples of different c and h $[\text{AX}_3]$ stacking (c)

Intermediate structures (also considered as hexagonal polytypes) contain different proportions of cubic layers (corner-sharing octahedra) and hexagonal layers (face-sharing octahedra). For instance, one can imagine (varying the h and c layers stacking sequence), strings of two (h), three (hh) or four (hhh) face-sharing octahedra that would be corner shared (c) or separated by layers of one (cc), two (ccc), three ($cccc$), ... corner-shared octahedra. Sizeable sequences of h/c layers are shown on the Fig. 1-2 (c) for $6H$ -BaMnO_{2.92} and $10H$ -BaMnO_{2.91} (Negas1971), $4H$ -BaMnO_{2.65} (Adkin2006), $4H$ -SrMnO₃ (Kuroda1981) and $4H$ -BaRuO₃ (Hong1997) and $6H$ - BaFeO_{3- δ} ($0.2 \leq \delta \leq 0.35$) (Grenier1989).

The stability of the variants of the structures adopted by those ABX₃ phases (A = electropositive cation) can be rationalized by the Goldschmidt tolerance factor (Goldschmidt1926). Compositions with tolerance factors equal to unity ($t=1$) have the geometrically ideal ratio of A-X and B-X bond lengths to adopt the cubic perovskite structure. Small deviations below unity ($t<1$) are accommodated by cooperative twisting and tilting distortions of the BX₆ octahedra in which the B-X-B bond angle is reduced below 180° to accommodate small A-site cations. If the tolerance factor takes values greater than unity ($t>1$), hexagonal perovskite structures are adopted in which face-shared BX₆ octahedra are created in order to expand the volume available for the A-cation (e.g.: large A cations such as Ba²⁺).

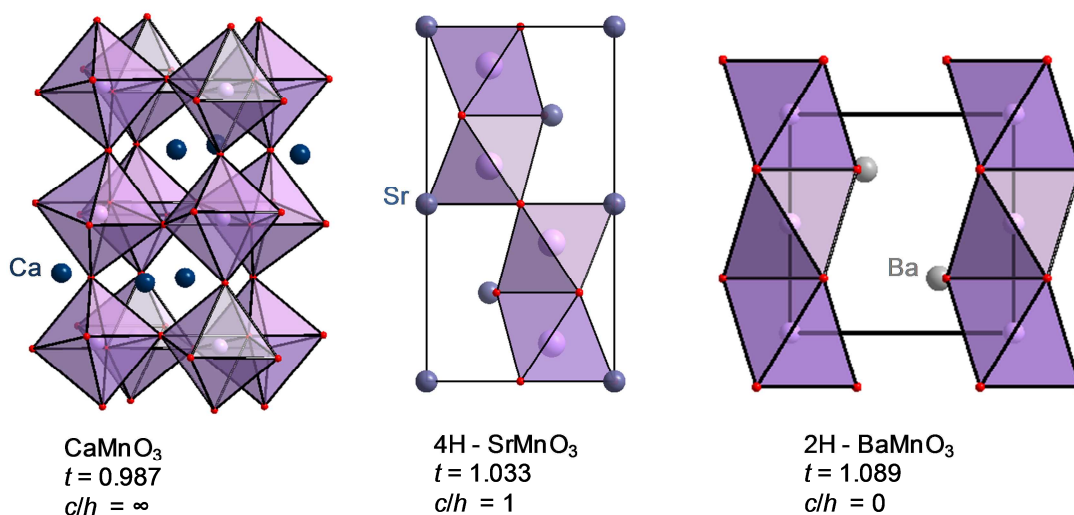


Fig. 1-2: The correlation between the Goldschmidt structural tolerance factor and the structural type in the AMnO₃ perovskites series (A = Ca, Sr and Ba)

The ratio of face-sharing to apex-sharing linkages in hexagonal perovskites can depend on the value of tolerance factor as illustrated by the structural progression within the $AMn^{4+}O_3$ series. Here, $CaMnO_3$ ($t = 0.987$) adopts a distorted cubic perovskite structure (only corner-sharing) (Poeppelemeier1982), while $SrMnO_3$ ($t = 1.033$) adopts a 4H structure (1/1 apex/ face-sharing) (Battle1988), and finally, $BaMnO_3$ ($t = 1.089$) adopts a 2H form (all face-sharing) (Cussen2000), (Fig. 1-2).

1. 2. Anion deficient and oxo-halides layers

J. Darriet and A. Subramaniam (Darriet1995) have intensively described and rationalized the number of polytypic structures which belong to the broad hexagonal perovskite-series, formed by succession of $[AX_3]$ and $[A_nX_m]$ mixed layers with $n + m \leq 4$. In this paper, the possibilities for alternative layers such as $[AX_2]$, $[AX]$..., are reported and their formation is explained by simple crystallographic relationships (as an example, the formation of a $[AO_2]$ layer by the reduction/rearrangement of a $[AO_3]$ layers).

In the following, we will mainly focus on some of these particular layers leading to the transformation of octahedral dimers into tetrahedral ones.

1.2.1. Disconnected tetrahedra dimers (c'- $[BaO_2]$ layers)

As a starting point, let consider corner sharing octahedra at both sides of a cubic c - $[BaO_3]$ (Fig.1-3) (example 5H' – $BaCoO_{2.8}$ (Parras1995)). After replacement of the central c - $[BaO_3]$ by an oxygen deficient cubic c' - $[BaO_2]$ layer, the new environment of the Co cations turns to tetrahedral. The two formed tetrahedra do not share their apical corners, forming disconnected tetrahedral layers. This is the case, for example, for the 5H – $BaCoO_{2.8}$ (Boulahya2005) (Fig.1-3).

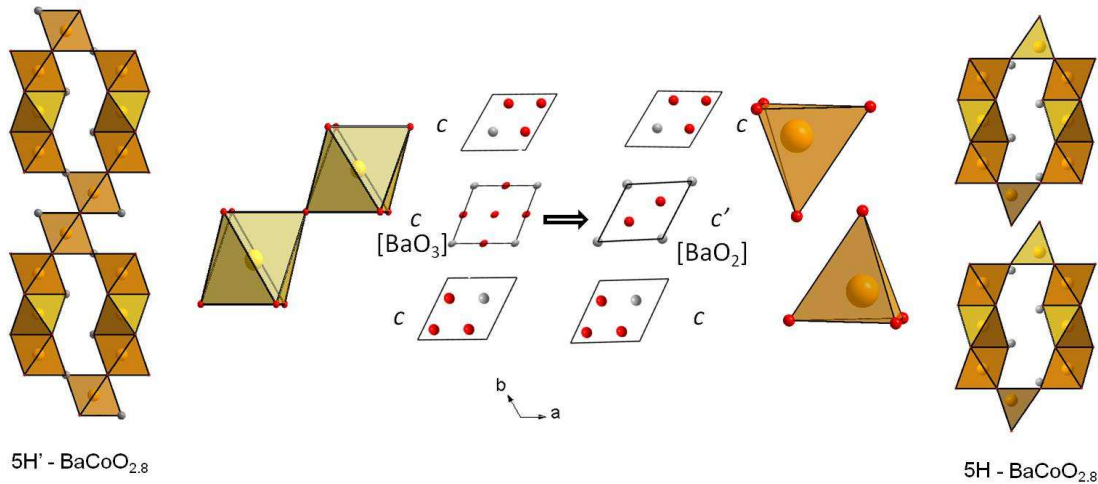


Fig.1-3: Schematic representation of the formation of a c' - $[BaO_2]$ layer and creation of a disconnected tetrahedra dimer

1.2.2. Connected tetrahedral dimers (via $[BaO]$ layers and/or $[BaOX]$ ($X = Cl, F$) layers)

If one consider as a starting point the $10H$ - $BaMnO_{2.91}$ and $6H'$ - $BaMnO_{2.92}$ structures (Negas1971) with face-sharing octahedral pairs $[M_2O_9]$ at both sides of a h - $[BaO_3]$ layer (Fig.1-4, (a)) the replacement of the h -layer by a hexagonal h' - $[BaOX]$ layer, X =halide (Fig.1-4, (a)) or vacancies (Fig.1-4, (b)), leads to tetrahedral environment for the B cations. Here, two tetrahedra share a common oxygen corner (M_2O_7 dimers) while the X -halogen or vacancy is not taking part to the coordination of the metal-cations. It is important to note that ideally, within this $c/h'/c$ stacking, the X anions occupy the centres of a Ba_5 trigonal bipyramid (this point will be intensively discussed about our results). According to bond-valence sum calculations and DFT relaxations (Ehora2007) this latter coordination is not well adapted to O^{2-} anions. Vacancies or monovalent anions such as X/OH^- should be preferred (i.e. calculations shows that the h' - $[BaO]$ layer is more stable that h' - $[BaO_2]$).

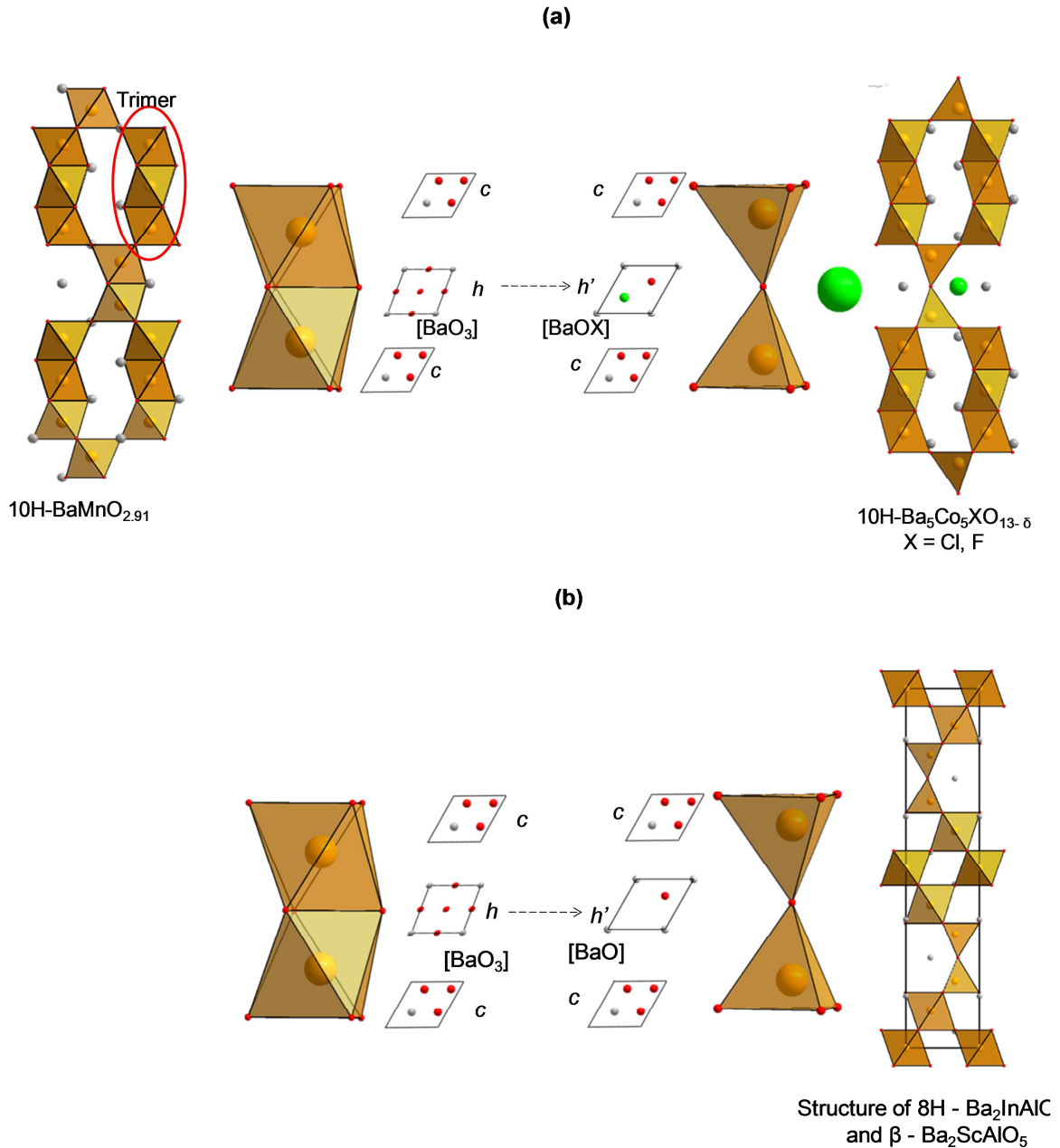


Fig.1-4: Schematic representation of the formation of (a) [BaOX] ($X = \text{Cl}$ and F) layers in: $\text{Ba}_5\text{Co}_5\text{XO}_{13-\delta}$ ($X = \text{Cl}, \text{F}$) (Ehora2007, Tancret2005, Kauffmann 2007c) and (b) [BaO] layers as in 8H - $\text{Ba}_2\text{InAlO}_5$ (Muller –Buschbaum1990) and β - $\text{Ba}_2\text{ScAlO}_5$ (Shpanchenko1990)

1.2.3. Other layers, the Br case

In some of the compounds at the basis of our work, the incorporation of $X = \text{Br}^-$ halides leads to different/unexpected layers, due to its critical anionic radius ($r_{\text{F}} = 1.33 \text{ \AA}$, $r_{\text{Cl}} = 1.81 \text{ \AA}$, $r_{\text{Br}} = 1.96 \text{ \AA}$, in a VI coordination). Double c' [$\text{Ba}_2\text{O}_2\text{Br}$] layers have been reported in this case ((Fig.1-5) leading to the two original polytypes 14H- $\text{Ba}_7\text{Co}_5\text{BrO}_{17-\delta}$ and 18R- $\text{Ba}_6\text{Co}_5\text{BrO}_{14-\delta}$ (Kauffmann2007). $\text{Ba}_6\text{Co}_5\text{BrO}_{14-\delta}$ can be described as deriving from 5H- $\text{BaCoO}_{2.8}$ (Boulahya2005) by replacing the c' - $[\text{BaO}_2]$ layer by two c' - $[\text{BaOBr}]$ layers, creating an 18-layers stacking sequence ($c'chhcc'$)₃. In the same manner, $\text{Ba}_7\text{Co}_6\text{BrO}_{17-\delta}$ can be derived from 12H- $\text{BaCoO}_{2.6}$ (Jacobson1980) by replacing the c' - $[\text{BaO}_2]$ layer by two c' - $[\text{BaOBr}]$ layers, creating the 14-layers stacking sequence ($c'chhhcc'$)₂. It leads to an extra degree of disconnection (along c) between terminal tetrahedra, and an important weakening of magnetic interactions between the individual blocks has been observed via spin-flop transitions (Toulemonde2010).

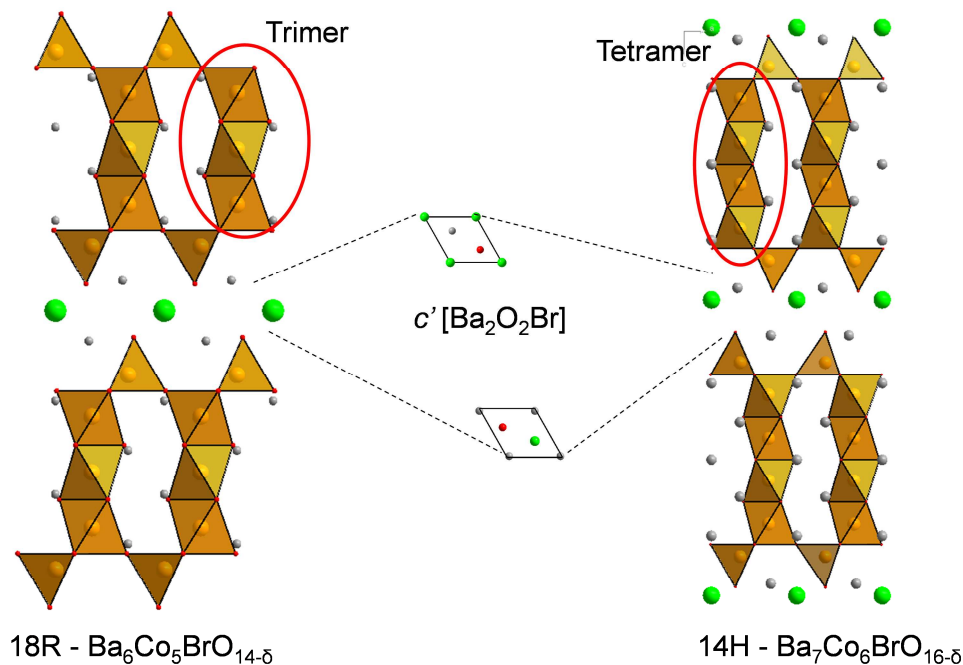


Fig.1-5: c' [$\text{Ba}_2\text{O}_2\text{Br}$] layers in bromo - cobaltites

1. 3. Cubic versus hexagonal layers: the driving force

We have seen that the structures adopted by ABX_3 phases (A = electropositive cations) are mainly ruled out by the structural tolerance factor (*Goldschmidt1926*). In the simple confrontation between hexagonal ($t > 1$) and cubic layers ($t < 1$), it is clear that hexagonal layers are preferred when B is too small for a 3D-corner sharing framework, leading to a face-sharing connections between the octahedra and smaller B---B distances.

However, according to the number of intermediates polytypes combining both h and c layers, the rationalization of the c/h ratio in the same chemical series appears topical. Here, we will particularly focus on the $BaBO_{3-\delta}$ (B = Mn, Fe, Co) series in which the incorporation of halides is at the basis of previous works by our group, and in which I have been involved during this work. Our choice for A = Ba^{2+} directly displaces t towards the hexagonal region due to its great ionic radius ($r_{Ba^{2+}} = 1.42 \text{ \AA}$ in an eight-fold coordination). About the adopted polytypes by the parent oxides, one should note that the rationalization via only the tolerance factor, even if federative, intrinsically implies several parameters such as the oxidation state of the transition metal B (r_B depends on the oxidation state) and consequently on the anionic non-stoichiometry. Then, the preferred location of oxygen vacancies within h - or c - slabs deserves attention and this is still a controversial point in the field of hexagonal perovskites.

-For instance, recent reinvestigations of the $BaMnO_{3-\delta}$ polytypes have undoubtedly fully located the oxygen vacancies in hexagonal layers (*Adkin2007*) even in strongly reduced compounds, e.g. 25% of oxygen vacancies in the h -layers of the 4H- $BaMnO_{2.65}$ polytype (*Adkin2006*) contrary to the previous structural models proposed by Gonzalez-Calbet and co-workers, based on electron diffraction data (*J.M. Gonzales – Calbet, 1993, 1994 and 1995a and 1995b*).

-Paradoxically, it is known that oxygen-deficiency in $BaCoO_{3-\delta}$ polytypes agglomerates in cubic-deficient c' - $[BaO_2]$ layers. It results that a “case by case” investigation may lead to important “general” contradictions and that a globalization of “all-metal-behaviours” appears rather risky. We have closely inspected the three concerned Ba-M-O systems (M=Co, Fe, Mn) on the basis of the evolution of the \bar{h}/h

ratio versus the mean oxygen vacancies, \bar{h} denoting all layers which do not create face-sharing connections = c , c' and h' layers (c' and h' are included here taking into account their “naturally deficient” character and “corner sharing interfaces”). It yields to general trends, as follows:

1.3.1. The BaCoO_{3-δ} system

Cobalt oxides have drawn considerable attention in the last few years due to their interesting electronic structure and various properties, such as colossal magnetoresistance, phase separation, aging and memory effects, mixed conductivity, superconductivity, and metal insulator transitions. This large panorama of potentialities is mainly based on the easy capacity of Co to adopt different oxidation degrees within variable coordination (see for instance *Helmut1993; Bednorz1986*). In the absence of oxygen vacancies, BaCoO₃ exhibits the ideal hexagonal 2H- structure (*Taguchi1977*) consisting of infinite chains of CoO₆ face-sharing octahedra, running along the c direction. Upon reduction, h -[BaO₃] are replaced by deficient ordered cubic c' -[BaO₂] layers, which create blocks with disconnected terminal CoO₄ tetrahedra, corner-shared with linear oligomers. The first investigation of this system by Zanne and co-workers (*Zanne1972*) was performed on powder samples and reveals a number of not-clearly identified hexagonal polytypes (they have been denoted 2H-BaCoO_{3-δ} ($2.85 < 3-\delta < 3.0$), 7H ($2.52 < 3-\delta < 2.575$), 12H ($2.43 < 3-\delta < 2.49$), 15H ($2.10 < 3-\delta < 2.23$), an orthorhombic phase BaCoO_{2.07} and finally BaCoO₂.

According to more recent results, the large number of reported phases in this early work could result from misinterpretation of XRD patterns due to the probable coexistence of several phases with closely related patterns in the samples. In fact, nowadays, only four structures are clearly identified:

- The 12H-BaCoO_{2.83} (strings of four face-sharing octahedra with terminal disconnected CoO₄ tetrahedra). It was first assigned to a mean O_{2.6} stoichiometry from redox-titration in early works (*Jacobson1980*), but considering the multiphase sample used in this early work and the uncontested aggregation of vacancies in c' -[BaO₂] layers (five [BaO₃] for one c' -[BaO₂]) we consider the O_{2.83} ideal calculated stoichiometry as the true-one.

- The 5H-BaCoO_{2.8} (oxygen content determined by neutron diffraction) with strings of three face sharing octahedra disconnected by terminal CoO₄ tetrahedra (Boulaya2005). We will also consider in the phase diagram shown in Fig.1-6, the 5H'-BaCoO_{2.74} polytype (hypothetic structure observed by high resolution electron microscopy (HREM), oxygen content determined by thermogravimetric reduction of the sample until the formation of BaO and Co) in which c-[BaO₃]-layers replace c'-[BaO₂] layers of the 5H-form (Parras1995). It is however probable that this early HREM-interpretation in fact concerns the 5H-form and the 5H' remains hypothetical.
- The cubic BaCoO_{2.23} that predominates in highly reducing conditions, from early reports (Strauss1951). During my work I isolated crystals of this phase (not reported in the manuscript) and verified the oxygen stoichiometry close to 2.
- The hexagonal BaCoO₂ with only [BaO₂] layers forming corner-sharing tetrahedra (Spitsbergen1960).

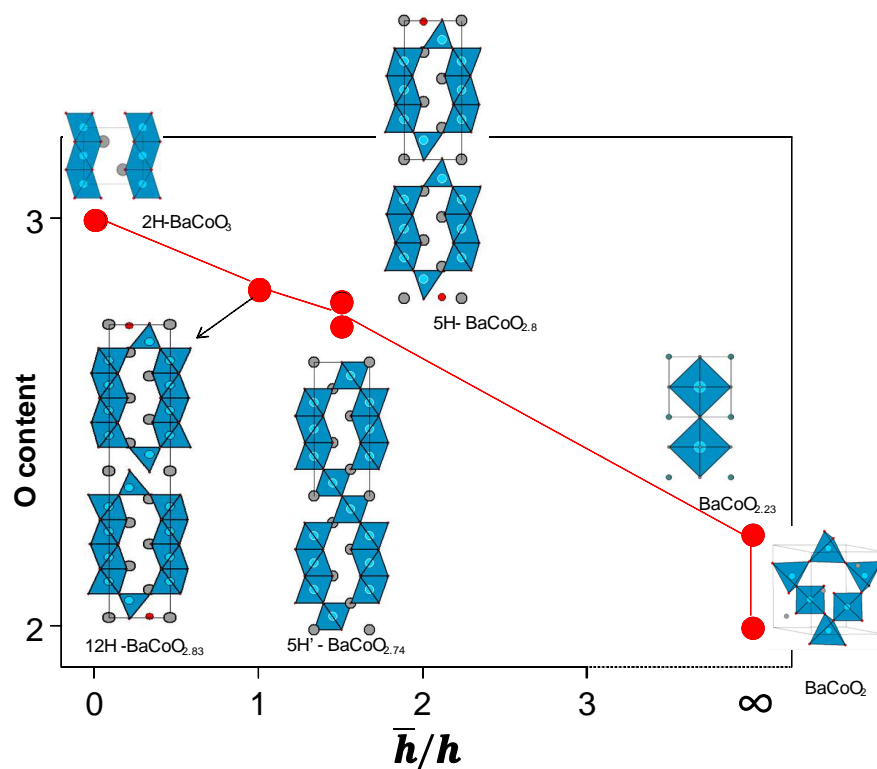


Fig.1-6. : Pseudo phase diagram for BaCoO_{3-δ} system: oxygen content as a function of the \bar{h}/h

Plotting the \bar{h}/h ratio versus the oxygen content allows us to distinguish a correlation between these two parameters (Fig.1-6). Taking into account the cubic-[BaO₂] deficient layers, it seems that the increasing \bar{h}/h ratio leads to the increase of

oxygen vacancies. Of course, in some way, it is driven by the tolerance factor since $r_{\text{Co}^{n+}}$ increases while cobalt is progressively reduced, but this (too)-direct presumption neglects the influence of O vacancies in the t -calculation. Our plotted (\bar{h}/h) against (O-content) behaviour is only based on structural observations and chemical analyses and gives factual trends of this complex system. **Then one can conclude that in the Ba-Co-O system, connection by faces vanish upon reduction and then the c/c'/h'-layers would be preferentially occupied by anion vacancies, logically accompanied by an \bar{h}/h increase upon reduction.**

1.3.2. The BaMnO_{3-δ} system

Starting from the ideal 2H-BaMn⁴⁺O₃ crystal type, first reports of other BaMnO_{3-δ} polytypes were given by Negas and Roth (*Negas1971*) who described a number of different phases (15R, 6H', 10H (*Fig.1-7*) in which the ratio of corner sharing (c) to face-sharing (h) layers is variable. Other terms have been discovered and described latter, but Gonzalez-Calbet and co-workers (*Gonzales – Calbet1993, 1994, 1995a and 1995b*) have rationalized these series of BaMnO_{3-δ} hexagonal phases, through the establishment of a relationship between the relative (h/c) proportions and the overall stoichiometry of the phase. This has been expressed by the relation: $\delta = (0.5c) / (h + c)$, where δ is the oxygen non-stoichiometry and c and h are the respective numbers of cubic and hexagonal layers in a repeat unit. This leads them to suggest that the most straightforward explanation for this relationship is that the anion- vacancies would be located in the cubic layers giving them an overall formula of [BaO_{2.5}] for the cubic layers, stacked with [BaO₃] hexagonal layers. Then, factually, the increase of c/h is followed by the increase of the oxygen non-stoichiometry from infinite MnO₆ octahedral strings (from 2H-BaMnO₃ (*Hardy1962*) to the most-reduced 4H-BaMnO_{2.65} (*Adkin2006*). In this latter reduced term, the oxidation content comes from neutron diffraction (ND) investigations.

Other polytypes have been prepared and finally characterized in a latter work by the same Oxford-group (*Adkin2007*). Contradictory, the fine structural analyses from ND experiments, show the systematic presence of O vacancies almost exclusively in the hexagonal (face-sharing) layers, on the opposite to what was described in prior works, and to what was observed for the Ba-Co-O system. Then,

paradoxically the increase of oxygen vacancies is accompanied by the relative decrease of the concentration of h -layers in which they are located. The preferred location of vacancies has been explained after the examination of the different coordination environments adopted by oxide ions in these structures, particularly at the level of the barium-oxygen bonds. It was proposed that the removal of hexagonal-oxygen would result in a lower energy-loss of the lattice due to their less bonding character. However the difference with the Ba-Co-O system suggests more complex reasons or combinations of reasons such as the fundamental difference between Co and Mn cations in terms of oxygen coordination. At least, on the basis of \bar{h}/h vs. the oxygen content Ba-Co-O and Ba-Mn-O behave similarly (Fig.1-7). **To conclude compounds of the Ba-Mn-O system respect the \bar{h}/h increase upon reduction, but h -layers agglomerate most of the oxygen vacancies.**

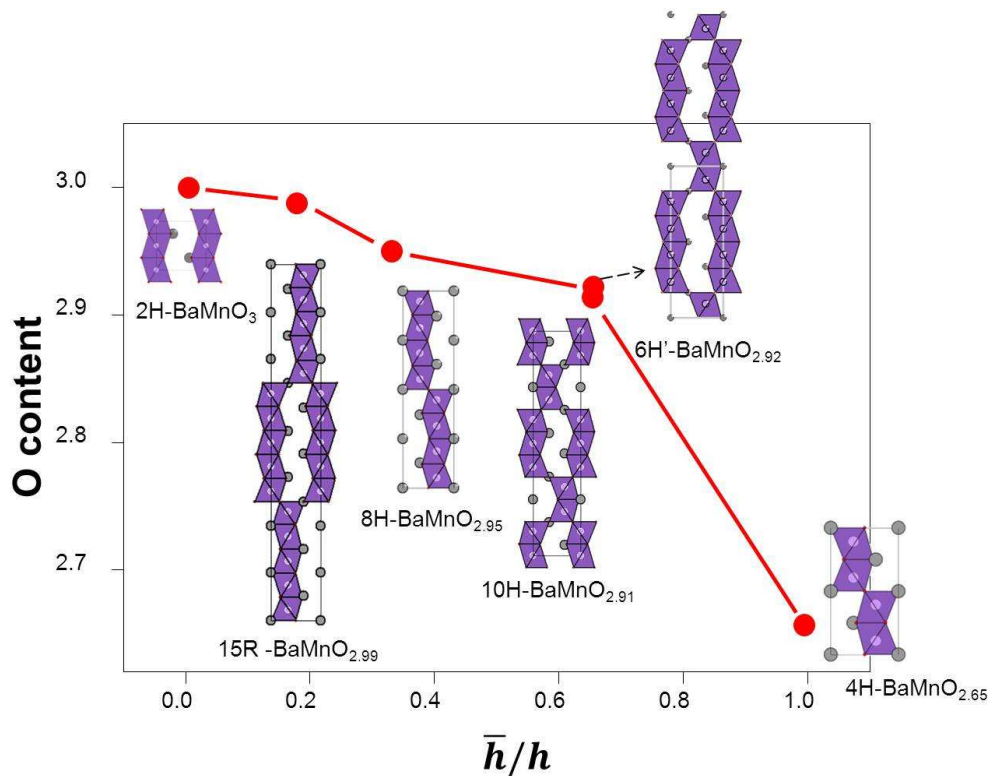


Fig.1-7: Phase diagram for BaMnO_{3-δ} system: Oxygen content as a function of the \bar{h}/h ratio in the BaMnO_{3-δ} system

1.3.3. The BaFeO_{3-δ} system

Despite the close chemical behaviour of Fe and Co cations, the crystal-chemistry of Ba-Fe oxides is different, probably due the important differences in ionic radius between high spin (HS) or low spin (LS) conformations that act as extra-parameters. As a symptom, no 2H-BaFeO_{3-δ} type structure was reported.

In general, in this system the oxygen defects show a great tendency for ordering, considering the progressive transition from the 6H-BaFeO_{3-δ} (small δ values) (*Grenier1989*) to the ordered monoclinic-distorted BaFeO_{2.5} with only *c*-layers and O/ ordering. Intermediate cubic deficient phases have been reported for $0.44 < \delta < 0.5$, but their stabilization involves meticulous synthesis, using highly “reactive” precursors and a severe control of the heating/cooling cycles under particular working atmospheres (*Gonzales – Calbet1990*). In a δ range between 0.2 – 0.4 in oxygen non-stoichiometry, the 6H hexagonal polytype exists, while after heating under oxygen, for $0.07 \leq \delta \leq 0.13$, a 12H polytype predominates.

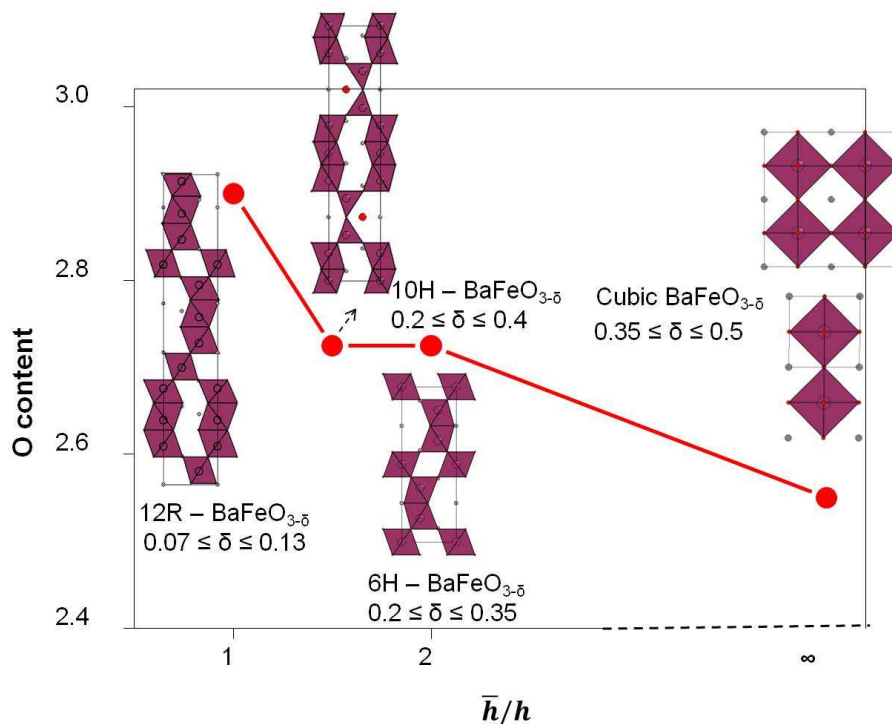


Fig.1-8: Phase diagram for BaFeO_{3-δ} system: Oxygen content as a function of the \bar{h}/h ratio in the BaFeO_{3-δ} system

Note also that for δ between 0.2 and 0.4, two 10H-polytypes (three face sharing octahedra connected by tetrahedral dimers) have been reported after decomposition of metal-organic precursors or synthesis in KOH solutions (*Zanne1971, Gomez2001, Delattre2004*). They are more or less distorted but both include central h' -[BaO₂] layers. We already explained in section 1.2.2. (Page 19) that we seriously doubt about the true existence of these h' -[BaO₂] layers in such a configuration for reasons detailed in (*Ehora2007*). In fact, one oxygen atom is not correctly bonded within its Ba₅ pyramid, and a vacancy or a counter anion present in the precursors (OH⁻, Cl⁻) would be better suited. However, we considered the published 10H-phases in the following diagram (Fig.1-8). **Once more, the \bar{h}/h ratio evolves in the same manner as for Co and Mn as a function of the oxygen content which suggests cubic (and ordered h') deficient layers.** The most reduced cubic BaFeO_{3- δ} term clearly contains deficient cubic-[BaO_{3- δ}] layers.

1.3.4. Mixed Ba(MM')O_{3- δ} compounds

This general behaviour is also respected in the literature-reported mixed compounds related to the (Mn/Co) and (Mn/Fe) Ba-O systems (Table 1-1). The reported compounds have generally been investigated by ND:

- In the former Mn/Co case, a 5H-phase (oxygen content (hereafter O.C.) = 2.80, $\bar{h}/h = 1.5$) succeeds to a 12H-phase (O.C. = 2.83, $\bar{h}/h = 1$).
- In the second system (Mn/Fe), a 10H-form (O.C. = 2.73, $\bar{h}/h = 1.5$) succeeds to a 6H-form (O.C. = 2.87 - 2.72, $\bar{h}/h = 0.5$).
- No mixed M=(Fe,Co) have been reported if one restrains our field of investigation to A= Ba only. It is clear that the introduction of mixed (A = Ba, Sr, La ...etc) sites is expected to strongly deviate the tolerance factor, and has not been considered here for comparison of homogeneous series even if some mixed compounds have been reported (La_{0.6}Sr_{0.4}Co_{1-y}Fe_yO₃ (y = 0 – 1) (*Duanping2008*)).

Table 1-1: \bar{h}/h ratio and oxygen content (O.C.) in hexagonal $Ba(MM')O_{3-\delta}$ compounds:

Compound	\bar{h}/h ratio / sequence	O.C.	Bibliography
Mn – Co			
5H - $BaMn_{0.2}Co_{0.8}O_{3-\delta}$	$(c+c')/h = 1.5$ (cc'chh)	2.80	Miranda2008
12H - $BaMn_{0.4}Co_{0.6}O_{3-\delta}$	$(c+c')/h = 1$ (cc'chhh) ₂	2.83	Miranda2007
Mn – Fe			
10H - $BaMn_{0.4}Fe_{0.6}O_{3-\delta}$	$(c+h)/h = 1.5$ (hch'ch) ₂	2.73	Miranda2007a
6H' - $BaMn_{0.6}Fe_{0.4}O_{3-\delta}$	$c/h = 0.5$	2.72	Miranda2009
6H' - $BaMn_{0.85}Fe_{0.15}O_{3-\delta}$	(hchhhc)	2.87	

1.3.5. Cobalt oxo-halides

We will now investigate the cobalt oxo-halides at the origin of this work. In the laboratory, we recently evidenced a series of modular halogeno-cobaltites, $Ba_{n+2}Co_{n+2}XO_{3n+4}$ (X=Cl, F), in which the slicing in $(n+2)h$ -individual blocks is achieved by hexagonal h' -[BaOX_{1-x}] halides-layers. Contrarily to what was ideally reported in the section 1.2.2. (Page 19), the X_{1-x} non-stoichiometry denotes slight deviations from the ideal h' -[BaOX] layer. h' layers create corner-sharing terminal CoO₄ tetrahedra linked to trimers (n=3) or tetramers (n=4) of face-sharing octahedra, (Fig.1-9). The atom-labelling available in all this manuscript is shown on Fig.1-9 for these two structural types.

For X = F and Cl, the n = 3 corresponds to a 10H polytype, while for n = 4 we have a 6H types. The rationalization of their domains of existence as a function of the redox was not performed so far. Considering the corner-sharing tetrahedra at both sides of the deficient h' -[BaOX_{1-x}] layers, we have performed this analysis in the same manner as for 10H-Fe oxides (\bar{h}/h vs. oxygen content). Preliminary, it is important to remind that for both X = F and Cl the 10H-forms results from the transformation at high temperature of the 6H-form (T = 1030°C for X = Cl). As observed on the TGA curves (Fig.1-10), this transformation is performed during an important reduction-wave, which intuitively validates the same behaviour as depicted for the oxides: 6H ($\bar{h}/h = 1$) → 10H ($\bar{h}/h = 1.5$ upon reduction).

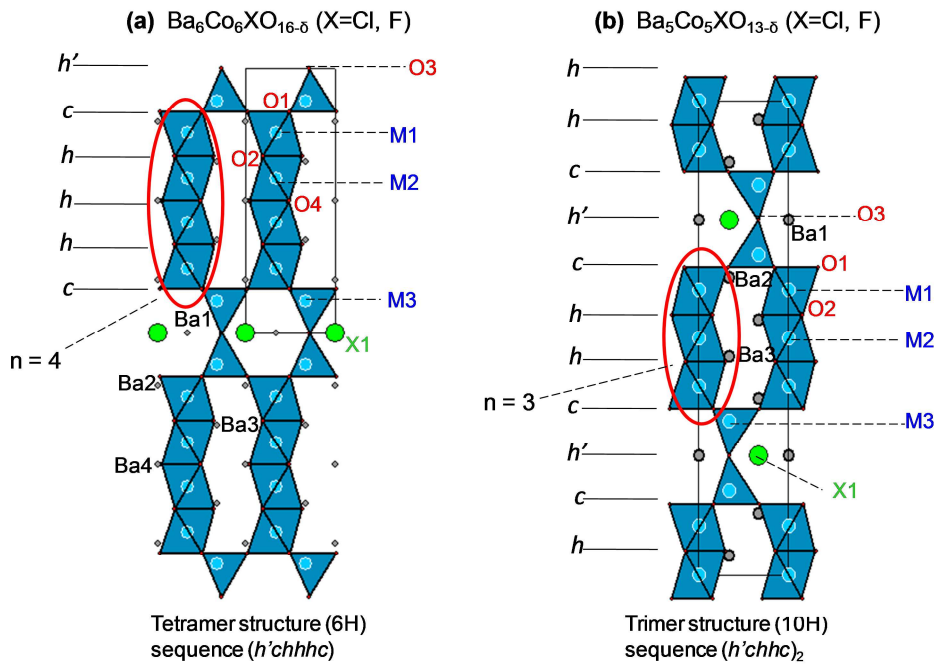


Fig.1-9: Tetramer (6H, (a)) and trimer (10H, (b)) structural types for cobalt oxohalides (halogen X = Cl, F) and atoms labeling used in this manuscript.

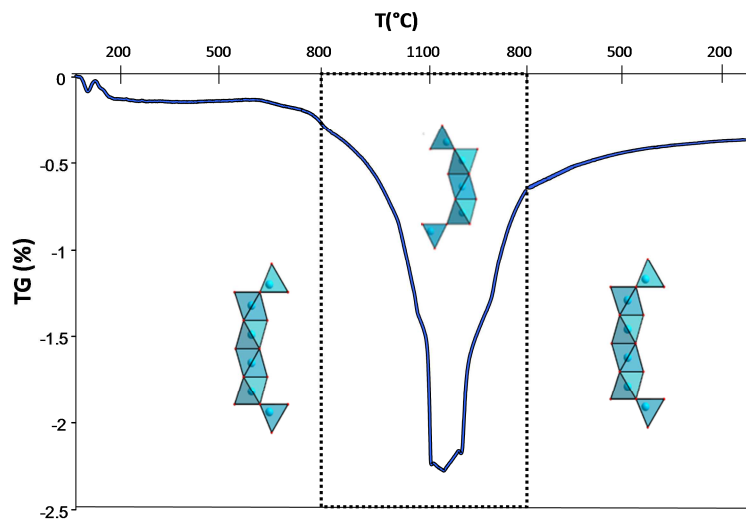


Fig.1-10: TGA curves $Ba_6Co_6ClO_{16-\delta}$ showing the 6H \leftrightarrow 10H phase transformation between 900 – 1100°C.

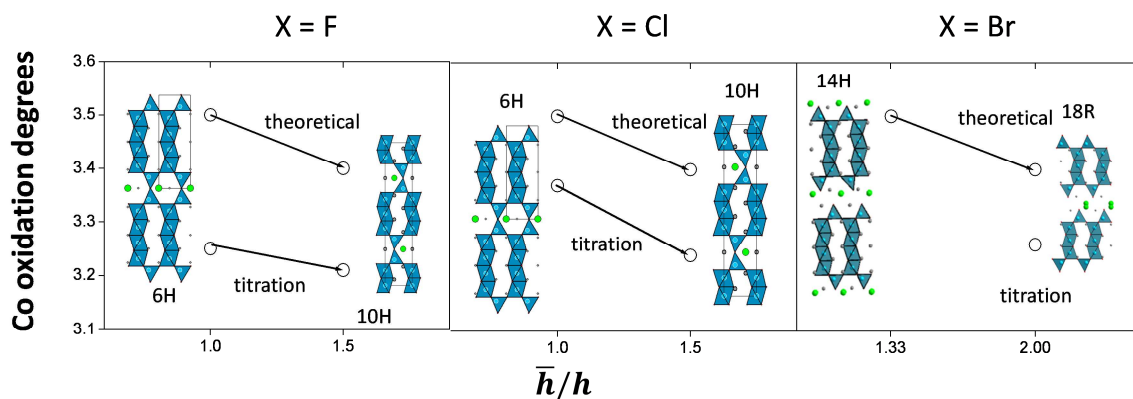


Fig.1-11: Phase diagram for cobalt oxo-halides: the dependence of \bar{h}/h ratio with Co oxidation degree. Theoretical data do not consider extra-oxygen vacancies

The phase diagram is shown on the Fig.1-11 as a function of the cobalt valence due to the mixed anionic nature ($O^{2-} + F^-$) of oxo-halides. The metal valences reported here were obtained by my recent chemical titrations (given in “Materials and method” section) and are generally in good agreement with previously reported non-stoichiometry from ND analyses (*Mentré2008 and 2010, Kauffmann2007a*). For the bromide case where the blocks are disconnected by $[Ba_2O_2Br]$ layers (*Kauffmann2007b*) this trend remains the same.

1.3.6. Conclusion:

For $BaMO_{3-\delta}$ ($M = Co, Fe, Mn$) as well as for the related oxo-halogeno cobaltites, we have established a dependence of the \bar{h}/h ratio versus the oxidation state of the metal. Then, corner-sharing connections will be preferred in more-reduced compounds. Our redox phase diagrams strongly suggest the preference of oxygen vacancies in the corner-sharing layers rather than in face-sharing ones, but factually it seems to depend on the nature of the cation. Of course, this behaviour is obvious in the cases where deficient c' - $[BaO_2]$ or h' - $[BaOX]$ layers concentrate the vacancies in an ordered manner. On the opposite, even if the announced increase with metal reduction is also verified for the $BaMnO_{3-\delta}$ system, oxygen vacancies concentrate in the hexagonal (face-sharing) layers, leading to strongly deficient h -layers. In conclusion, at moderate reduction stages, we conserve a $M^{3/4+}$

mixed valence which indicates, from the viewpoint of local geometry, that Co and Fe are well adapted to corner-sharing MO_{6-x} deficient polyhedra, while Mn prefers linear oligomers of deficient MO_{6-x} groups sharing faces and edges (Fig.1-12).

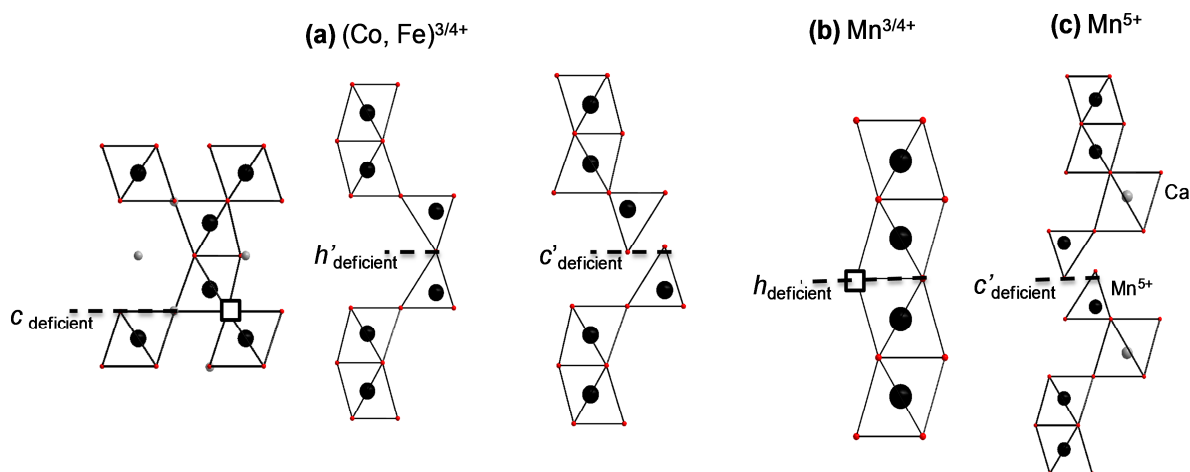


Fig.1-12: Corner-sharing deficient polyhedra preferred by Co and Fe at valence state 3 or 4 (a); $Mn^{3+/4+}$ prefer linear oligomers of face sharing deficient MO_6 octahedra (b); Mn^{5+} prefers tetrahedral coordination (c)

This fact is partially explained by the likely creation of (Co/Fe) O_4 tetrahedra at both sides of c' or h' -layers while a true tetrahedral coordination for Mn is only reported for Mn^{5+} , out of the redox range concerned here (e.g. $Ba_7Mn_5Ca_2O_{19}$ (Floros2002), $Ba_8Mn_6Ca_2O_{22}$ (Floros2000) and $Ba_6Ru_2Mn_2Na_2O_{17}$ (Quarez2003)). This aspect (phase diagram vs. redox, location of the vacancies rationalization) will be explored in details for new oxo-halides in this work.

Chapter 2

Chapter 2. Mixed $\text{BaMX}_{0.2-x}\text{O}_{3-\delta}$ systems

This chapter is dedicated to the extension of the previously observed Ba-halogeno-cobaltites to mixed metallic system $M = \text{Fe}, \text{Co}, \text{Mn}$. We already argued the choice of Ba^{2+} as the A cation because of his larger ionic radius favouring hexagonal perovskites. The complex phase diagrams described for Fe, Mn and Co oxides let us examine in details the possibility to incorporate $X=\text{F}, \text{Cl}$ and Br in these chemical systems, keeping in mind our wishes to rationalize the observed phases as a function of several parameters (redox, vacancies location, ...etc). Interestingly in all these compounds, the electrical and magnetic properties are based on the capacity of the transition metal to adopt different oxidation states. Indeed, the aim of this work is then to tune the nature and oxidation state of the metallic cations in targeted hexagonal perovskite structures in order to:

- rationalize the predominant crystal structure
- understand possible cationic segregation effects over the available sites
- probe the evolution of magnetic/electric properties
- find potential new polytypes

2. 1. $\text{BaMX}_{0.2-x}\text{O}_{3-\delta}$ (M = Mn, Fe, Co; X = Cl, F) phase diagrams

A series of Co substitutions in the $\text{Ba}_{n+2}\text{Co}_{n+2}\text{XO}_{3n+4}$ ($X=\text{Cl}$ or F) ($n = 3/\text{trimer}$ and $n = 4/\text{tetramer}$) compounds, using Fe, Mn or both, were performed in a first stage. Our syntheses are detailed below. It is important to note that in contrast to pure Cobalt-compounds, the mixed compounds show only one stable polytype (trimer or tetramer or a mixture of both) with no drastic influence of the thermal treatment (controlled cooling versus quenching, etc...), other way said, if the Co-tetrameric compounds displays a HT transition into trimer, this is not the case of mixed M/M' compounds. Then, depending on these preliminary results, the X ratio was adapted in a second stage to the observed polytype in order to match the

stoichiometric formula Ba₅M₅X₁O_{13-δ} for trimers and Ba₆M₆X₁O_{16-δ} for tetrameric compounds.

Synthesis of the compounds:

2.1.1.a) Ba(Co,Fe)X_{0.2-x}O_{3-δ}.

Ba₅Co_{5-y}Fe_yFO_{13-δ} (y = 1 - 5) compounds were synthesized as follows: a stoichiometric mixture of BaCO₃ (Sigma-Aldrich, 99%), Co₃O₄ (Alfa Aesar, 99.7%), Fe₂O₃ (Prolabo, 99%), BaF₂ (Prolabo, 99%) was heated in air at 900°C, for 24 h, in an alumina crucible, after preliminary grinding. The mixture was then cooled to room temperature in 6 hours.

The synthesis of the Ba₅Co_{5-y}Fe_yClO_{13-δ} (y = 1 - 5) solid solution was performed starting with BaCO₃ (Sigma-Aldrich, 99%), Co₃O₄ (Alfa Aesar, 99.7%), Fe₂O₃ (Prolabo, 99%) and BaCl₂·2H₂O (Prolabo, 99%). The mixture was intimately ground in an agate mortar and then heated in air at 1000°C, for 48h, in an alumina crucible before cooling to room temperature in 6 h.

Some terms were prepared by introducing lower quantities of BaX₂ in order to induce, by synthesis, halogen vacancies with the aim of studying the effect on the thermal behaviour of these compounds. This will be discussed latter (section 2.2.1.b)) Thus were obtained the terms Ba₅Co₂Fe₃F_{0.6}O_{13-δ} (synthesis in sealed gold tube, at 950°C for 48h, quenched), Ba₅Co₂Fe₃Cl_{0.6}O_{13-δ} and Ba₅Co₂Fe₃Cl_{0.7}O_{13-δ} (synthesis - as described before, for chlorine solid solution). The term Ba₅Fe₅Cl_{1-x}O_{13-δ} (x = 0.5) was also obtained in a sealed gold tube heating the reactants at 900°C for 48h followed by air quenching at room temperature. In air, the same Cl-deficient synthesis gives a biphasic mixture with Ba₃Fe₂Cl₂O₅ (*Leib1985*) as an impurity.

2.1.1.b) Ba(Co,Mn)X_{0.2-x}O_{3-δ}

The syntheses of these compounds are rather difficult and not well reproducible. It implies high temperature treatments and multiple re - grinding steps, starting with BaCO₃ (Sigma-Aldrich, 99%), Co₃O₄ (Alfa Aesar, 99.7%), MnO (Sigma-Aldrich, 99%) and BaCl₂·2H₂O (Prolabo, 99%) or BaF₂ (Aldrich, 99.99%) heated at 700°C for 12h in order to insure the homogeneity of the sample. The sample is then quenched to room temperature and pressed into pellets, heated at 1000°C for 72h

and quenched again to room temperature. After a regrinding, the powder obtained is mixed with 1/10 molar excess of $BaCl_2 \cdot H_2O$ or (BaF_2 for oxo-fluorides) and heated again at $1000^\circ C$ for 48h, with another quenching at room temperature. The black powder obtained was washed with hot water on a filter paper in order to eliminate the $BaCl_2/BaF_2$ excess.

2.1.1.c) $Ba(Mn,Fe)X_{0.2-x}O_{3-\delta}$

The synthesis was performed starting with $BaCO_3$ (Sigma-Aldrich, 99%), Co_3O_4 (Alfa Aesar, 99.7%), Fe_3O_4 (Prolabo, 99%) and $BaCl_2 \cdot 2H_2O$ (Prolabo, 99%) or BaF_2 (Aldrich, 99.99%) carefully weighted in stoichiometrical ratio (Ba/total transitional metal = 5/5) and well grounded, heated at $900^\circ C$ for 48h (96h for F-compounds, followed by air quenching). For Cl – compounds, the temperature was then raised at $1100^\circ C$ and maintained for another 48 h, followed by an air quenching at room temperature.

2.1.1.d) $Ba(Co,Mn,Fe)X_{0.2-x}O_{3-\delta}$

The stoichiometric and homogenous mixture of $BaCO_3$ (Sigma-Aldrich, 99%), Co_3O_4 (Alfa Aesar, 99.7%), Fe_3O_4 (Prolabo, 99%), MnO (Sigma-Aldrich, 99%) and $BaCl_2 \cdot 2H_2O$ (Prolabo, 99%) or BaF_2 (Aldrich, 99.99%) is heated at $900^\circ C$ for 48h ($950^\circ C$ for F compounds; after that, the furnace was left to cool down). For Cl compounds, the temperature was raised at $1100^\circ C$ and maintained for 48h, followed by an air-quenching to room temperature.

The synthesis procedures presented here are of course the results after optimisation of the synthesis method implying several synthesis attempts. We should also precise that since Ba/M is always 1/1 (indifferent the structural type), Ba_5 or $6M_5$ or $6X_{1-x}O_{13}$ or $16-\delta$ (where x = halogen vacancies and δ = oxygen vacancies) will be some times simplified at $BaMX_{0.2-x}O_{3-\delta}$.

2.1.1. Predominant phases in the oxo – chloride phase diagram:

The results of all the syntheses can be summarized in a pseudo-ternary diagram having non-doped Co, Fe, and Mn compounds at the triangle extremities. The predominating phases in the case of binary combinations (Co-Fe, Co-Mn and Fe-Mn) are on the diagram edges and in the case of ternary (Co, Mn and Fe) substitutions, in the interior (Fig.2-1 for Cl and Fig.2-2 for F). All the compounds represented in these diagrams are obtained in powder form (pure or multiphasic mixtures) and the detailed structural characterization will be discussed later.

Oxo-chloride phase diagram

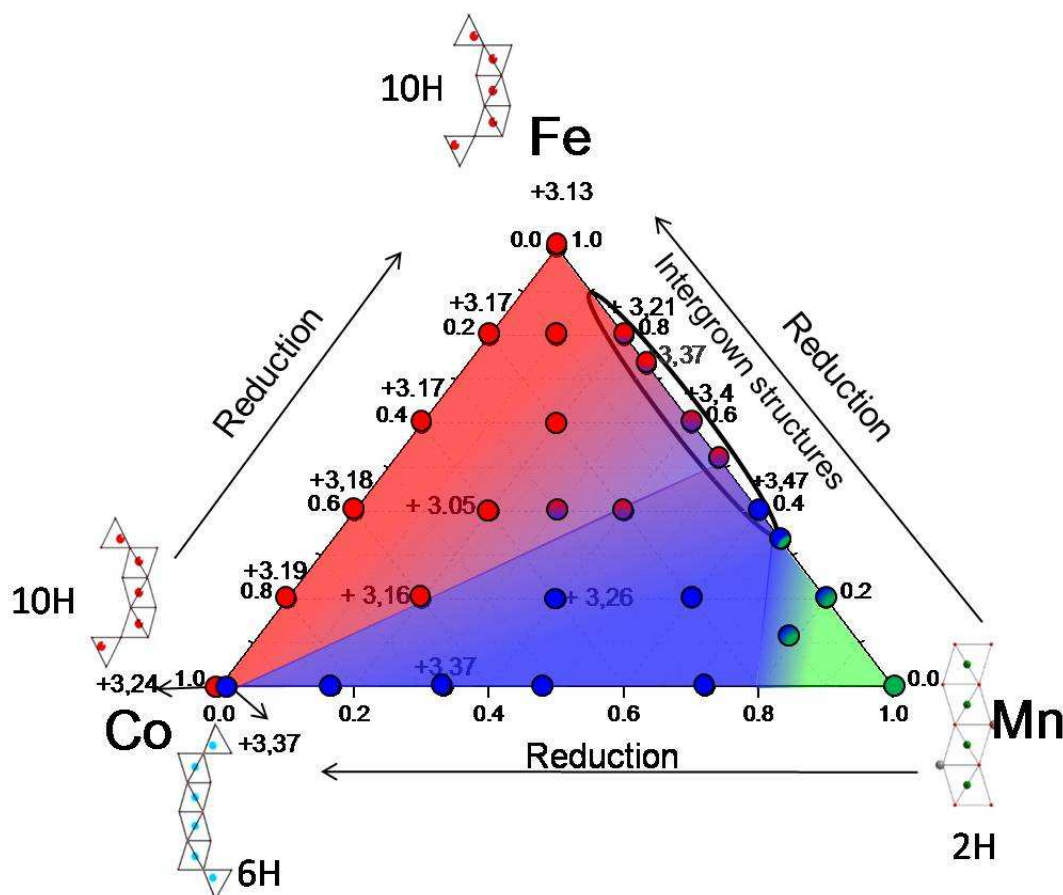


Fig.2-1: Structural-tendency diagram in the $Ba(Co,Fe,Mn)_1Cl_{0.2-x}O_{3-\delta}$ system. The tetramer (6H) structures are represented in red, the trimer (10H) structures in blue and the 2H - $BaMnO_3$ in green. The oxidation degrees determined by iodometric titration are also given. Multicolor dots show multi-phased samples.

2.1.2.a) Line Co – Fe (binary substitutions $Ba(Fe,Co)Cl_{0.2-x}O_{3-\delta}$)

In the cobalt-only case, let recall that tetrameric (more oxidized) or trimeric (more reduced) polytypes are obtained depending on the preparation/cooling method. For this line, the X-ray diffractograms of all the obtained compounds correspond to $10H-Ba_5M_5Cl_{1-x}O_{13-\delta}$ (trimeric form) whatever the thermal treatment (slow cooling or quenching). According to the average oxidation degree of the transitional metal determined by iodometric titration (and confirmed by neutron diffraction when available), a decrease of metal valence is observed as Co is replaced by Fe (from $Co^{+3.37}(6H)/Co^{+3.24}(10H)$ to +3.13 for $BaFeCl_{0.2-x}O_{3-\delta}$. **As stated previously, this reduction will reinforce an increase of the \bar{h}/h ratio, then passing from the tetrameric to trimeric structure.** Moreover, compared to other lines of the diagram, (see below) the easy preparation of single-phased compounds highlights the stability of Fe in the trimeric 10H-structure. As also observed for the Ba-Fe oxides, the reported phases never display linear face-sharing of n octahedra with $n > 3$. As a matter of fact, in our relatively “mild” synthesis conditions (compared to what is already reported in literature: $T > 1300^\circ C$, O_2 atmosphere, N_2 quenching; see for instance *Floros2002*), one could conclude that the combination of iron and Cl in hexagonal perovskite displaces the mean metal valence from $M^{+3.5}$ to M^{+3} .

2.1.2.b) Line Co – Mn (binary substitutions $Ba(Co,Mn)Cl_{0.2-x}O_{3-\delta}$)

The XRD patterns can be indexed using either pure 6H mixed Co–Mn compounds, either biphasic mixtures of 6H compounds and 2H- $BaMnO_{3-\delta}$, depending on the Mn/Co ratio (with the increase of Mn/Co ratio, is increasing also the yields of 2H- $BaMnO_{3-\delta}$ obtained). The presence of this 2H-phase as well as the stabilization of only the 6H structural oxo – chloride Co/Mn type is compatible with the greater oxidation degrees of the metals with the incorporation of Mn and to its preference for longer face-sharing octahedral strings. The redox titration was performed for the single-phased Mn/Co = 0.33/0.67 giving a rather high valence of +3.37, similar to what titrated on the Co-tetrameric compound. This relationship can be summarized

by: $Mn/Co \uparrow \leftrightarrow O.D. \uparrow \leftrightarrow \bar{h}/h \downarrow$; other way said, on increasing Mn/Co ratio, the average oxidation degree (O.D.) increases, at the origin of a \bar{h}/h decrease (\rightarrow tetrameric form stable).

We already mentioned in the synthesis-section, punctual difficulties to isolate Co/Mn single-phased materials (2 weeks synthesis with different steps and heating temperatures) and the general irreproducibility which sometimes lead to a mixture of two 6H-compounds or sometimes to a 6H/2H mixture. This competition between stable compounds is at the basis of the stabilization of a new phase that combines both the characteristics of oxo-halide cobaltites (blocks with terminal tetrahedral dimers delimited by the h' -[BaOCl] layer) and characteristics of Ba/Mn-oxides (= long-face-sharing strings = hexamer) at high Mn/Co ratio (0.75/0.25) ($Ba_8Co_2Mn_6ClO_{22}$ published in *Iorgulescu2010*). This new compound will be detailed in the section 2.2.3. (Page 73). **At least, about the general observation in this line, we can confirm once more, the stabilization of the 6H-polytype assorted with the mean oxidation of M during the Mn incorporation.**

2.1.2.c) Line Fe – Mn (binary substitutions $Ba(Fe,Mn)Cl_{0.2-x}O_{3-\delta}$)

The results of our redox titrations shown on the Fig.2-1 validate the important oxidation effect of the Mn-incorporation in the Fe-rich matrix. Taking into account the results observed for the two previous lines, the Fe/Mn substitution is all the more interesting since, clearly, the two 5H (Fe-effect) and 10H (Mn-effect) polytypes should be in competition. Once more, accordingly to XRD and iodometric titrations, the mean behaviour can be also summarized by: $Mn/Fe \uparrow \leftrightarrow O.D. \uparrow \leftrightarrow \bar{h}/h \downarrow$ (\rightarrow tetrameric form favoured). Along the line, several zones are distinguished according to the Mn substitution y- ratio in $BaFe_{1-y}Mn_yCl_{0.2-x}O_{3-\delta}$:

- $0 \leq y < 0.4$: biphasic mixture of 10H and 6H polytypes, 10H predominant (red area in the phase diagram)
- $0.4 \leq y < 0.6$: biphasic mixture 10H + 6H polytypes, 6H predominant (blue area)
- $0.6 \leq y < 0.8$: biphasic mixture 6H + 2H polytypes, 6H predominant (blue area)
- $0.8 \leq y \leq 1$: biphasic mixture 2H + $BaCl_2$ (green area)

Note also the practical difficulties to distinguish the phases in competition, due to the similarities between their XRD patterns. For instance the XRD pattern of the $y = 0.4$ term is very tricky since it can be indexed with only one 10H-unit cell but, in reality, an intergrown structure was observed by HRTEM. This aspect will be largely detailed in the 2.2.4. (Page 81). **Despite these difficulties, on the basis of the predominant phase, the increasing relative amount of the 6H phase with the mean metal valence is once again observed.**

2.1.2.d) Ternary substitution Ba(Co,Fe,Mn)Cl_{0.2-x}O_{3-δ}

These substitutions permit us to create the central areas represented on the phase diagram (Fig.2-1). The structural types stabilized follow the general trends observed on the binary lines. In fact, starting from the systematic 10H-structure found for the Co/Fe compounds, the Mn ratio y in Ba(Co,Fe)_{1-y}Mn_yCl_{0.2-x}O_{3-δ} acts as the decisive factor. We identified:

- $0 \leq y \leq 0.2$: 10H (red zone)
- $0.2 < y \leq 0.3$: biphasic mixture of 6H + 10H (red + blue zone)
- $0.3 < y \leq 0.6$: 6H (blue zone)
- $0.6 < y \leq 0.8$: biphasic mixture of 6H + 2H (none predominant) (blue + green zone)
- $0.8 < y \leq 1$: predominant non-halogenated 2H (green zone).

2.1.2. Predominant phases in the oxo-fluoride phase diagram:

A similar phase diagram has been established in the case of oxo-fluoride compounds. It is shown on the Fig.2-2. Generally we can observe the same tendencies than for the oxo-chloride compounds leading to three major zones: predominant 10H, 6H and non-fluorinated 2H-phases. Then (starting from Co end-members) the mean reducing effect after incorporation of Fe (or oxidation after incorporation of Mn) coincides with predominant 10H (or 6H) phase. For both X = F and Cl, the Mn rich zone leads to inhomogeneous mixture with evidence of major 2H-BaMnO₃ compound.

However, some differences between the two diagrams can be noted as detailed below.

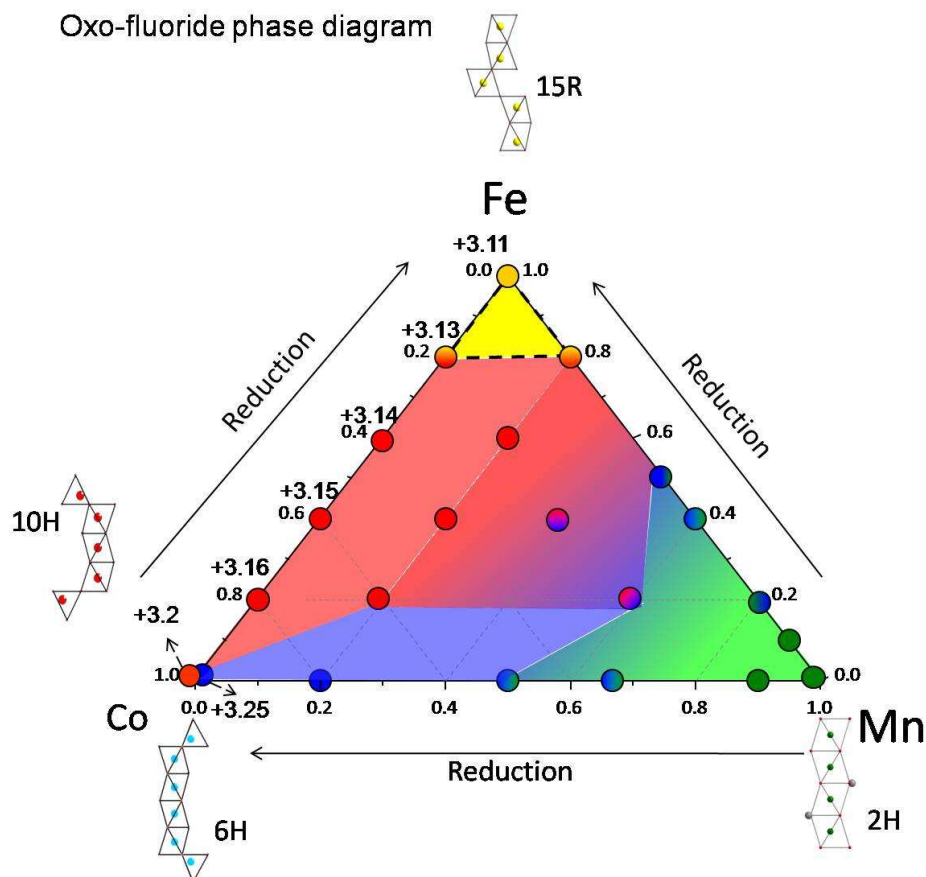


Fig.2-2: Structural tendency diagram in the $Ba(Co,Fe,Mn)_1F_{0.2-x}O_{3-\delta}$ system. The tetramer (6H) structures are represented in red, the trimer (10H) in blue, the 2H- $BaMnO_{3-\delta}$ and $Ba_5Mn_5O_{16}$ in green and finally, the 15R – $Ba(Fe,Co,Mn)_1F_{0.2-x}O_{3-\delta}$ in yellow (Sturza2010). The oxidation degrees as determined by iodometric titration are also given.

2.1.3.a) The 6H area (oxidized blue zone):

This zone is less extended in the F-case than in the Cl-one. This phenomenon can be explained by the difference in the metal valences (obtained by titration) between Cl-compounds (generally more oxidized) and F-compounds (more reduced). As we will see later, due to the small F^- radius, the oxo-fluorides show an extra degree of disorder in their $h^-[BaOF]$ able to accommodate extra oxygen

vacancies in the next-layers compared to the oxo-chlorides. In other words, it turns out that while Cl⁻ is well located in its ideal position of the h' -[BaOCl], F⁻ is more or less in competition with oxygen position within this same h' layer. It generally leads to more disordered and anion-non stoichiometric compounds.

2.1.3.b) Fe -rich zone (yellow zone):

Contrary to the Cl case, for large Fe rich compounds, the apparition of a novel 15R or 6H phases are observed (*Sturza2010*), compounds that have been investigated in another PhD work at the laboratory. The predominant 15R structure is based on the $(cch'ch)_5$ sequence. The stabilisation of this phase corresponds to a rather low oxidation degree of Fe (+3.11, determined by iodometric titration in good accordance with the neutron diffraction refinements). Such a low oxidation degree can be accommodated only in the case of large amount of anionic (F and/or O) vacancies. Here we do not deal anymore with ordered h' -[BaOF] layers but with strongly disordered h' -[BaF_{1-x}O_{3-δ}] layers. But once more we observe that the \bar{h}/h ratio increases upon reduction, since all hexagonal layers correspond to partially fluorinated h' -layers in this compound ($\bar{h}/h \rightarrow \infty$ accordingly to the $(cch'ch)_5$ sequence of the fluorinated 15R-form). This zone will not be detailed in this manuscript but for interested readers, they can refer to *Sturza2010, 2011 and 2011b*.

2.1.3. Predominant polytypes: General conclusions

In our synthesis conditions, the introduction of iron displaces the mean metal valence from +3.5 towards +3, reduction that reinforces an increase of the \bar{h}/h ratio, passing from a tetrameric structure to a trimeric one. On the opposite, the incorporation of Mn determines the increase of the average oxidation degree ($M^{+3.5} \rightarrow M^{4+}$), oxidation that decreases the \bar{h}/h ratio.

In the next section, each line of the two phase diagrams will be explored in details through a full structural characterization by XRD and neutron diffraction (in some cases). Magnetic and electrical characterisations have also been investigated.

2. 2. Structural characterization of the mixed $BaMX_{0.2-x}O_{3-\delta}$ systems

2.2.1. $Ba_5(Co,Fe)_5XO_{13-\delta}$ (X = Cl, F)

We have seen that the Co for Fe substitution stabilizes the 10H phase and is accompanied by a progressive reduction of the mean metal valence according to redox titrations. This line of the phase diagram is summarized for X = F and Cl in Fig.2-3. The changes from the 6H- $Ba_6Co_6XO_{16-\delta}$ (stabilized from slow cooled solids) to the 5H- $Ba_5(Co,Fe)_5XO_{13-\delta}$ (prepared in all tested conditions) comforts the increase of the h' ratio upon reduction while main of the vacancies are organized in the h' -[BaOX] layers compared to h -[BaO₃] layers. However, on the basis of the parent structure of the Co-only compounds, it appears interesting to investigate in details the crystal structures in such systems to clarify particular points such as the cationic distribution, the thermal behaviour and the distribution of oxygen vacancies.

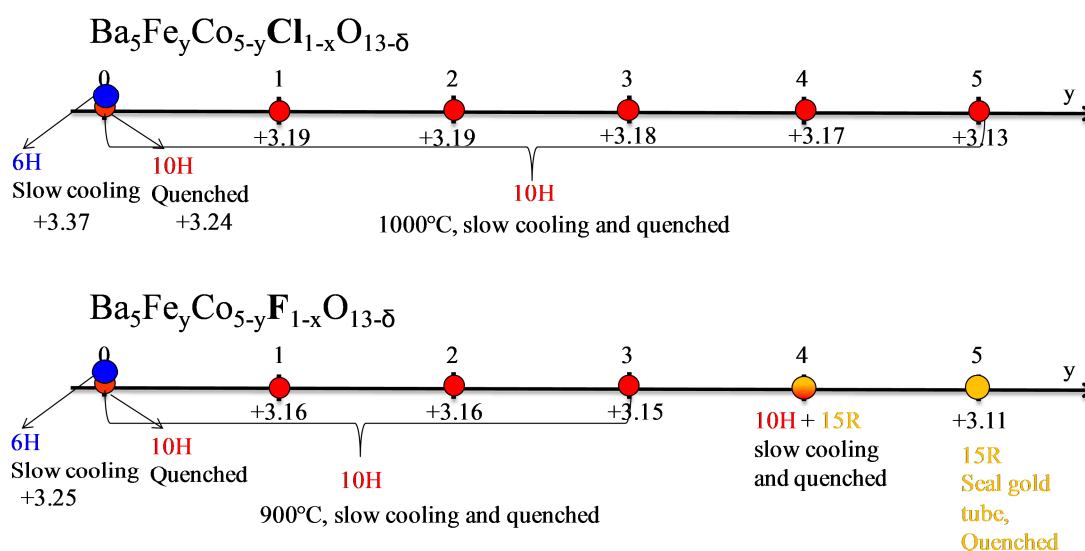


Fig.2-3: Summarized phase diagram for Co – Fe binary substitution

About this last point, it is clear that our redox titrations show valences much lower than the ideal $M^{+3.4}$ expected for stoichiometric $Ba_5M_5X_1O_{13}$ compounds. Then, the localization of extra vacancies (in addition to those inherent to the h' -

[BaOX] layers) deserves attention, especially in the context described in the first Chapter.

In addition, we have to take into account that the interest of Co–Fe substituted materials could reside in several modified properties, for example, the enhancement of the mixed electronic/ionic transport applicable to electrochemical systems such as in $La_{0.6}Sr_{0.4}Co_{1-y}Fe_yO_3$ selected as a promising cathode-material (i.e. LSCF, *Duanping2008*, *Mizusaki1983 and 1989*) or in the increase of the magnetic transition temperature by Fe-doping, since Fe – based perovskites generally show high magnetic ordering temperatures (685K for $SrFeO_2F$ (*Berry2008*), 730 K for 15R and 6H- $BaFeFyO_{3-x}$ polytypes (*Sturza2011*). This magnetic aspect will be explored latter (see section 2.3.2. (Page 98).

2.2.1.a) Room temperature lattice parameters

As the $y = 0$ (cobalt-only) 10H-terms of each solid solution are prepared at high temperature after quenching at room temperature from the reduction of the 6H-compounds, the stability of the mixed 5H-Fe/Co compounds was tested during our synthesis-procedures after air quenching at room temperature, slow cooling, fast cooling and heating at higher temperature. For all treatments, the 10H- $Ba_5Co_{5-y}Fe_yClO_{13-\delta}$ ($y = 1 - 5$) terms of the solid solution are stable, while F ones are stable only until 950°C.

Fig.2-4 shows the RT-XRD patterns for the most representative prepared compounds and validates single phases except for Fe-rich fluorinated samples. The profile refinement (pattern matching) was performed using the FullProf software in order to estimate the cell parameters evolution. The volume is plotted in Fig.2-5 (a) while lattice parameters values are gathered in Table 2-1. The volume evolution is in good accordance with the introduction of a larger cation in the structure, increasing with the increase of the Fe ratio (y) (Fig.2-5 (a)) ($Ba_5Co_{5-y}Fe_yXO_{13-\delta}$).

In this type of compounds for Co-only, a high-spin (HS) Co^{3+} in coordination IV / low-spin (LS) $Co^{3+/4+}$ in coordination VI model was proposed from DFT calculations (*Mentré2010*). In coordination VI, the ionic radius for Co^{3+}_{LS} is 0.53 Å (*Shannon1976*) while Taguchi *et al.* reported that the ionic radius for the LS Co^{4+} ion with a coordination VI is 0.518 Å from the cell parameter of cubic perovskite-type $SrCoO_{3-\delta}$ (*Taguchi1977*). For Fe^{3+} and Fe^{4+} , Shanon reported an ionic radius of

0.55Å (LS) and 0.585Å for Fe^{4+} while, in coordination IV, the ionic radius for Fe^{3+} is 0.49Å. In any cases, a good agreement between the theoretical and experimental diffractograms was achieved (Fig.2-5 (b)).

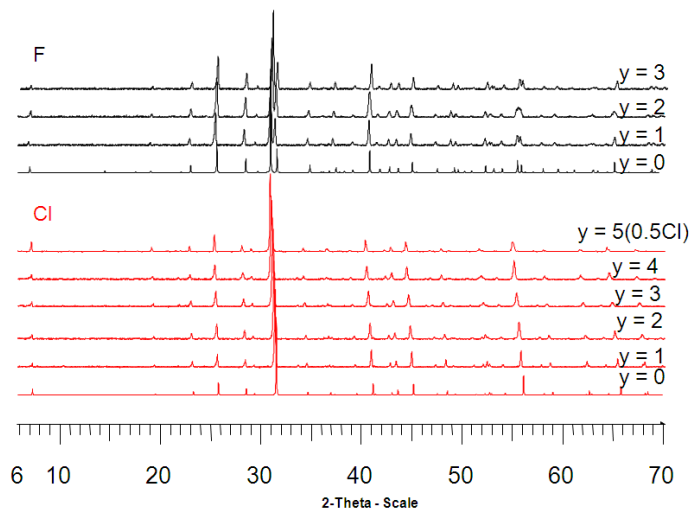


Fig.2-4: XRD patterns for $Ba_5Co_{5-y}Fe_yX_{1-x}O_{13-\delta}$. In black are given the diffractograms corresponding to fluorine solid solution and in red for chlorines one

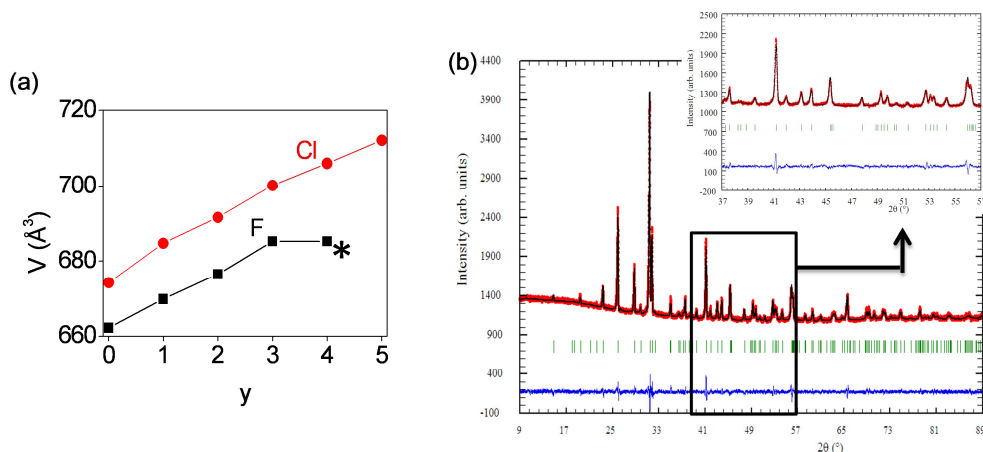


Fig.2-5: (a) Lattice volume evolution vs. y ($Ba_5Co_{5-y}Fe_yX_{1-x}O_{13-\delta}$) for oxo-chloride (red) and oxo-fluoride (* $y = 4 = Ba_5Fe_3Co_1FO_{13-\delta} + 15R - BaFeF_{0.2-x}O_{2-\delta}$) (black); (b) XRD powder profile refinement for $Ba_5Co_4Fe_1FO_{13-\delta}$

Table 2-1: $Ba_5(Co,Fe)_5X_{1-x}O_{13-\delta}$ ($X = \text{halogen, oxygen}$) synthesis method, obtained structural type, cell parameters and space group. The oxidation degrees (O.D.) and oxygen content (O.C.) determined by redox titration before and after TG are also given:

y (Fe)	X	Synthesis	Structural type (space group)	Lattice parameters (Å)	Before TG	After TG		
					(Titration O.D. O.C.)	Titration	Calculated by mass loss	
F	0	1	gold tube, 1030°C, 72h, Quenched	10H ($P6_3/mmc$)	a = 5.681(8), c = 23.700(5)	+3.20 12.50		
	1	1	Air, 900°C, 24h	10H	a = 5.690(9), c = 23.921(5)	+3.16 12.40		
	2	1	Air, 900°C, 24h	10H	a = 5.711(1), c = 23.981(6)	+3.15 12.38		
	3	1	Air, 900°C, 24h	10H	a = 5.730(1), c = 24.087(4)	+3.14 12.37	+3.20 12.50	+3.13 12.33
		0.6	gold tube, 950°C, 48h, Quenched	10H	a = 5.744(5), c = 24.120(2)	+3.29 12.74	+3.33 12.82	+3.28 12.69
	4	1	Air, 900°C, 24h	10H+15R($R\bar{3}m$)	a = 5.731(1), c = 24.087(4)	+ a = 5.753(8), c = 36.234(6)		
Cl	0	1	Air, 900°C, 48h 1030°C, 48h, Quenched	10H	a = 5.660(9), c = 24.300(5)	+3.24 12.61		
	1	1	Air, 1000°C, 24h	10H	a = 5.697(9), c = 24.357(5)	+3.19 12.47		+3.12 12.29
	2	1	Air, 1000°C, 24h	10H	a = 5.718(7), c = 24.428(4)	+3.18 12.46		
	3	0.6	Air, 1000°C, 24h	10H	a = 5.745(2), c = 24.454(4)	+3.04 12.10	+2.84 11.61	+2.89 11.94
		0.7	Air, 1000°C, 24h	10H	a = 5.739(2), c = 24.449(4)	+3.13 12.33	+3.06 12.20	+3.04 12.11
		1	Air, 1000°C, 24h	10H	a = 5.741(5), c = 24.528(3)	+3.18 12.43	+2.98 11.95	+2.98 11.95
		1	Air, 1000°C, 24h, gold tube	10H	a = 5.759(6), c = 24.574(3)	+3.17 12.43		
	4	1	Air, 1000°C, 24h	10H+Ba ₃ Fe ₂ Cl ₂ O ₅ ($I2_13$)	a = 5.759(6), c = 24.574(3)	+ a = 9.971(3)		
	5	0.5	Closed gold tube, 900°C, 48h, Quenched	10H	a = 5.781(1), c = 24.614(1)	+3.13 12.30	+3.00 12.00	+2.82 11.79

2.2.1.b) Thermal behaviour

The thermal behaviour of the $Ba_5Co_{5-y}Fe_yCl_{1-x}O_{13-\delta}$ compounds was investigated until 1000°C , all the studied compounds being stable below this temperature, while, for all the $Ba_5Co_{5-y}Fe_yF_{1-x}O_{13-\delta}$ compounds, a phase transformation was observed between $950 - 1000^\circ\text{C}$ attributed to fluorine loss similarly to what was observed in the parent 10H $Ba_5Co_5FO_{13-\delta}$ (Ehora2007b). This phase decomposition has been investigated in detail and occurs as follows:

- Decomposition of $Ba_5Co_{5-y}Fe_yF_{1-x}O_{13-\delta}$ at $T > 900^\circ\text{C}$:

The HT-XRD patterns for $Ba_5Co_2Fe_3FO_{13-\delta}$ ($y=3$) is representative of the full solid-solution behaviour and is given in Fig.2-6 (a).

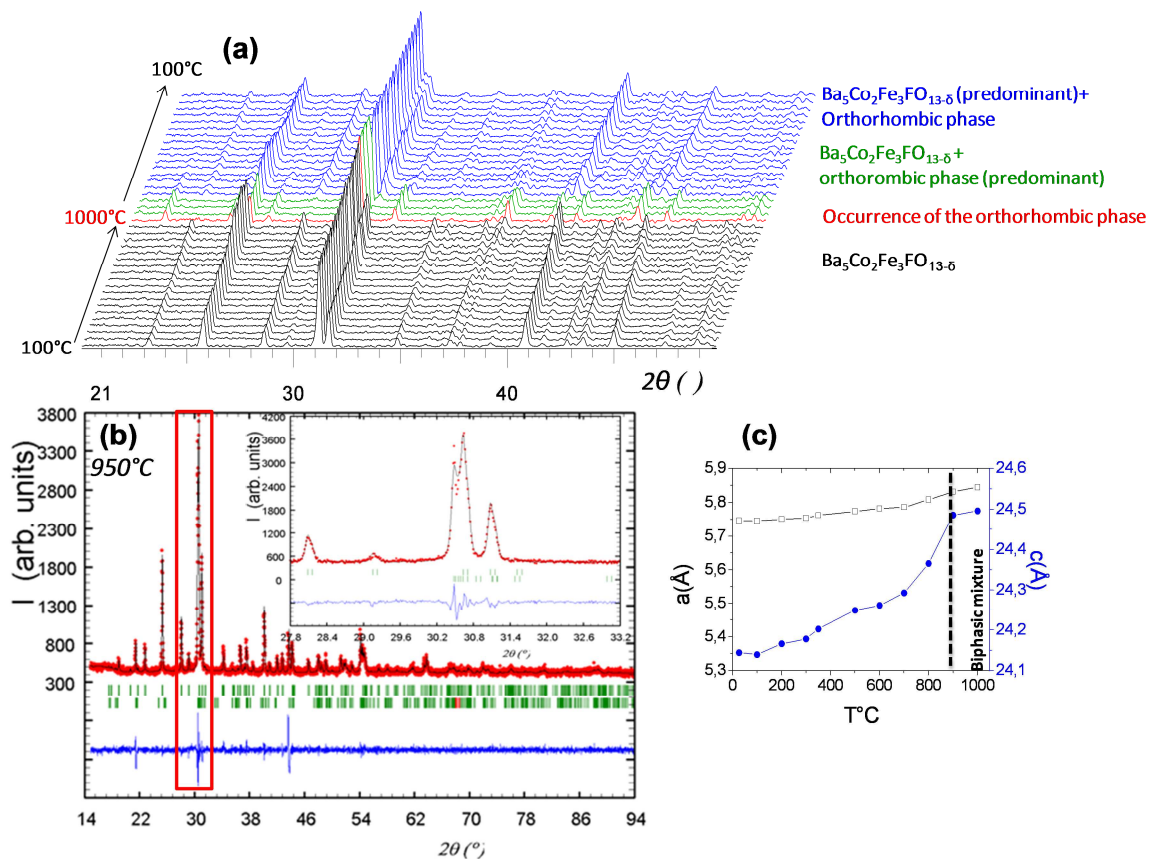


Fig.2-6: (a) High temperature XRD patterns for $Ba_5Co_2Fe_3FO_{13-\delta}$. In green, biphasic mixture with the orthorhombic phase predominant; in blue, biphasic mixture with $Ba_5Co_2Fe_3FO_{13-\delta}$ predominant; (b) Pattern matching for biphasic mixture of $Ba_5Co_2Fe_3FO_{13-\delta}$ (first phase)+ orthorhombic phase at 950°C ; (c) Cell parameters evolution for $Ba_5Co_2Fe_3FO_{13-\delta}$ until 1000°C

The subsequent observed phenomena are:

- From room temperature to 950°C, no phase modification is observed (black patterns), the XRD patterns being indexed as a single 10H- $Ba_5Co_2Fe_3FO_{13-\delta}$
- Between 950 - 1000°C, a biphasic mixture is appearing, likely due to the Fluorine loss. At 1000°C, it was indexed using a biphasic mixture of an orthorhombic C-centred compound (determined using DicVol, see Materials and method section, refined cell parameters: $a = 14.363(9)$ Å, $b = 9.997(7)$ Å, $c = 5.861(2)$ Å) and a 10H Fe -doped compound ($P6_3/mmc$, refined parameters: $a = 5.831(2)$ Å, $c = 24.486(1)$ Å). The pattern matching is shown in Fig.2-6 (b).
- This phase transformation is not reversible, comforting the idea of a F removal. Upon cooling, (1000°C – RT) (Fig.2-6 (c)), the high temperature XRD patterns are also indexed using the biphasic mixture.

2.2.1.c) Thermo gravimetric analysis:

In order to probe the redox properties, TGA have been performed for several samples using two consecutive heating/cooling cycles (cycle 1 (black) and 2 (red) on the figure Fig.2-7). Typical plots are shown on this figure for the terms $Ba_5Co_4Fe_1ClO_{13-\delta}$, $Ba_5Co_2Fe_3ClO_{13-\delta}$, $Ba_5Fe_5Cl_{0.5}O_{13-\delta}$, $Ba_5Co_2Fe_3FO_{13-\delta}$, $Ba_5Co_2Fe_3F_{0.6}O_{13-\delta}$. We also give the metal valence corresponding to redox titrations (denoted as “*titr.*” on Fig.2-7) and those deduced from the experimental weight-loss (TGA on Fig.2-7), considering only oxygen losses. Note that most of the starting oxidation states have been titrated about 12 months after the initial synthesis of the samples. This point is particularly important since we will establish in the latter discussion that the majority of the compounds evolve even while stocked at room temperature in closed boxes.

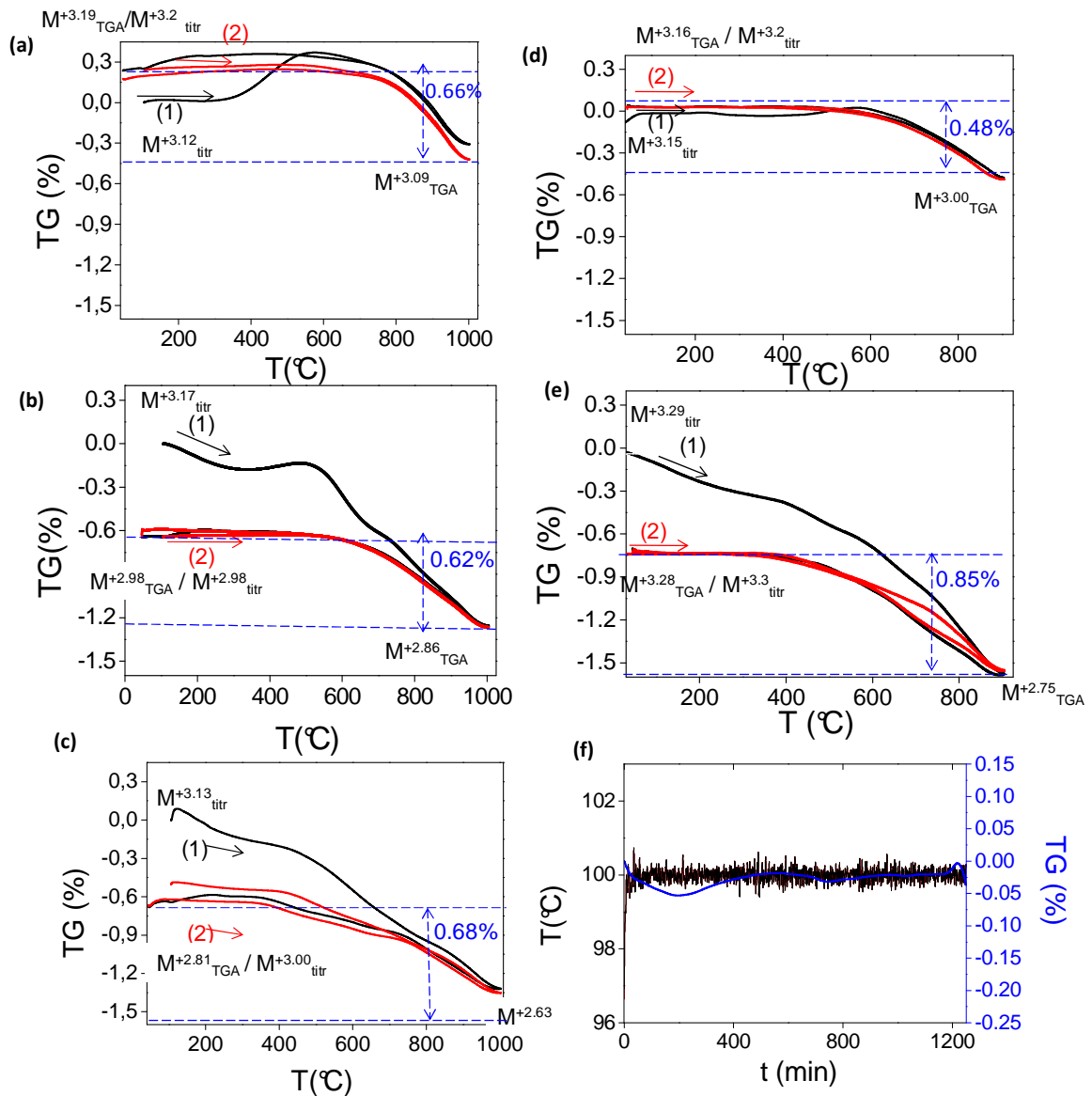


Fig.2-7: TGA curves for (a) $Ba_5Co_4Fe_1ClO_{13-\delta}$, (b) $Ba_5Co_2Fe_3ClO_{13-\delta}$, (c) $Ba_5Fe_5Cl_{0.5}O_{13-\delta}$ (d) $Ba_5Co_2Fe_3FO_{13-\delta}$, (e) $Ba_5Co_2Fe_3F_{0.6}O_{13-\delta}$ and TG isotherm analysis for $Ba_5Co_4Fe_1ClO_{13-\delta}$ (f). The first heating cycle is given in black and notated (1) and the second in red, notated (2).

For all Co/Fe compounds, one can generalize the mean behaviour step by step as follows:

a) First heating ramp (Fig.2-7, in black)

It seems to adopt variable behaviour, not depending on the Fe/Co ratio, nor on the X (= F or Cl) nature, nor on the halogen stoichiometry imposed by the synthesis. Most of the samples show a weight loss up to 0.6% until 600°C

(Fig.2-7 b, c, e), while others show a primary oxidation wave (Fig.2-7, a) or a weight conservation (Fig.2-7, d).

This aspect is not well understood and could reflect water/carbonate departure that would occur after a “long-time-conservation” of the samples in air. Furthermore, in most of the cases, the primary behaviour seems to include a partial oxidation (inflexion point around 500-600°C) similarly to what is observed but somewhat exaggerated in Fig.2-7, a. Multiple phenomena could interact. In fact evidences of the evolution in air of the sample are given in the Fig. 2-8 where two samples are titrated at different times (as-prepared, one year after, after heating/cooling and 6 months latter). In fact we would expect no changes between these four states since the applied thermal treatment is very similar to the synthesis thermal treatment.

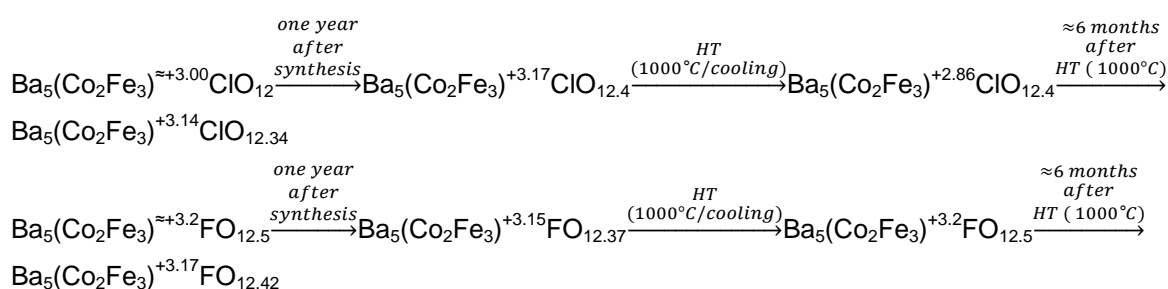


Fig. 2-8: Schematic representation of redox titration at different times for Ba₅Co₂Fe₃ClO₁₂ and Ba₅Co₂Fe₃FO_{12.5}

The disparities (exaggerated for the Cl compound) validate a time-evolution. For these reasons, we will rather focus on the next thermal cycle (end of cycle 1 + cycle 2) which seems common to all compounds: **in fact all the samples show an important reduction/re-oxidation on heating above 600°C and subsequent cooling cycles.**

b) First cooling ramp (Fig.2-7, in red):

This reduction is fully reversible on cooling for all the samples, and the samples are stable on cooling between 500°C and RT. Taking into account that the synthesis of most of the samples by controlled-cooling (similarly to this cooling ramp), the difference in weight between the starting point and this “plateau” indicate RT-instability during the time of exposition in air (spontaneous reduction? carbonate/water fixation?). Using a TG isotherm analysis at 100°C during 1200

minutes, we try to identify the eventual oxygen loss or gain for the composition $Ba_5Fe_1Co_4ClO_{13-\delta}$ freshly heated at high temperature and slow cooled at RT. No significant changes in the compound mass were observed, suggesting that the RT “air-instability” observed is a rather slow process (Fig.2-7, f). We did not try to rationalize the difference between the incorporation of Cl^- against F^- or the effect of the Fe/Co ratio.

2.2.1.d) Thermal induced structural changes

High temperature XRD analyses have been performed on several samples to correlate the results of TGA investigations (first irreversible cycle, reduction/re-oxidation evidences) with the changes of the lattice parameters. For this, thermo diffraction experiments were performed using D8 Advance –HTK1200N (Bruker-AXS) ($Cu-K\alpha$ radiation) diffractometer, from R.T. until 1000°C for oxo-chloride compounds/ until 900°C for oxo-fluoride and back to room temperature, every 50°C in heating and every 100°C in cooling. Typical results are shown on the Fig.2-9 for one oxo-chloride and one oxo-fluoride.

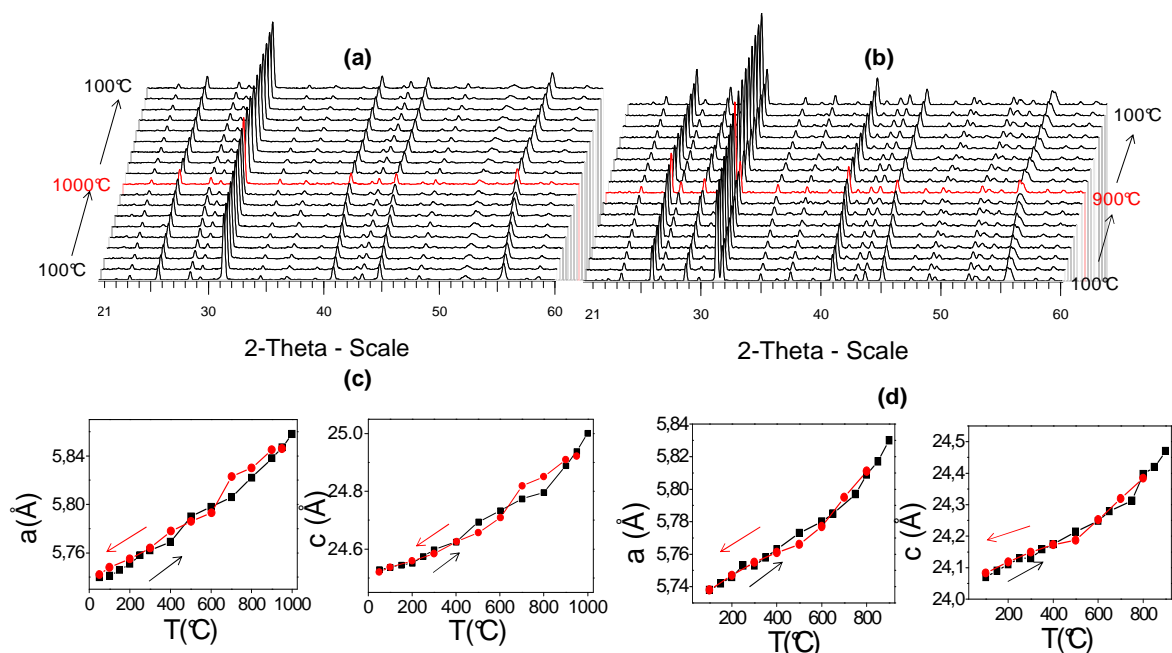


Fig.2-9: HT-XRD for $Ba_5Fe_3Co_2ClO_{13-\delta}$ (a) and $Ba_5Co_2Fe_3FO_{13-\delta}$ (b); lattice parameters dependence on the temperature for $Ba_5Co_2Fe_3ClO_{13-\delta}$ (c) and $Ba_5Co_2Fe_3FO_{13-\delta}$ (d)

In contrast to what was observed from the first ramp of the TGA, the evolution of the a and c parameters is monotone and reflects both the standard thermal expansion that could be combined with a lattice dilatation upon reducing on heating, (due to the increase of the ionic radii) and contraction during re-oxidation (on cooling). However slight anomalies are observed around 600°C , temperature at which the TGA first cycle shows the discussed concavity, but their amplitudes are too weak compared to the total evolution to conclude. The Rietveld analysis at several temperatures has been performed, and particularly we have paid attention to the evolution of the $M - M$ distances ($M = \text{Fe/Co}$ in the various offered crystal positions).

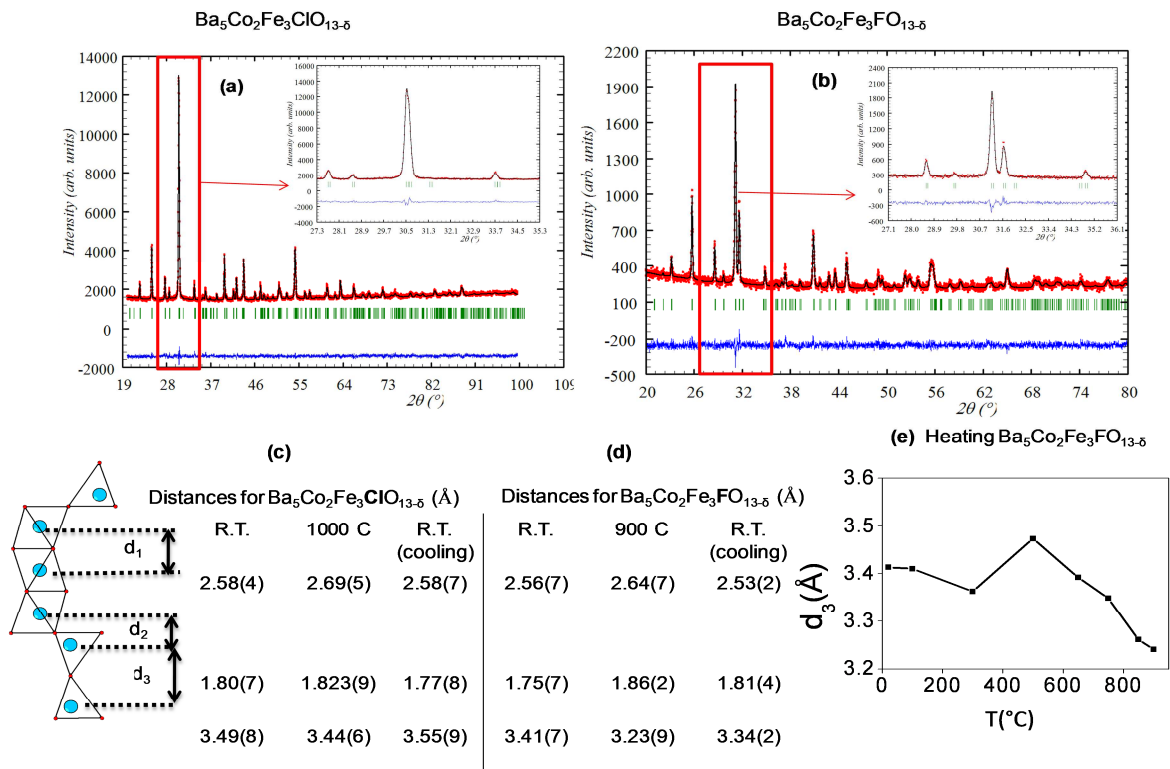


Fig.2-10: (a) Rietveld refinement for $Ba_5Co_2Fe_3ClO_{13-\delta}$ at 1000°C ($R_{\text{Bragg}} = 9.2\%$, $R_F = 9.99\%$), (b) Rietveld refinement for $Ba_5Co_2Fe_3FO_{13-\delta}$ at 900°C ($R_{\text{Bragg}} = 10.5\%$, $R_F = 10.3\%$), (c) The z – projection of the $M - M$ distances for $Ba_5Co_2Fe_3ClO_{13-\delta}$ at RT, 1000°C and back at RT, and for $Ba_5Co_2Fe_3FO_{13-\delta}$ (d); (e) The evolution with the increase of the temperature (heating) of $M(Td) - M(Td)$ distance for $Ba_5Co_2Fe_3FO_{13-\delta}$ compound

The Rietveld refinement revealed a diminution of the intermetallic d3 separation within the tetrahedral dimers (at both sides of the h' -layers) with the temperature for both Cl and F compounds (Fig.2-10 (c) and (d)), this expansion being particularly reinforced in the F case (Fig.2-10 d and e). It also appears that the other M—M separations projected along the c -axis shows the expected contraction on heating and dilatation on cooling. Also, the fine analysis of distances with the temperature shows a structural reorganization between the *initial* and *cooled-back* states, within a unit-cell that remains apparently not modified, on the basis of the unit cell lattices.

Then it seems that the thermal evolution involves structural singularities mainly located at the level of the h' -layers. The structural characterization will be completed by neutron diffraction (ND). Correspondingly to the concavity observed in TGA first cycle around 600°C, and to the anomalies observed in the case of the cell parameters evolution in temperature, the evolution of the d3 ($M(Td)$ – $M(Td)$) distance on heating (Fig.2-10 (e) – $Ba_5Co_2Fe_3FO_{13-\delta}$ is given as example) also shows an anomaly around the same temperature.

2.2.1.e) Neutron diffraction

According to neutron specificities (possibility to discriminate Fe from Co, while it is not possible with XRD; accurate location and quantification of oxygen atoms), we used Room temperature neutron diffraction (LLB, 3T2, $\lambda = 1.225\text{\AA}$) in order to:

- determine the Fe/Co cationic distribution
- analyse the oxygen content and anionic vacancies on all sites
- probe the magnetic ordering that could be active even at room temperature.

Three terms of the fluorine solid solution ($y = 1 - 3$) and one term of the chlorine solid solution ($y = 4$) were investigated by ND with a particular attention to the cationic distribution and the location of extra-oxygen vacancies in the cubic or hexagonal layers of the 10H structures, as already discussed in chapter 1. The results are gathered in Table 2-2:

Table 2-2: ND Rietveld refinement results for:

Ba₅Co₄Fe₁F_{1-x}O_{13-δ} → refined: Ba₅(Co_{4.02}Fe_{0.98})F_{0.98}O_{12.51}, R_{Bragg}=6.27%, R_F=4.70%;

Ba₅Co₃Fe₂F_{1-x}O_{13-δ} → refined: Ba₅(Co_{3.02}Fe_{1.98})F₁O_{12.75}, R_{Bragg}=5.83%, R_F=3.94%, R_{mag}=16.2%;

Ba₅Co₂Fe₃F_{1-x}O_{13-δ} → refined: Ba₅(Co_{2.01}Fe_{2.99})F_{0.95}O_{12.55} R_{Bragg}=5.83%, R_F=3.94%, R_{mag}=16.2%;

*Ba₅Co₁Fe₄Cl_{1-x}O_{13-δ} → refined: Ba₅(Co_{3.9}Fe_{1.1})Cl_{0.85}O_{12.80} R_{Bragg}=3.46%, R_F=2.25%, R_{mag}=7.51%;

* = impurity Ba₃Fe₂Cl₂O₅

Atom	Wyck.	Occ.	x	y	z	U (Å ²)
Ba1	2b	1	0	0	1/4	0.0096(6) 0.0071(5) 0.0291(2) 0.0142(4)*
Ba2	4f	1	1/3	2/3	0.1361(2) 0.1360(2) 0.1352(1) 0.1273(2)	0.0085(6) 0.0065(4) 0.0046(5) 0.0154(3)
Ba3	4f	1	2/3	1/3	0.0389(2) 0.0377(2) 0.0381(1) 0.0380(2)	0.0096(5) 0.0071(5) 0.0080(7) 0.0139(4)
Co1/Fe1 marginal octahedra	4e	0.637(5)/0.213(5) 0.560(1)/0.440(1) 0.426(5)/0.674(5) 0.826(8)/0.174(8)	0	0	0.1029(2) 0.1041(1) 0.1060(1) 0.1071(8)	0.0050(1) 0.0108(9) 0.0076(5) 0.0051(2)
Co2/Fe2 central octahedra	2a	0.972(8)/0.028(8) 0.840(9)/0.160(9) 0.701(9)/0.299(9) 0.617(8)/0.383(8)	0	0	0	0.0050(2) 0.0027(2) 0.0075(1) 0.0049(2)
Co3/Fe3 tetrahedra	4f	0.768(5)/0.232(5) 0.530(1)/0.470(1) 0.260(6)/0.740(6) 0.167(7)/0.833(7)	2/3	1/3	0.1782(2) 0.1780(1) 0.1779(2) 0.1758(9)	0.0107(1) 0.0072(7) 0.0116(4) 0.0047(2)
O1	12k	0.938(8) 0.970(6) 0.946(4) 0.984(5) 0.987(8)	0.8391(2) 0.8390(3) 0.8391(1) 0.8351(2)	0.6782(4) 0.6780(6) 0.6782(2) 0.6712(4)	0.1501(1) 0.1501(1) 0.1501(1) 0.1479(8)	0.0112(2) 0.0113(3) 0.0103(9) 0.0113(2)
O2	12k	1	0.1471(2) 0.1493(2) 0.1490(2) 0.1491(3)	-0.1471(2) -0.1493(2) -0.1490(2) -0.1491(3)	0.0501(1) 0.0501(1) 0.0498(9) 0.0475(9)	0.0112(2) 0.0113(3) 0.0103(9) 0.0113(2)
O3	6h	0.319(5) 0.310(6) 0.293(5) 0.300(5) 0.330(5)	0.7364(2) 0.7312(4) 0.7520(6) 0.7298(4) 0.3009(6)	0.3682(1) 0.3651(2) 0.3760(3) 0.3649(2) 0.6018(3)	1/4 1/4 1/4 1/4 1/4	0.0112(2) 0.0113(3) 0.0103(9) 0.0113(2) 0.0469(4)
F	6h	0.333(3) 0.317(5)	0.2941(4) 0.2930(4)	0.5882(2) 0.5860(2)	1/4	0.0407(4) 0.0487(1)
Cl	2c	0.848(8)	1/3	2/3		0.0262(1)

a) Cationic distribution

After a preliminary pattern matching stage, the atomic parameters and isotropic displacement parameters of the parent $Ba_5Co_5ClO_{13-\delta}$ compound were introduced in the refinement. After the adjustment of the atomic positions, the mixed cationic site occupations were refined with respect to the full occupancies of all sites $a_i[Fe]+a_i[Co]=1$ (a_i = occupation). After the refinement of the isotropic displacement factors (B_{iso}), the occupancies of oxygen and halogen were refined in order to determine the anions vacancies. For the $y = 2$ and $y = 3$ terms (F) and $y = 4$ (Cl), a magnetic contribution was also considered. This will be discussed in the section 2.3.2. For the four compounds, the atomic coordinates and occupancies are given in the Table 2-2. A lowest Fe ratio was refined in the central octahedral site comparatively to the surrounding octahedra and the tetrahedra. This behaviour for Fe was already observed in compounds like $6H'$ - $BaMn_{0.85}Fe_{0.15}O_{2.87}$ (Miranda2009) (Fig.2-11).

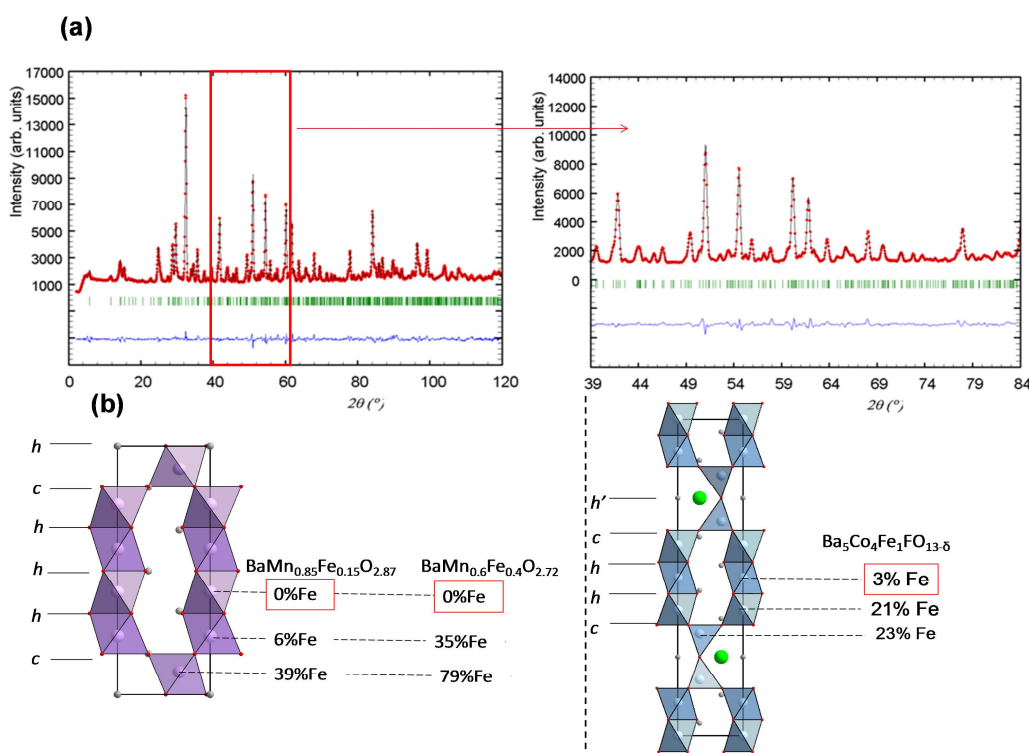


Fig.2-11: (a) Neutron diffraction Rietveld refinement for $Ba_5Co_4Fe_1FO_{13-\delta}$ (see agreement factors in Table 2-2); (b) Cationic distribution determined by neutron diffraction for $BaMn_{0.85}Fe_{0.15}O_{2.87}$ and $BaMn_{0.6}Fe_{0.4}O_{2.72}$ (Miranda2009) and $Ba_5Co_4Fe_1FO_{13-\delta}$ showing low amount of Fe in the central faces sharing octahedra.

b) Anionic vacancies• Oxygen vacancies

The oxygen atom of the h' -[BaOX] layer was placed on a $6h$ ($2x, x, 1/4$) position, split around a special position (3 fold axis), with respect to the non-doped compounds (Kauffmann2008, Ehora2007, Mentré2008). Significant amount of O vacancies were refined in this site (**position O3: refined occ. 29% to 32% to compare to the ideal 33% for this splitted position, Table 2-2**). This position corresponds to the apical corner of the tetrahedra, and vacancies at this level presume a certain degree of disorder.

Table 2-3: Comparison between the average oxidation degrees (noted O.D.) and oxygen content (O.C.) determinate by Redox titration vs. neutrons refinement (see Table 2-2) for Ba₅Co_{5-y}Fe_yXO_{13-δ}:

	y	Redox titration		Neutron diffraction	
		O.D.	O.C.	O.D.	O.C.
F	0	+3.2	12.5		
	1	+3,16	12,4	+3.19	12.51
	2	+3,16	12,38	+3.30	12.75
	3	+3,15	12,37	+3.21	12.56
CI	0	+3.24	12.61		
	1	+3,19	12,47		
	2	+3,19	12,46		
	3	+3,18	12,43		
	4	+3,17	12,43	+3.29	12.82
	5	+3.13	12.30		

In good accordance with the previous observations deduced from the first chapter, the extra oxygen vacancies were refined in the c-layers (**position O1: refined occ. 94% to 99%, Table 2-2**). Contrarily, the refinement of the occupancy of the oxygen in the hexagonal layers leads to a full site occupancy (**position O2: refined occ. 99% to 100%, Table 2-2**). Strikingly, the presence of the oxygen vacancies in the cubic layer involves that some corner-sharing tetrahedra are oxygen deficient in their basal plane also (\rightarrow Co/FeO_{4-x} units), while the central octahedra remain fully VI coordinated. This point will be discussed later. The deduced metal valence is compared to the results of our redox titrations in Table 2-3 which give a relatively good agreement. Nevertheless, one have to keep in mind that except for $y = 1$ (F), all the compounds investigated by ND were magnetically ordered at room temperature and that the refinement of the occupation of all the anions was performed in the presence of a magnetic phase, lowering the accuracy of the full-

refinement. Consequently, the paramagnetic Ba₅Co₄Fe₁O_{13-δ} shows the better chemical/diffraction agreement.

- Halogen vacancies

Oxo-fluoride: based on the same model as for the parent Ba₅Co₅FO_{13-δ} with presence of off-centered F atoms from ND data (*Mentré2010*), the fluorine atom was displaced from its central *2c* ($1/3, 2/3, 1/4$) to a *6h* ($2x, x, 1/4$) position, $1/3$ occupied. An improvement of the refinement follows. The model was first tested for Ba₅FeCo₄FO_{13-δ} (paramagnetic at room temperature) and then applied to all the other terms.

Oxo-chloride: In this case (ND data for Ba₅Fe₄Co₁ClO_{13-δ}), the similar peripheral split of Cl increases the agreement factors implying that the model cannot be applied to chlorine atoms, so this one was kept in its central position. This behaviour was attributed to the larger anionic radius of Cl comparing to F. As we will show later, the same model (split F, non-split Cl) will be observed for mixed Cl/F sites for the 10H - Ba₅Co₅Cl_{1-y}F_yO_{13-δ} ($0 \leq y \leq 1$) compounds by maximal entropy method on single crystal (chapter 3).

2.2.1.f) High temperature in-plane reorganization

R.T. neutron diffraction data show that, while the central octahedra remain fully octahedral, the presence of the oxygen vacancies in the *h'* and *c* layers involves that some corner-sharing tetrahedra are oxygen deficient. In addition, according to the TGA plots, even more oxygen vacancies are created on heating, within a unit-cell that remains apparently unchanged back at room temperature (high temperature XRD). We have also seen that the evolution of the M–M distances involves a structural reorganization between the initial and cooled-back states (fig.2.11)

The mechanism that we propose is based on the observation of Fourier difference maps in the [BaOX] layer. For instance, in the R.T. Ba₅Fe₁Co₄FO_{13-δ} compound, the difference-Fourier map of the [BaOF] layer reveals high residual nucleon densities on three positions at $\approx 1.17\text{Å}$ from the central/ideal position of the F anion and at $\approx 1.26\text{Å}$ from the central/ideal position of O. Then, a “*push-and-pull*” mechanism (Fig.2-12) can be proposed implying that the fluorine atom would be partially displaced from its position, and then coming within the M coordination while

the apical O atom would be pushed forwards (or be absent). In such a case, we could reasonably estimate a basal F-O distances to about 2.62 Å (from Fourier peaks) instead of the ideal 3.27 Å (distance between the central F and O positions). This would allow a minor part of the F anion to complete the coordination sphere of the $M(T_d)$. At the same time, in order to create adequate space for the F motion, in-plane Ba atoms would also be shifted as shown by residual nucleon densities around the Ba-sites (Fig.2-12).

This *push-and-pull* mechanism would be probably driven and exaggerated by the creation of vacancies in the upper *c*-layer. Then ideally a slightly distorted MO_{3+1} tetrahedron would be changed into $MO_2 \text{ } _1F_1O_1$ distorted polyhedron (Fig.2-12, right panel) upon heating, according to an important reorganization of the *h'*-layers. According to our HT structural data, this would be the main reason at the origin of the striking M-M distance reduction upon heating. Probably, the shift of the apical O anions, far from the ideal position, drives the M shift towards the *h'*-layer.

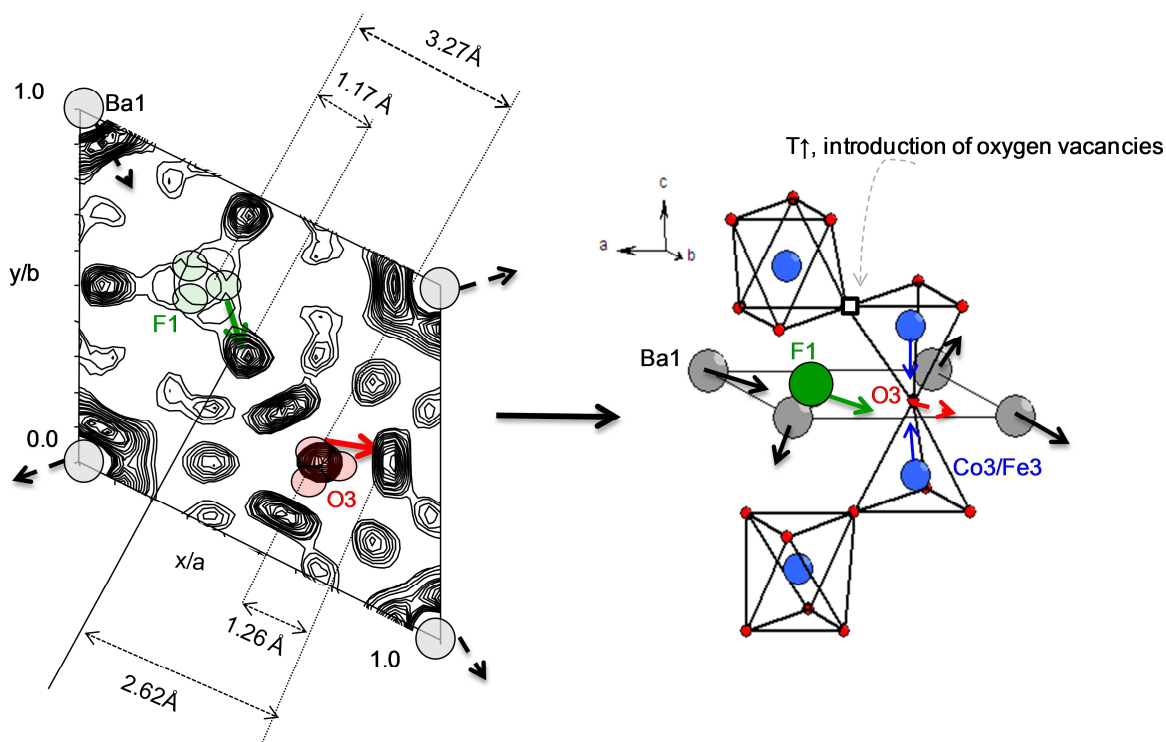


Fig.2-12: Fourier difference map in the $[BaOF]$ layer, after RT-ND Rietveld refinement for $Ba_5Fe_1Co_4FO_{13-\delta}$ (right) and the proposed “push and pull” mechanism (left)

2.2.1.g) Conclusion in few points

In this part, the structural characterization of the Fe–Co binary system was presented. The principal conclusions at this point are:

- A **5H phase** is always observed for F and Cl. According to neutron diffraction data, the **majority of Co is concentrated in the central octahedra** of the face-sharing octahedral trimers, while in the marginal octahedra and tetrahedra, the Co – Fe distribution is random, without any clear preference (for $Ba_5Co_2Fe_3FO_{13-\delta}$, 42% Co / 62% Fe in marginal octahedron and 26% / 74% in the tetrahedron).
- ND data show also the presence of **oxygen vacancies both in the h' -[BaOX] layer, and in the c -[BaO₃] layer** and extra nucleon densities in the h' -layers. This disorder, even if weak at R.T. should be exaggerated upon heating while vacancies should be created in the cubic layers. The proposed “**push – and – pull**” **mechanism** involves the displacement of the atoms in the [BaOX] layer in such a manner that the fluorine anion will complete the coordination sphere of the tetrahedral metal. This is accompanied by a lowering of M-M distances upon heating.
- For $Ba_5Co_5X_{1-x}O_{13-\delta}$, a $Co^{+3/+4}(Oh)/Co^{3+}(Td)$ charge distribution was validated by DFT calculations in these kinds of structures (*Mentré2010*). In the $Ba_5Fe_yCo_{5-y}X_{1-x}O_{13-\delta}$ compounds, we still attributed also the **Co(Td) to trivalent Co**, but we have to note the **difficulty to attribute an oxidation degree to Fe** in different environments due to the stability of $Fe^{+2/+3/+4}$ in various coordination.

2.2.2. $Ba_6(Co,Mn)_6XO_{16-\delta}$ (X = Cl, F)

2.2.2.a) Difficulties and limits

In the first chapter, we have seen during the investigation of the ternary Co/Mn/Fe system that the substitution of Co by Mn mainly stabilizes the 6H phase, this being accompanied by a progressive increase of the average oxidation degree of the transition metal (oxidation). We have also mentioned the difficulty and apparent non–reproducibility of the synthesis of the mixed Co/Mn substituted compounds. Even so, in the case of oxo-chlorides, we have been able to obtain in some cases large amount of single phase materials suitable for neutron diffraction. As already discussed in the first part of this chapter, the preparation of oxo-fluorides is even

more difficult and systematically leads to mixture of predominating 6H and Ba/Mn oxides possibly Co-substituted. The main results are summarized in the Fig.2-13.

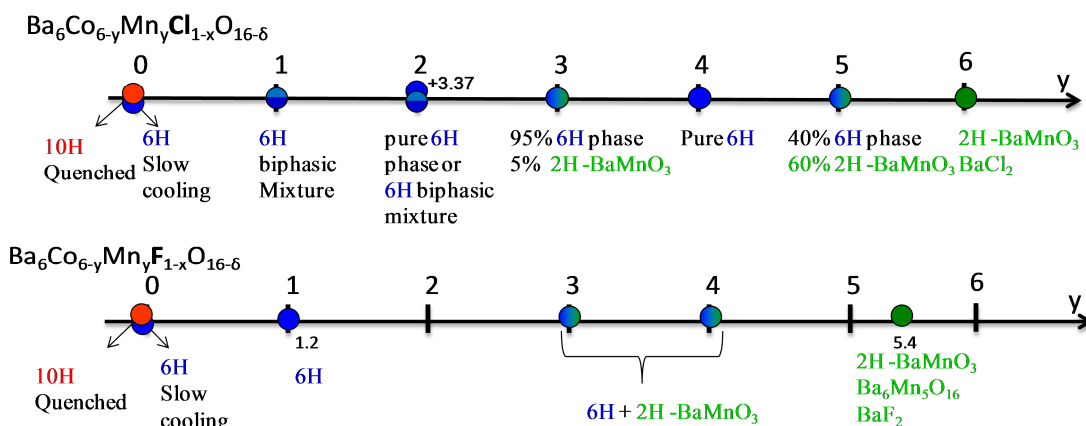


Fig.2-13: Summarized phase diagram for Co – Mn binary substitution

We do not have clear explanations for the poor Mn/Co miscibility in the 6H-crystal structure compared to the previously described Fe/Co binary system. However the great stability of the 2H-BaMnO₃ probably represents an important obstacle. The syntheses of the BaCo/Mn oxo-halides are reported in section 2.1.1.b) (Page 36). In fact the recent literature (see two examples below) gives several examples of mixed Mn/Co oxides whose long-time-syntheses appear relevant since they involve temperatures > 1000°C and several regrinding stages.

- 12H-BaCo_{0.6}Mn_{0.4}O_{3-δ}** was prepared from a well ground stoichiometric mixture of BaCO₃ (Aldrich, 99.98%), MnCO₃ (Aldrich, 99%), and Co₃O₄ (Aldrich, 99.98%). The mixture was heated in a platinum crucible at 950°C in air for 24 h. After, the sample was treated at 1100°C for 2 days and then quenched under liquid nitrogen to room temperature. This process was repeated four times with intermediate grinding to ensure homogeneity. (Miranda2007)
- 5H-BaCo_{0.8}Mn_{0.2}O_{2.83}** was prepared using the mixed oxide route from a well ground stoichiometric mixture of BaCO₃ (Aldrich, 99.98%), MnCO₃ (Aldrich, 99%) and Co₃O₄ (Aldrich, 99.98%) The mixture was decarbonated at 800 °C for 48 h, reground and then heated in a Pt crucible at 1000 °C for 2 days before being slow-cooled to room temperature at a cooling rate of a 4 °C/min. This process was repeated five times with intermediate grinding in an attempt to ensure sample homogeneity. Finally, the black powder was reground prior to heat treatment at 1050 °C for 48 h and then slowly cooled to room temperature at a rate of 4 °C/min. (Miranda2008)

However, due to the presence of halides, in our cases, we have limited the temperature to 1000°C but multiplied the heating/grinding stages and test several cooling types. Even so, we did not find a systematic method to prepare single-phase materials. Our most representative results are detailed case by case as follows:

2.2.2.b) $Ba_6(Co,Mn)_6ClO_{16-\delta}$ case

a) Phases identification

The Fig. 2-14 shows the RT-XRD patterns of most representative prepared compounds. As no continuity seems achieved during our synthesis, the results of the XRD will be detailed term by term:

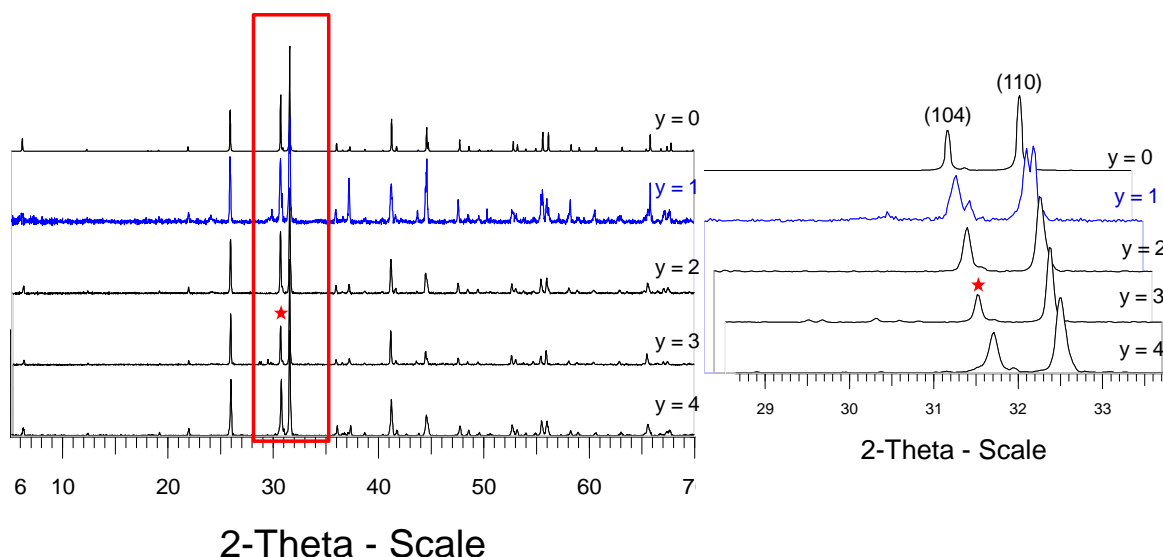


Fig. 2-14: XRD patterns of $Ba_6Co_{6-y}Mn_yClO_{16-\delta}$ (blue \rightarrow the biphasic mixture, see later). The $2H - BaMnO_3$ as impurity for $y = 3$ can be observed by the difference in intensity of the (104) line (marked with a red star) comparing to others (extinct for $2H - BaMnO_{3-\delta}$)

a) Term $y = 1$

$Ba_6Co_5Mn_1ClO_{16-\delta}$ displays a XRD pattern with a splitting of all diffraction lines with half-half intensities (Fig.2-15, (a) and (b)). The theoretical XRD pattern of the $2H-BaMnO_3$ phase (*Hardy1962; Chamberland1970; Negas1971*) (often found as a secondary phase in this binary diagram) is also shown on this figure, leading to the conclusion that presence of this phase as impurity, despite similar XRD patterns,

could not explain the splitting of all diffraction lines (line (104) given as example in Fig.2-15, (b)).

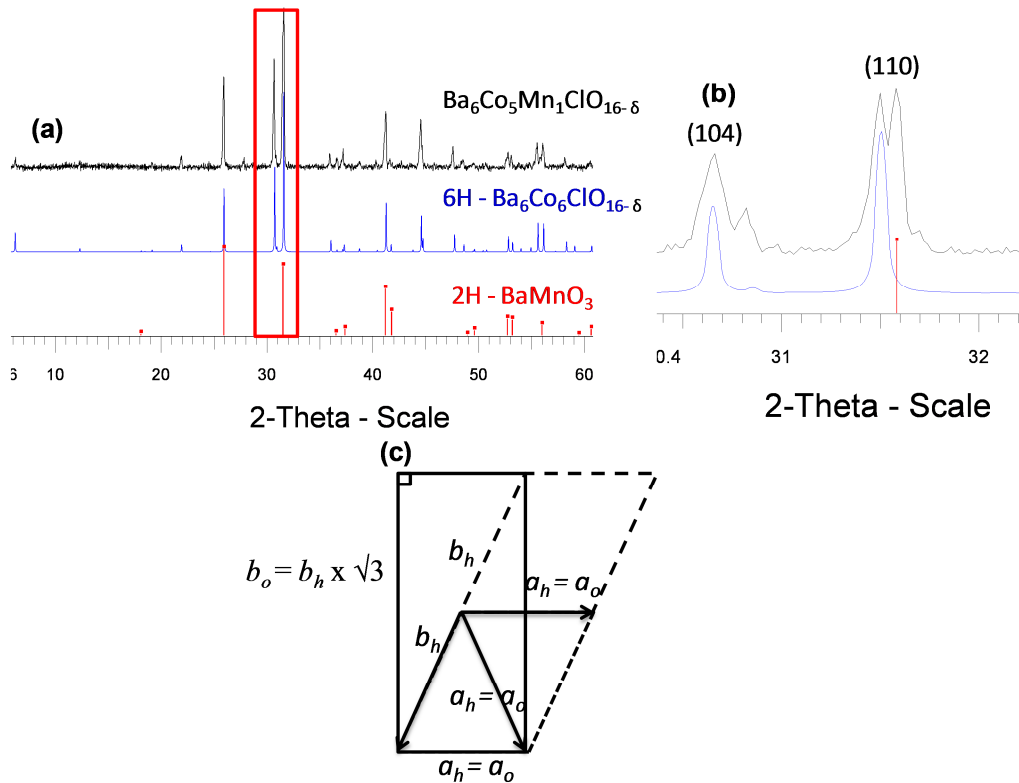


Fig.2-15: XRD pattern superposition ((a) and (b)) of $Ba_6Co_5Mn_1ClO_{16-\delta}$ (black), $Ba_6Co_6ClO_{16}$ (blue) and $2H-BaMnO_3$ (red) showing that $2H-BaMnO_3$ = impurity could not explain the splitting of all diffraction lines); hexagonal to orthorhombic lattice deformation (c)

- The profile-fitting (zoomed area) using an **ideal hexagonal symmetry** is shown on the Fig. 2-16 (a) and shows strong discrepancies ($R_{Bragg} = 15.3\%$, $R_F = 13.5\%$).
- The **deformation of the cell from hexagonal to orthorhombic** (Fig.2-15, (c)) is rather common and consists on an elongation of one parameter within the (a , b) plane such that the trigonality is not anymore respected, (see $10H-BaFeO_{2.80}$ (Delattre2004) with the orthorhombic $Cmcm$ space group). We have long hesitated about this possibility due to the correct agreement obtained after pattern-matching of the XRD pattern ($R_{Bragg} = 12.5\%$, $R_F = 8.32\%$, space group , $a = 14.55(8) \text{ \AA}$, $b = 5.69(5) \text{ \AA}$, $c = 9.88(5) \text{ \AA}$, $\alpha = \beta = \gamma = 90^\circ$), see Fig. 2-16 (b). However, latter high resolution XRD experiments at low angles have revealed that the reflexion 001 also

seems splitted (Fig. 2-16 (d)). This fact refutes the orthorhombic deformation hypothesis.

- An alternative possibility involves two hexagonal phases with close cell parameters, Fig. 2-16 (c), refinement: phase 1: $a = 5.69(4)$, $c = 14.53(1)$ Å and phase 2: $a = 5.67(6)$ and $c = 14.54(3)$ Å.
- As we can see, the two latter refinements lead to comparable refinements. However we retained this “mixture model” as the most plausible, since only this sample shows this splitting in good agreement with the poor Co/Mn miscibility met in the full Co/Mn composition range. It would imply a Co/Mn repartition in two related phases with different Co/Mn ratio.

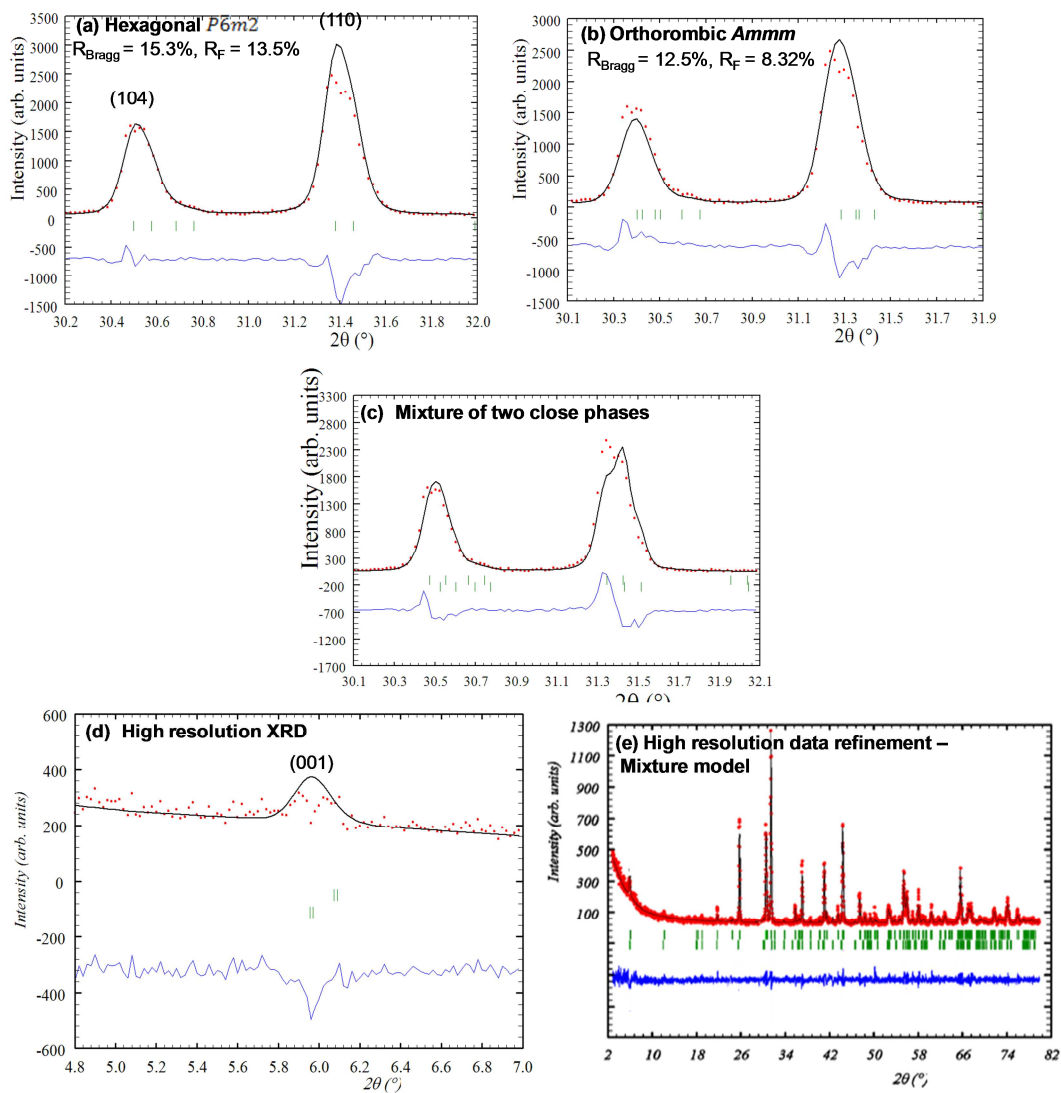


Fig. 2-16: XRD investigation in the case of $y = 1$ term

Indeed, the high temperature behaviour of this sample is of interest and also gives clues for the veracity of the “2-phases mixture” model. It is shown on the Fig.2-17.

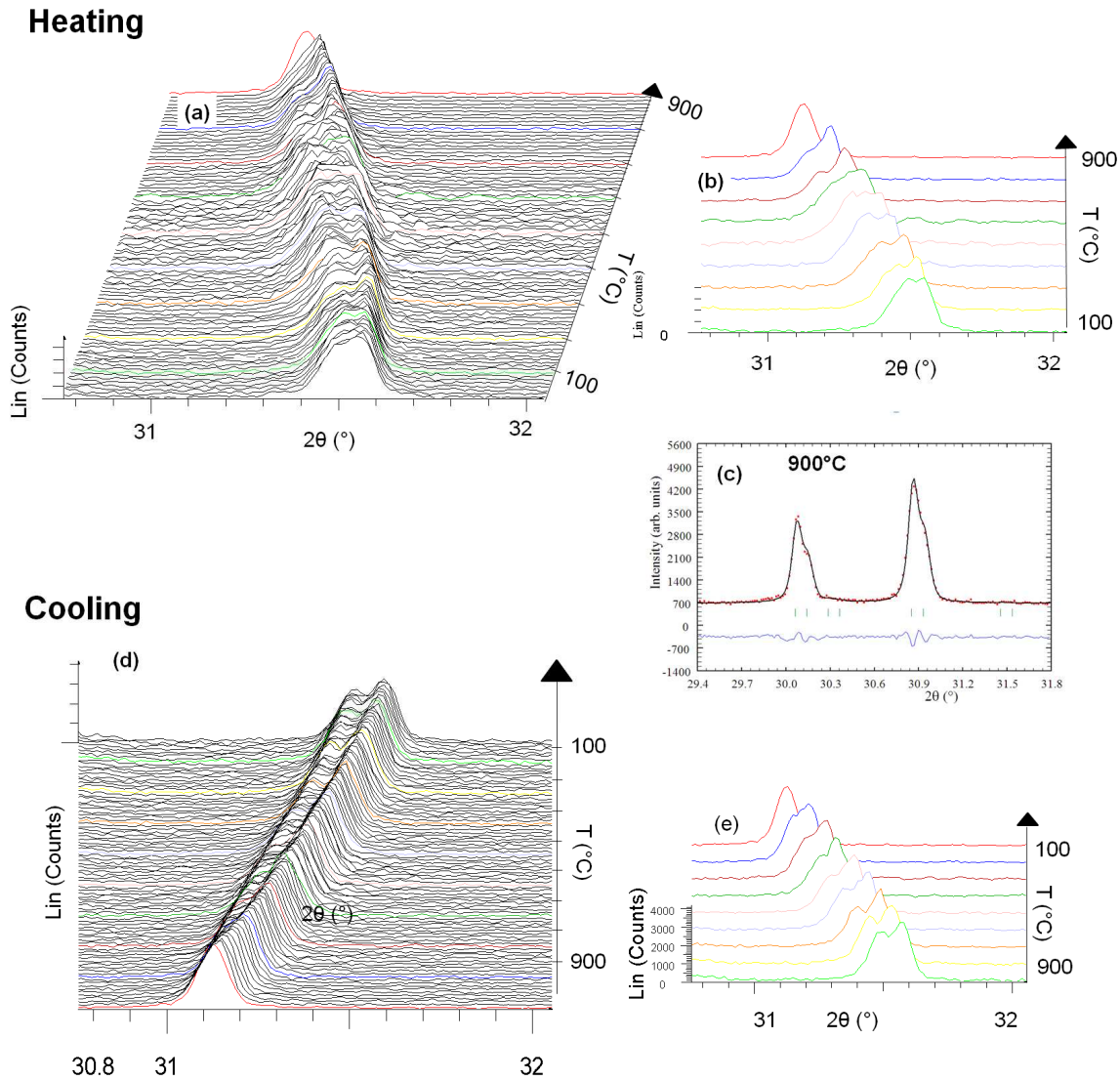


Fig.2-17: $Ba_6Mn_1Co_5ClO_{16-\delta}$ HT-XRD in heating (a) and (b); (c) Pattern matching at 900°C ($P\bar{6}m2$, $a = 5.791(3)\text{\AA}$, $c = 14.749(4)\text{\AA}$); (d) and (e) $Ba_6Mn_1Co_5ClO_{16-\delta}$ HT-XRD in cooling

Clearly pictures several distinct phenomena:

- From RT to 700°C, the splitting seems to be accentuated leading to a broadest multiplet structure at 700°C. Then the lattice evolution of the two phases is different, as expected from their different Co/Mn ratio.

- Above 700°C, we observe a coalescence of the individual components leading to a **single phase materials at high temperature**. The lattice parameters of this phase have been successfully refined through a pattern matching procedure at 900°C leading to parameters $a = 5.791(3)\text{\AA}$ and $c = 14.749(4)\text{\AA}$.
- A phase separation is observed on cooling which involves a **reversible phenomenon**. Then thermodynamics plays against the stabilization of single phase materials in the Co/Mn system and the relative ratio of each metal should be considered as a crucial parameter for the structural stabilization of a single 6H-material. Several answers about that point will be given after the investigation of the $\text{Ba}_6\text{Co}_4\text{Mn}_2\text{ClO}_{16-\delta}$ term by ND.

b) Terms $y > 1$

The term $y = 2$ (Mn) of the solid solution was obtained only once pure (but in big yields – 6g – sufficient for neutron diffraction). The Rietveld refinement and the accordance factors for the refinement of this pattern are given in Fig.2-18, (a). The term $y = 3$ was always obtained in a biphasic mixture with 2H- BaMnO_3 (~ 5%). $y = 4$ (Mn) was always obtained as single phase, but only in small yields (Rietveld refinement and accordance factors in Fig.2-18, (b)). Larger amounts of Mn do not stabilize the h' -[BaOX] layers and long strings of face-sharing octahedral predominate (e.g. 2H- BaMnO_3).

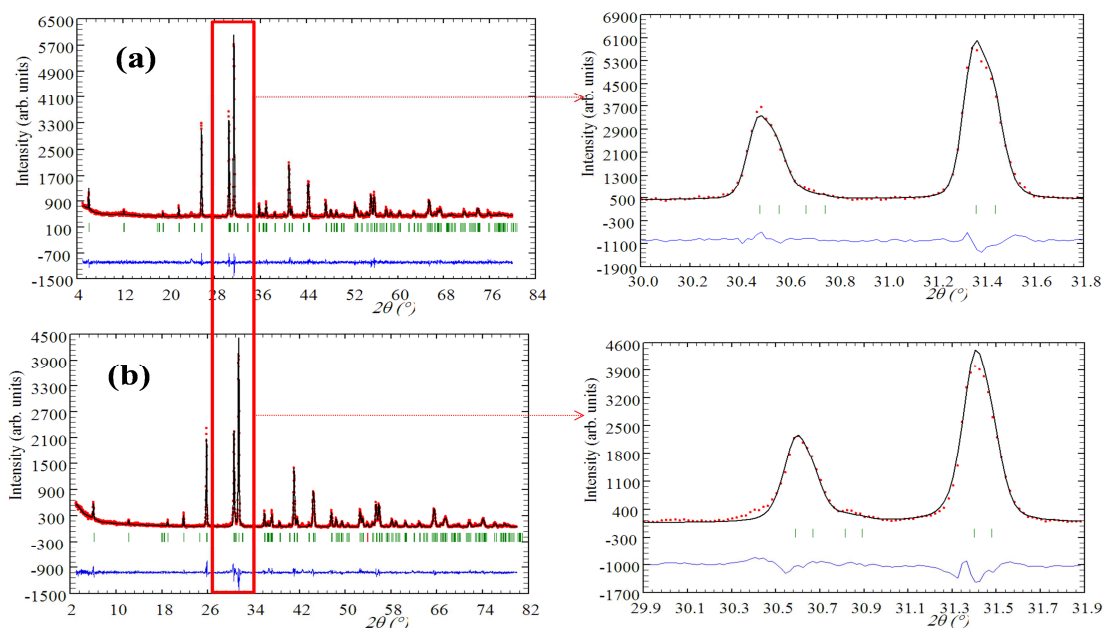


Fig.2-18: $\text{Ba}_6\text{Co}_{6-y}\text{Mn}_y\text{ClO}_{16-\delta}$ XRD Rietveld refinement: (a) $y = 2$ ($R_{\text{Bragg}} = 5.35\%$; $R_F = 6.24\%$) and (b) $y = 4$ ($R_{\text{Bragg}} = 7.71\%$, $R_F = 5.76\%$)

b) Lattice parameters evolution

The cell parameters of the Mn/Co oxo-chlorine 6H-phase (present solely or in a mixture) was determined by pattern matching using FullProf. It shows small modification of the cell volume along the Co/Mn substitution ($\Delta a \approx 0.1 \text{ \AA}$ and $\Delta c \approx 0.15 \text{ \AA}$) (Fig.2-19). It reflects the small difference between the ionic radius of $Co^{3+/4+}$ between $0.4 - 0.6 \text{ \AA}$ and 0.53 \AA for Mn^{4+} (assuming that Mn will not occupy the tetrahedral sites) in configuration VI (*Shannon1976*). A deeper analysis appears complicated since we sometimes deal with biphasic mixture for certain y values.

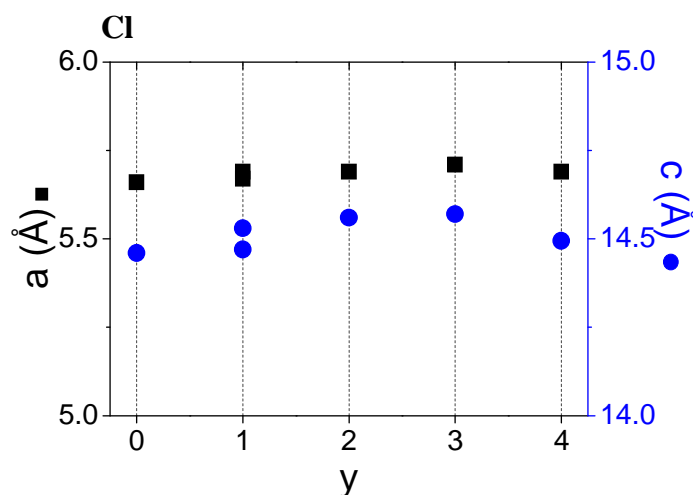


Fig.2-19: $Ba_6Co_{6-y}Mn_yClO_{16-\delta}$ cell parameters evolution, c parameter is given in blue and a parameter in black.

2.2.2.c) $Ba_6(Co,Mn)_6FO_{16-\delta}$ case

As discussed before, the case of oxo-fluoride Co/Mn solid solution is even worse regarding that only a 6H-single-phase was obtained for $Ba_6Co_{4.8}Mn_{1.2}FO_{16-\delta}$ ($y = 1.2$) (Fig.2-20). The $y = 3$ pattern matching correspond to a triphasic mixture of a 6H phase (probably doped with Mn) together with phases corresponding to 2H- $BaMnO_3$ and $Ba_6Mn_5O_{16}$ (probably doped with Co). For the $y = 3$ and 4, a biphasic mixture of a 6H phase together with 2H- $BaMnO_3$ was observed and the $y = 5.4$ term was a triphasic mixture of 2H- $BaMnO_3$, $Ba_6Mn_5O_{16}$ and a 6H structural type phase. Then, we conclude that problems due to Mn/Co segregation in competing phases are

strongly interacting, at least more than in the oxo – chloride case. Here one could propose that according to its big ionic radius Cl^- is more easily “templating” the 6H-form. The refinement of the cell parameters of the only pure term ($Ba_6Co_{4.8}Mn_{1.2}FO_{16-\delta}$) yields $a = 5.680(2)$ Å, $c = 14.300(1)$ Å. Again, a small difference between the cell parameters can be observed when replacing Co by Mn ($Ba_6Co_6FO_{16-\delta}$ - $a = 5.661(1)$ Å and $c = 14.270(1)$ Å).

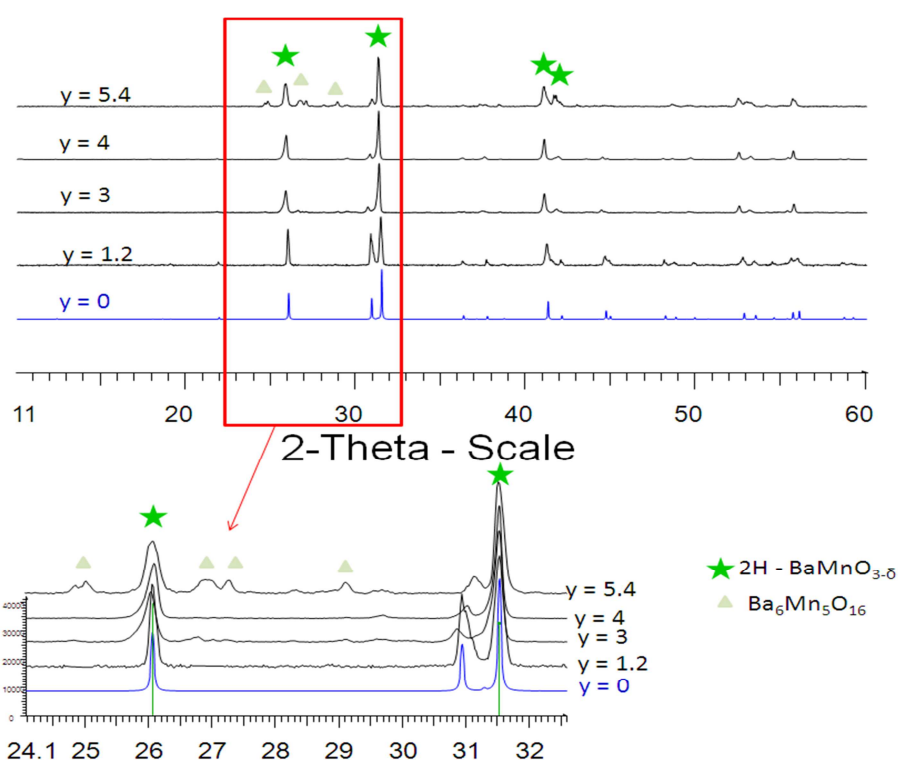


Fig.2-20: $Ba_6Co_{6-y}Mn_yFO_{16-\delta}$ XRD patterns; in black - terms from $y = 1.2$ to 5.4 ; in blue $Ba_6Co_6ClO_{16-\delta}$ theoretical XRD pattern

2.2.2.d) Mn/Co cationic distribution

In order to investigate the Co/Mn relative distribution in the three crystallographic positions offered by the 6H-structural type we studied the $y = 2$, $X = Cl$ term $Ba_6Mn_2Co_4ClO_{16-\delta}$ (the only obtained as single phase in large quantity $\approx 6g$) by neutron diffraction (Fig.2-21 – Rietveld refinement and agreement factors). The refinement was conducted with mixed refined Co/Mn sites, but keeping the total

occupation constant. We note that the particular occupancies of M1 : Co (63%, $b = -0.373$) / Mn (37%, $b = 0.25$) lead to problems in the refinement of the z coordinate due to the almost null contribution of this site in the structure factors, *i.e.* $a_i[\text{Co}]x_{\text{Co}} + a_i[\text{Mn}]x_{\text{Mn}} \approx 0$ (a_i = site occupation). Then, the value $z = 0.7531$ was fixed to those of the parent Ba₆Co₆ClO_{16-δ} compound. The atomic coordinates and anisotropic displacement parameters are given in Table 2-4.

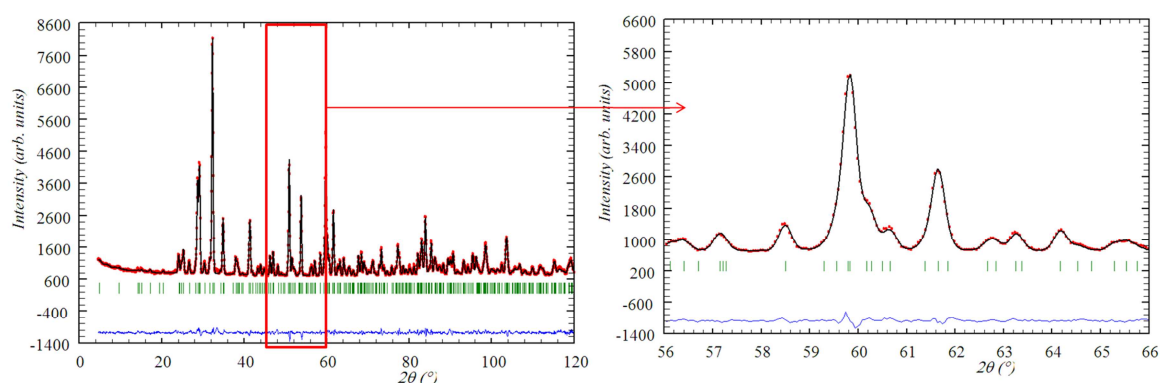


Fig.2-21 Ba₆Co₄Mn₂ClO_{16-δ} ND Rietveld refinement, $R_{\text{Bragg}} = 3.91\%$, $R_F = 2.82\%$

Table 2-4: Ba₆Mn₂Co₄ClO_{16-δ} ND Rietveld refinement: atomic positions and isotropic displacement parameters (calculated formula: Ba₆Mn_{2.03}Co_{3.96}Cl_{0.942}O_{15.646}; calculated average oxidation degree: +3.37; titration average oxidation degree: +3.37):

Atom	Wyck	Occ	x	y	z	Biso (Å ²)
Ba1	1c	1	1/3	2/3	0	0.0144(7)
Ba2	2g	1	0	0	0.7963(2)	0.0038(6)
Ba3	2i	1	2/3	1/3	0.3532(2)	0.0087(9)
Ba4	2h	1	0	0	0.5	0.0111(9)
Co1/Mn1	2h	0.635(3)/0.365(3)	1/3	2/3	0.75318	0.0228
Co2/Mn2	2h	0.346(2)/0.654(2)	1/3	2/3	0.5848(8)	0.0030(7)
Co3/Mn3	2h	1/0	2/3	1/3	0.8792(5)	0.0010(8)
O1	6n	0.941(6)	0.012(2)	-0.494(1)	0.8307(1)	0.0083(1)
O2	6n	1	0.1872(5)	-0.6255(5)	2/3	0.0083(1)
O3	3j	1/3	0.644(1)	0.356(1)	0	0.0083(1)
O4	3k	1	0.031(1)	-0.484(1)	1/2	0.013(2)
Cl1	1a	0.942(1)	0	0	0	0.0216(9)

The Mn cations preferentially occupy the face-sharing polyhedra while tetrahedra are solely occupied by Co cations. Inside the tetramers, it also appears that Mn prefer the central M2 positions (65% Mn / 35% Co) while marginal sites are occupied by 63% Co / 37% Mn. Similar behaviour has been reported for the case of the 12H-BaCo_{0.6}Mn_{0.4}O_{2.83}) (*Miranda2008*) (71%Mn in this site comparative with 33% in marginal octahedra). This behaviour seems to be valid in the tetrameric structures only, since a different tendency has been reported for the 5H-crystal structure (trimeric) of BaCo_{0.8}Mn_{0.2}O_{2.8} (*Miranda2007*) stabilized at low Mn incorporation rate. These three structures and the cationic distributions are shown on the Fig.2-22 (a), (b), and (c). By comparison, one should recall that in the case of the 10H-Ba₅(Co,Fe)₅XO_{13-δ} compounds, the central octahedra site is filled preferentially by Co, while for the marginal octahedra and tetrahedral sites, a mixed Co/Fe distribution is observed.

Interestingly, the tetrahedral sites are Co-filled in good agreement to what was suggested in Chapter 1, section 1.3.e) regarding the preferred pentavalent oxidation state for Mn in a tetrahedral environment, sometimes met in perovskites derivatives (Fig.2-22 (d), (e), and (f) (e.g. Ba₇Mn₅Ca₂O₁₉ (*Floros2002*) and Ba₈Mn₆Ca₂O₂₂ (*Floros2000*) or Ba₆Ru₂Mn₂Na₂O₁₇ (*Quarez2003*)). This tetrahedral preference for Co will be comforted by DFT calculations performed on a similar compound Ba₈Mn₆Co₂ClO_{22-δ} detailed in the next section.

Finally, regarding the M–M distances and keeping in mind the low evolution of the *c* lattice parameters observed by X – ray diffraction along the Co/Mn line, the central M2-M2 distance increased with the Mn substitution while M2-M1 decreases (Fig.2-22 (g)) At least the Co3-Co3 distances remain unchanged in good agreement with the conservation of its Co³⁺ filling. As already mentioned about the Co/Fe line, the trivalent Co³⁺ valence in the tetrahedra was validated by DFT calculations in the Co₂O₇ units within these kinds of structures (*Mentré2010*).

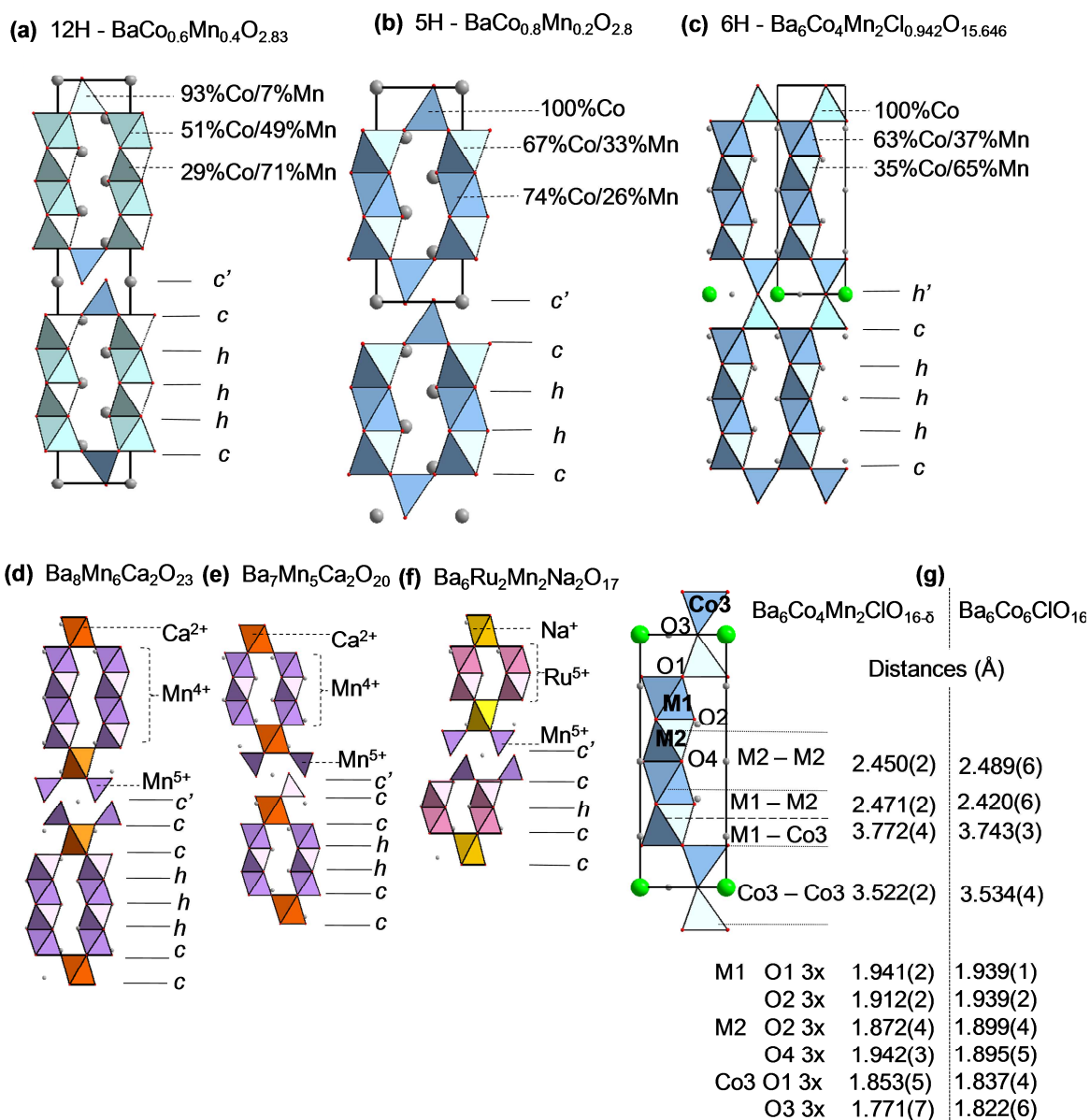


Fig.2-22: (a), (b), (c) cationic distribution for Co – Mn mixed compounds;

(d), (e), (f) examples of structures with Mn tetrahedral;

(g) metal – metal and metal – oxygen distances for $Ba_6Co_4Mn_2ClO_{16-\delta}$ and $Ba_6Co_6ClO_{16-\delta}$ from neutron diffraction refinement

a) Oxygen vacancies and possible charge distribution

On the opposite to Co/Fe system, it appears possible to assign cation valence in this Co/Mn compound on the basis of the occupancies of the anionic sites. In addition to the partial deficiency refined for the Cl position (*h'*-layers), once more only the c-[BaO₃] layer shows extra vacancies (occ. O1 = 94%), the refinement of the occupations for h layers leading to fully occupied positions. It leads to the formula Ba₆Co_{3.96}Mn_{2.03}Cl_{0.942}O_{15.646} associated to +3.37 average oxidation degrees for Co/Mn. This is in good agreement with our iodometric titration (+3.37). Then an ideal charge distribution could be proposed: Co^{III}(Td)+Co^{III}(Oh_{marginal})+Mn^{IV}(Oh_{central}) leading to a (Co/Mn)^{+3.37}.

This attribution takes into account several features:

- phases with Mn^{IV} (2H-BaMnO₃) as a second phase in rich Mn-terms
- the increase of the mean oxidation state observed after Mn incorporation.
- the increase of M2-M2 distances that would likely results from a greatest Mn⁴⁺ - Mn⁴⁺ electrostatic repulsion at the centres of the octahedral site.
- the shortening of the M1-M2 distance that involves Co³⁺ rather than Co^{3.5+} as in the parent Ba₆Co₆ClO_{16-δ}
- the observations made on 12H-BaMn_{0.4}Co_{0.6}O_{2.83} (*Miranda2008*) compounds where a similar charge distribution is proposed.

2.2.2.e) Conclusion in few points

The structural characterisation by XRD of the Co–Mn binary substitutions both with Cl⁻ and F⁻ as anion was presented. The most important concluding aspects are listed below:

- The stabilization of the 6H structural type accompanied by a progressive increase of the average oxidation degree
- The **difficulty and the non– reproducibility of the synthesis** of the mixed Co/Mn substituted compounds involve low thermodynamic stabilities and bad Co/Mn miscibility within the 6H-phase.
- The cationic distribution calculated from neutron diffraction refinement for Ba₆Mn₂Co₄ClO_{16-δ} displays the **preference of Mn for central faces sharing**

octahedral (0.35Co/0.65Mn), while in the marginal octahedra, a 0.63Co/0.37Mn cationic distribution was observed. The tetrahedra are occupied only by Co which validates the instability of Mn^{III} and Mn^{IV} in tetrahedra.

- Regarding the oxygen vacancies, these were refined in the h' -[BaOX] layers and c layers in accordance with what was observed for $Ba_5(Co,Fe)_5XO_{13-\delta}$. A similar partial disorder within h' -layers could be suggested.
- Contrary to $Ba_5(Co,Fe)_5XO_{13-\delta}$ compounds, for which the proposition of a charge distribution model appears ambitious, in this case, the following formulation can be proposed: $Ba_6(Co^{III}_{1.26}/Mn^{IV}_{0.74}(Oh_{\text{marginal}}))(Co^{III}_{0.7}/Mn^{IV}_{1.3}(Oh_{\text{central}})Co^{III}_2(Td)Cl_{0.942}O_{15.646}$ leading to an average oxidation degree of 3.37 in agreement with the titration results.

2.2.3. The structure of $Ba_8Co_2Mn_6ClO_{22-\delta}$, a new quasi-1D-hexagonal perovskite polytype containing novel 8H-blocks

In the Ba-Co/Mn-Cl-O system, the competition between several forms is at the origin of the stabilization of a new structural polytype which will be presented in this section. It corresponds to the $n = 6$ term of the $Ba_{n+2}M_{n+2}XO_{3n+4}$ ($M = Co, Mn, Fe; X = Cl, F$) series ($Ba_8Co_2Mn_6ClO_{22}$). Typically it was observed in the green zone of the diagram from Fig.2-1. The synthesis method and structural characterisation by single crystal XRD will be presented together with the elemental analysis and a theoretic cationic distribution based on the previous observations and demonstrated by DFT calculations.

2.2.3.a) Synthesis

Single-crystals of the 8H - $Ba_8Mn_6Co_2ClO_{22-\square}$ compound was synthesized as follows: 2 g of a mixture of $BaCO_3$ (Sigma-Aldrich, 99%), Co_3O_4 (Alfa Aesar, 99.7%), MnO (Sigma-Aldrich, 99%) and $BaCl_2 \cdot 2H_2O$ (Prolabo, 99%) were weighted in the 11:4/3:8:1 ratio then heated in air at 700°C for 12 h after grinding. The mixture was then pressed into pellets, reheated at 1000°C for 58 h, and quenched in liquid nitrogen. After another grinding, the powder was mixed with an excess of $BaCl_2 \cdot 2H_2O$

in the 1:10 ratio and heated again at 1000°C for 48 h. The crucible was further cooled to 300°C at 10°C/h and then quenched to room temperature. The excess of $BaCl_2$ was washed with hot water. Black metallic crystals were thus obtained.

2.2.3.b) Structural description

The spots were indexed in a hexagonal cell in the $P m2$ space group like $Ba_6Co_6ClO_{16-\delta}$ compound, the term $n = 4$ of the $Ba_{n+2}Co_{n+2}XO_{3n+4}$ ($X = Cl, F$) series. The refined a parameter is 5.7207(2) Å and $c = 19.4099(10)$ Å, compared to $a = 5.669(2)$ Å and $c = 14.465(5)$ Å for $Ba_6Co_6ClO_{16-\delta}$.

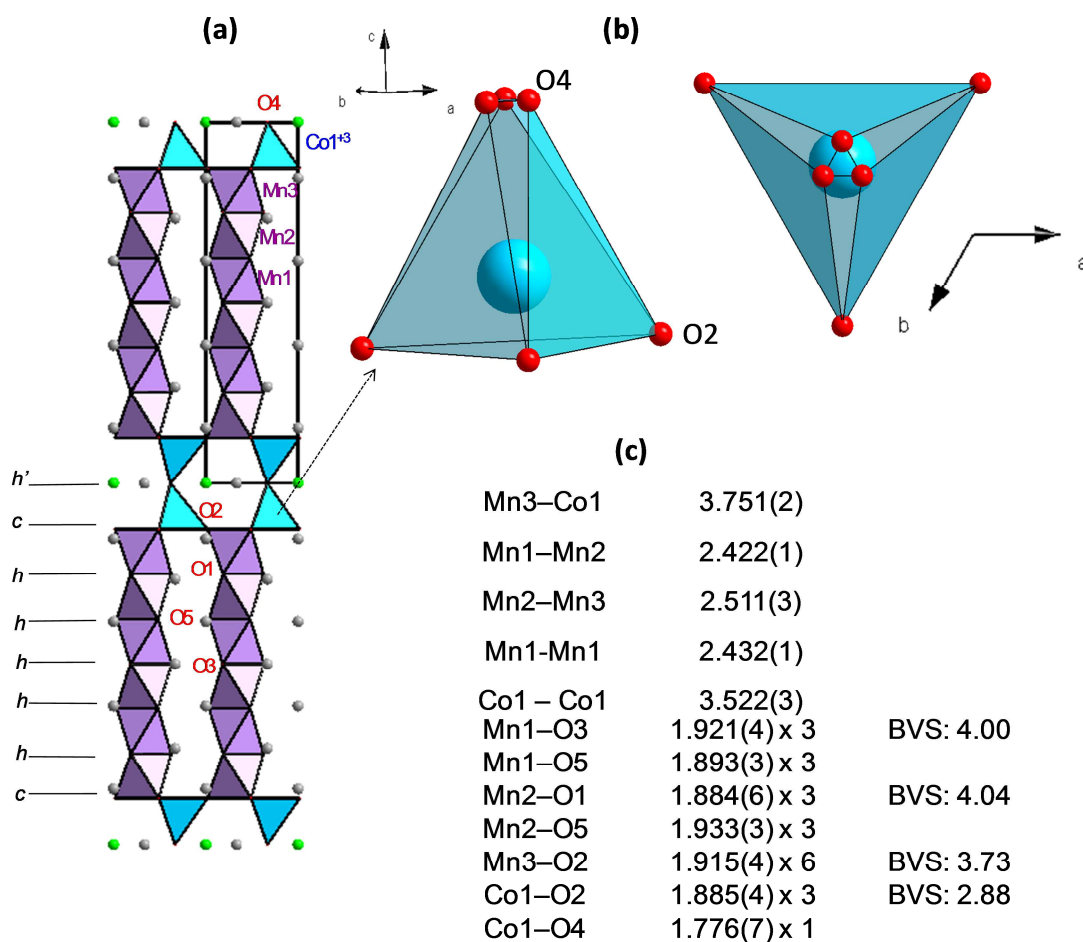


Fig.2-23: (a) Crystal structure of $8H - Ba_8(Co,Mn)_8ClO_{22}$ with the sequence in h , c and h' layers (b) distorted tetrahedra, (c) $M - M$ and $M - O$ distances (BVS = bond valences)

The structure is formed by linear groups of six face-sharing octahedra, linked together by the corners of terminal capping tetrahedra. It thus corresponds to the $n = 6$ member of the $Ba_{n+2}(Co,Mn)_{n+2}ClO_{3n+4}$ series (Fig.2-23) presented in the previous sections (10H-structure: $n = 3$; 6H-structure: $n = 4$). In terms of hexagonal (h) and cubic (c) layers, the corresponding stacking sequence is 8H-($chhhhhch'$) where c and h denote $[BaO_3]$ layer and h' $[BaOCl]$ layers. The connection between the blocks is achieved by the tetrahedral corners of the central $[BaOCl]$ layers. As already observed in related oxo-halide – cobaltites, the corresponding oxygen position corners are 0.20 Å off-centred out of their ideal position (O4 in Fig.2-23 (b)) leading to slightly distorted tetrahedra.

- Cationic distribution

At this stage, since Mn and Co atoms are not distinguishable by XRD ($Z = 25$ and 27 , respectively), crystallo-chemical features should be carefully taken into account.

a) Tetrahedral site: as already discussed in previous section, in hexagonal perovskites, tetrahedral manganese is generally assigned to its Mn^{2+} or Mn^{5+} valence state (Floros2002; Quarez2003). Such valences are unlikely in the title compound (mean $\sim +3.6$ metallic state) deduced from the ideal $Ba_8M_8ClO_{22}$ formula. Consequently, as discussed before, the tetrahedral sites would accommodate Co^{3+} species.

b) Octahedral site: on the opposite, the M–O (1.876(3) Å–1.955(3) Å) and M–M (2.425(3) Å –2.513(2) Å) bond distances do not allow us, to distinguish between Mn, Co or mixed Mn/Co occupancies within the face-sharing hexamers (by comparison with related oligomers in $BaMnO_{3-\delta}$ (Adkin2007) and $BaCoO_{3-\delta}$ (Boulahya2005 ; Hector2001) polytypes or $Ba_6(Co,Mn)_6ClO_{16-\delta}$ compounds).

2.2.3.c) Elemental analysis (Microprobe EPMA)

In Fig.2-24, (a) we give a microprobe analysis photo of the crystals from the preparation. Cameca SX100 electron probe microanalyser (EPMA) was used to perform elemental analysis (Fig.2-24, (b), (c) and (d)). The quantification of the

present elements was performed as described in section “Materials and methods”. In order to decrease matrix effects and to benefit from the structural similarity, pellets of the parent $n = 4$, $Ba_6Co_6ClO_{16-\delta}$, compound were used as standards. Means and standard deviations were calculated from measurements carried out at five different places on each sample. To ensure a good statistic representative of the chemical formula, 28 single crystalline samples were tested. After normalization to 8 Ba, the Co/Mn ratio given by the quantitative analysis is 2.5(4)/5.5(4), leading to the approximate formula $Ba_8Co_{2.5}Mn_{5.5}ClO_{22}$. Indeed, the question of the relative Mn/Co distribution in the four independent crystallographic sites of the structure is still very topical. What about the stability of the suggested tetrahedral preference for cobalt? To answer this open question, we performed *ab initio* electronic structure calculations in order to calculate the most stable cationic repartition. This technique already demonstrated its efficiency in these series of compounds (Kauffmann2006, Kauffmann2008).

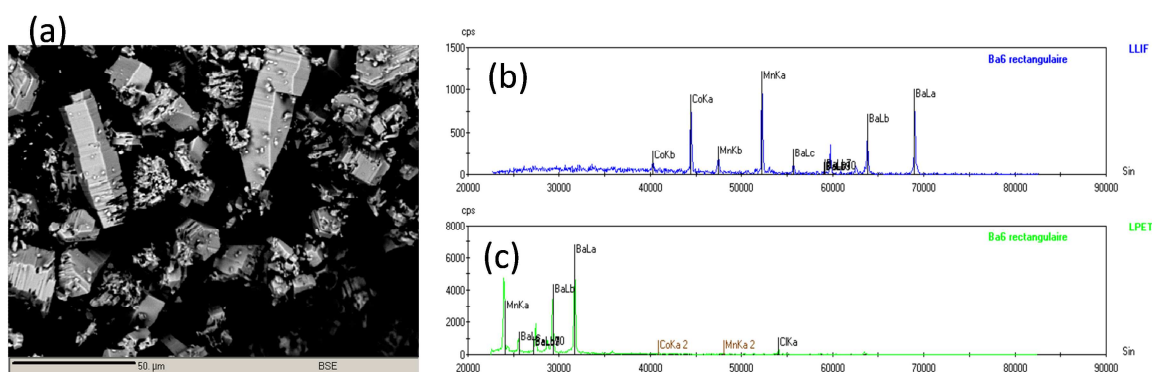


Fig.2-24 : (a) $Ba_8(Co,Mn)_8ClO_{22}$ crystals - Microprobe image; Elemental identification and quantification for one crystal in (b) for Co and Mn using a LiF crystal and in (c) for barium and Cl using a PET crystal.

2.2.3.d) Cationic distribution by Density Functional Theory (DFT)

The calculations were carried out by Dr. Houria Kabbour, UCCS, using the Vienna *ab initio* simulation package (VASP) (Kresse2004). The calculations were performed within the generalized gradient approximation (GGA) for the electron exchange and correlation corrections using the Perdew–Wang functional and the

frozen core projected wave vector method (Perdew1992, Kresse1999). A plane wave energy cutoff of 500 eV, a total energy convergence threshold of 10^{-6} and 122 k points in the irreducible Brillouin zone were used (k points sampling was increased until no significant change in the relative total energies was observed). GGA plus on-site repulsion (GGA + U) (Dudarev1998) calculations were also employed to account for the strong electron correlation associated with the 3d electrons on the Co and the Mn atoms. The calculations were performed using a site-to-site spin configuration, either ferromagnetic (FM) or antiferromagnetic (AFM).

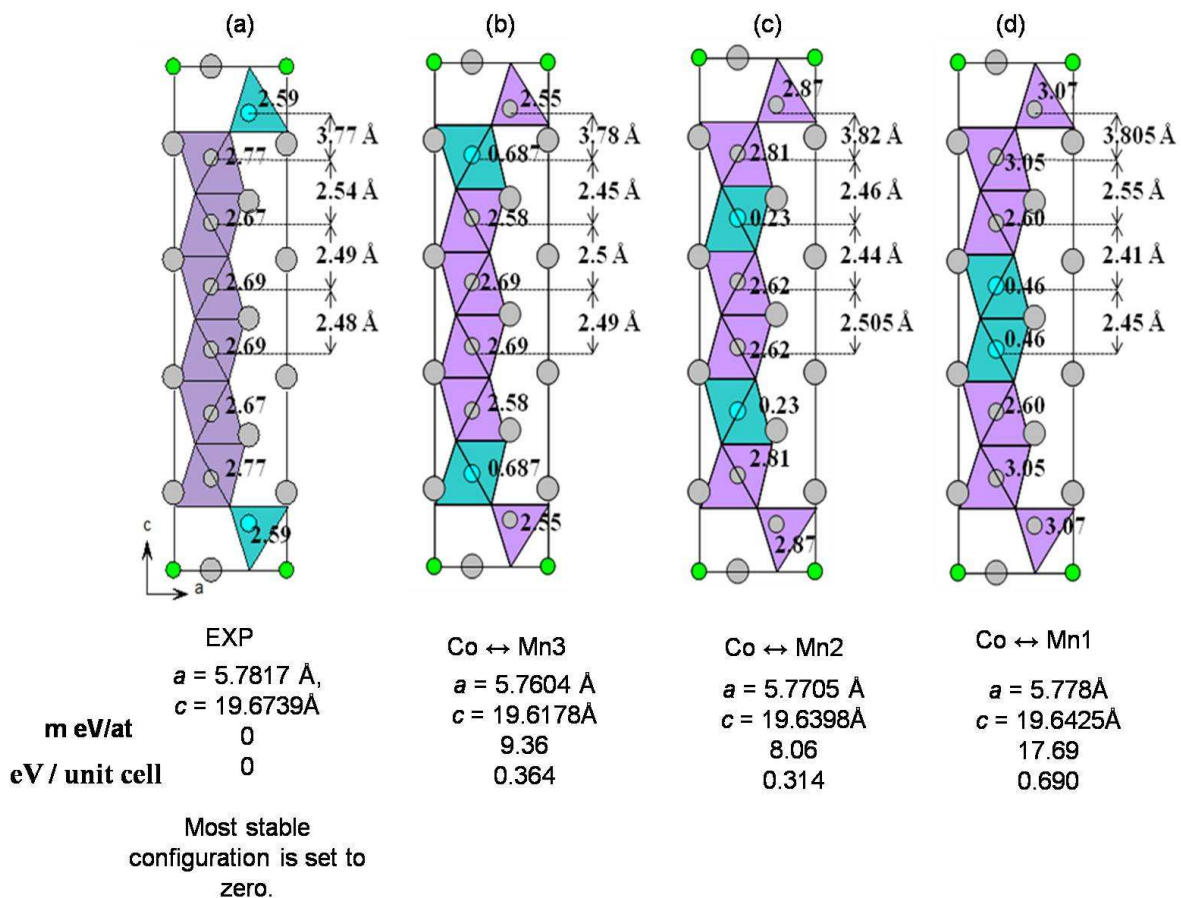


Fig.2-25: Cobalt/manganese distributions considered for DFT total energy calculations. The Co atoms are located in (a) the tetrahedra, (b) the edge octahedra, (c) the intermediate octahedra and (d) the central octahedra of the oligomers. Relative energies (the most stable one is set to 0) are indicated underneath each structure and correspond to the AF spin configuration in the GGA approximation. Mn is given in purple and Co in green

With respect to both the chemical ratio $Co/Mn \approx 2/6$ determined by microprobe analysis, and the site multiplicities imposed by the $P\bar{6}m2$ space group (three $Oh-2(h)$ and one $Td-2(i)$ Wyckoff sites), only four fully ordered configurations are thus to be tested (Fig.2-25). The total energy was calculated for each model. The most stable structure is found to be when Co atoms are located in tetrahedra for both FM and AFM calculations in good agreement with crystallo-chemical clues. Regarding the electron correlation of the metal atoms 3d states using GGA + U calculations, the addition of onsite repulsion U did not change the trend observed within GGA only approximation. We can finally propose the actual chemical composition of this new material, i.e. $Ba_8Co^{3+}(Td)_2Mn^{4+}(Oh)_6ClO_{22}$, which is the $n = 6$ member of the $Ba_{n+2}(Co,Mn)_{n+2}ClO_{3n+4}$ series with a segregation of Mn and Co atoms in octahedra and tetrahedra, respectively. We note that Co in the two central octahedra sites is the structure with the high energy.

To our knowledge, it is the first example of such face-sharing octahedral hexamers ($n_{octa} = 6$), besides some $n_{octa} = 2, 3, 4, 5$ and infinite ones. Clearly, the structural edifice results from a combination of $BaMnO_{3-\delta}$ (the 15R polytype displays the longest $n = 5$ linear oligomers apart from the hexamers in the title compound) and $BaCoO_{3-\delta}$ polytypes (the terminal tetrahedra are formed by oxygen deficient $[BaO_2]$ in the Ba-cobaltites). Here, the cationic ordering likely stabilizes the 8H-form, since cationic Mn/Co order seems to depend on the structural type in the commonly observed linear structures: $5H-BaCo_{0.8}Mn_{0.2}O_{2.80}$, $12H-BaMn_{0.4}Co_{0.6}O_{2.83}$ (*Miranda2008; Miranda2007*) and $Ba_6Co_4Mn_2ClO_{16-\delta}$ (see section 2.2.2.b)).

2.2.3.e) Powder synthesis

Despite several attempts, the synthesis of the single-phase powder was not possible. All the attempts give a biphasic reaction mixture with maximum 80% $Ba_8(Co,Mn)_8ClO_{22}$ and 20% $Ba_6Co_6ClO_{16}$ for reason already explained in section Chapter 1. (Page 60). In Fig.2-26 (a) and (b) is given the Rietveld refinement of one such biphasic mixture.

Given the structural similitude, a differentiation between the two compounds in neutron diffraction is complicated and was not attempted. The theoretical neutron patterns for the biphasic mixture, using a percentage of 80%

$Ba_8(Co,Mn)_8ClO_{22}$ and 20% $Ba_6Co_6ClO_{16}$ calculated with FullProf program between 0 and $160^\circ 2\theta$ is given in Fig.2-26(c) and we can see that there are only two peaks that do not belong to both phases (Fig.2-26(d)).

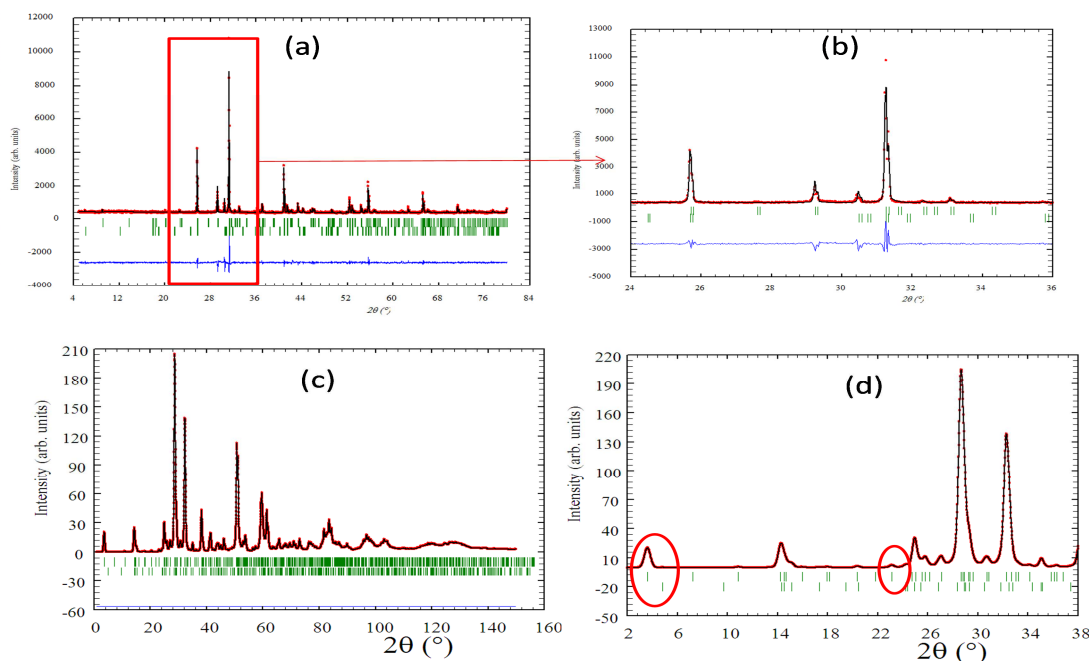


Fig.2-26: (a) and (b) Rietveld refinement of X – ray pattern of biphasic mixtures obtained during the attempts to synthesize the pure powder of $Ba_8(Co,Mn)_8ClO_{22}$. (80% phase hexamer: $R_{Bragg}=6.38\%$, $R_F = 6.75\%$ and 20% phase tetramer: $R_{Bragg} = 7.58\%$, $R_F = 7.86\%$); (c) and (d) Theoretical neutrons powder pattern calculated for a 80% hexamer + 20% tetramer.

2.2.3.f) Magnetic / electric potentialities

Furthermore, in the absence of sizeable single crystals, it is rather difficult to conclude on the magnetic and electric behaviour of the compound. However several trends could be announced. The 2H- $BaMnO_3$ antiferromagnetically orders at relatively high temperature, $T_N = 59$ K, which pictures strong AFM exchanges between adjacent sites and between chains (Cussen2000). On the basis of the ideal $Mn(Oh)/Co(Td)$ ordered model, similar AFM frustrated effects are expected. Furthermore the connections of the linear hexamers by strong AFM Co_2O_7 dimers (Kauffmann2008) should extend the AFM exchanges in three dimensions. In addition, the corner-sharing $Co-O-Mn$ super-exchanges are expected to be also

antiferromagnetic since Mn doping deteriorates the ferromagnetism in the La_{0.7}Sr_{0.3}Co_{1-y}Mn_yO₃ system (Phuc2003).

However, the possible presence of small amount of cobalt inside the hexamers would create direct Co–Co FM exchanges, (Kauffmann2008) playing in favour of a spin-glass state as observed in Ba(Co,Mn)O_{3-δ} compounds (Cussen2000, Phuc2003). Then regarding the knowledge on similar compounds, the latter is expected to be an insulating antiferromagnet. The analysis of the density of states topology allows us also to propose a trend for the electronic configuration, i.e. Co³⁺(Td) (d⁶ high spin) and Mn⁴⁺(Oh) (d³), in relatively good agreement with the electroneutrality if one considers a small amount of Mn³⁺ in the linear hexamers. As discussed in the previous section, a similar cationic distribution was observed by neutron diffraction for Ba₆Co₄Mn₂ClO_{16-δ}, with Mn displaying a preference for the central octahedral site (35%Co/65%Mn), Co in the tetrahedral site and 63%Co/37%Mn in the marginal octahedra. For this compound, a Ba₆(Co^{III}_{1.26}/Mn^{IV}_{0.74}(Oh_{marginal}))(Co^{III}_{0.7}/Mn^{IV}_{1.3}(Oh_{central}))Co^{III}₂(Td)Cl_{0.942}O_{15.646} → (Co/Mn)^{+3.34} formulation was proposed in good accordance with the oxidation degree determined by iodometric titration (3.37).

Indeed, on the basis of Co(Td) in the state Co³⁺ as seen in related compounds from first principles studies, the average oxidation state of Mn(Oh) should be Mn^{3.83+}. It is however clear that, to confirm this tendency, further electrical and magnetic investigation needs confrontation with experimental data and/or calculations using a broader set of parameters and spin configurations. One should also keep in mind that the structural model used for computations is restricted to fully occupied atoms without vacancies, and also without mixed site occupancies.

2.2.3.g) Conclusion

In few points, the conclusions at this part are:

- A new term of the Ba_{n+2}Mn_{n+2}XO_{3n+4} (M = Co, Fe, Mn; X = Cl and F) series was isolated and fully structurally characterized.
- It corresponds to the **n = 6 term** of the series and is formed by 6 face sharing octahedra and corner sharing tetrahedra.

- It is the first example of such **face-sharing octahedral hexamers** ($n_{\text{octa}}=6$), beside some: $n_{\text{octa}}=2$ (4H-BaMnO_{2.65}, *Adkin2006*), $n_{\text{octa}}=3$ (10H-Ba₅Co₅XO_{13-δ}, *Mentré2008*; 5H-BaCoO_{2.8} *Boulahya2005*), $n_{\text{octa}}=4$ (Ba₆Co₆XO_{16-δ}, *Tancret2005*, *Ehora2007a*), $n_{\text{octa}}=5$ (15R-BaMnO_{2.99}, *Taguchi1977*) and some infinite ones (2H-BaCoO₃, *Taguchi1977*; 2H-BaMnO₃ *Negas1971*).
- The synthesis method and single crystals XRD characterization were presented.
- A **Co(Td)/Mn(Oh) cationic distribution was confirmed by DFT calculations** and it is in accordance with our observations on similar compounds.

2.2.4. Ba(Mn,Fe)₁X_{0.2-x}O_{3-δ} (X = Cl, F)

The Mn–Fe substitutions are potentially the most interesting phases since a competition between the 6H (Mn rich) and 10H (Fe rich) polytypes is expected and already mentioned previously. The phase diagram for this line is recalled in Fig.2-27. For some terms, intergrown structures were observed and will be discussed in this section, with our most representative structural results, about this particular binary line.

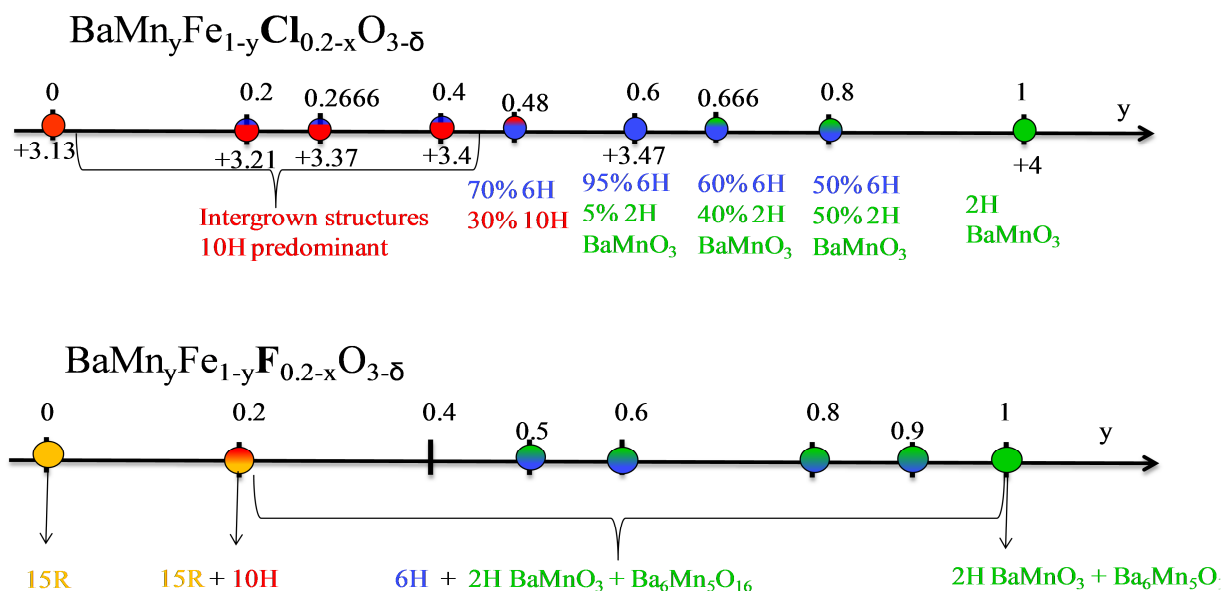


Fig.2-27 : Phase diagram for Mn – Fe substitutions.

2.2.4.a) Phases identification for $BaMn_yFe_{1-y}Cl_{0.2-x}O_{3-\delta}$ Difficulty to distinguish the polytypes in competition

The XRD patterns of some selected terms are given in Fig. 2-28 . They can be indexed using biphasic mixtures with different predominant polytypes depending on the Mn ratio (y), but at this stage we have to mention the extreme difficulty to distinguish the polytypes in competition due to the strong similitude between all patterns. For example, for $0 \leq y < 0.4$ area (red patterns in Fig. 2-28), the presence of the 6H polytype is rather difficult to observe but is characterized by its (104) reflexion (Fig. 2-28, (c)). In this range, its weak intensity reveals a minor amount of the phase which was confirmed by ED investigations for $y = 0.4$ (see latter).

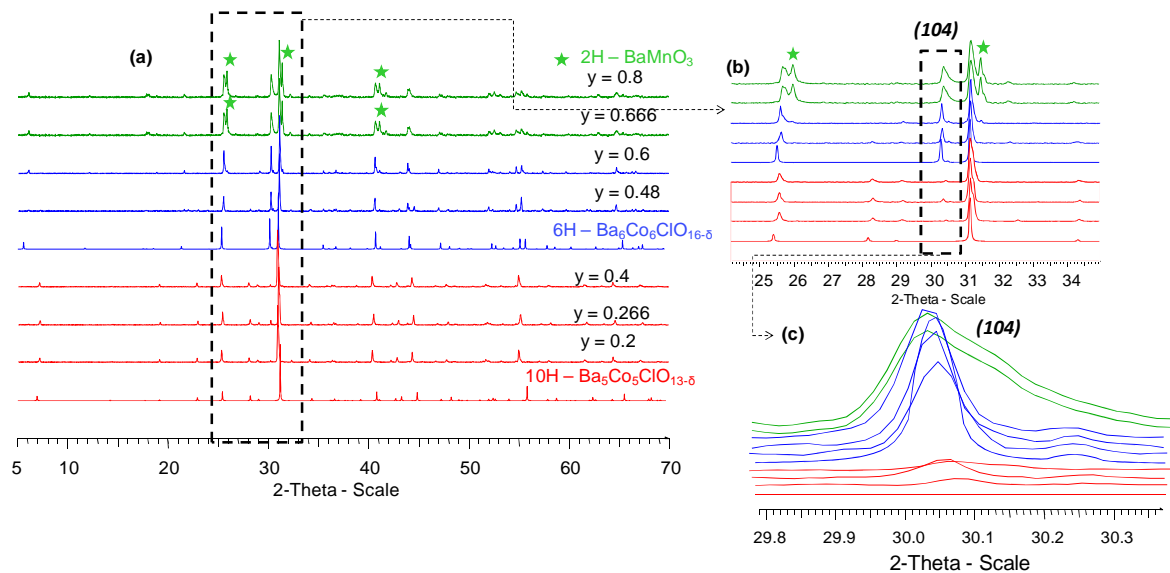


Fig. 2-28: XRD patterns (with different zooms) for $BaMn_yFe_{1-y}Cl_{0.2-x}O_{3-\delta}$; $0.2 \leq y \leq 0.4$, 10H predominant, red; $0.48 < y \leq 0.6$ 6H predominant, blue; $0.66 \leq y \leq 0.8$, 2H predominant, green; $2H - BaMnO_3$ (green stars)

However the following tendencies have been pointed out:

- $0 \leq y < 0.4$: biphasic mixture 10H + 6H polytypes, 10H predominant + minor presence of the $2H - BaMnO_3$
- $0.4 \leq y < 0.6$: biphasic mixture 10H + 6H polytypes, 6H predominant + minor presence of the $2H - BaMnO_3$
- $0.6 \leq y < 0.8$: biphasic mixture 6H + 2H polytypes, 6H predominant

- $0.8 \leq y \leq 1$: biphasic mixture 2H + $BaCl_2$

The difficulty to distinguish the different polytypes using our XRD data is highlighted in Fig.2-29 where the Rietveld refinements using one 10H polytype-only and a biphasic mixture 6H+10H for $BaMn_{0.4}Fe_{0.6}Cl_{0.2-x}O_{3-\delta}$ ($Ba_5Mn_2Fe_3ClO_{13-\delta}$) are compared (Fig.2-29, (b)).

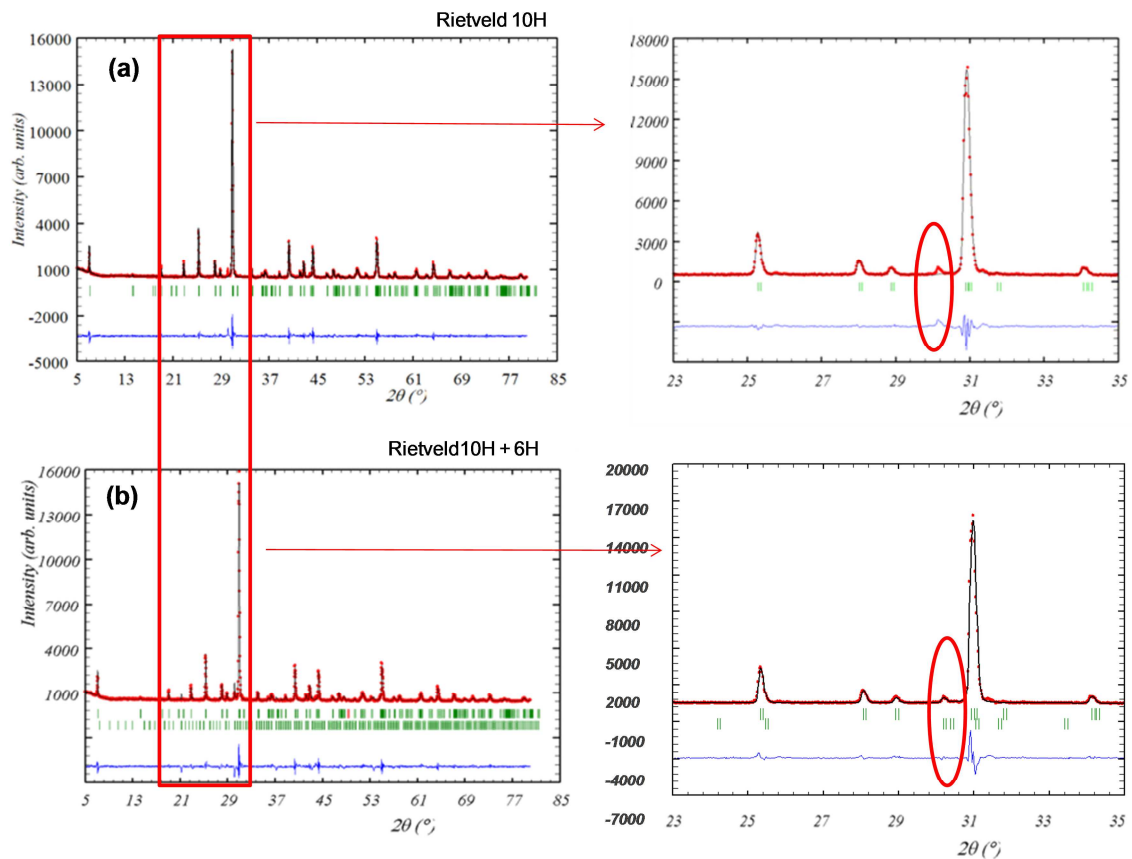


Fig.2-29: (a) single phase Rietveld refinement for $BaMn_{0.4}Fe_{0.6}Cl_{0.2-x}O_{3-\delta}$ ($R_{Bragg} = 6.87\%$, $R_F = 7.89\%$) and (b) Rietveld refinement 10H + 6H biphasic mixture (phase 10H: $R_{Bragg} = 7.88\%$, $R_F = 6.39\%$ and phase 6H: $R_{Bragg} = 14.3\%$, $R_F = 12.1\%$).

a) Fe/Mn poor miscibility

We have performed a pattern matching on the XRD powder patterns of all the prepared samples using mixtures of 6H, 10H and 2H polytypes. The cells volume evolutions are given in Fig.2-30. Clearly according to these volume evolutions, three phases should be present with variable ratio, depending on y . Lattice parameters are gathered in Table 2-5 along with the oxidation degrees values determined by titration

(mean oxidation number over a mixture of phases). The titration shows the expected increase of the metal valence versus y for $BaMn_yFe_{1-y}Cl_{0.2-x}O_{3-\delta}$, while the phases in presence follow the $10H \rightarrow 6H \rightarrow 2H$ progression, according to a limited Mn/Fe miscibility in each phase.

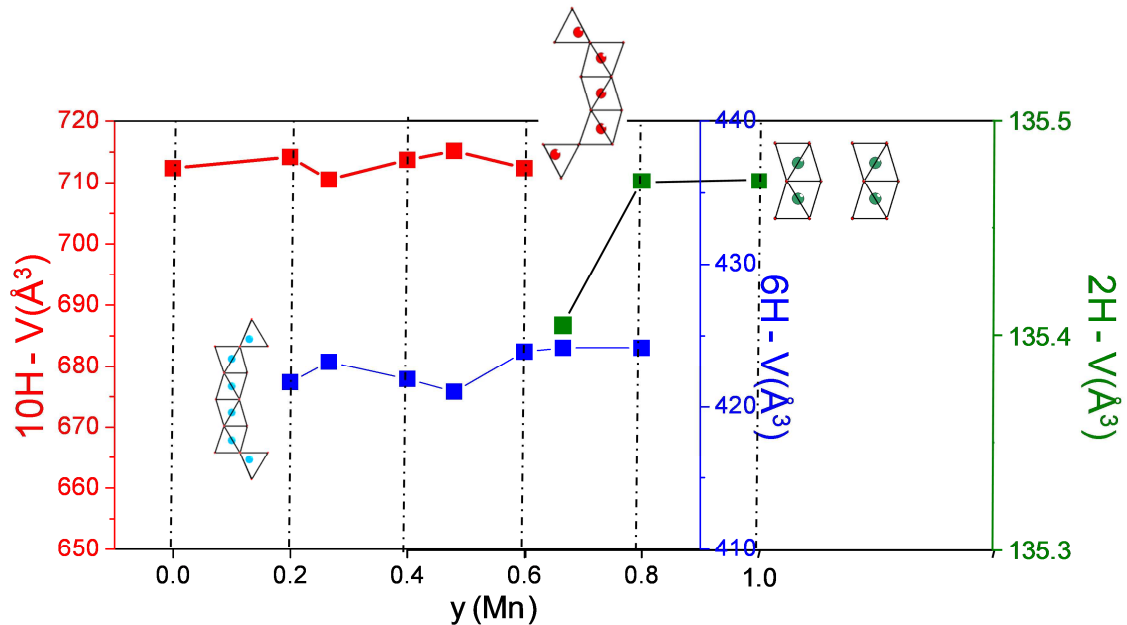


Fig.2-30 : Lattice volume evolution for the 10H (red), 6H (blue) and 2H (green) polytypes. The Mn ratio ($y - BaMn_yFe_{1-y}Cl_{0.2-x}O_{3-\delta}$) is given on the OX axis.

Table 2-5: XRD refinement information and titration results for $BaMn_yFe_{1-y}Cl_{0.2-x}O_{3-\delta}$ (O.D. = oxidation degrees, O.C. = oxygen content):

y	Structural type	O.D. (O.C.)	$a(\text{Å})$ $c(\text{Å})$
0	10H	3.13 (12.30)	$a = 5.780(1)$ $c = 24.612(1)$
0.2	10Hpredominant+6H	3.21	$a = 5.779(2)$ $c = 24.687(1)$ + $a = 5.761(4)$ $c = 14.689(2)$
0.266	10Hpredominant+6H	3.37	$a = 5.770(2)$ $c = 24.619(1)$ + $a = 5.768(2)$ $c = 14.682(1)$
0.4	10Hpredominant+6H	3.41	$a = 5.780(2)$ $c = 24.687(1)$ + $a = 5.763(3)$ $c = 14.701(2)$
0.48	10H+6H		$a = 5.779(2)$ $c = 24.704(2)$ + $a = 5.750(2)$ $c = 14.689(7)$
0.6	10H +6Hpredominant	3.47	$a = 5.771(2)$ $c = 24.729(8)$ + $a = 5.772(2)$ $c = 14.718(8)$
0.66	6H + 2H- $BaMnO_{3-\delta}$		$a = 5.750(6)$ $c = 14.722(2)$ + $a = 5.686(6)$ $c = 4.807(7)$
0.8	6H + 2H- $BaMnO_{3-\delta}$		$a = 5.747(7)$ $c = 14.721(4)$ + $a = 5.701(5)$ $c = 4.809(4)$

b) Impossibility to simulated ND data using 10H + 6H and 2H– BaMnO_3 mixture

However, RT- ND data could not be simulated using a triphasic mixture of 10H + 6H and 2H– BaMnO_3 . The corresponding Pattern-matching/Rietveld refinements are given in Fig. 2-31 (a)/(b), but revealed the presence of none or badly – indexed peaks both at low and high 2θ angles which avoid a reliable refinement even using the three phases.

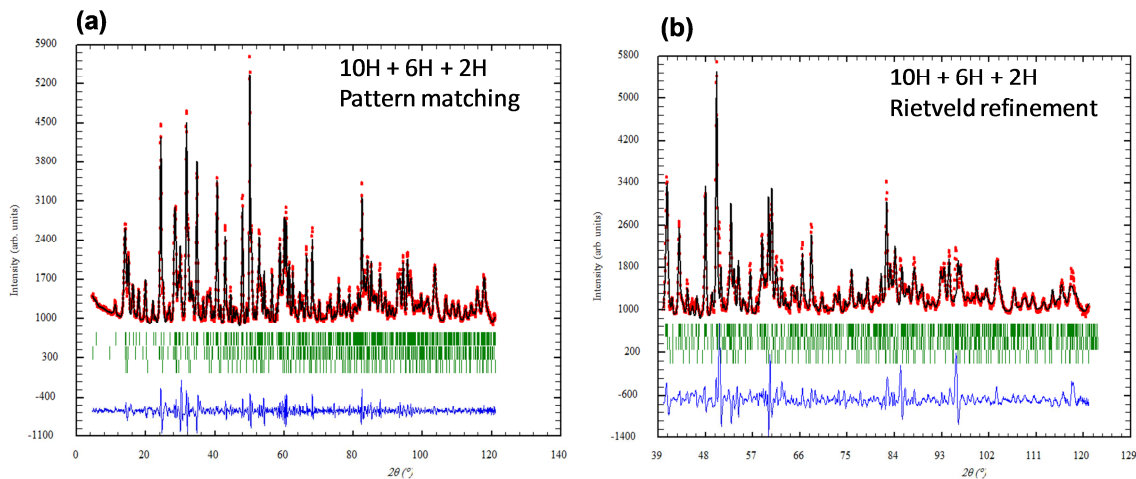


Fig. 2-31: ND refinement for $\text{BaMn}_{0.4}\text{Fe}_{0.6}\text{Cl}_{0.2-x}\text{O}_{3-\delta}$ (a) pattern matching 10H + 6H + 2H and (b) Rietveld with the same phases

c) New intergrowths

For a better understanding, HR Electron Microscope analyses were performed by Professor Marielle Huvé. We give below the results in few points:

- The [001] zone axis pattern (ZAP) of the $\text{BaMn}_{0.4}\text{Fe}_{0.6}\text{Cl}_{0.2-x}\text{O}_{3-\delta}$ sample shows no extra spot and is consistent with the cell parameters refined from XRD for all phases, $a \sim 5.7\text{Å}$ (Fig. 2-32, (a)), but the [010] ZAP shows a great disorder discussed here after.
- Some images of the [100] ZAP (Fig. 2-32, (b)) and their corresponding HRTEM images (Fig. 2-32, (c)) display a perfect regularity along c according to the 10H-phase model ($c \sim 24.5\text{Å}$, S.G. $P6_3/mmc$). The $00l$ ($l=2n+1$) spots presence, (not allowed with the 6_3 axis) is due to double diffraction effects and disappear after sample- tilting.

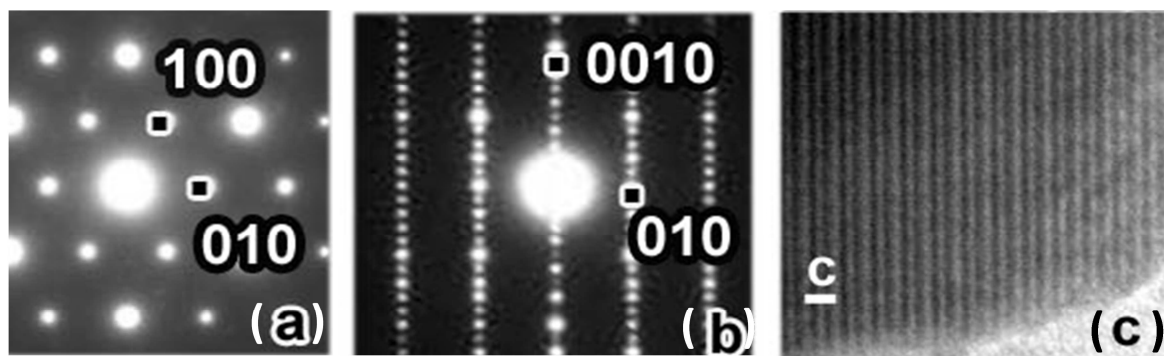


Fig. 2-32: SAED and Electron Microscopy for $BaMn_{0.4}Fe_{0.6}Cl_{0.2-x}O_{3-\delta}$; (a) [001] zone axis pattern; (b) [100] ZAP; (c) image corresponding to (b)

However, for some crystals, more or less intense streaks appear along c^* . The image corresponding to a [010] ZAP with intense streaks reveals a great disorder (Fig. 2-33, (a)). To interpret this disorder, images were simulated for an ideal 10H structure. According to the simulation, for a thickness of 56.5 Å and a defocus of 20 nm, the contrast matches the experimental one, displaying a contrast between bright (octahedral trimers strings) and less-bright dots (tetrahedral dimers) (Fig. 2-33, (b)).

In the experimental image (Fig. 2-33, (d)) the number of less bright contrasts (assigned to tetrahedral dimers) conserve its thickness, while the number of bright dots (=octahedral trimers strings) vary and can reach up to 7 or 8 (instead of one for the ideal-10H). Then, the recombination between the ideal 10H-contrast slices (Fig. 2-33, (c)) leads to experimental observed contrasts. For instance the zone noted 7 (seven bright spots) corresponds to the stacking of 15 octahedra between terminal tetrahedral dimers (Fig. 2-33, (e)). Indeed, the corresponding 43Å length could be considered as a local c parameter with n octahedra-long chains ($c = (2 \times 2.5)_{\text{tetrahedra}} + (n \times 2.6)_{\text{octahedra}}$).

This local structure would correspond to a Mn-rich composition, where the presence of Fe is determining the presence of h' layers by intermediate Fe_2O_7 tetrahedra, as described for the hexameric structure see section 2.2.3. (Page 73). A number of intergrown-intermediate polytypes are observed on the experimental figure (=zones 3, 4, 7, 8) (Fig. 2-33, (a)).

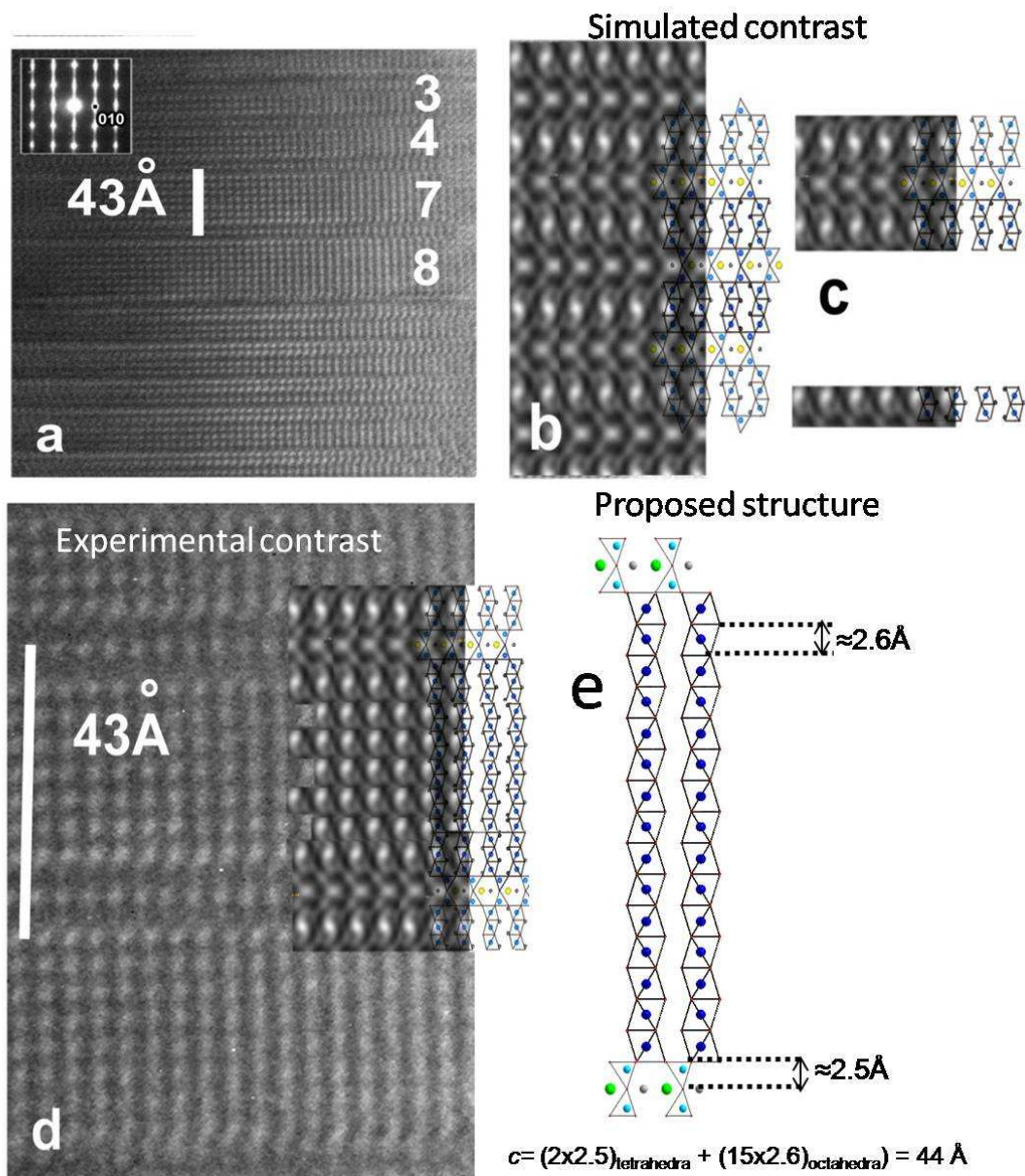


Fig. 2-33: (a) Image corresponding to a [100] EDP of $BaMn_{0.4}Fe_{0.6}Cl_{0.2-x}O_{3-\delta}$ sample displaying intense streaks along c^* ; (b) Simulated image based on the refined structure ($P6_3/mmc$, $a = 5.77\text{Å}$, $b = 24.69\text{Å}$) for a defocus of 20 nm and a thickness of 56 Å; (c) Parts of the simulated images of the 10H structure from (b), used for the reconstruction of the experimental contrast; (d) Experimental image and superposition with the reconstructed contrast leading to a stacking of 15 octahedra; (e) Calculation of a local c parameter leading to 43.1 Å, value which corresponds to the experimental measured distance of 43 Å.

The composition of the investigated term, determined by EDS on the basis of 3 crystallites with similar compositions, gives $Ba_5Mn_{0.64}Fe_{4.36}Cl_{0.9}O_{13-\delta}$ ($BaMn_{0.13}Fe_{0.87}Cl_{0.18}O_{3-\delta}$). We can conclude that in the Mn/Fe line, the maximal Mn miscibility would correspond to the formula $Ba_5Mn_{0.64}Fe_{4.36}Cl_{0.9}O_{13-\delta}$ within the 10H-structure. The increase of the Mn ratio gives a predominating 6H-phase (Mn rich) which intergrowths with 2H and 10H fragments.

d) Thermal behaviour

Since for the Co compounds, the HT treatment (1030°C) creates the tetramer \rightarrow trimer transformation, the thermal stability of the Mn–Fe intergrown structure was tested. The HT XRD data were collected using a D8 Advance - XRK900 (Bruker-AXS) diffractometer from R.T. to 1000°C and back for $BaMn_{0.4}Fe_{0.6}Cl_{0.2-x}O_{3-\delta}$ (Fig.2-34) and show a large thermal stability.

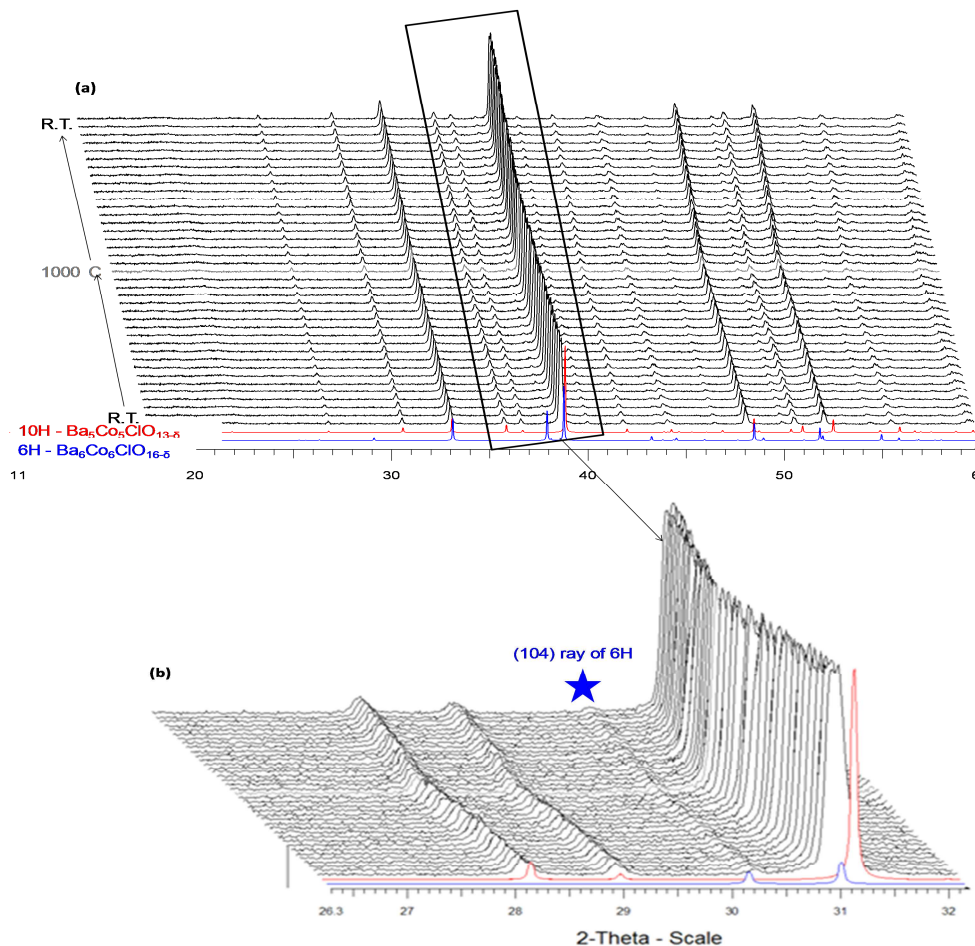


Fig.2-34: HT - XRD for $BaMn_{0.4}Fe_{0.6}Cl_{0.2-x}O_{3-\delta}$ in heating (R.T. \rightarrow 1000°C) and cooling (1000° \rightarrow R.T.). For comparison, 10H - $Ba_5Co_5ClO_{13-\delta}$ (red) and 6H $Ba_6Co_6ClO_{16-\delta}$ (blue) powder patterns are also given.

2.2.4.b) Phases identification for $BaMn_yFe_{1-y}F_{0.2-x}O_{3-\delta}$

The oxo-fluoride case is not simpler since no pure compounds have been obtained. However, according to XRD investigations, several zones can be distinguished depending on the Mn ratio (y).

- $0 \leq y \leq 0.2$: biphasic mixture 15R (*Sturza2010*) + 10H polytypes (corresponding to the yellow area in the phase diagram discussed in the section 2.1.3.b))
- $0.2 < y \leq 0.6$: biphasic mixture 10H + $Ba_6Mn_5O_{16}$ (*Boulahya2005*)
- $0.6 < y \leq 0.9$: biphasic mixture of 2H – $BaMnO_3$ and 6H (predominant)
- $0.9 < y \leq 1$: 2H – $BaMnO_3$ + BaF_2

XRD patterns for $BaMn_yFe_{5-y}F_{0.2-x}O_{3-\delta}$ are given in Fig.2-35. We did not further investigate this system.

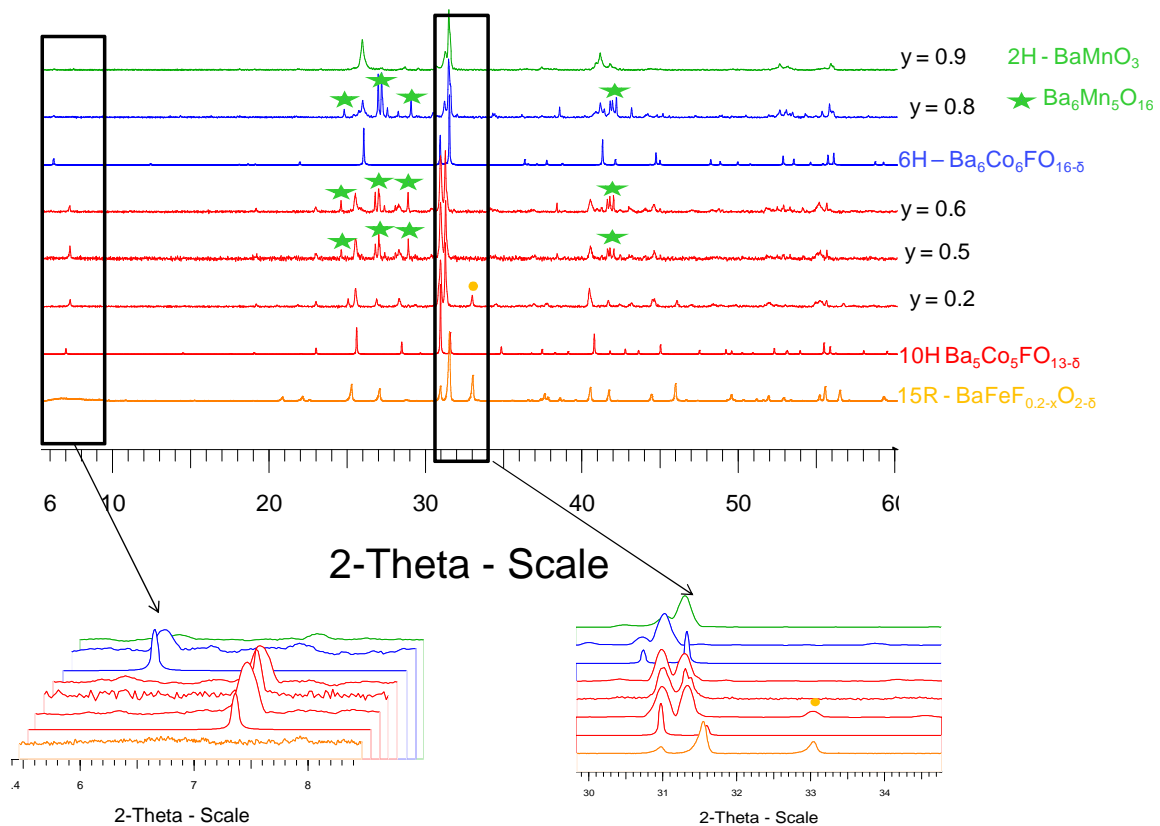


Fig.2-35: X –ray powder diffraction patterns for fluorine solid solution: $y = 1$ (15R + 10H) – orange; $1 < y \leq 3$ (10H + $Ba_6Mn_5O_{16}$) – red; $y = 4$ (6H + $Ba_6Mn_5O_{16}$ + 2H - $BaMnO_3$) – blue; $4 < y \leq 5$ ($Ba_6Mn_5O_{16}$ + 2H - $BaMnO_3$ + BaF_2) - green

2.2.4.c) Conclusions

In this part, the synthesis and structural characterisation of Mn–Fe mixed oxo–halides were presented. The principal conclusions can be summarized as follows:

- The XRD powder investigations revealed that the **predominant structural type depends on the Mn ratio (10H→ 6H→ 2H)**; the mean overall oxidation degrees increase as the Mn ratio increases, consistent with the observations from section 2.1.2.b)
- The absence of significant lattice evolution would suggest a **poor miscibility of Mn in the 10H-Fe polytype** estimated about $y = 0.13$
- Meanwhile, the several polytypes can **create fully disordered intergrowths between the 10H, 6H and 2H forms**.
- Then, based on the observations of other systems (6H' - $BaMn_{0.85}Fe_{0.15}O_{2.87}$ (Mn/Fe: 0.95/0.05 in marginal octahedra, 1/0 in central octahedra and 0.6/0.4 for the corner sharing octahedron) and $BaMn_{0.6}Fe_{0.4}O_{2.72}$ (0.6/0.4, 1/0, 0.2/0.7 respectively), determined by neutron diffraction (*Miranda2009*) a cationic distribution with **Mn preferentially in the central faces sharing octahedra**, Fe in tetrahedral site and Fe/Mn mixed marginal octahedral sites can be proposed, all within intergrown structures with trimer, tetramer and infinite chains randomly distributed.

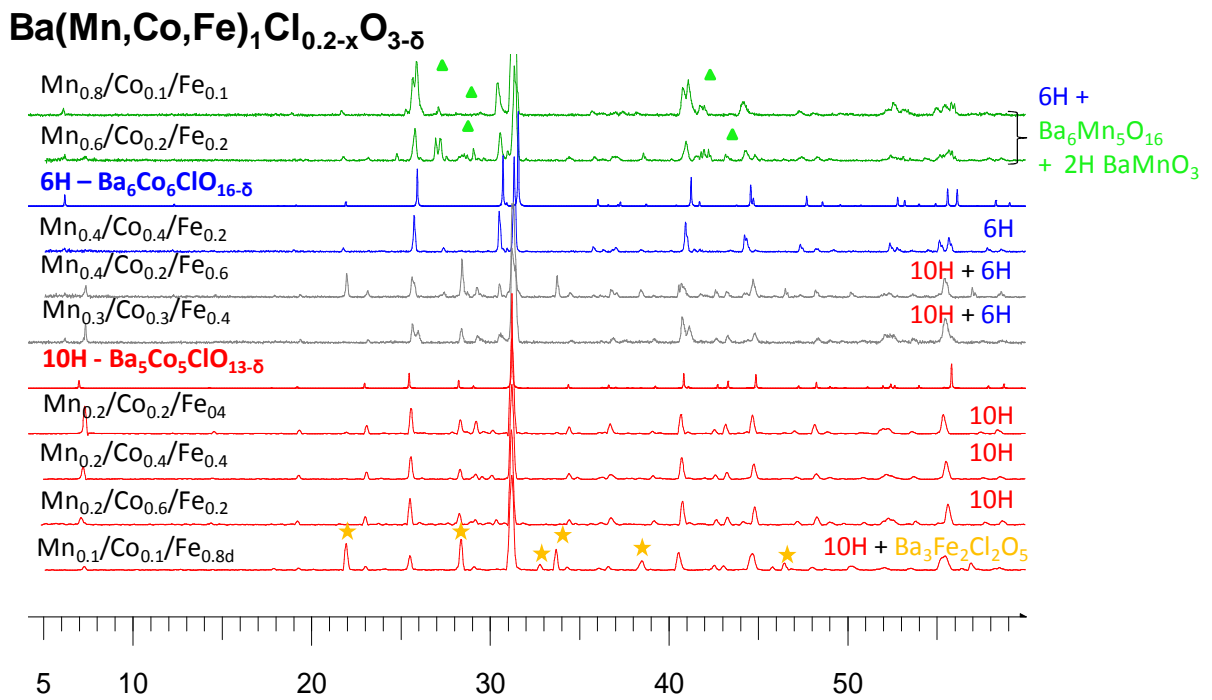
2.2.5. $BaMX_{0.2-x}O_{3-\delta}$ (M = Mn + Fe + Co; X = Cl, F) ternary substitutions

In this short section, the structural characterisation by XRD powder diffraction of ternary Co, Fe, Mn compounds will be presented. The general results permit us to create the central areas represented on the phase diagrams (see sections 2.1.2. and 2.1.3.). The structural types stabilized follow the general trends observed on the binary lines. In fact, starting from the systematic 10H-structure of oxygen-poor Co/Fe compounds, the Mn ratio y in $Ba(Co,Fe)_{1-y}Mn_yCl_{0.2-x}O_{3-\delta}$ acts as the decisive factor. The XRD patterns in the ternary substitution case are given in Fig.2-36. The corresponding structural polytypes, cell parameters (for pure preparations) together with the oxidation degrees determined by iodometric titration

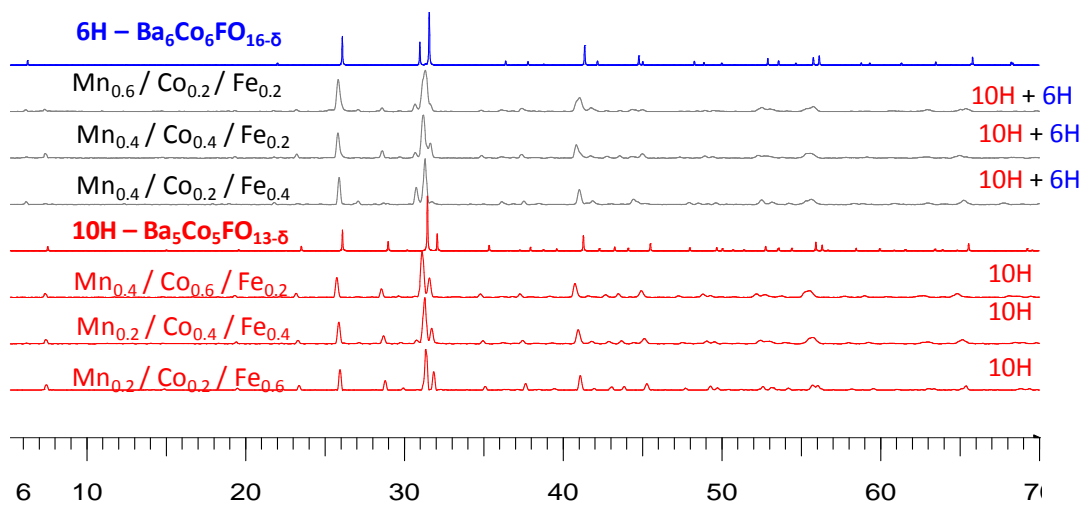
are given in Table 2-6. As observed, we can stabilize single phases or biphasic mixtures with one predominant polytype (10H or 6H) depending on the Mn ratio in the compound corresponding with the phase diagram discussed in the section 2.1.1. (Page 38). We did not go into the details of these phases but they help to establish the full phase diagrams.

Table 2-6: XRD powder investigations results for Ba(Co,Mn,Fe)X_{0.2-x}O_{3-δ}. The average oxidation degrees (O.D.) along with oxygen content (O.C.) determined by iodometric titration, the cell parameters determined by pattern matching are also presented.

X	Compound formulation	Structural type	O.D.	O.C.	Cell parameters
		10H +	3.09		
	BaMn _{0.1} Co _{0.1} Fe _{0.8} Cl _{0.2} O ₃	Ba ₃ (Fe ⁺³) ₂ Cl ₂ O ₅			
	Ba ₅ Mn _{0.2} Co _{0.2} Fe _{0.6} Cl _{0.2} O ₃	10H	3.10	12.30	
	BaMn _{0.2} Co _{0.4} Fe _{0.4} Cl _{0.2} O ₃	10H	3.11	12.30	a = 5.732(2), c = 24.441(1)
Cl	BaMn _{0.2} Co _{0.6} Fe _{10.2} Cl _{0.2} O ₃	10H	3.17(4)	12.40	a = 5.685(2), c = 24.332(4)
	BaMn _{0.3} Co _{0.3} Fe _{0.4} Cl _{0.2} O ₃	10H +6H	3.26		
	BaMn _{0.4} Co _{0.2} Fe _{0.4} Cl _{0.2} O ₃	10H +6H + Ba ₅ Mn ₃ ClO ₁₂			
	BaMn _{0.4} Co _{0.4} Fe _{0.2} Cl _{0.2} O ₃	6H	3.26	12.60	a = 5.723(2), c = 14.578(1)
	BaMn _{0.6} Co _{0.2} Fe _{0.2} Cl _{0.2} O ₃	6H +Ba ₆ Mn ₅ O ₁₆ +2H-BaMnO3			
	BaMn _{0.8} Co _{0.1} Fe _{0.1} Cl _{0.2} O ₃	6H + 2H-BaMnO3 + Ba ₆ Mn ₅ O ₁₆			
	BaMn _{0.2} Co _{0.6} Fe _{0.2} F _{0.2} O ₃	10H	a = 5,705(2); c = 23,894(1)		
	BaMn _{0.2} Co _{0.4} Fe _{0.4} F _{0.2} O ₃	10H	a = 5,730(4); c = 24,055(2)		
	BaMn _{0.2} Co _{0.2} Fe _{0.6} F _{0.2} O ₃	10H	a = 5,755(5); c = 24,141(2)		
F	BaMn _{0.4} Co _{0.4} Fe _{0.2} F _{0.2} O ₃	10H+6H	a = 5,714(5); c = 23,952(3)		
			a = 5,709(4); c = 14,362(1)		
	BaMn _{0.4} Co _{0.2} Fe _{0.4} F _{0.2} O ₃	10H +6H	a = 5,735(3); c = 24,051(3)		
			a = 5,715(3); c = 14,411(2)		
	BaMn _{0.6} Co _{0.2} Fe _{0.2} F _{0.2} O ₃	10H +6H	a = 5,669(2); c = 14.278(3)		
			a = 5,682(1); c = 24.009(7)		



2-Theta - Scale



2-Theta - Scale

Fig.2-36: X – ray powder patterns for $Ba(Co,Fe,Mn)X_{0.2}O_{3-\delta}$. In blue are given the diffractograms that can be indexed using a 6H type structure compound, in red, the one with 10H structure, while $Ba_3Fe_2Cl_2O_5$ is given in orange and 2H - $BaMnO_3$ / $Ba_5Mn_6O_{16}$ in green.

2. 3. Magnetic and electrical characterization of mixed $BaMX_{0.2-x}O_{3-\delta}$ systems

On the basis of previous characterizations of the parent cobalt oxo-halides ($X = F, Cl$ for both the trimeric and tetrameric forms), we will now describe our investigations of electric and magnetic properties in the extended $M = Co/Fe/Mn$ oxo-halide system. In this section, the magnetic measurements, neutrons diffraction and the electrical conductivity experiments will be discussed for some of those mixed compounds. In a first stage, let briefly recall the magnetic structures and properties already published for the alone Co-based compounds.

2.3.1. State of the art on $Ba_5Co_5XO_{13-\delta}$ and $Ba_6Co_6XO_{16-\delta}$ ($X = Cl, F$) properties

2.3.1.a) Magnetic structure and proprieties of parent oxo-halides

Both $X = F$ and Cl , $Ba_5Co_5XO_{13-\delta}$ and $Ba_6Co_6XO_{16-\delta}$ compounds display a particular antiferromagnetic (AFM) behavior. It was described in several previous papers from our group (*Kauffmann2006, 2007a, 2007b, 2007c and 2008, Ehora2007, 2007a and 2007b, Mentré2008 and 2010, Toulemonde2010*). These so-called particularities arise from several features characteristic of these series. The concerned magnetic behaviours are gathered in the Fig. 2-37 and Fig.2-38.

Briefly, one should recall:

- Generally, the magnetic susceptibilities show rather broad phenomena while the Néel temperatures (determined accurately from ND experiments) are not well distinguished.
- Important antiferromagnetic/ferromagnetic exchanges interplay in competition, since the refined magnetic structures involve FM magnetic intra-blocks and AFM inter-block couplings.
- In any cases, the local-ordered-moments refined for face-sharing Co positions are weak or null, which was assigned to both a strong electronic delocalization along the linear trimeric and tetrameric string, but also to a tendency for octahedral cobalt to retain a LS configuration.

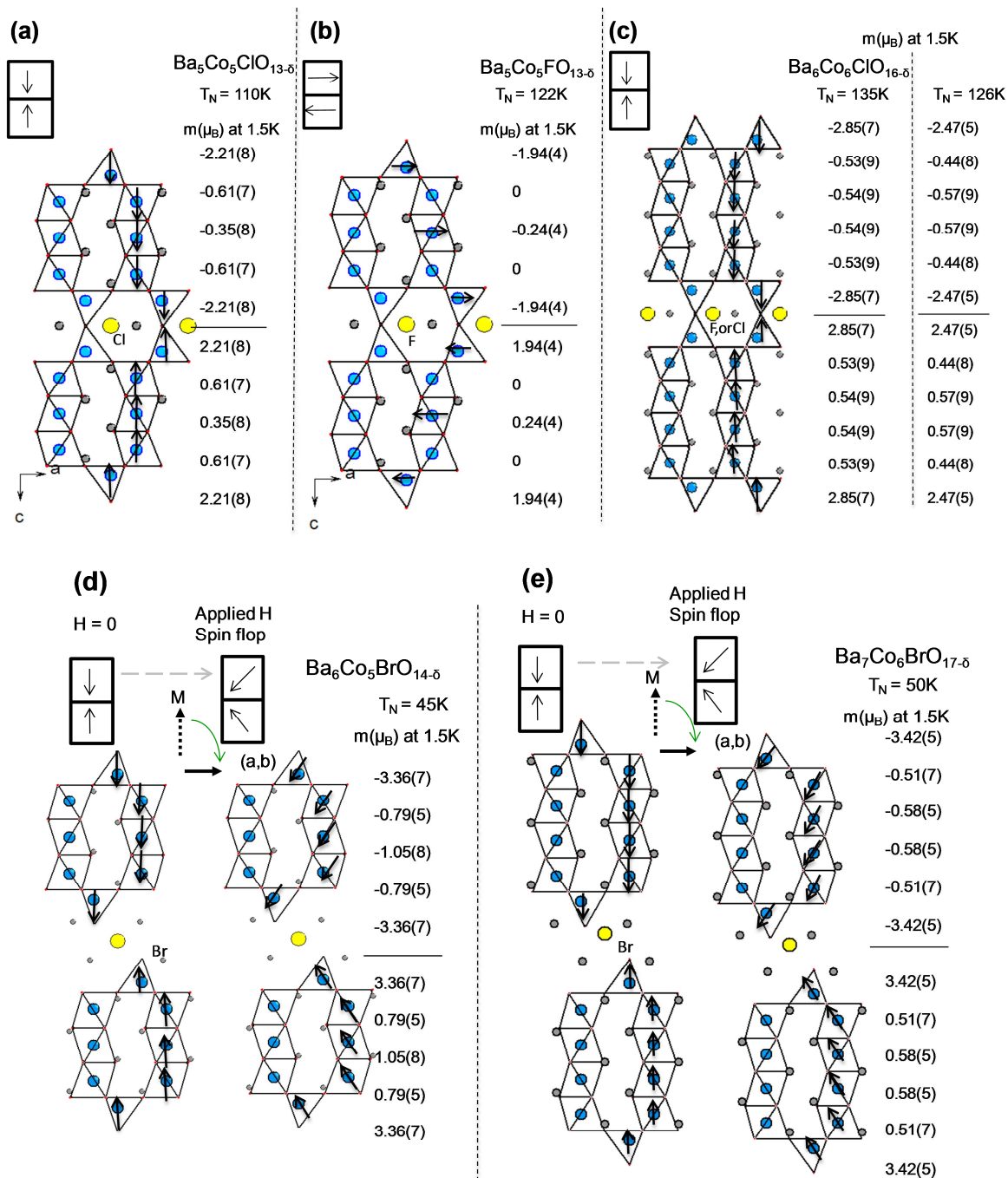


Fig. 2-37: Magnetic structures, magnetic moments values at 1.5K and Néel temperatures for (a) $Ba_5Co_5ClO_{13-\delta}$, (b) $Ba_5Co_5FO_{13-\delta}$ (c) $Ba_6Co_6XO_{16-\delta}$ (Mentré2008, Kauffmann2006, Mentré2010) and the spin flop in the case of (d) $Ba_6Co_5BrO_{14-\delta}$ and (e) $Ba_7Co_6BrO_{17-\delta}$ (Kauffmann2007b, Toulemonde2010)

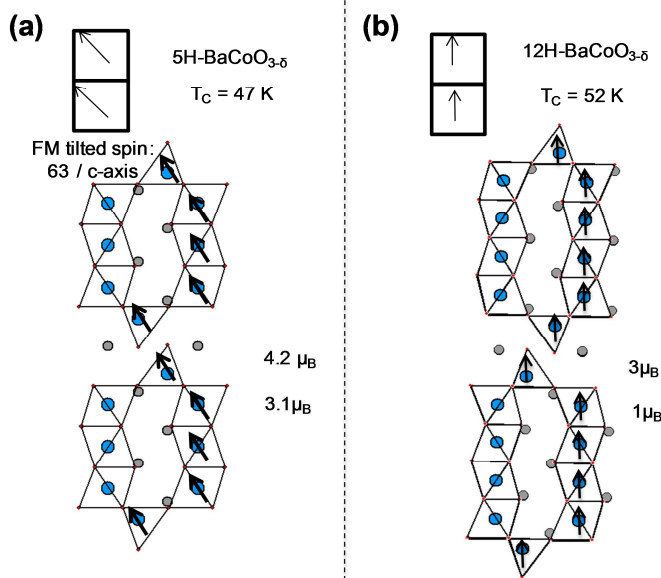


Fig.2-38 : Magnetic structures, magnetic moments values at 1.5K and Néel temperatures for (a) 5H - $\text{BaCoO}_{3-\delta}$ (Boulahya2005) and (b) 12H - $\text{BaCoO}_{3-\delta}$ (Jacobson1976, Hébert2007)

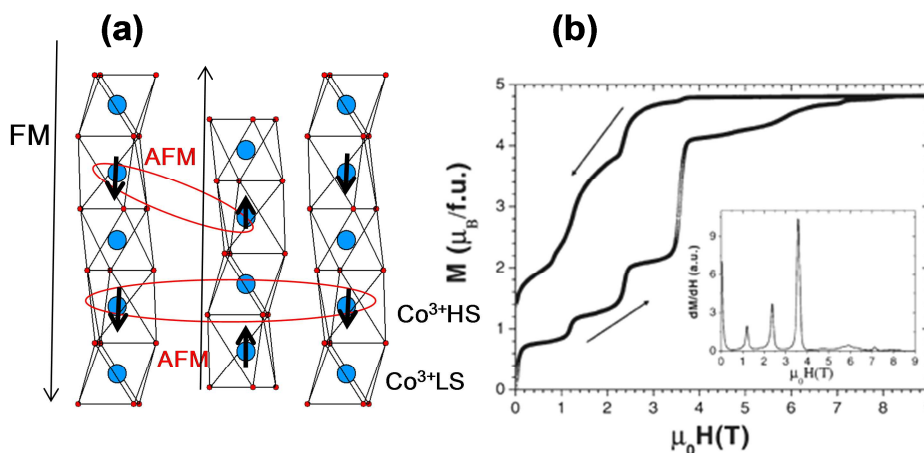


Fig.2-39: (a) Ferromagnetic chains in $\text{Ca}_3\text{Co}_2\text{O}_6$ with AFM inter – chains frustrations; (b) Field dependence of the magnetization of $\text{Ca}_3\text{Co}_2\text{O}_6$ crystals at 2K with the magnetic field H applied along the chain axis. The arrows indicate the increasing and decreasing filed process down to 2K. Insert: field dependence of the corresponding derivative dM/dH , (Maignan2000, Maignan2004, Hardy2004)

Even within 2D-FM blocks, we suspect strong AFM interactions between adjacent columns, such as those responsible for the frustration in the 1D- $Ca_3Co_2O_6$ Fig.2-39, (a)) (*Maignan2000, Maignan2004, Hardy2004*) compounds, responsible for magnetization plateau (Fig.2-39, (b)). Those latter could also be partially responsible for the weak local moments detected on octahedral Co, since the non-ordered local magnetic anisotropy would not be detected by ND. The Néel temperatures are listed in Fig. 2-37 and Fig.2-38 (*Mentré2008*) with the refined magnetic moments, stronger at the AFM - connection between tetrahedra (*Ehora2007, Kauffmann2007c, Kauffmann2006*).

Additionally, it is striking that while for the $Ba_5Co_5ClO_{13-\delta}$ and $Ba_6Co_6XO_{16-\delta}$ ($X = Cl$ and F), the absence of any $00l$ magnetic satellites involves magnetic moments collinear to the c -axis (*Kauffmann2006, Kauffmann2007c, Ehora2007 and 2007b*) (Fig. 2-37 (a) and (c)), for $Ba_5Co_5FO_{13-\delta}$, an (a, b) in-plane orientation of the magnetic moments was refined (*Ehora2007*) (Fig. 2-37 (b)). It was attributed to the important deformation of the tetrahedra in this particular case, modifying the spin-orbit coupling/magnetic anisotropy (*Mentré2010*). This aspect will be further explained in the next chapter of this manuscript.

Finally, one should briefly report the effect of the spatial separations between those FM blocks. It was achieved in the $Ba_6Co_5BrO_{14-\delta}$ and $Ba_7Co_6BrO_{17-\delta}$ compounds in which the inter-leave is formed by double $[Ba_2O_2Br]$ layers. In this case, the interactions between the tetrahedra are strongly weakened and lead to a metamagnetic behaviour assorted with a complex magnetic-phase diagram reported in *Toulemonde2010*. Briefly, an AFM coupling between FM blocks was detected in absence of magnetic solicitation, while an applied field progressively reorientates the moments ferromagnetically in the basal-planes Fig. 2-37, (d) and (e)). In addition the parent 5H and 12H $BaCoO_{3-\delta}$ oxides also show FM intra-blocks couplings but FM inter-blocks exchanges due to the disconnected tetrahedra (Fig.2-38 (a) and (b)).

This collection of compounds with different bulk-properties, all of them containing similar FM blocks, is at the origin of a promising magnetic lego-like game concept that we try to develop at the laboratory. Then the Fe/Co/Mn substitution should give new insights about the understanding of the concerned phenomena.

2.3.1.b) Electric properties of parent Co-oxo-halides

All the Co-based compounds display a semi-conducting behavior and resistivities increase with the degree of connection between the blocks. This feature is shown on the Fig.2-40 (b) which suggests a predominant conducting character of the 1D-channels along the c axis in the 3D-oxohalides. This feature was checked recently by single-crystals measurements on $Ba_5Co_5ClO_{13-\delta}$. Clearly the strongly anisotropic transport ($\rho_{a,b} > \rho_c$) plays in favour of preferential paths along c (Wang2009).

If one compares trimeric and tetrameric transports, it was observed in the $X = F$ case a smaller resistivity for the tetrameric case (Fig.2-40 (a)), but this feature was not clearly rationalized. At least it was assigned to a different charge distribution and subsequent concentration of carriers inside the face-sharing trimers and tetramers (Mentré2010).

Finally, we observe slight anomaly on $\rho = f(T)$ at T_N as shown on the Fig.2-40 (b) for $Ba_5Co_5ClO_{13-\delta}$. A change in the transport regime is efficient at both sides on T_N (Yamaura2000, Wang2009, Mentré2008).

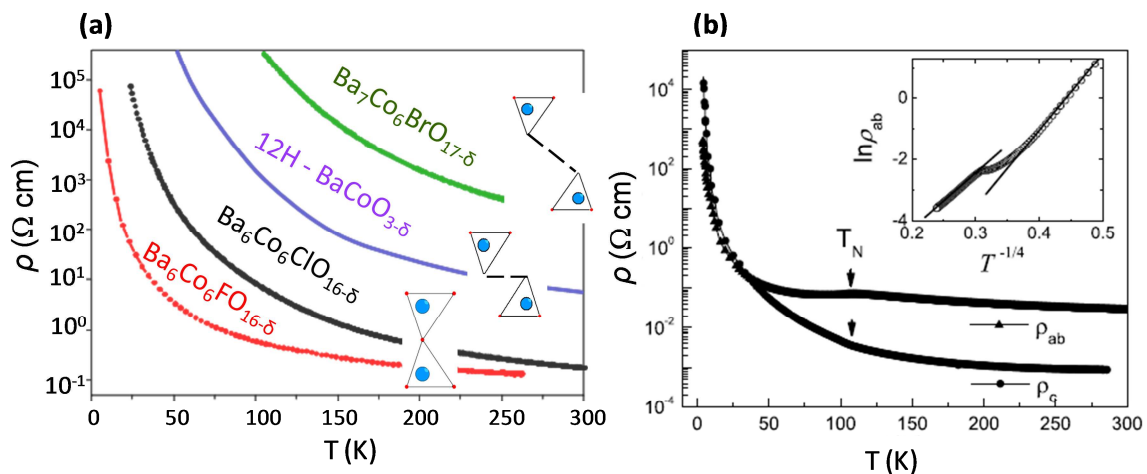


Fig.2-40 : $\rho = f(T)$ (logarithmic scale) determined on bulk (a) (Mentré2008). The dependence of the resistivity with the temperature for $Ba_5Co_5ClO_{13-\delta}$ (single crystals, Wang2009) in the (a, b) plane and along c axis determined on single crystal (b); in insert of (b), plot of $\ln \rho_{ab}$ versus $T^{-1/4}$ for $T > 20 \text{ K}$.

2.3.2. Ba₅(Co,Fe)₅XO_{13-δ} (X = Cl, F)

We have seen that the substitution by Fe of Co leads to the trimeric 10H-structure for both oxo-chlorides and oxo-fluorides. This structural predominance was explained by the progressive mean metal reduction on increasing the Fe content which concomitantly stabilizes the low *c/h* polymorph (see chapter 2, section 2.2.1.). As marked before, the interest of Co–Fe substituted materials resides in, for example, the enhancement of the mixed electronic/ionic transport applicable to electrochemical systems such as in La_{0.6}Sr_{0.4}Co_{1-y}Fe_yO₃ selected as a promising cathode-material (= LSCF, *Duanping2008, Mizusaki1983 and 1989*) or in the increase of the magnetic transition temperature by Fe-doping, since Fe – based perovskites generally show high magnetic ordering temperatures (ex: 685K for SrFeO₂F (*Berry2008*), 730K for 15R - BaFeF_{0.2}O_{3-δ} (*Sturza2011*)).

2.3.2.a) Ba₅(Co,Fe)₅XO_{13-δ} (X = F, Cl) magnetic susceptibility

The magnetic measurements are experimentally described in the “Materials and Methods” section. It was measured for the Ba₅Co_{5-y}Fe_yXO_{13-δ} compounds: *y* = 1 – 3, for X = F and *y* = 1 – 4 for X = Cl at H = 2000Oe. All the susceptibility and magnetization curves are given in annexes (A4 and A5). The compounds are antiferromagnetic below T_N, this latter being strongly dependent of the Fe content. The Néel temperatures and effective moments/ Curie-Weiss temperatures of paramagnetic domains are listed in the Table 2-7.

We recall that the Curie-Weiss law is given by $\chi(T) = \frac{C}{(T-\theta)}$. The effective moment is calculated as follows: $\mu_{\text{eff}} = \sqrt{8C} = \sqrt{8/p}$ where *p* is the slope found after the linearization of the paramagnetic $\chi^{-1}(T)$ curve. The effective moments is theoretically calculated as $\mu_{\text{eff}} = 2\sqrt{n_i(S_i)(S_i + 1)}$, *n_i* being the stoichiometric amount of the atom *i* of spin *S_i*.

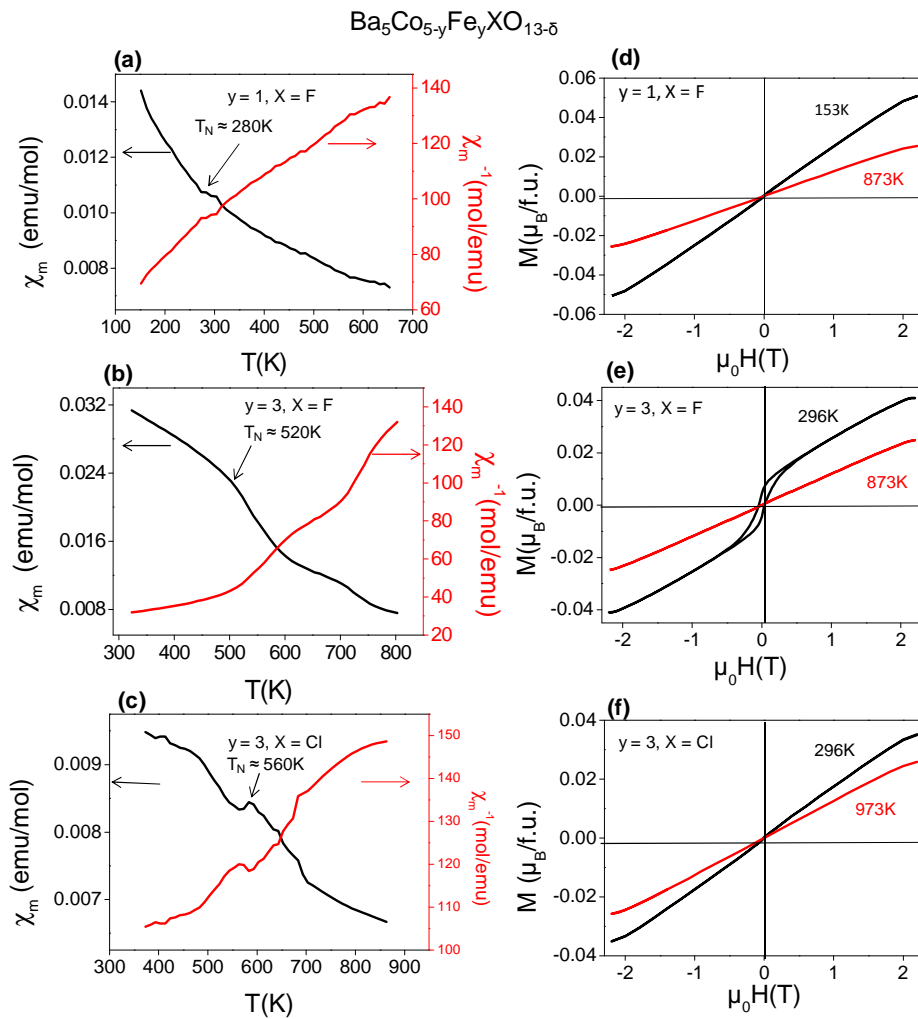


Fig.2-41 : $\chi_m = f(T)$ and $\chi_m^{-1} = f(T)$ at $H=20000e$ for (a) $y = 1, X = F$ (b) $y = 3, X = F$ and (c) $y = 3, X = Cl$; and $M = f(\mu_0H)$ at different T (K) for different compositions

We have evoked for Co parent compounds the unclear distinction of T_N (see 2.2.1) on susceptibility plots. Typically only accidents are observed at T_N while the conductivity continues to increase on cooling. The substitution with Fe does not help, at this level. For instance Fig. 2-41 (a) shows $\chi_m(T)$ and $\chi_m^{-1}(T)$ for $y = 1, F$ in which the weak anomaly at $T \approx 280K$ is assigned to the magnetic ordering temperature. Also, due to the high-temperature VSM measurements, the collected data are more or less noisy, such that the deduction of the effective-moment can be difficult. Particularly, increasing the Fe content increases T_N such that the collected paramagnetic domain is too small for a correct linear regression of the Curie-Weiss law.

Clearly the evolution of the effective moment with the Fe content is against the theoretical approximations (given in the Table 2-7 for Co^{3+}_{HS} ($S=2$) and Fe^{3+}_{HS} ($S=5/2$). However, considering Fig. 2-41 (b) for $y = 3$, $X = F$ and (c) $y = 3$, $X = Cl$, one can view the relative imprecision on μ_{eff} . The relatively large Curie-Weiss constant suggests important antiferromagnetic couplings (Table 2-7).

Table 2-7: Magnetic data for $Ba_5Fe_yCo_{5-y}XO_{13-\delta}$ from magnetic susceptibility and low temperature neutron diffraction: *Ehora2007** Kauffmann2007c

	y	Magnetic susceptibility			Neutron diffraction m (μ_B) at 1.5K			
		T_N (K)	μ_{eff} ($\mu_B/f.u.$)	$\mu_{eff th}$ ($\mu_B/f.u.$)	θ_{CW} (K)	Co1/Fe1	Co2/Fe2	Co3/Fe3
F	0*	122	7.16	10.95 ($5Co^{3+}_{HS}$ ($S = 2$))	-345	0.57(9)	0.44(8)	2.47(5)
	1	≈ 280	8.16	11.44	-488	0.73(9)	0.46(8)	2.68(5)
	2	≈ 470	7.64	11.91	-303	1.29(5)	0.92(6)	3.02(4)
	3	≈ 520	7.67	12.36	-303	2.50(6)	1.39(5)	3.37(7)
Cl	0**	126	9.21	10.95 ($5Co^{3+}_{HS}$ ($S = 2$))	-766	0.61(7)	0.35(8)	2.21(8)
	1	≈ 200	6.66	11.44	-260			
	2	≈ 440	8.53	11.91	-586			
	3	≈ 560	7.30	12.36	-208			
	4	≈ 550 (?)	***	13.23 (Fe^{3+}_{HS} ($S=5/2$))	***	3.42(6)	1.64(7)	4.07(7)
	5	Fe ₃ O ₄ in presence						

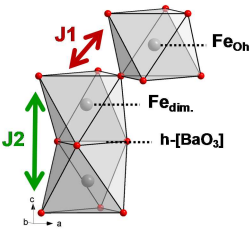
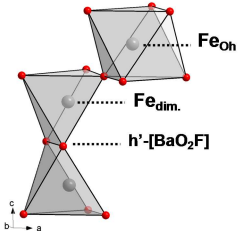
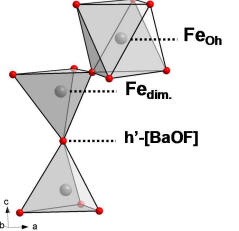
Finally, one should mention that even if in most of the cases the magnetization curve $M=f(\mu_0H)$ below T_N indicate no residual magnetic moments (Fig. 2-41 (d) and (f)) some compounds such as $y = 2$, F and $y = 3$, F display a weak ferromagnetic component (typically a remanent moment of $M_c = 0.01 \mu_B/f.u.$ at $T = 296K$ for $y = 3$, F (Fig. 2-41 (e)). It could result from several disorder aspects related to the Fe/Co distribution, and to the competition between FM and AFM exchanges while Co-Co, Fe-Fe or Co-Fe interact. Also the presence of small amount of FM impurities cannot be excluded, especially dealing with Fe-based oxides.

The most striking point about $Ba_5Co_{5-y}Fe_yXO_{13-\delta}$ solutions concerns the high T_N observed after introduction of a significant amount of Fe (Fig. 2-41 (c) for $y = 3$, $X = Cl$, T_N around 560K). Recently has been established for fluorinated Fe-perovskites, by DFT calculations, (Sturza2011, Sturza2011b) that this behaviour is mainly driven by magnetic exchanges at the Fe-O-Fe tetrahedral junction (J_2 (magnetic super exchange parameter) for tetrahedral pairs in Fig. 2-42. First, we

should note that the negative sign corresponds to an AFM coupling and the positive sign to an FM coupling. In the compound studied, the modification of the J1 was proved to depend only of the Fe oxidation degree, but a very small modification of the values, as Fe oxidation degree is decreasing, was observed (*i.e.* 123K for Fe⁺⁴ and 115K for Fe⁺³, of course passing from AFM to FM conform to the Kanamori-Goodenough (KG) rules (Goodenough1963). The corresponding couplings are clearly enhanced in the second case (J2), the large modification of J2 being attributed, on one part, to the local geometry modification, *i.e.* progressive passage from face-sharing octahedral pairs → edge-sharing pyramidal → corner-sharing tetrahedral pairs, and of the modification of the Fe oxidation degree on the other part.

In our compounds, the conservation of the local geometry is still accompanied by large T_N values; this can be explained by the increase of mainly J2 due to the modification of Fe oxidation degree, our compounds showing T_N which are among the highest observed in the series of hexagonal perovskites. In these wide series, in absence of incorporation of X halides, the magnetic expansion is confined within face-sharing octahedra.

Fig.2-42: DFT calculations for face-sharing octahedral pairs → edge-sharing pyramidal → corner-sharing tetrahedral pairs junctions in the 6H-BaFeF_yO_{3-δ} (Sturza2011):

Compound	6H-BaFeO ₃ (Fe ⁴⁺)	6H-BaFeO _{2.66} F _{0.33} (Fe ^{3.66+})	6H-BaFeO _{2.33} F _{0.33} (Fe ³⁺)	
Local Environment				
J1	d _(Fe-Fe) (Å)	3.873	3.82-3.92	3.822/3.792
	<Fe-O-Fe	177.21°	170.1°-175.7°	165.2°/164.3°
	J1 (K)	123.21	-5.90	-115.04
J2	d _(Fe-Fe) (Å)	2.572	2.758	3.476
	<Fe-O-Fe	85.62°	94.9°-95.0°	171.07°
	J2 (K)	-41.17	-79.54	-247.26

2.3.2.b) $Ba_5(Co,Fe)_5XO_{13-\delta}$ ($X = F, Cl$) magnetic structures

Low temperature neutron diffraction data have been collected for $y = 1, 2, 3$ $X = F$ and for $y = 4$ of $X = Cl$ at the LLB using G41 diffractometer described in section “Materials and method”. In the same chapter are given the practical information related to the refinement of the magnetic structures. The temperature domain investigated is between 1.5K and 350K.

In Fig.2-43 (a) as representative example ($y = 3, X=F$), the 3D-magnetic ordering is demonstrated by the increase of the intensity of some peaks. These peaks also correspond to Bragg angles within the nuclear structure, such that a conservation of the nuclear periodicity for the magnetism is suggested (propagation vector: $k=0,0,0$). The magnetic moments values at 1.5K are given in Table 2-7 for all the 4 investigated compounds. The ND pattern after refinement for $y = 3$ term of the solid solution at 1.5K is given as example in Fig.2-43, (b) (R - factors given in the legend of the Fig.2-43.).

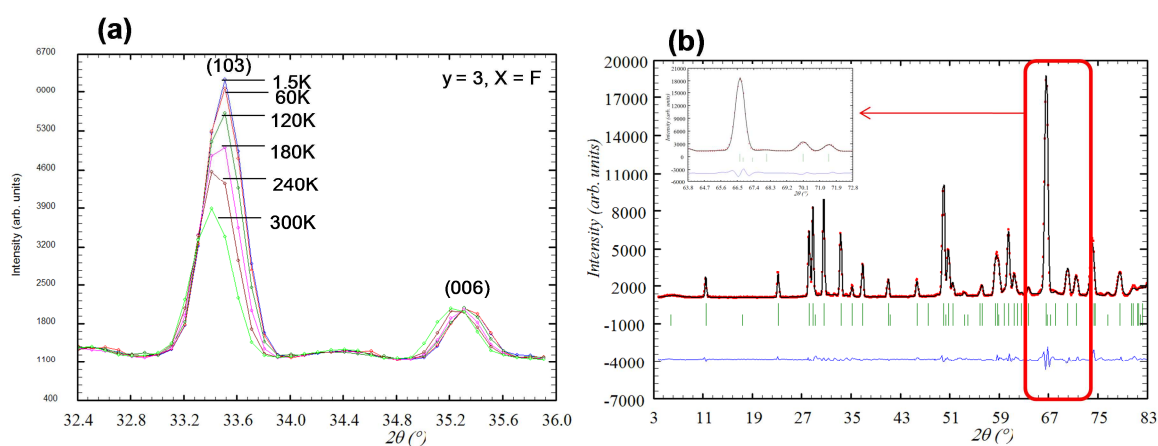


Fig.2-43: (a) magnetic coupling illustrated by the increase of the intensity of some peaks also corresponding to Bragg angles within the nuclear structure, (103) here, in the case of $Ba_5Fe_3Co_2FO_{13-\delta}$; (b) neutron diffraction refinement for $y = 3, F$ term of the solid solution at 1.5K ($R_{Bragg} = 3.18\%$, $R_F = 2.62\%$, $R_{mag} = 4.71\%$).

- Effect of Fe introduction on the magnetic structure:

The absence of $00l$ magnetic components suggests the orientation of the spins along the c -axis. This is due to the fact that the spin-neutron interaction is of dipolar nature, and the diffracted magnetic intensity concerns the component of the spins perpendicular to the scattering vector. By analogy with the parent compounds (FM intra block, AFM inter-block) we first tried to refine similar models for the Fe-doped terms. These models did not converge and adding an extra degree of freedom for the spins give raise in any case to a AFM site-to-site interaction, as shown on Fig.2-44. This result is all the more astonishing that it concerns any of the refined compounds even with low Fe content ($y = 1$).

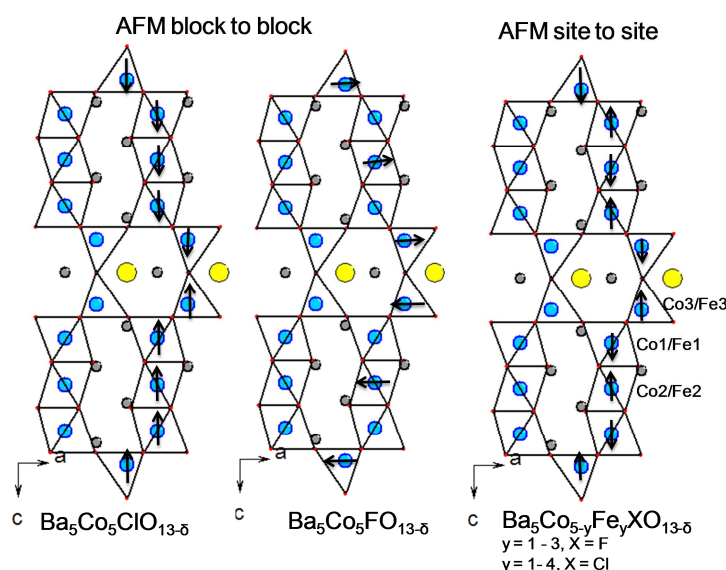


Fig.2-44 : Magnetic structure for $Ba_5Co_5ClO_{13-\delta}$, $Ba_5Co_5FO_{13-\delta}$ and $Ba_5Co_{5-y}Fe_yXO_{13-\delta}$ ($X = Cl, F$)

The analyses of the results show that:

- As in the case of parent Co-compounds, the tetrahedral atoms display the larger magnetic moments (Fig.2-45).
- An increase of the magnetic moments with the increase of the Fe content is also observed on all of the octahedral sites (Fig.2-45, (e)).
- The most remarkable is the increase of the value of the magnetic moment in the marginal octahedra since in the case of $Ba_5Co_5XO_{13-\delta}$, null ($X = F$) or very low

magnetic ($X=Cl$, $MCo1=0.6\mu_B$) moments were refined in these sites (Kauffmann2008, Mentré2010, Ehora2007b). This can be explained recalling that the central octahedron is weakly occupied by Fe even for rich Fe compounds ($y = 4$) while marginal sites host a significant Fe concentration, (see section 2.2.1.e) Page 54).

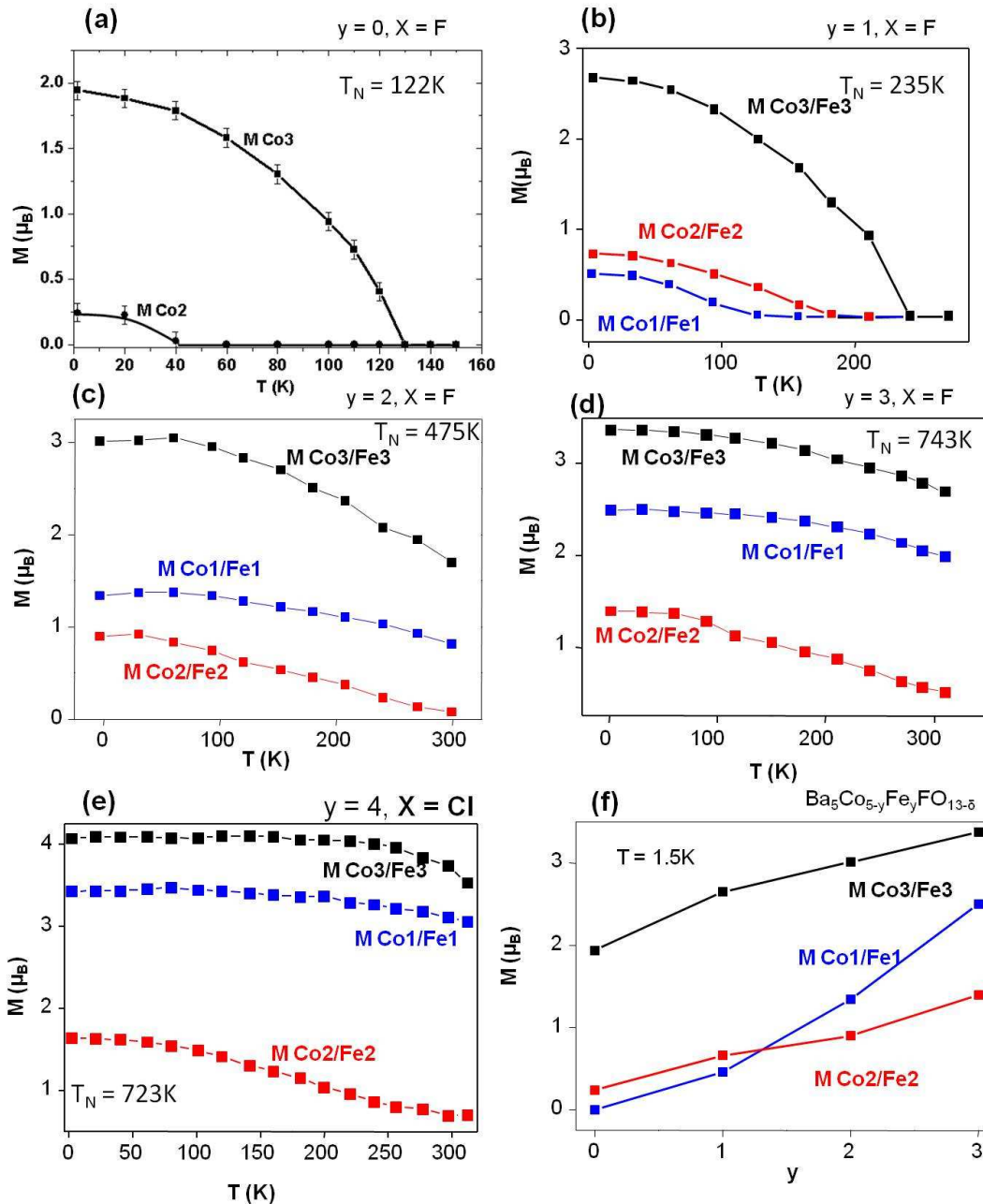


Fig.2-45 : $Ba_5Co_{5-y}Fe_yFO_{13-\delta}$ magnetic moments evolution with the temperature for (a) $y = 0, X = F$ (Ehora2007b); (b) $y = 1, X = F$; (c) $y = 2, X = F$; (d) $y = 3, X = F$; and (f) $y = 4, X = Cl$. The magnetic moment evolution with the increase of the Fe content at 1.5K in the three crystallographic different sites for $X = F$ is given in (e).

- Conclusion:

To summarize, the effect of the Fe introduction in the structure is given below using the analysis of the magnetic ordering rationalized step by step along the structure for the Co-oxo-halides compounds (*Kauffmann2008*) on the basis of simple exchange rules, considering Co^{3+}/Co^{4+} cations.

- Between two blocks, corner-sharing tetrahedral Co-O-Co is observed strongly AFM. **The introduction of Fe does not modify this feature, hardly predictable from Kanamori-Goodenough (KG) rules (*Goodenough1963*)**
- In the block, the tetrahedral/octahedral connection is FM which was predicted from KG rules for Co-O-Co angle close to 180° . **Apparently, the incorporation of Fe, even in a small ratio is sufficient to turn these exchanges into AFM exchanges at this level.**
- Finally, the FM coupling observed between weak moments inside the Co face-sharing strings was assigned to electronic delocalization, FM direct exchanges and a significant ratio of LS- Co^{3+} in the strings. **Here the introduction of Fe is supposed to break such exchanges by strong electronic localization due to the different Co and Fe nature. In such case the Co-O-Fe super-exchange should predominate, and the observed negative couplings is similar that what was observed at the previous tetrahedral/octahedral connection.**

2.3.2.c) Transport properties of $Ba_5(Co,Fe)_5XO_{13-\delta}$ (X = F, Cl)

The electric resistivities at low temperature have been measured as described in “Materials and methods” section and they are given in Fig. 2-46. All the terms of the oxo-chlorides and oxo-fluorides solid solutions show an insulator behaviour. As a general statement, the resistivity increases with the Fe content (Fig. 2-46, (a) and (d)). This behaviour is in good agreement with what was observed from magnetic structures. Clearly, the substitution of Co for Fe in terminal octahedral and tetrahedral (section 2.2.1.e) is expected to localize electrons at least in the face-sharing strings. Then the observed increase of local magnetic moments into an AFM magnetic structure even with low Fe-content pictures the general localization into more

insulator states. Also, it should be remembered that the lattice dilatation which accompanied the Fe incorporation plays in favour of limited inter-atomic overlapping and electrons hopping. The same phenomenon was observed for $La_{0.6}Sr_{0.4}Co_{1-y}Fe_yO_3$ ($y=0-1$) solid solution by *Duanping2008*, *Mizusaki1983* and *1989*. On the other hand, the creation of oxygen vacancies with the increase of Fe/Co ratio (detailed in the section 2.1.2.a.) give us the possibility to anticipate an improved ionic conductivity increase.

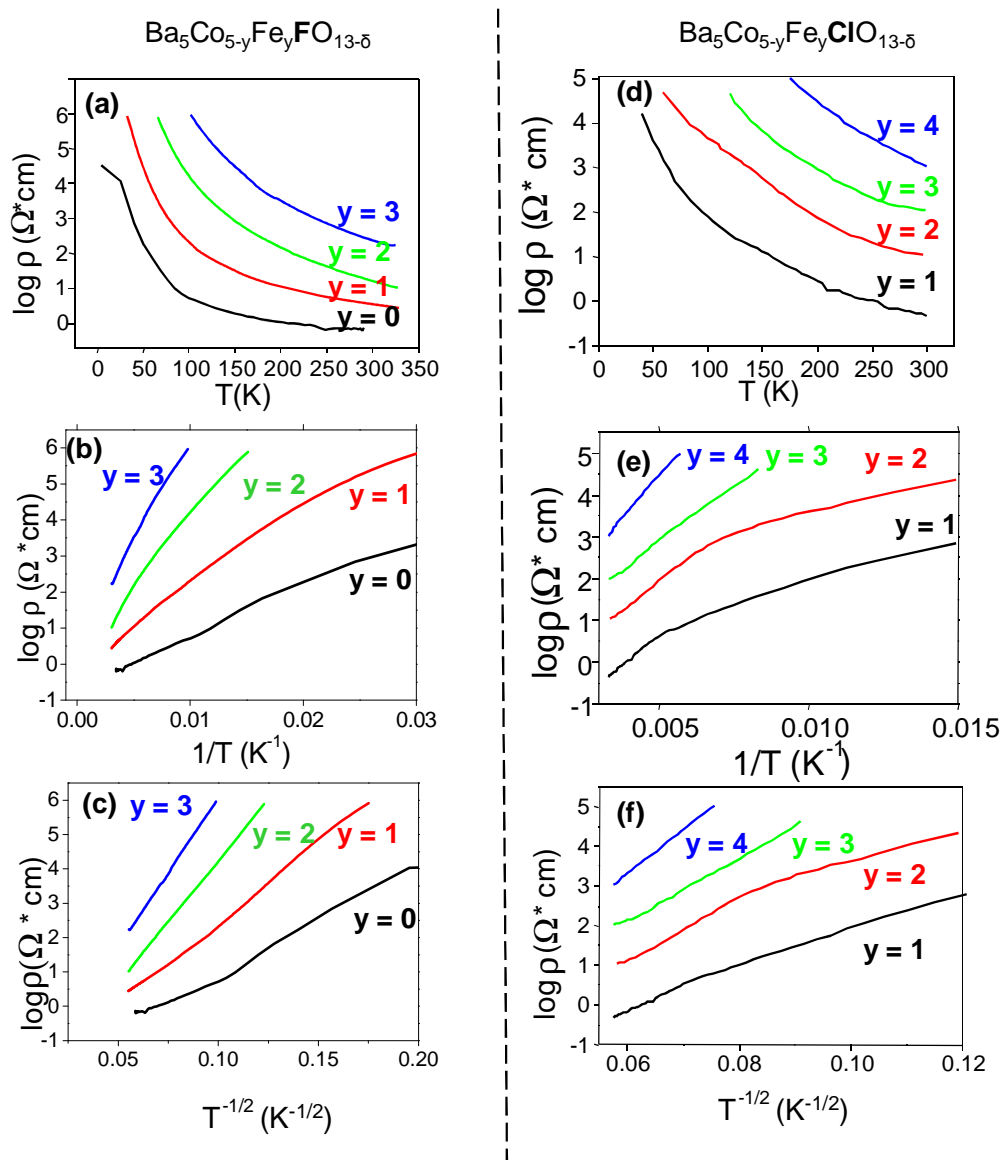


Fig. 2-46 : Resistivity for $Ba_5Co_{5-y}Fe_yFO_{13-\delta}$ polycrystalline samples (a) $\log \rho = f(T)$; (b) $\log \rho = f(T^{-1})$; (c) $\log \rho = f(T^{-1/2})$ and resistivity for $Ba_5Co_{5-y}Fe_yClO_{13-\delta}$ (d) $\log \rho = f(T)$; (e) $\log \rho = f(T^{-1})$; (f) $\log \rho = f(T^{-1/2})$

- Variable Range Hopping model

Since transport measurements on Fe/Co compounds have been measured on polycrystalline samples, one should be very careful about their interpretation. However, in Fig. 2-46(b), (c), (e) and (f) are represented the resistivity logarithm dependence with the T^{-1} and $T^{-1/2}$. By comparison with the Arrhenius model ($\rho = Ae^{(-Ea)}/kT$) for the former, the linearity of the second implies a transport possibly governed by a “Variable Range Hopping” mechanism within a localized electronic states (Hill1976, Mansfield1991). Particularly, the $T^{-1/2}$ dependence suggests a mono- dimensional conductivity type “Hopping 1D” probably along c axis favoured by the structural anisotropy in these materials. The same behavior was observed in the case of the parent compounds (Kauffmann2007c, Ehora2007b). In addition, the preferred conductivity along c was measured on single crystal (Wang2009) in good agreement with a mono-dimensional transport.

2.3.3. Ba₆(Co,Mn)₆XO_{16-δ} (X = Cl)

2.3.3.a) Magnetic properties

We have mentioned the difficulties to prepare the Co/Mn tetrameric compounds and the bad reproducibility of our syntheses. It has partially conditioned the choice of the selected samples for their physical properties measurements, namely $y = 4$, $X = \text{Cl}$, which was obtained pure in all experiments. The magnetic susceptibility curves ($\chi_m = f(T)$) at $H=2000\text{Oe}$ and magnetization ($M = f(\mu_0H)$) at 2K dependence are given in Fig.2-47 (a) and (b), for Ba₆Co₂Mn₄ClO_{16-δ}. We recall that a Mn preference for octahedral sites was observed for several compounds (see Ba₆Co₄Mn₂ClO_{16-δ} cationic distribution, section 2.2.2.d) (Page 68) such that for this particular composition, Mn₄O₁₅ tetramers are expected, separated by Co₂O₇ dimers.

The magnetic susceptibility (Fig.2-47, (a)) curves shows a typical paramagnetic behavior, with a broad anomaly around 10 K. In the high temperature domain the Curie-Weiss law gives $\mu_{\text{eff}}=12.21\mu_B/\text{f.u.}$ ($\rightarrow 4.58\mu_B/\text{metal}$) and $\theta_{\text{CW}} = -556\text{K}$. The value of the effective moment is in good agreement with an ideal $2\text{Co}^{3+}(\text{S}=2)$ (Td), $2\text{Mn}^{4+}(\text{S}=3/2)$ (Oh), and $2\text{Mn}^{3+}(\text{S}=2)$ (Oh) distribution, $\mu_{\text{eff}}= 11.22$

μ_B /f.u. We recall that the Co^{3+} valence of tetrahedral positions in this structural type is supported by previous DFT calculations (Mentré2010). Below the transition, a second paramagnetic regime seems to dominate $\chi(T)$ plots. Between 2 and 8K, it was fitted from the corresponding data-points leading to $\mu_{\text{eff}} = 2.66 \mu_B$ /f.u. which corresponds to less than one $Mn^{3+}(S=3/2)$ ($\rightarrow 3.87\mu_B$) remaining “free” at low temperature. It is too big to be assigned to “residual” intrinsic paramagnetism (edges of the crystals, defects, etc...). The $\chi_m - \chi_{\text{para}}$ plot is shown on the Fig.2-47, (c). Its shape is reminiscent of low dimensional systems such as AFM linear clusters of spins, probably driven by the AFM Co-Co dimers. We note that at high temperature the deviation from the Curie-Weiss law occurs around 150 K which could correspond to the AFM setting within cobalt dimers. The bordering Mn would also participate, but do not yield a 3D AFM ordering. The central Mn could remain “uncoupled”.

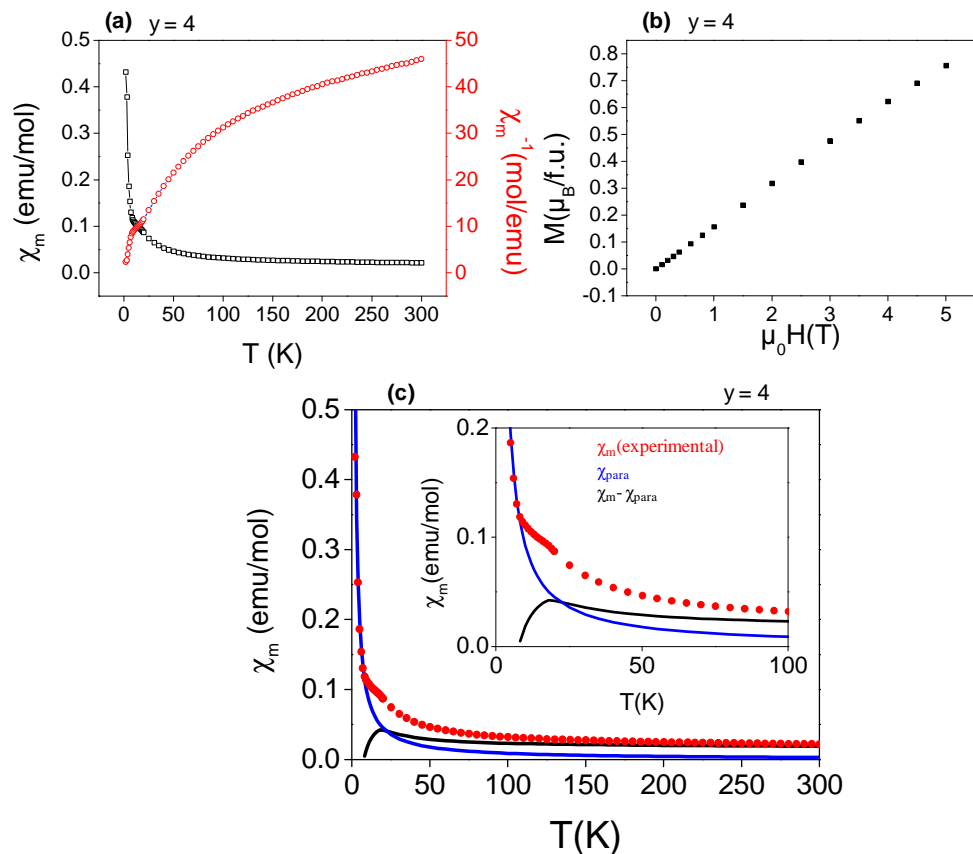


Fig.2-47: $Ba_6Co_2Mn_4ClO_{13-\delta}$ magnetic susceptibility at $H=20000e$ (a); magnetization at 2K (b). In (c) is given the experimental χ_m (red), the low temperature paramagnetic curve χ_{para} (blue) and the $\chi_m - \chi_{\text{para}}$ plot (black) (in insert, zoom between 0 - 100K)

This hypothesis remains an assumption and others scenario may happen as suggested by related compounds presents in the literature. For example, for $BaMn_{0.2}Co_{0.8}O_{2.8}$ (trimer) (Miranda2008), a model of random anisotropic, non-interacting monodomain ferromagnetic clusters was proposed. The randomness in anisotropy is introduced by the Mn ions and is preventing the transition into long-range three-dimensional ferromagnetic order achieved in the parent compound $BaCoO_{2.8}$ at ~ 47 K (Boulahya2005). The magnetic behavior was considered to be intermediate between the spin glass system observed for $BaMn_{0.4}Co_{0.6}O_{2.83}$ (Miranda2008) and the ferromagnetic $T < 47$ K ordered $BaCoO_{2.8}$ (Boulahya2005). Clearly, whatever the mechanisms are in our compounds the Mn/Co co-presence seems to break a 3D magnetic ordering.

2.3.3.b) Low temperature electric proprieties

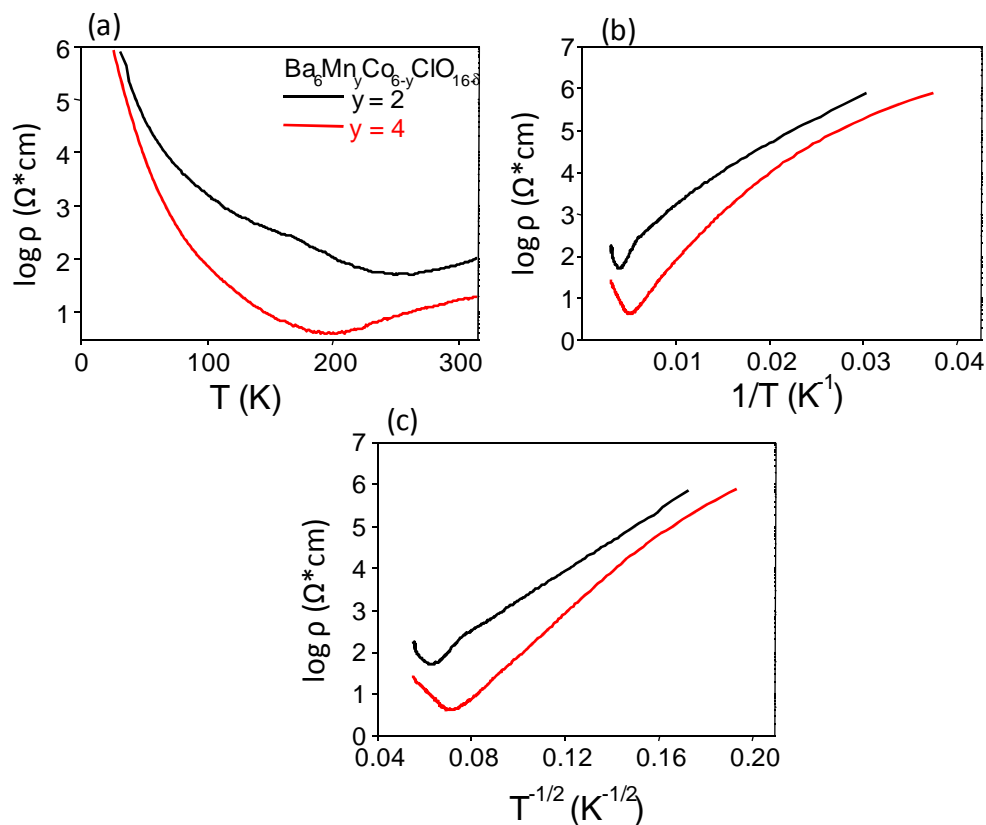


Fig.2-48 : Resistivity evolution with the temperature (a), inverse of the temperature (b) and $T^{1/2}$ (c) for $y = 2$ (black) and $y = 4$ (red) terms of the $Ba_6Co_{6-y}Mn_yClO_{16-\delta}$ series.

The resistivity evolution with the temperature T (a), T^{-1} (b) and $T^{-1/2}$ (c) for $Ba_6Mn_2Co_4ClO_{16-\delta}$ and $Ba_6Mn_4Co_2ClO_{16-\delta}$ are given in Fig.2-48, (a). It was measured with the standard four-probes method on densified pellets. First we have to consider these results precautionary because the presence of a mixture of phases cannot be absolutely excluded in these systems while hardly detectable by XRD, as highlighted during the investigation of the Fe-Mn line. Also we had difficulties to reproduce the 4-probes experiments, sometimes leading to “out of range data” even at room temperature. However, for $y = 2$ and $y = 4$, the initial decrease of the resistivity on cooling suggests metallic states. No corresponding anomaly was detected on the magnetic susceptibility for $y = 4$ except the progressive deviation from the Curie-Weiss law. At lower temperature, the systems turns back to the standard insulating state observed for most of the doped (Co/Fe) and un-doped (Co) compounds. Once more the 1D-VRH model seems predominant (Fig.2-48, (b)). This metallic \rightarrow insulator behaviour, if real, is not understood at the time.

Supplementary information

2. 4. Supplementary information

Annexes 1: Single crystal X –ray diffraction for Ba₈(Co,Mn)₈ClO₂₂

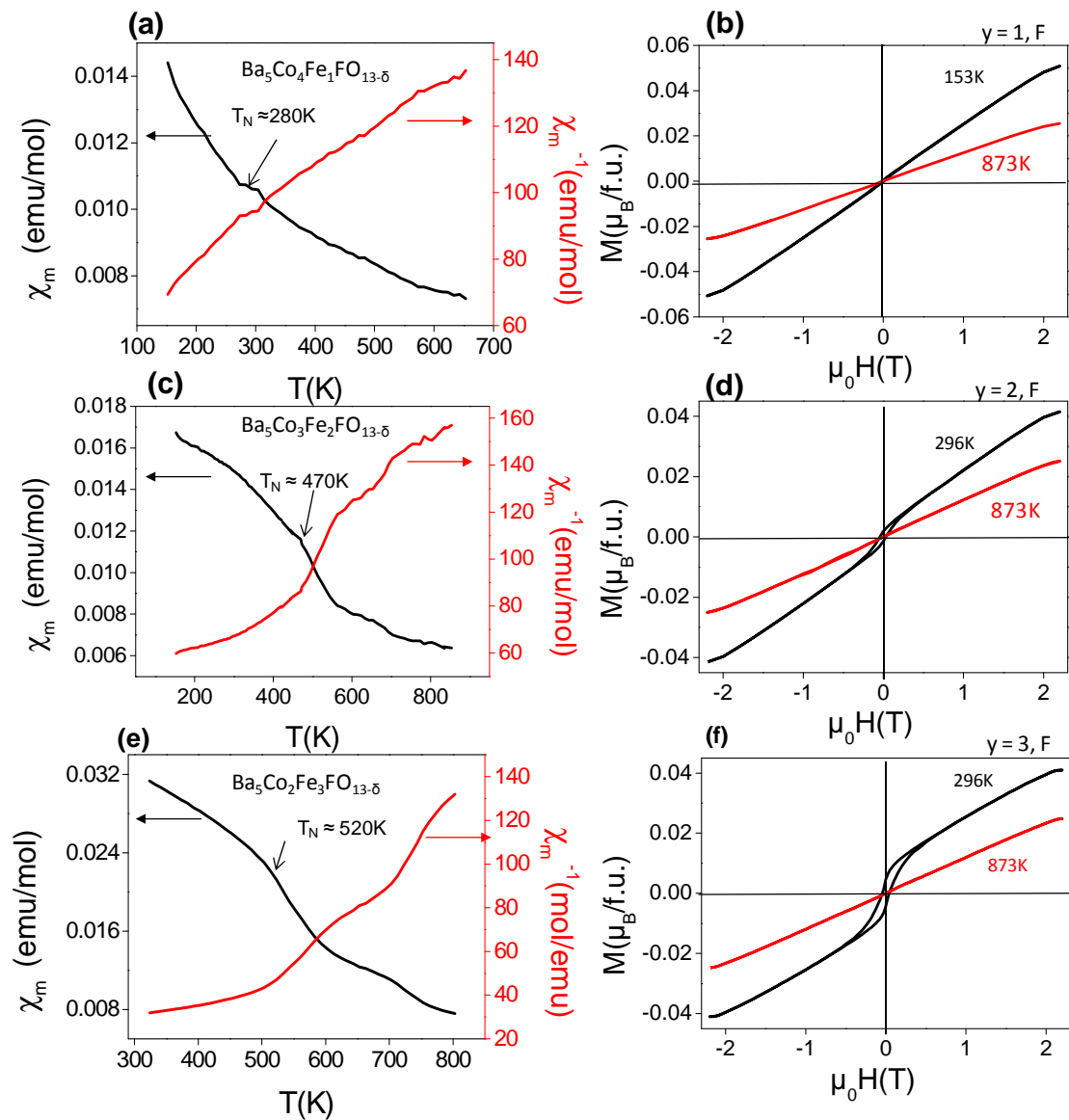
Crystal data	
Crystal symmetry	hexagonal
Space group	$P\bar{6}m2$
Unit cell (Å and °)	$a = 5.7207(2)$ $c = 19.409(1)$
Volume (Å ³)	550.11(4)
Z	1
Mw , Calculated density (g/cm ³)	1933.6, 6.8667
F(000)	1211
Data collection	
Equipment	Bruker X8
Radiation MoKα (Å)	0.71073
Scan mode	ω/φ - scan
Recorded angular range θ (°)	3.27 – 45.4
	$-11 \leq h \leq 11$
Recording reciprocal space	$-11 \leq k \leq 11$ $-38 \leq l \leq 38$
Number of measured reflections	45059
Number of independent reflections	1879
Number of independent reflections [$I > 3\sigma(I)$]	1763
μ (mm ⁻¹) ($\lambda = \text{MoK}\alpha$)	19.04
Absorption correction	Multiscan (Sadabs)
Transmission Tmin/Tmax	0.4968(3)
R merging factor (%)	3.9
Refinement parameters	
Software, refinement type	Jana 2006, L.S. on F
Number of refined parameters	54
R ₁ (F) all (%)	3.65,3.35
wR ₁ (F) all (%)	5.82,5.79
Goodness of fit	3.56
Max / Min $\Delta\rho$ e/Å ³	6.69 / -7.66

Annexes 2: Atomic parameters from single crystals XRD for $Ba_8(Co,Mn)_8ClO_{22}$

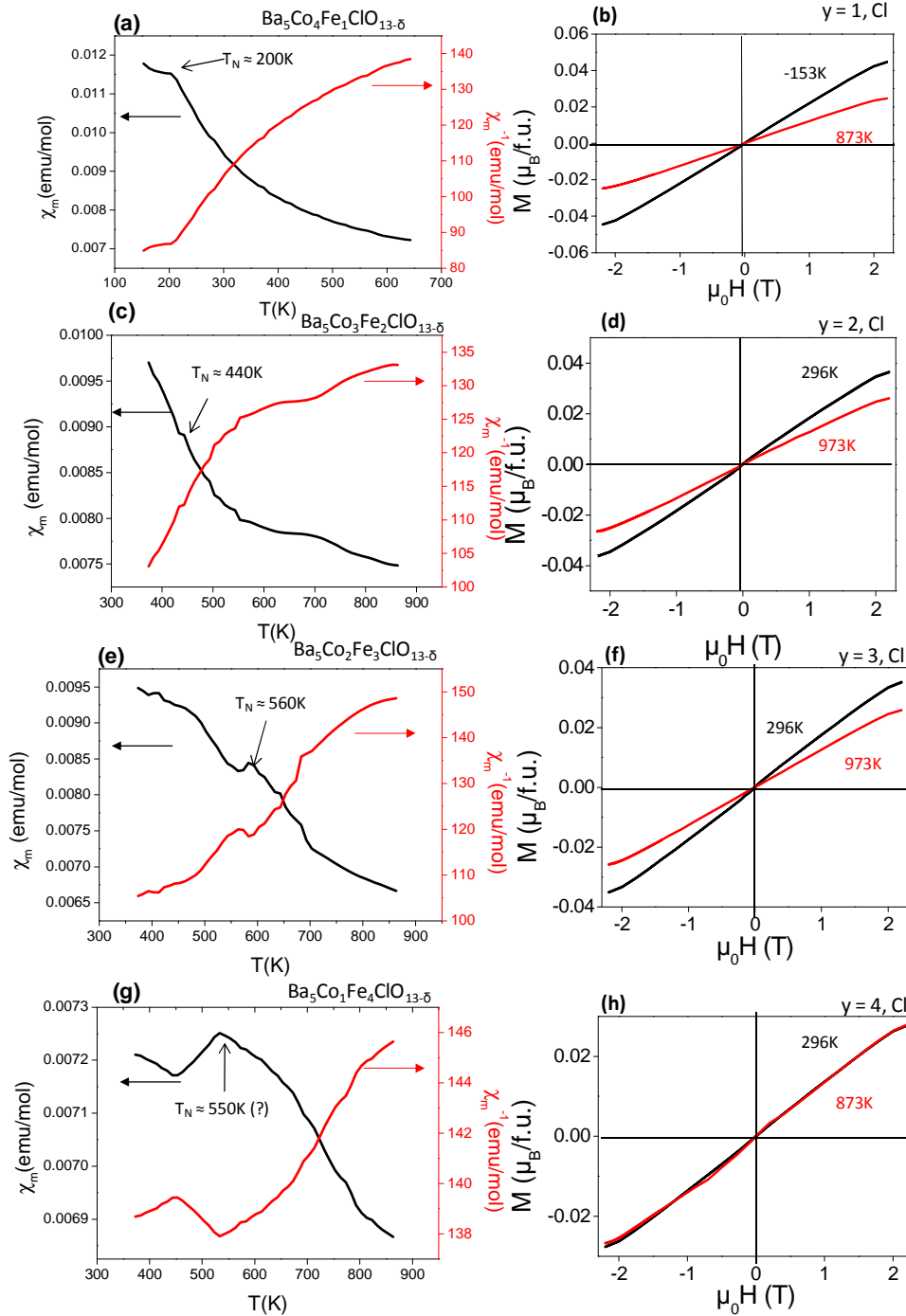
Atom	Wyck.	Site	Occ.	x	y	z
Ba1	2i	3m.		2/3	1/3	0.26610(3)
Ba2	2g	3m.		0	0	0.38267(3)
Ba3	2g	3m.		0	0	0.84689(3)
Ba4	1c	-6m2		1/3	2/3	0
Ba5	1f	-6m2		2/3	1/3	1/2
Mn1	2h	3m.		1/3	2/3	0.43735(7)
Mn2	2h	3m.		1/3	2/3	0.31242(7)
Mn3	2h	3m.		1/3	2/3	0.18292(7)
Co1	2i	3m.		2/3	1/3	0.09055(7)
Cl1	1a	-6m2		0	0	1
O1	6n	.m.		0.1876(5)	0.8124(5)	0.2508(2)
O2	6n	.m.		1.0173(5)	0.5087(5)	0.1270(2)
O3	3k	mm2		0.1839(7)	0.8161(7)	1/2
O4	3j	mm2	0.3333	0.617(4)	0.308(4)	0
O5	6n	.m.		0.4823(4)	0.5177(4)	0.3764(1)

Annexes 3: Anisotropic displacement parameters, in \AA^2 for $Ba_8(Co,Mn)_8ClO_{22}$:

Atom	U_{11}	U_{22}	U_{33}	U_{12}	U_{13}	U_{23}
Ba1	0.0067(1)	0.0067(1)	0.0115(3)	0.0033(7)	0	0
Ba2	0.0065(2)	0.0065(2)	0.0179(3)	0.0032(8)	0	0
Ba3	0.0069(1)	0.0067(1)	0.0083(2)	0.0035(7)	0	0
Ba4	0.0179(3)	0.0179(3)	0.0145(4)	0.0089(3)	0	0
Ba5	0.0058(2)	0.0058(2)	0.0170(4)	0.0029(9)	0	0
Mn1	0.0036(2)	0.0036(2)	0.0046(5)	0.0018(2)	0	0
Mn2	0.0031(2)	0.0031(2)	0.0039(5)	0.0016(2)	0	0
Mn3	0.0030(2)	0.0030(2)	0.0027(5)	0.0015(2)	0	0
Co1	0.0076(3)	0.0076(3)	0.0063(5)	0.0038(4)	0	0
Cl1	0.0460(2)	0.046(2)	0.0070(2)	0.0229(2)	0	0
O1	0.0095(1)	0.0095(1)	0.0091(5)	0.0056(5)	-0.0003(7)	0.0003(7)
O2	0.0049(2)	0.0103(1)	0.0143(7)	0.0024(8)	-0.0049(2)	-0.0025(8)
O3	0.0104(2)	0.0104(2)	0.0062(2)	0.0061(2)	0	0
O4	0.0401(3)	0.0191(1)	0.0051(5)	0.0201(3)	0	0
O5	0.0064(1)	0.0064(1)	0.0075(15)	0.0061(4)	-0.0003(5)	0.0003(5)



Annexes 4: $\chi_m = f(T)$ and $\chi_m^{-1} = f(T)$ at $H=20000e$ for $Ba_5Co_{5-y}Fe_yFO_{13-\delta}$: $y = 1$ (a), $y = 2$ (c), $y = 3$ (e). The magnetization curves $M=f(\mu_0H)$ are given for $y = 1$ in (b), $y = 2$ (d) and $y = 3$ (f)

$Ba_5Co_{5-y}Fe_yClO_{13-\delta}$ 

Annexes 5: $\chi_m = f(T)$ and $\chi_m^{-1} = f(T)$ at $H=2000G$ for $Ba_5Co_{5-y}Fe_yClO_{13-\delta}$: $y = 1$ (a), $y = 2$ (c), $y = 3$ (e), $y = 4$ (g); $M=f(\mu_0H)$ curves for $y = 1$ in (b), $y = 2$ (d), $y = 3$ (f), $y = 4$ (h)

Chapter 3

Chapter 3. Anionic substitution in the 10H and 6H forms

3. 1. State of the art: importance of the halogen nature on the magnetic and electric properties

In this section, a short recall of the magnetic and electrical properties of the oxo-halides described in the previous chapter will be presented, focusing on the importance of the versatile connection/disconnection between the structural building-units achieved by modification of X. The results presented in this part concern the M=Co compounds investigated in previous works.

3.1.1. Connected FM blocks (F and Cl) vs. disconnected FM blocks (O and Br)

In the case of fluorine and chlorine, the FM blocks are AFM coupled at the tetrahedral level (Fig.3-1, (a) and (b)). The intra-dimer exchanges (Co-O-Co super-exchanges) are strong and mainly drive the setting of the 3D- magnetic ordering below T_N . We already explained that the linear octahedral chains (trimer and/or tetramers) play as FM connectors mainly by direct Co-Co exchange ($d \sim 2.5\text{\AA}$) in all the reported compounds but hold weak magnetic moments that may fluctuate below T_N ($\sim 100\text{K}$ depending on X and on the length of the oligomer). Here, the vision of FM block is ideal and one should also take into account the in-plane inter-chain couplings, likely AFM (leading to probable frustration, according to the triangular arrangement of the chains within the (a, b) plane).

The parent 5H and 12H $\text{BaCoO}_{3-\delta}$ oxides also show FM intra-blocks couplings but FM inter-blocks exchanges due to the disconnected tetrahedra and different super-super exchange Co-O-O-Co paths (Fig.3-1, (c)). However these

exchanges, that bridge the magnetic blocks, are expected lower due to the strongest Co-Co elongation in good agreement with the lower ordering temperature ($T_c \sim 40\text{K}$).

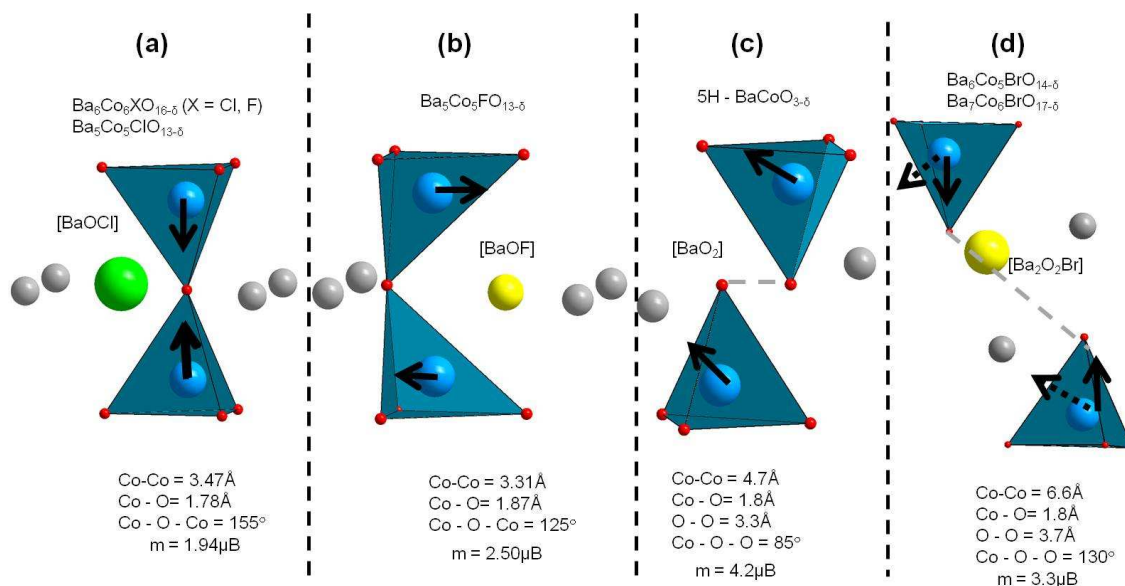


Fig.3-1 : The effect of the spatial separation/ connection between the FM blocks

An even larger spatial separations between the FM blocks is achieved in the $\text{Ba}_6\text{Co}_5\text{BrO}_{14-\delta}$ and $\text{Ba}_7\text{Co}_6\text{BrO}_{17-\delta}$ compounds in which the inter – blocks are formed by double $[\text{Ba}_2\text{O}_2\text{Br}]^-$ layers. In this case, the interactions between the tetrahedra are strongly weakened and result in a metamagnetic behaviour assorted with a complex magnetic-phase diagram (Toulemonde2010). The AFM coupling between FM blocks (Fig.3-1, (d)) was detected in absence of magnetic sollicitation, while an applied field reorients the moments towards the (a,b) plane.

Transport properties: The connection/disconnection of the structural blocks also play an important role also in the transport properties, the resistivities increasing with the degree of disconnection between the blocks, as shown in section 2.3.1.b) (Page 97).

3.1.2. Magnetocrystalline anisotropy versus X

While in the case of F and Cl tetrameric compounds and chlorine trimeric compound the absence of any $00l$ magnetic satellites on ND diffraction patterns involve magnetic moments collinear to the c -axis (*Kauffmann2006; Kauffmann2007c, Ehora2007; Ehora2007b*) (Fig.3-1, (a)), the F-trimeric case shows the magnetic spins in the (a,b) plane (*Ehora2007*) ((Fig.3-1, (b)). This was attributed to the important deformation of the tetrahedra in trimer F particular case, modifying the spin-orbit coupling/magnetic anisotropy (*Mentré2010*). In fact, in $\text{Ba}_5\text{Co}_5\text{FO}_{13-\delta}$, F^- vacancies enable a strong off-centring of the oxygen positions ($\Delta=0.87 \text{ \AA}$ from its ideal position) in the h' [BaOF] layer which reduce the intra-dimer Co-O-Co angle to 125° . In the case of $\text{Ba}_5\text{Co}_5\text{ClO}_{13-\delta}$, the large Cl radius constrains the in-plane oxygen to stay around its central position ($\Delta=0.37 \text{ \AA}$) (*Kauffmann 2007c*). We validated that this distortion is enough to change spin-orbit coupling, responsible for the magnetocrystalline anisotropy:

DFT calculations: For this purpose, DFT based calculations combined with spin-orbit-coupling (SOC) analysis and extended Hückel tight binding calculation (EHTB) were used (*Mentré2010*). The DFT electronic structure calculations have shown that, in this series, the charge distribution can be described by considering high spin Co^{3+} state (d^6) for $\text{Co}(Td)$ and low-spin $\text{Co}^{3+/4+}$ state for $\text{Co}(Oh)$. Using this high spin d^6 configuration for the $\text{Co}(Td)$, the SOC analysis combined with EHTB calculations show that the local geometries of the Co_2O_7 dimmers involve pronounced differences in the split pattern of the d states leading to different spin orientations. To summarize, the difference in the spin orientations, observed from neutron diffraction experiments, arises from the fact that the distortions of the Co_2O_7 dimers in the two compounds are different.

3.1.3. "History" of the proposed charge distribution

The first investigations on these systems (*Kauffmann2007c; and 2008; Ehora2007 and 2007b*) led to the following conclusions regarding the charge distribution:

- trimer and tetramer F : $\text{Co}^{4+}_{\text{IS}} (\text{Td}) / \text{Co}^{3+}_{\text{LS}} (\text{Oh}_{\text{central}}) / \text{Co}^{3+}_{\text{LS}} (\text{Oh}_{\text{marginal}})$
- trimer and tetramer Cl: $\text{Co}^{4+}_{\text{IS}} (\text{Td}) / \text{Co}^{3+}_{\text{LS}} (\text{Oh}_{\text{central}}) / \text{Co}^{3+}_{\text{HS}} (\text{Oh}_{\text{marginal}})$
- trimer and tetramer Br: $\text{Co}^{4+}_{\text{IS}} (\text{Td}) / \text{Co}^{3+}_{\text{LS}} (\text{Oh}_{\text{central}}) / \text{Co}^{3+}_{\text{LS}} (\text{Oh}_{\text{marginal}})$

It was matching reasonably the experimental effective moments for each compounds and it was in relatively good agreement with the high values of magnetic moment refined in the tetrahedral site by ND (suggesting $\text{Co}^{4+}_{\text{IS}}$) and the null/weak moment refined for the Co in the octahedral oligomers for F and Br (suggesting $\text{Co}^{3+}_{\text{LS}}$), while for Cl, a small magnetic moment was refined for the marginal octahedral Co.

Later on, in the light of new investigation (DFT calculations) (*Mentré2010; Toulemonde2010*), this charge distribution was contested, a $\text{Co}^{3+}_{\text{HS}} (\text{Td})$ and mixed $\text{Co}^{3+/4+}_{\text{HS/LS}} (\text{Oh})$ charge distribution being proposed. This charge distribution is consistent with the refined values of the local moments, as with the experimental μ_{eff} values.

3. 2. Short chapter presentation

This chapter is dedicated to the study of anionic substitution (*i.e.* the influence of the halogen (or other "unexpected" anions such as carbonate groups)) in trimeric and tetrameric compounds on the structural, magnetic and electrical futures.

The **first section** of this chapter is dedicated to the study of the influence of the halogen nature in trimer and tetramer anion–substituted compounds. Thus, the F - Cl solid solutions (for trimers and tetramers) will be presented as well as a new Pt–doped trimer with X=Br, showing connected tetrahedra.

The **second section** of this chapter is dedicated to compounds with carbonate groups. The first example concerns two compounds with important disconnections between structural blocks achieved by the introduction of carbonate

groups ($\text{Ba}_2\text{Co}_4\text{ClO}_7$ and $\text{Ba}_2\text{Co}_4\text{BrO}_7$, *Kauffmann2007*). The disconnection between magnetic blocks is at the base of the concept of magnetic Lego that we try to develop in the group.

At the end of this chapter, new compounds with different ordering of 1D CoO_6 -face sharing columns and carbonates columns will be presented. Also, as consequence of the attempts to substitute the anion in tetramer structures by $(\text{OH})^-$ groups, the $2\text{H}-\text{BaCoO}_3$ compound (*Taguchi1977*) was obtained by an easy synthetic route presented hereafter. Some investigations on these powders will be shortly given in the section 3. 5. , Page 159).

3. 3. Synthesis of the compounds

In this section, we briefly give the synthesis method of the compounds presented hereafter:

1. $\text{Ba}_5\text{Co}_5\text{Cl}_{1-y}\text{F}_y\text{O}_{13-\delta}$

The syntheses of $\text{Ba}_5\text{Co}_5\text{ClO}_{13-\delta}$ and $\text{Ba}_5\text{Co}_5\text{ClO}_{13-\delta}$ pure powders (terms $y=0$ and $y=1$) are relatively difficult:

- $y = 0$: In order to stabilize the pure powder, a heating at 900°C for stabilizing the tetramer structures is required, followed by a high temperature heating (1030°C). The stabilization of trimer structures at higher temperature than tetramer structures will be discussed later. The synthesis mixtures are then quenched to room temperature (*Kauffmann2007c*).

- $y=1$ is prepared using an excess of BaF_2 and the reaction takes place in a sealed gold tube. After air quenching, the dark powder obtained is washed with hot water in order to eliminate the BaF_2 excess (*Ehora2007b*).

- $\text{Ba}_5\text{Co}_5\text{Cl}_{1-y}\text{F}_y\text{O}_{13-\delta}$ solid solution ($y=0.2; 0.4; 0.5; 0.6; 0.7; 0.8$) synthesis was made by heating, in an alumina crucible, the homogenous mixture of BaCO_3 (Sigma-Aldrich, 99%), Co_3O_4 (Alfa Aesar, 99.7%), $\text{BaCl}_2 \cdot 2\text{H}_2\text{O}$ (Prolabo, 99%) and BaF_2 (Aldrich, 99.99%) in stoichiometric amounts, at 900° for stabilizing the tetramer structure. The furnace temperature was then raised at 1030°C for 72h, followed by a quenching in air to room temperature. Dark powder is thus obtained.

2. $Ba_6Co_6Cl_{1-y}F_yO_{16-\delta}$

The synthesis of these compounds was already described previously (Kauffmann2007c, Ehora2007b) as starting with an homogenous mixture of $Ba_6Co_6ClO_{16-\delta}$ and $Ba_6Co_6FO_{16-\delta}$ in stoichiometric amounts, well ground and introduced in an alumina crucible heated at 900°C for 72h with intermediary regrinding. Then, the oven was cooled down to room temperature in 6h.

3. $Ba_5(Co, Pt)_5BrO_{13-\delta}$

The $Ba_5(Co, Pt)_5BrO_{13-\delta}$ compound was synthesised by the flux method in a platinum crucible starting with $BaCO_3$ (Sigma-Aldrich, 99%), Co_3O_4 (Alfa Aesar, 99.7%) and $BaBr_2$ (Alfa Aesar, 99%) in a $BaBr_2$ flux, heated at 1000°C for 48h and cooled with 10°C/h to 800°C, than quenched at room temperature. The $BaBr_2$ excess was washed with hot water. Black, hexagonal crystals were thus obtained. As presented in section □(Page 152)), analysis on single crystals reveals that the Pt from the crucible reacts with the synthesis mixture, stabilizing a trimer octahedral string connected by tetrahedral dimers.

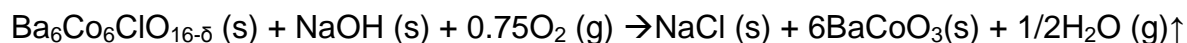
4. $Ba_2Co_4(X,CO_3)O_7$, (X=Cl, Br)

The syntheses of the two compounds have been described in Kauffmann2007. The black crystals have been obtained by the flux method using $BaCl_2 \cdot 2H_2O$ flux, starting with $BaCO_3$ (Sigma-Aldrich, 99%), Co_3O_4 (Alfa Aesar, 99.7%), and $BaCl_2 \cdot 2H_2O$ (Prolabo, 99%) in the 1:1:10 molar ratio. The well ground mixture was heated in air at 1100 °C for 48 h in an alumina crucible. The mixture was then slowly cooled at 30°C/h to room temperature. After dissolving the excess of $BaCl_2$ or $BaBr_2$ with hot water, black hexagonal plate-like crystals of approximate size 0.1-2 mm were isolated from the reaction product.

5. $2H-BaCoO_3$

According to the literature, the synthesis method for 2H- $BaCoO_3$ is rather difficult involving high O_2 pressure (200 bar at 900°C for 24h) (Taguchi1977). In a attempt to replace the Cl anion from the $Ba_6Co_6ClO_{16-\delta}$ compound with $(OH)^-$ groups, we have been able to obtain a large quantity of 2H- $BaCoO_3$ by heating in air, at

500°C a mixture of $\text{Ba}_6\text{Co}_6\text{ClO}_{16}$ and NaOH in excess. The reaction mixture was slow cooled (10°C/h) at room temperature. The resulting powder was then washed with hot distilled water in order to dissolve the NaCl presumed to be formed in the reaction given below:



6. 2H-Ba(Co,CO₃)O_{3-δ}

In an attempt to synthesized compounds similar to $\text{Ba}_7\text{Mn}_5\text{Ca}_2\text{O}_{21}$ and $\text{Ba}_8\text{Mn}_6\text{Ca}_2\text{O}_{22}$ (*Floros2000 and 2002*), but with Co instead of Mn, we have obtained the compound presented in section 3.5.2. (Page 168) This synthesis was performed as follows: a stoichiometric, well grounded, mixture of BaCO_3 (Sigma-Aldrich, 99%), Co_3O_4 (Alfa Aesar, 99.7%) and CaCO_3 (Aldrich 99%) in 7/5/2 molar ratio pressed into pellets was placed in an alumina crucible on a BaCO_3 layer in order to avoid the adsorption of the Ba in the alumina crucible and heated at 900°C for 12h. The temperature was then increased to 1100°C for 75h. The crucible was then quenched at room temperature. After regrinding, the sample was heated at 900°C in an oven under O_2 flux for 24h and the oven was left to cool down to room temperature.

3. 4. Trimer and tetramer Cl – F solid solutions

3.4.1. 10H (trimer) Cl–F solid solution

In this part, the structural characterization on powder and/or single crystal XRD, as well as neutron diffraction of the anion-exchanged $\text{Ba}_5\text{Co}_5\text{Cl}_{1-y}\text{F}_y\text{O}_{13-\delta}$ solid solution will be presented. It includes the evolution of the cell parameters determined from XRD, and the structural models from neutrons data. The influence of the mixed Cl/F halogen site on the structure is discussed. Also, the influence on the magnetic and electrical properties will be studied using low temperature neutron diffraction and physical characterizations. The synthesis of this chemical system is described in section 3. 3. (Page 123).

3.4.1.a) Lattice parameters evolution

The superposition of diffraction patterns shows a progressive shift of the (hkl) peaks to higher 2θ when F^- is replaced by Cl^- (Fig.3-2, (a) and (b)). If on one hand, for the $hk0$ lines no shift is observed (for example, the (110) peak ($\approx 30^\circ$ in 2θ)), on the other hand, for $l \neq 0$ a strong displacement is observed (see for instance the (107) peak (Fig.3-2, (b)), showing the increase of only the c parameter with the introduction of Cl^- in the structure.

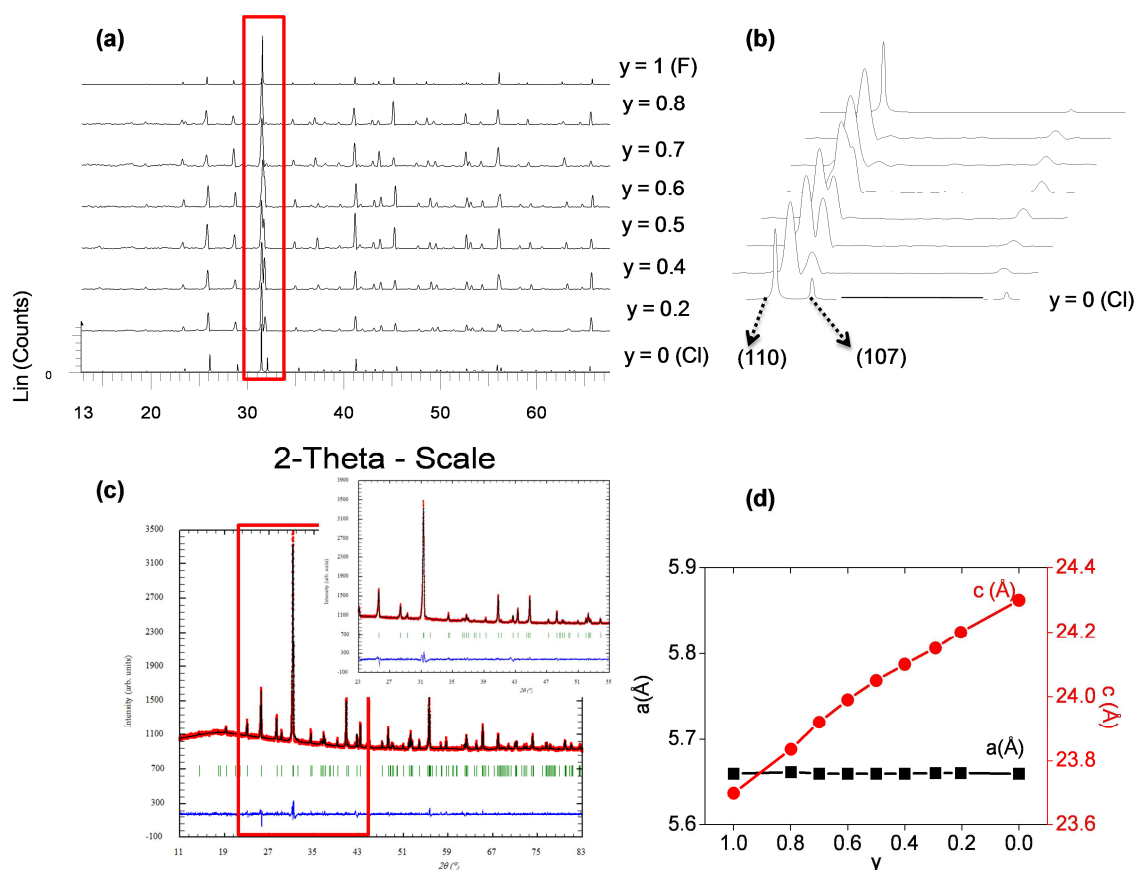


Fig.3-2: (a) and (b) XRD patterns for $Ba_5Co_5Cl_{1-y}F_yO_{13-\delta}$, zoom on (110) and (107) lines; (c) Pattern matching refinement for $Ba_5Co_5Cl_{0.2}F_{0.8}O_{13-\delta}$; (d) lattice parameters evolution for $Ba_5Co_5Cl_{1-y}F_yO_{13-\delta}$

The lattice parameters were refined using FullProf software (see for instance the result for $Ba_5Co_5Cl_{0.2}F_{0.8}O_{13-\delta}$ Fig.3-2 (c)). The evolution of the cell parameters (Fig.3-2, (d)) is in good agreement with the introduction of a larger anion ($r_{Cl^-}=1.81$, $r_{F^-}=1.33$ in VI coordination, Shannon1976) in the structure (the c parameter progressively decreases from 24.3 Å for $y=0$ (Cl) to 23.7 Å for $y=1$ (F)).

This feature highlights the main compressibility of this structural type along the *c* axis and the particular role of the hexagonal [BaOX] layer as a versatile spacer.

3.4.1.b) Structure investigation by powder neutron diffraction

In addition to the two parent-compounds ($y=0$ and $y=1$) already described in *Kauffmann2007c*, *Ehora2007b*, the room temperature neutron diffraction was performed for the $y = 0.2$, 0.5 and $y = 0.8$ terms of the solid solution using 3T2 diffractometer (see the Materials and methods section) (for refinements results, see Supplementary information, Annexes 1, Page 181).

a. Mixed halogen site refinement

Refinements were performed using FullProf software. In a first step, the mixed anionic sites occupations were refined, keeping the sum of the two anions occupancies restrained to full occupancy ($ai[Cl] + ai[F] = 1$, where ai = site occupancy). However, in the $y=0$ (pure F) compound, anionic vacancies were refined from neutron diffraction data leading to the formula: $Ba_5Co_5F_{0.7}O_{12.579}$. We thus undertook, in a second step, constraint-free refinements (Table 3-1).

Table 3-1: Comparison between the refinement results, using the restraint for the halogens occupations $ai[F]+ai[Cl]=1$ and without restraint; the percent of occupied site (% site) for $Ba_5Co_5Cl_{1-y}F_yO_{13.5}$ in the second case is also given:

y	Refinement $ai[Cl] + ai[F] = 1$			Constraint - free refinements			
	Cl / F	R _{Bragg} (%)	R _F (%)	Cl / F	R _{Bragg} (%)	R _F (%)	%site
1	0/1	7.66	6.49	0.757(8)/0	7.35	6.27	75.7
0.8	0.066(4)/0.934(4)	6.56	4.85	0.186(9)/0.740(9)	6.37	4.67	92
0.5	0.365(4)/0.634(4)	5.09	3.75	0.500(2)/0.407(2)	4.91	3.56	90
0.2	0.597(3)/0.403(3)	6.14	4.53	0.620(9)/0.365(9)	6.01	4.35	98
0	1/0	2.68	2.62	1/0	2.68	2.62	100%

For instance, for $y=0.8$ the agreement factors in the case of restrained refinement are $R_{Bragg}=6.56\%$ and $R_F=4.85\%$. The ratio between F and Cl is 0.934(4) and 0.066(4) respectively. When the constraint is removed and the two occupations

refined (refinement given in figure Fig.3-3), the final ratio become 0.740(9) F for 0.186(9) Cl (close to the experimental 0.8F/0.2Cl) with lower agreement factors ($R_{\text{Bragg}}=6.37\%$ and $R_F=4.67\%$). The total occupancy is refined at 92%. Clearly, the Cl incorporation limits the anionic vacancies on the X site.

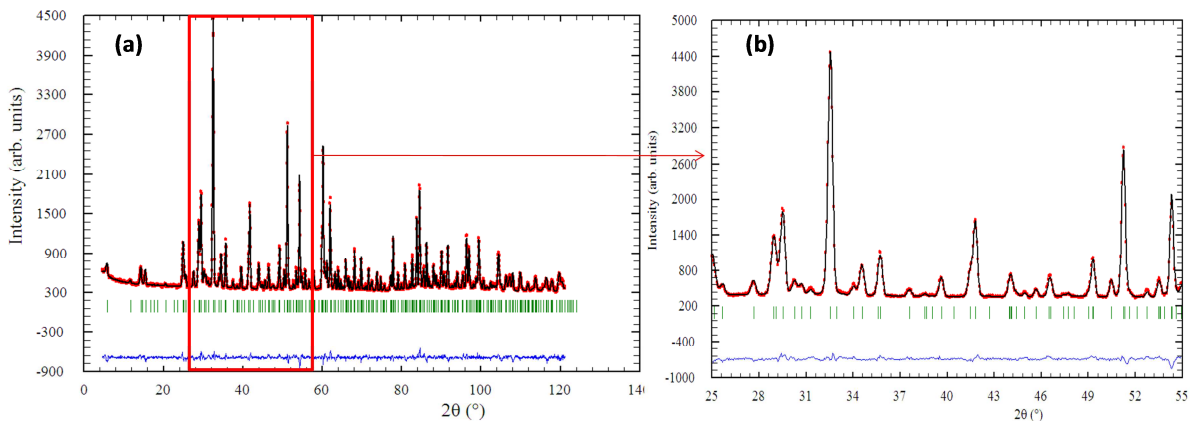


Fig.3-3: (a) Rietveld refinement for $y = 0.8$ (F) of $\text{Ba}_5\text{Co}_5\text{Cl}_{1-y}\text{F}_y\text{O}_{13-\delta}$; (b) zoom on 25–55 in $2\theta^\circ$

b. Halogen environment - Ba5 pyramid

The replacement of a Cl anion by F lead to the decrease of the X–Ba2 distances in good accordance with the introduction of a smaller anion in the h' [BaOX] layer (Fig.3-4).

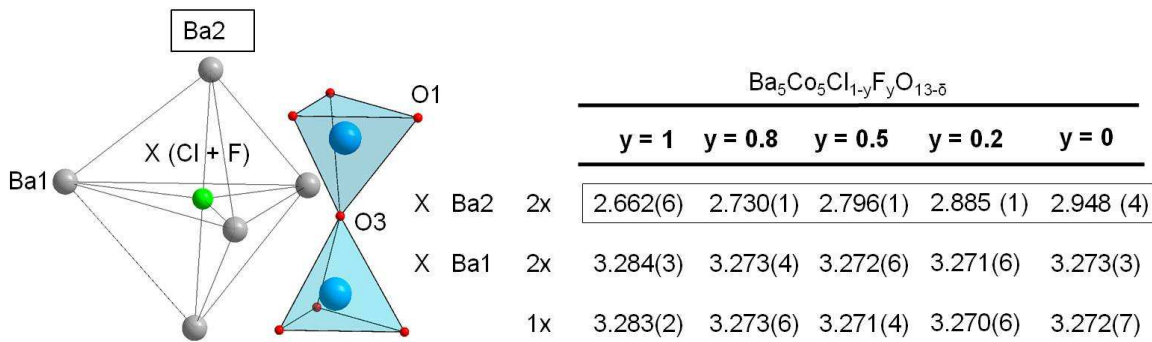


Fig.3-4: Ba5 pyramid around halogen. Comparison between Ba – X distances (from neutron diffraction data for $y = 1, 0.8, 0.5, 0.2$ and 0 of $\text{Ba}_5\text{Co}_5\text{Cl}_{1-y}\text{F}_y\text{O}_{13-\delta}$)

Meanwhile, the evolution of Ba1–X distances is very small when the replacement of F by Cl is made. These observations are in good accordance with the elongation of the unit cell only along c axis.

c. Oxygen vacancies

The oxygen atom from the h' [BaOX] layer was placed on a $6h$ ($2x, x, 1/4$) position (i.e. the same position for $y = 0$ and $y = 1$) (Mentré2008; Kauffmann2007c; Ehora2007) (Annexes 1). The refinement of the occupation in this site reveals no dependence with the F/Cl ratio. On the opposite, the two other available sites show a greater deficiency, especially in the cubic layer.

Table 3-2: Neutron diffraction and titration results regarding the oxygen content and oxidation degrees:

y	Neutron diffraction		Redox titration	
	Oxidation degree	Oxygen content	Oxidation degree	Oxygen content
1	3.18	12.58	3.20	12.50
0.8	3.25	12.66	3.21	12.54
0.5	3.26	12.70	3.22	12.55
0.3			3.22	12.56
0.2	3.28	12.73	3.23	12.59
0	3.21	12.53	3.24	12.60

The oxidation degrees calculated from neutron diffraction data and those determined by iodometric titration are given in Table 3-2. A relatively good accordance between the two techniques is noticeable. A small increase of the oxidation state for Co with the replacement of Cl for F can be observed. The influence of oxygen vacancies is exaggerated by the vacancies on the X-site which follows the same trends along the Cl/F line. The final refinements results for the three investigated compounds are given in Annexes 1. The refined formulas are thus:

- $\text{Ba}_5\text{Co}_5\text{F}_1\text{O}_{13}$ (ideal): $\text{Ba}_5\text{Co}_5\text{F}_{0.75}\text{O}_{12.58}$ (refined)
- $\text{Ba}_5\text{Co}_5\text{Cl}_{0.2}\text{F}_{0.8}\text{O}_{13}$ (ideal): $\text{Ba}_5\text{Co}_5\text{Cl}_{0.18}\text{F}_{0.74}\text{O}_{12.66}$ (refined)
- $\text{Ba}_5\text{Co}_5\text{Cl}_{0.5}\text{F}_{0.5}\text{O}_{13}$ (ideal): $\text{Ba}_5\text{Co}_5\text{Cl}_{0.5}\text{F}_{0.41}\text{O}_{12.70}$ (refined)
- $\text{Ba}_5\text{Co}_5\text{Cl}_{0.8}\text{F}_{0.2}\text{O}_{13}$ (ideal): $\text{Ba}_5\text{Co}_5\text{Cl}_{0.62}\text{F}_{0.37}\text{O}_{12.73}$ (refined)
- $\text{Ba}_5\text{Co}_5\text{Cl}_1\text{O}_{13}$ (ideal): $\text{Ba}_5\text{Co}_5\text{Cl}_1\text{O}_{12.53}$ (refined)

Table 3-3: Neutron diffraction refinement results regarding the presence of oxygen vacancies.

y (F)	F/Cl (2c)	O1 (12k) (c layers)	O2 (12k) (h layers)	O3 (6h) h' [BaOX]
1	0.757(8)/0	0.948(5)	0.986(7)	0.325(9)
0.8	0.740(9)/0.186(9)	0.969(6)	0.975(5)	0.333(9)
0.5	0.407(2)/0.500(2)	0.962(6)	0.989(5)	0.332(6)
0.2	0.365(9)/0.620(9)	0.974(5)	0.983(5)	0.330(7)
0	0/1	0.974(5)	0.948(5)	0.333(9)

d. Distortion of the Co₂O₇ units

As expected from the chemical modification of the h'-[BaOX] layers, in the face-sharing trimers, no significant modification of the interatomic distances can be evidenced (Table 3-4). This was expected since the only changes in the structures are at the h' [BaOX] layer level. Meanwhile, the Co–Co distances in the tetrahedral dimers are increasing with the incorporation of Cl in the sample.

At this level, two features interact:

- The elongation of the c parameter, especially influent at the level of the Co₂O₇ dimers.
- The distortion of the tetrahedra due to variable in-plane shifting of the O3 corner already observed for the two limit-compounds (Fig.3-5, (a)) y=1 terms of the solid solution. This shift of O3 from its central position decreases as F is replaced by Cl due to the smaller ionic radius of F and subsequent in-plane reorganization similar to the “push-and-pull” mechanism described for Ba₅Co_{5-y}Fe_yXO_{13-δ} case in the section 2.2.1.d) (Page 52) ($\Delta_{y=1}=0.87 \text{ \AA}$, $\Delta_{y=0.8}=0.47\text{\AA}$, $\Delta_{y=0.5}=0.37\text{\AA}$, $\Delta_{y=0.2}=0.35\text{\AA}$, $\Delta_{y=0}=0.37 \text{ \AA}$).

This effect is particularly well illustrated on the Fourier-difference maps of the corresponding plane for Ba₅Co₅FO_{13-δ} (see Fig.3-5 (b)). It leads to Co-O-Co angles far from the ideal angle value of 180° (for y=1 the angle is 125.3°). The evolution of this angle between y=0 and y=1 is plotted in Fig.3-5, (c) and appears more pronounced between the terms y=0.5 (156.9°) and y=1 (125.3°). Then, the most deformed local Co₂O₇ dimeric structure is associated with smaller F anions in the [BaOX] layers. The introduction of Cl in the structure, even in weak amounts, will reduce the tetrahedral distortion by reducing the shift of the oxygen from its central

position, due to its big anionic radius. This will be even more pronounced for the new compound $\text{Ba}_5\text{Pt}_1\text{Co}_4\text{BrO}_{13.5}$ in which the introduction of an even larger anion will reduce more the tetrahedral distortion (see section □ (Page 152)). From the magnetic point of view, this aspect is also fascinating since a change of magneto-crystalline anisotropy as a function of the distortion of the dimeric units was reported (Mentré2010).

Table 3-4: Co – Co and Co – O distances (Å) determined from neutron diffraction data and comparison with the parent compounds:

Atoms		y = 1	y = 0.8	y = 0.5	y = 0.2	y = 0
Co1	Co2	2.493(2)	2.497(5)	2.502(9)	2.503(9)	2.501(2)
Co1	Co3	3.733(2)	3.716(4)	3.726(7)	3.735(9)	3.733(2)
Co3	Co3	3.313(3)	3.346(6)	3.469(8)	3.496(1)	3.518(4)

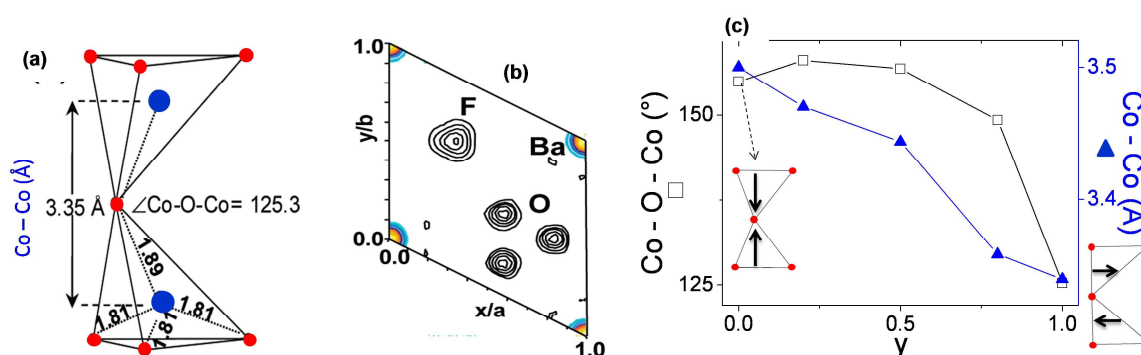


Fig.3-5: (a) The deformation of tetrahedra in $y=0$ $\text{Ba}_5\text{Co}_5\text{FO}_{13.5}$ with the Co – O and Co – Co distances in the tetrahedra (Å) and Co – O – Co angle ($^\circ$), (b) Fourier map for [BaOF] layer; (c) Evolution of the Co – Co distances and Co – Co bonds lengths in $\text{Ba}_5\text{Co}_5\text{Cl}_{1-y}\text{F}_y\text{O}_{13.5}$ solid solution

3.4.1.c) Single crystals structure investigation

So far, F/Cl compounds PND yields partially deficient X sites located in their ideal positions. However, at this level a closer inspection have been possible help to the growth of single crystals in one of our mixed F/Cl samples. It gives us the possibility to investigate the mixed halogen site by the maximal entropy method, a technique which enables to see clearly the observed local electronic density of a compound. The crystals were obtained by melting the powder of the $y=0.8$ (F) term of the solid solution at 1050°C for 12h and then slowly cooled with $50^{\circ}\text{C}/\text{h}$ until 800°C and quenched at R.T. Several black crystals obtained were tested using single crystals XRD and the best one was collected until $2\theta=94.92^{\circ}$. The structure refinement gives 0.762/0.238 F/Cl ratio, corresponding to experimental ratio from the melted powder. The crystal parameters are $a=5.698(3)$ Å and $c=24.106(1)$ Å and correspond to the powder refined parameters of the 0.7F/0.3Cl term ($c=24.15$ Å on powder). The refinement was conducted keeping the $ai[\text{Cl}] + ai[\text{F}] = 1$ overall sum due to the poor XRD-contrast of the F anions.

- Maximal entropy method (MEM)

The fully complete collected data set was used to calculate the MEM maps for reason already discussed in previous section. We have paid a more important attention to the electronic density around mixed halogen site (Fig.3-6). Then, the halogen site seems to be split on three bordering positions but keeping the central position occupied also (Fig.3-6). This particular shape can be explained considering the split of the fluorine atom on three positions (70%), surrounding the central chlorine atom (30%).

To model these observations, the fluorine atom was moved from his central $2c$ position ($1/3, 2/3, 1/4$) to one $6h$ ($x, 2x, 1/4$). We have tried to refine this disorder, but the refinement was unstable. However, we can propose a hypothetical model in which the central Cl and the shifted F anions are disordered in the crystals. This disorder also influences the shape of the electronic densities of Ba2 (at the top of the X site in the next cubic $[\text{BaO}_3]$ layer). The electronic density of Ba2 is elongated pointing towards the halogen site ((Fig.3-6)). Taken further the model figured above, Ba2 is also split on two positions: a central position Ba2 and a Ba2'

position, depending of its closer X-neighbour. When central X=Cl then Ba2 is ideally located. When X=F, the Ba atom migrates in the Ba2' position closer to the X-site. Unfortunately, it is not possible to perform the same MEM analysis on powder neutron diffraction. However, the examination of the Fourier difference maps, even if less accurate, leads us to conclude to same tendency for the density around halogen atom (Fig.3-7).

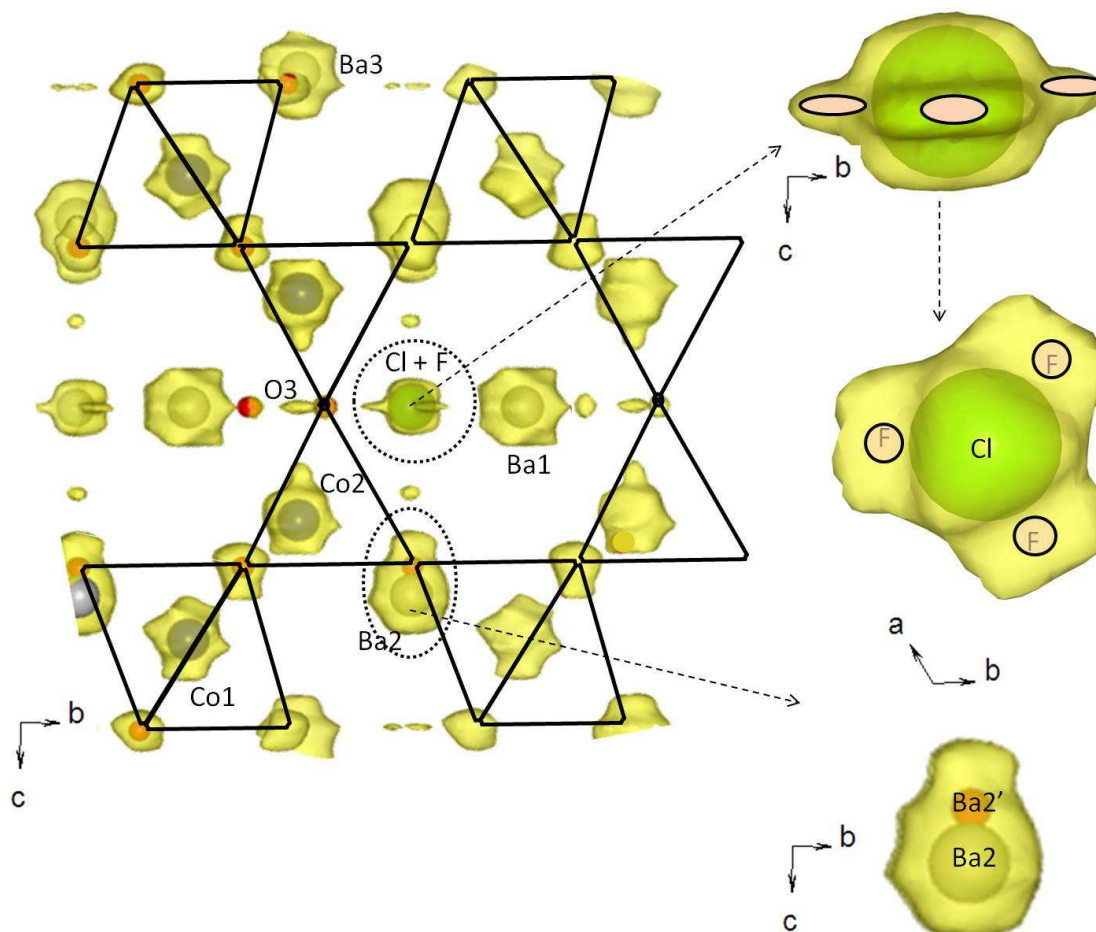


Fig.3-6: Electronic density from MEM in h' $[\text{BaOX}]$ ($X=\text{Cl} + \text{F}$) layer

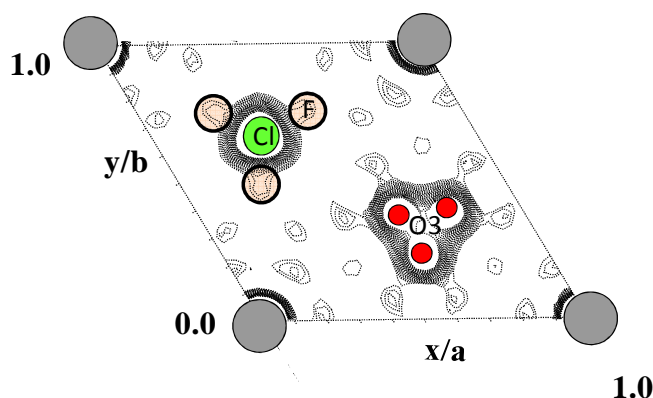


Fig.3-7: Difference Fourier map around [BaOX] layer for $Ba_5Co_5Cl_{0.2}F_{0.8}O_{13-\delta}$ after neutron powder diffraction

3.4.1.d) Summary structural investigation $Ba_5Co_5Cl_{1-y}F_yO_{13-\delta}$

To summarize, several features are to be highlighted:

- We deal with versatile deficient and disordered structural compounds with a clear influence of the F/Cl ratio.
- The structural modifications due to this substitution is especially influent at the level of the Co_2O_7 pairs around the h' -[BaOX] layers.
- Generally the Cl-rich compounds show a greater mean Co-oxidation state. This is due to two concomitant effects : the greatest X deficiency for $X=F^-$ and a slightly greater concentration of oxygen vacancies (in the cubic-layers and face sharing octahedral for $X=F$)
- For steric reasons, F is slightly displaced out of its ideal position while Cl is central. As a consequence, the surrounding Ba site of the next layer is also disordered on two close positions.
- For similar steric reasons, the corner-oxygen of the h' -[BaOX] layers (O3) is also more displaced out of its central position for $X=F$. This leads to a progressive distortion of the Co_2O_7 tetrahedral pairs (shortening of Co-Co distances and decreasing of the Co-O-Co angle for rich F terms).

3.4.1.e) Ba₅Co₅Cl_{1-y}F_yO_{13-δ} solid solution properties

- Magnetic properties

On the basis of the previous conclusions, it is clear that we are dealing with complex systems in term of disorder and also in terms of Co³⁺ and Co⁴⁺ distribution. Basically, the general trends of the parent compounds respect the several magnetic characteristics listed in section 2.3.1.a) , (Page 93). The evolution of magnetic characteristics upon the Cl for F substitution is expected to give raise to even more complex behaviors. In this section we will use several datasets collected on several magnetometer systems, i.e. SQUID-data, VSM-data and DC-field extraction-data from several collaborations between our group and other groups (IPCMS, CRISMAT, IEMN...). The magnetic susceptibility data were collected as described in the “Materials and Method” section. The susceptibility dependence on the temperature is given in Fig.3-8 at different magnetic fields (H=200Oe in blue, 500Oe in red, 1000Oe in black and 10000Oe (only available for y=0 and y=1) in green) for all investigated terms.

a) *Néel temperature and paramagnetic regime*

In fact, by anticipation of the ND-magnetic structures described later, we must note that the Néel temperatures (T>98K) are not the most important accidents found on the $\chi(T)$ plots but corresponds to small sharp anomalies. It is shown for all the series in Fig.3-8 (a), (b), (c), (d) and (e) with the applied field mentioned on the figure. The Néel temperatures and paramagnetic characteristics are listed in Table 3-5.

Table 3-5: Information from the magnetic susceptibility curves and magnetic moment refined from neutron diffraction at 1.5K (see later):

y	Magnetic susceptibility			Low temperature neutron diffraction		
	T _N (K)	μ_{eff} (μ_{B} /f.u.)	θ_{CW} (K)	MCo1 (μ_{B}) (O _h _{marginal})	MCo2 (μ_{B}) (O _h _{central})	MCo3 (μ_{B}) (Td)
0	110	9.21	-766	0.61(7)	0.35(8)	2.21(7)
0.3	107	10.32	-1009			
0.4	111	10.54	-961			
0.6	98	8.99	-561			
0.8				0	0.39(5)	2.35(6)
1	122	8.16	-416	0	0.24(4)	1.94(4)

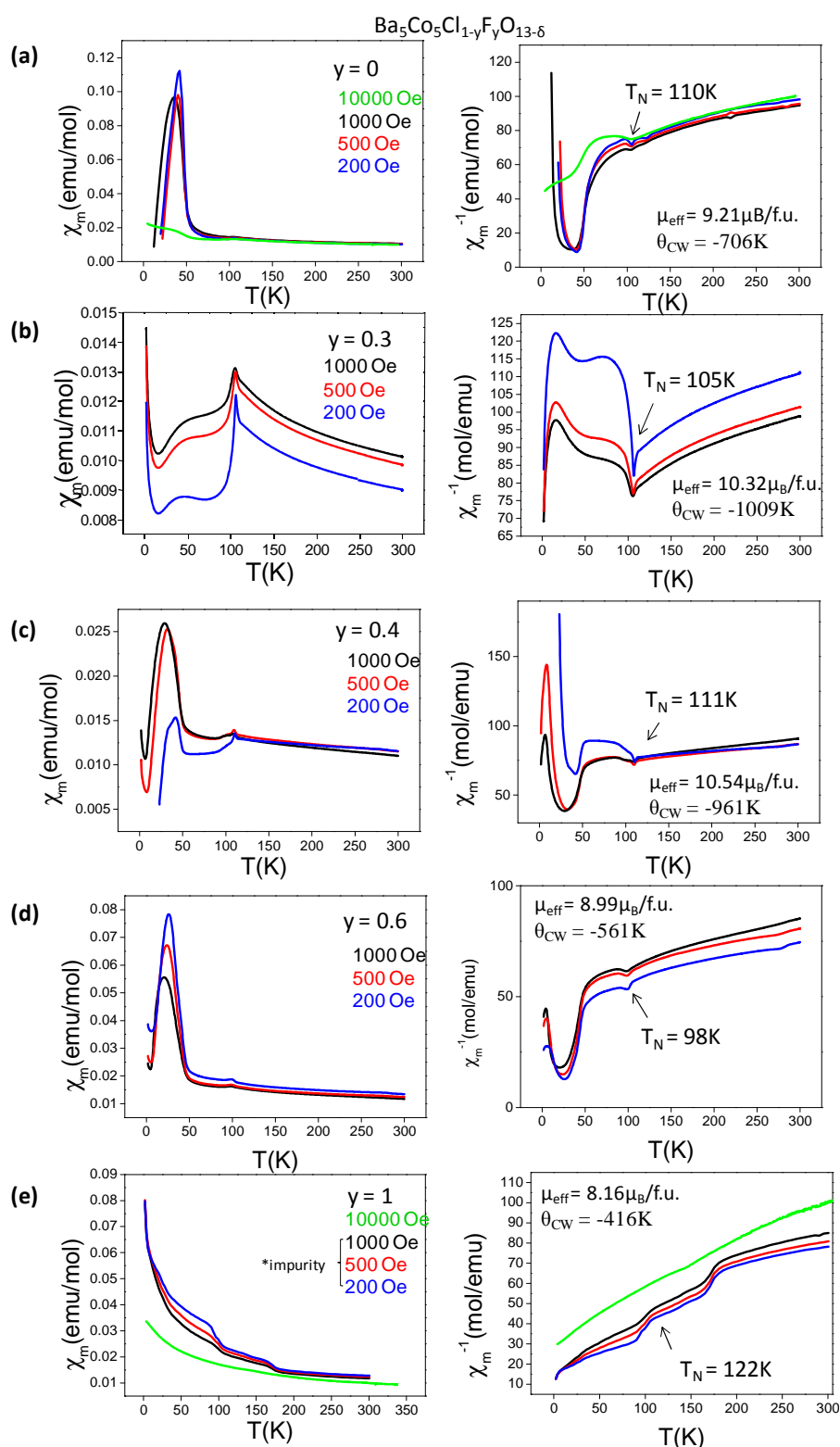


Fig.3-8: χ_m and χ_m^{-1} for $y = 0$ (a); $y = 0.3$ (b); $y = 0.4$ (c); $y = 0.6$ (d); $y = 1$ (e) at different magnetic field H ($H = 1000$ Oe – black, $H = 500$ Oe – red, $H = 200$ Oe in blue and 10000 Oe in green)

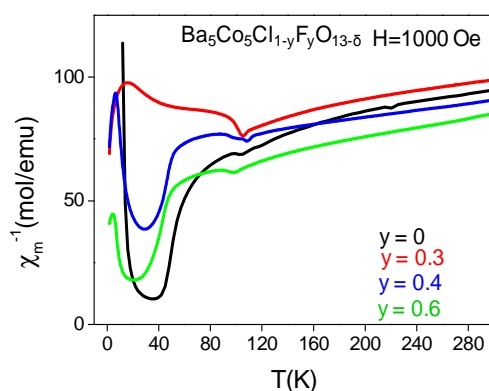


Fig.3-9: Evolution of the inverse of magnetic susceptibility with the temperature for the pure investigated terms at $H=1000\text{Oe}$

The ordering temperature does not follow a monotone evolution versus the y value but at least, can we observe greater values for the two extreme compounds ($T_N = 110\text{K}$ for $y=0$ and $T_N=122\text{K}$ for $y=1$). We can conclude that the increase of the structural disorder observed above plays against a cooperative alignment of magnetic spins within a 3D-ordered model. In addition, the examination of the paramagnetic data show no progressive evolution for θ_{CW} or μ_{eff} with y (F) ($9.27\mu_{\text{B}}/\text{f.u.}$ for $y=0$ and $8.16\mu_{\text{B}}/\text{f.u.}$ for $y=1$) (Table 3-5, Fig.3-8).

Regarding the cationic distribution, the Co case is very complicated due to important spin-orbit coupling and also to the possibility to stabilize different spin configurations (High spin=HS and low spin=LS and Intermediate Spin=IS (Korotin1996, Fauth2002)) depending on the oxidation degree and on the environment (tetrahedral or octahedral) (Radaelli2002, Hu2004). The theoretical effective moments assorted with the number of cationic electronic configurations (spin-only approximation) are listed below for information (Table 3-6). As already explained, with the help of DFT calculations, we proposed that the tetrahedral cobalt is assigned to $\text{Co}^{3+}_{\text{HS}}$ while in the octahedral chains the situation is much more ambiguous. A mixture of Co^{3+} , Co^{4+} within unclear electronic configurations was deduced from both low local moments calculated by DFT and refined from ND data. In addition, the short Co-Co separation implies a degree of metal-metal bonding that should exalt direct exchanges and strong electronic delocalization within the linear units.

We can anticipate that a good justification of the experimental μ_{eff} within a clean distribution of cations is rather impossible. For instance for $y=1$

($\mu_{\text{eff}}=8.16 \mu_B/\text{f.u.}$), two models can approach this value but the theoretic values do not match the experimental one:

- $[(\text{Co}^{3+}_{\text{HS}})_2] (\text{Td}) [(\text{Co}^{4+}_{\text{LS}})_2](\text{Oh}_{\text{marginal}})[\text{Co}^{3+}_{\text{LS}}](\text{Oh}_{\text{central}})$, $\mu_{\text{eff}}=7.34\mu_B/\text{f.u.}$
- $[(\text{Co}^{3+}_{\text{HS}})^2] (\text{Td}) [(\text{Co}^{3+}_{\text{LS}})_2](\text{Oh}_{\text{marginal}})[\text{Co}^{4+}_{\text{LS}}](\text{Oh}_{\text{central}})$, $\mu_{\text{eff}}=7.14\mu_B/\text{f.u.}$

Table 3-6: $\text{Co}^{4+/3+}$ possible spins configuration in octahedral and tetrahedral environment

		Octahedral environment	Tetrahedral environment
Co^{3+}	HS	$t_{2g}^4 e_g^2 : S = 2$	$e_g^3 t_{2g}^3 : S = 2$
	IS	$t_{2g}^5 e_g^1 : S = 1$	
	LS	$t_{2g}^6 e_g^0 : S = 0$	$e_g^4 t_{2g}^2 : S = 1$
Co^{4+}	HS	$t_{2g}^3 e_g^2 : S = 5/2$	$e_g^2 t_{2g}^3 : S = 5/2$
	IS	$t_{2g}^4 e_g^1 : S = 3/2$	$e_g^3 t_{2g}^2 : S = 3/2$
	LS	$t_{2g}^5 e_g^0 : S = 1/2$	$e_g^4 t_{2g}^1 : S = 1/2$

a) Spin Fluctuation below T_N

Below T_N , we have already mentioned (section 2.3.1. , Page 93) that the AFM ordering consists in FM blocks antiferromagnetically ordered with strong tetrahedral moments and weak or null octahedral moments (or at least no ordered components as refined by ND). If one observes the $\chi(T)$ plots shown on the Fig.3-8 an important component centred around 40 K is evidenced almost systematically and was already detected in our preliminary investigation of the parent compounds by a broad anomaly concave upward. Its origin is not still clearly elucidated but we can observe that its relative intensity varies erratically versus the applied field and versus the y (F) value. At least it seems weaker for $y=1$ (Fig.3-8, (e), even if it is hard to conclude since the low field have been performed on a multiphase sample and only high field data are available for a pure phase (given in green in Fig.3-8, (e)). However, it seems that for both $y=0$ (Fig.3-8, (a)) and $y=1$ (Fig.3-8, (e)), the available high field susceptibility show a strongly weakened peak. Furthermore, this particular phenomenon was observed on $\text{Ba}_5\text{Co}_5\text{ClO}_{13-\delta}$ single crystals (Wang2009) with H in

the (*ab*) plan, but not for the magnetic field parallel to the *c* axis (Fig.3-10, (a)). It is known in related 1D-compounds such as $\text{Ca}_3\text{Co}_2\text{O}_6$ (Maignan2000, Maignan2004, Hardy2004) and 2H-BaCoO_3 (Pardo2007) that AFM inter-chain exchanges likely create in-plane frustration, strongly compatible with the local magnetic disorder in the octahedra.

Then we suspect that:

- Below T_N , the 3D-ordering is achieved between strongly coupled AFM Co_2O_7 dimers, such that the trimeric units play the role of FM connectors (mainly by FM direct exchanges).
- On further cooling, the competition between intra- and inter- trimers vary with strong spin-fluctuation maximal at 40K.
- Below this temperature the AFM ordering is robust with no net moment but weak magnetic local moments on the FM-connectors partially due to the AFM exchanges in plane.

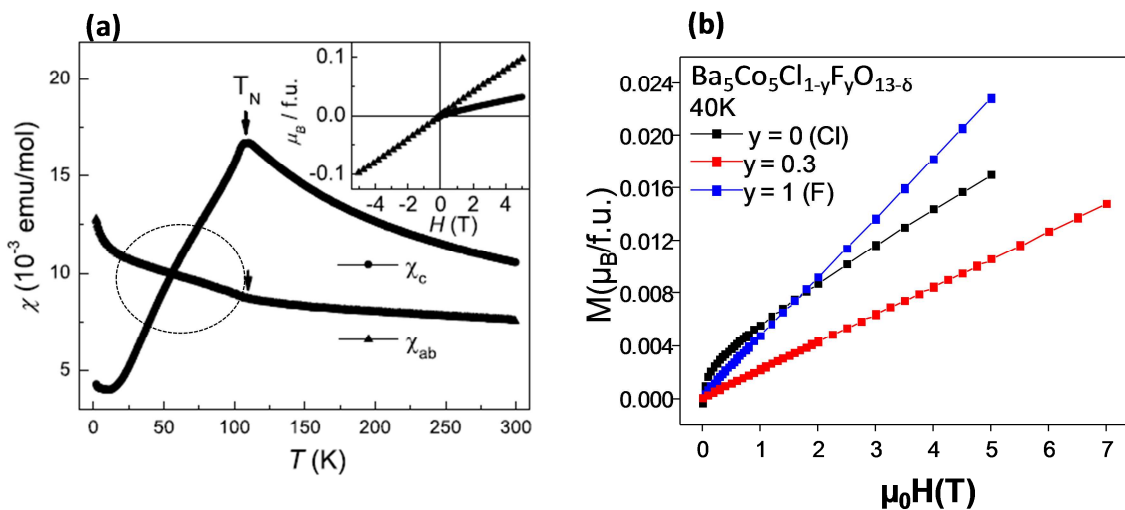


Fig.3-10: (a) Temperature dependence of susceptibility for $\text{Ba}_5\text{Co}_5\text{ClO}_{13-\delta}$ single crystal at 5000 Oe for magnetic field $\parallel c$ axis (circle) and $\parallel (ab)$ plan (triangular). In the insert, $M(\mu_0 H)$ at 4.3K (from Wang2009); (b) $M = f(\mu_0 H)$ for $y = 0$, $y = 0.3$ and $y = 1$ at 40K.

Another clue for this so-called “fluctuation” is given by a careful examination of magnetization plots at 40K (~temperature of the maximum) (Fig.3-10,

(b)). For $y=0$ (intense peak) the expected linearity of $M=f(\mu_0H)$ is not respected and shows the setting of FM domains-like before the high field domain. On the opposite, for $y=0.3$ and 1 (weak fluctuations compared to the anomaly at T_N) the linearity expected for an AFM ordering is well respected.

- Magnetic structures

Another lightening of the magnetic behaviour is given by the analysis of the magnetic structures refined by ND diffraction. As reported in (Mentré2010) and discussed in section 3.1.2. , the strong distortion of the tetrahedral pairs for the $Ba_5Co_5F_{0.75}O_{12.579}$ compound is responsible for the change of magneto-crystalline anisotropy (Co-O-Co=125°, magnetic spins in the (a,b) plane). However, the overall behavior remains the same, i.e. same FM octahedral blocks connected via AFM tetrahedral ones. We also note that small moments for $y=0$ have been refined on every octahedral sites only on the central octahedra for $y=1$.

The progressive evolution of the tetrahedral distortion along the $Ba_5Co_5Cl_{1-y}F_yO_{13-\delta}$ line (Fig.3-5) suggests an intermediate magnetic-orientation in mixed Cl-F compounds. Consequently, an F-rich compound ($y=0.8$) was investigated by neutron diffraction at low temperature using G41 diffractometer (see section "Materials and Method"). In this compound the tetrahedral dimers are characterized by Co-O-Co=149.3°. For this compound we observe the same magnetic satellites as those observed for $y=0$, growing below 100K ($=T_N$). The patterns superposition is given in Fig.3-11(a) and (b). It involves magnetic moments parallel to the c -axis. The final R_{mag} is 7.83% (at 1.8K). The refined magnetic moments are given in Table 3-5 and the final refinement is given in Fig.3-11 (c) and (d). We observe that the magnetic moments in the terminal octahedral of the trimers are null. In fact they converge to $M = 0.14\mu_B$ but the R value is not modified while they are fixed to 0. Meanwhile, the Co in the tetrahedral site (Co3) has the strongest magnetic moment ($1.94\mu_B$ for $y = 1$ (F); $2.36 \mu_B$ for $y = 0.8$ and $2.21 \mu_B$ for $y = 0$). The magnetic moment value for central Co in the octahedral trimer at 1.5K is comparable with the value refined for $Ba_5Co_5XO_{13-\delta}$ ($0.35 \mu_B$ for $y = 1$; $0.39 \mu_B$ for $y = 0.8$, $0.24 \mu_B$ for $y = 0$).

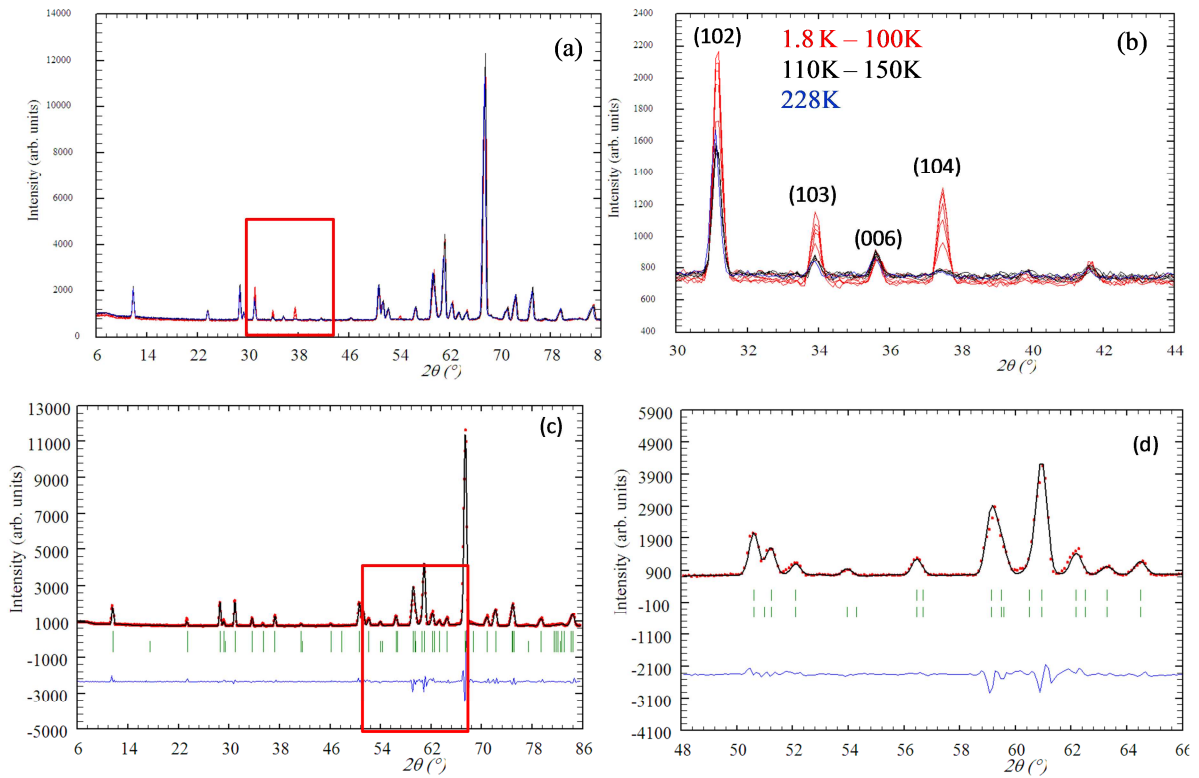


Fig.3-11: (a) Low temperature neutron diffraction patterns from 1.8 to 100K (red), 110 to 150K (black) and 228K in blue; (b) Zoom between 2θ 30 and 44° ; (c) Magnetic structure refinement at 1.8K using the orientation of the magnetic moments along the c axis; (d) Zoom between $48 - 66^\circ 2\theta$

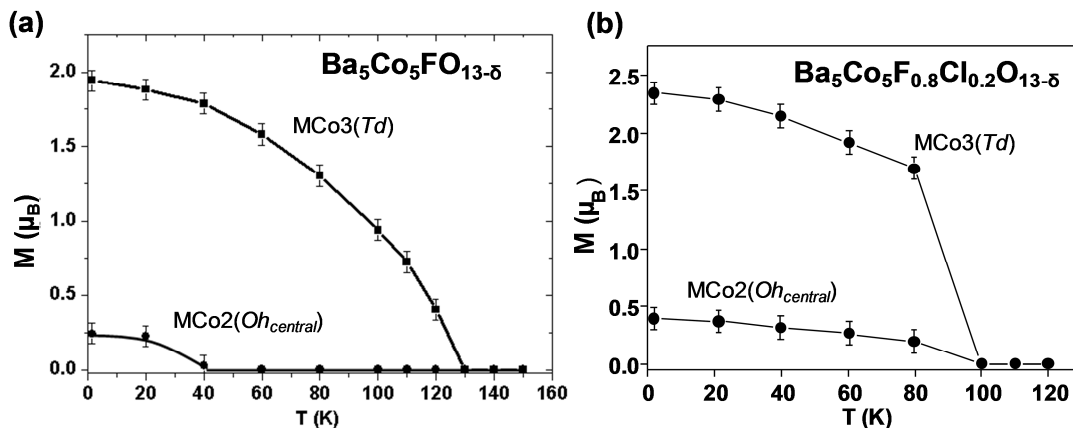


Fig.3-12: Evolution of the magnetic moments with the temperature for (a) $y = 1(\text{F})$ (Ehora2007) and (b) $y = 0.8$ of $\text{Ba}_5\text{Co}_5\text{Cl}_{1-y}\text{F}_y\text{O}_{13-\delta}$

In the same way, we tried to deviate the magnetic moments accordingly to the two models shown at both sides of the block interface in Fig.3-13. The first one converged to $\theta=10^\circ$ without a significant improvement of the refinement ($R_{\text{mag}}(\theta/180+\theta)=7.78\%$ versus $R_{\text{mag}}(\theta=0)=7.83\%$ at 1.8K). The second one corresponds to a canted structure and should lead to a strong magnetic component not experimentally observed. This model did not converge. Then we can conclude that the magnetocrystalline anisotropy change is only available for strongly distorted tetrahedra (these polyhedra are driving the magnetic ordering) and that a "minor" shifting of oxygen corners towards their ideal position immediately flip the full magnetic structure. We could also propose that the weak magnetic fluctuation below T_N for $y = 1$ arises from the in-plane magnetic orientations. It could limit local magnetic re-ordering due to the $\text{FM}_{\text{intra}}/\text{AFM}_{\text{inter}}$ competition, the latter AFM exchanges being due to in-plane frustration.

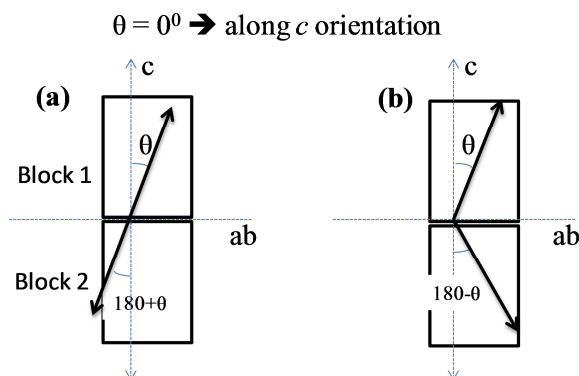


Fig.3-13: Possible magnetic spins orientations (a) $\theta/180+\theta$ and (b) $\theta/180-\theta$ for $\text{Ba}_5\text{Co}_5\text{Cl}_{1-y}\text{F}_y\text{O}_{13-\delta}$

- Electric properties of $\text{Ba}_5\text{Co}_5\text{Cl}_{1-y}\text{F}_y\text{O}_{13-\delta}$ solid solution

The resistivity of several terms of the tetrameric Cl/F solid solution was measured as described in the "Materials and method" section. Here, it is noteworthy that it was not possible to prepare bars of $y=0$ since it involves a rapid quenching of the 6H form, leading to multiphase samples. For $y=0$, it was shown on single crystals that the electronic conductivity occurs preferentially along c (see section 2.3.1 (Page 93), Wang2009). All compounds are semi-conductors, but no perfect linearization

has been possible using Arrhenius plots or 1D-VRH models (Fig. 3-14, (b) and (c)). At this point one should recall that the measurements are performed on polycrystalline samples (compactness~75%) and that inter-granular effects should intervene. However, clearly, an increase of the resistivity by several orders of magnitude follows the incorporation of Cl⁻. This effect is the same as for the tetrameric 6H-Cl/F solid solution (see later) but even much more pronounced. Then, the dominant phenomenon involves the cell-volume dilatation while Cl is incorporated. We have seen that this evolution is rather important and probably play on the interatomic orbital overlapping and easiest carrier conduction.

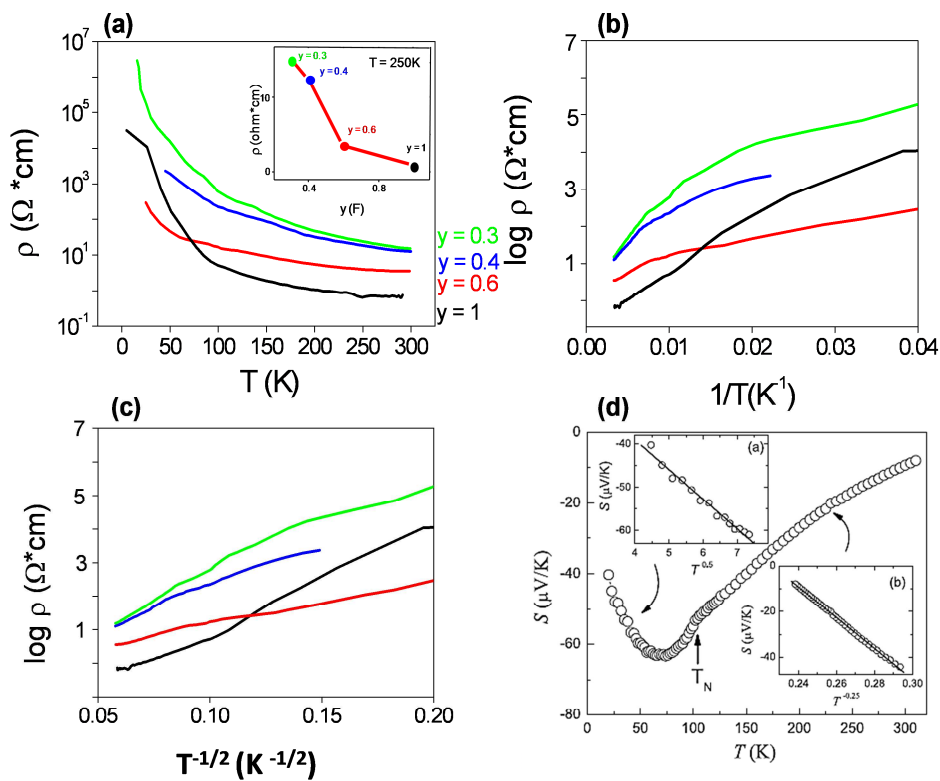


Fig.3-14: Resistivity dependence with T (a), T^{-1} (b), $T^{-1/2}$ (c) for $y=1, 0.6, 0.5, 0.4$; (d) Seebeck measurements for $\text{Ba}_5\text{Co}_5\text{ClO}_{13-\delta}$ single crystals (from Wang2009)

Two reasons could be argued:

- the first concerns the unit cell volume reduction at the F-rich side which should play for strongest orbital overlapping and easiest electron hopping
- the $y=0$ ($\text{Ba}_5\text{Co}_5\text{ClO}_{13-\delta}$) compound was shown to have a negative Seebeck coefficient (*i.e.* the charge carriers are electrons) (Wang2009) (Fig. 3-14, (d)); then the experimental reduction with the incorporation of F⁻ likely increase the

concentration of carriers and then increase the conductivity (or decrease the resistivity). Both of these effects probably intervene concomitantly at the origin of the drastic change of the transport properties.

3.4.1.f) Conclusion in few points

- The solid solution $\text{Ba}_5\text{Co}_5\text{Cl}_{1-y}\text{F}_y\text{O}_{13-\delta}$ was synthesised by solid state reaction at high temperature followed by a quenching in air at room temperature (see part 3.3).
- The cell parameters evolution is in good agreement with the enlargement of the c parameter due to the introduction of a larger anion ($\text{Cl} \rightarrow \text{F}$) in the $[\text{BaOX}]$ layer.
- Within the $[\text{BaOX}]$ layers, the mixed Cl/F halogen site was accurately examined using MEM on single crystal corresponding to $y=0.7$. A slight displacement of F out of its ideal position is observed while Cl remains ideally located on 3-fold axis.
- From titration results, the compounds are progressively reduced towards the F rich zone. Considering unchanged Co^{3+} tetrahedra for any y variation, this variation of oxidation degree should be effective in the trimeric units.
- According to neutron diffraction, the oxygen vacancies are distributed on cubic and hexagonal layers of the trimers with a preference for h-layers.
- For steric reasons ($r_{\text{Cl}} > r_{\text{F}}$), an important distortion of the tetrahedra is observed in the F-rich area due to off-centring of the oxygen corners of the $[\text{BaOX}]$ layers. It is at the origin of the magnetocrystalline anisotropy change for the F ($y=1$) compound in which moments are aligned in the (a,b) plane. However for $y=0.8$, the magnetic anisotropy involves moment aligned along c , similarly to all of the related compounds.
- The magnetic structures systematically show weak or null (ordered components of) moments in the trimeric units. It arises from a combination of effects (low spin $\text{Co}^{3+}/\text{Co}^{4+}$ octahedral configuration, direct exchange through strong electronic delocalization, local magnetic disorder due to in-plane frustration between the trimers). Then the magnetic ordering is driven by the alignments of the tetrahedral pairs through disordered-FM connectors (i.e. through trimeric units).
- This latter frustration is at the probable origin of the strong peak often observed below T_N (centred around 40K) and assigned to in-plane fluctuation. This phenomenon is limited by the application of a high magnetic field. In the $y=1$ (F) case,

the in-plane alignment of the moments is at the probable origin of the weak-fluctuation.

- Trimer Cl-F mixed compounds display a n-conductivity (electrons carriers, negative Seebeck coefficient). Then, the progressive reduction upon F incorporation would likely increase the concentration of carriers and then increase the conductivity (or decrease the resistivity). We will detail these results in the next section, by comparison with tetramer compounds.

3.4.2. 6H (tetramer) Cl – F solid solution

The $\text{Ba}_6\text{Co}_6\text{Cl}_{1-y}\text{F}_y\text{O}_{16-\delta}$ solid solution was already briefly investigated by M. Kauffmann and G. Ehora in recent theses manuscripts (*Kauffmann2007c*, *Ehora2007b*). We will only recall the most important observations available for this case of mixed Cl – F tetrameric compounds and will also present new insights after my personal work. First one should recall that these compounds are prepared at 900°C and slowly cooled. This lower temperature compared to the previous trimeric case involves a possible better control of the final X stoichiometry. Generally, we also already discussed the greater mean Co valence in the tetramers ($\sim\text{Co}^{+3.37}$) compared to the tetramers ($\sim\text{Co}^{+3.24}$).

3.4.2.a) Powder XRD analysis and lattice parameters evolution

The powder XRD patterns of the investigated terms ($y=0$ to 1) show pure samples (Fig.3-15, (a) and (b)). In Fig.3-15, (c) an example of pattern matching for $y=0.5$ is given. Like in the previous trimeric case, the refined lattice parameters show a decrease of only the c parameter directly related to the replacement of Cl by F (Fig.3-15, (d)). The cell parameters and oxidation degrees determined by iodometric titration are gathered in Table 3-7.

A diminution of the mean cobalt oxidation degree as y increase can be observed. Then we stand in a comparable situation as the trimeric case, and one

could expect a similar increase of X (in the [BaOX] layers) and O vacancies (in hexagonal and cubic [BaO_{3-x}] layers) while F is introduced.

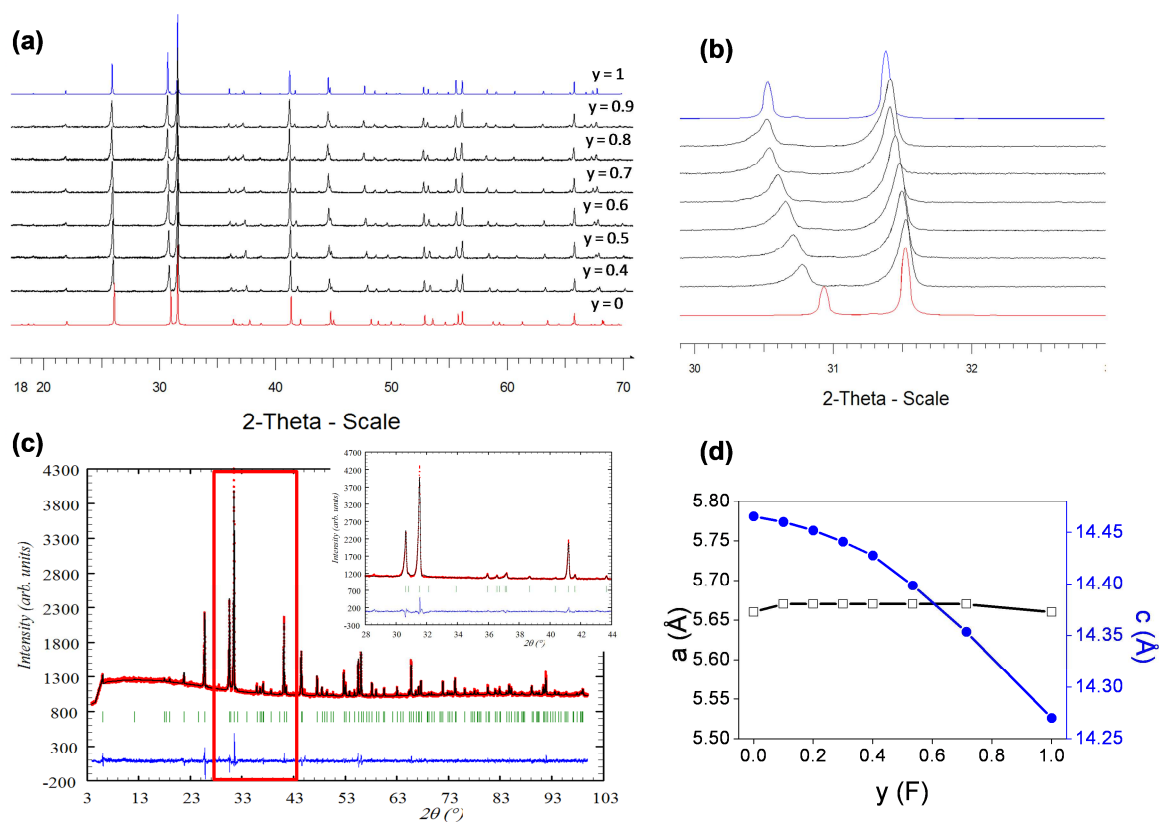


Fig.3-15: (a) X – ray powder patterns of $Ba_6Co_6Cl_{1-y}F_yO_{13-\delta}$, (b) zoom on (110); (c) pattern matching for $y = 0.5$ with zoom; (d) unit cell parameters evolution

Table 3-7: Lattice parameters and iodometric titration results for $Ba_6Co_6Cl_{1-y}F_yO_{16-\delta}$

y	Lattice parameters (Å)	Iodometric titration oxidation degree, oxygen content
0	$a = 5.66, c = 14.46$	+3.37, 15.61
0.1	$a=5.670(1), c=14.459(4)$	
0.2	$a=5.668(1), c=14.451(4)$	+3.34, 15.51
0.3	$a=5.669(7), c=14.443(4)$	
0.4	$a=5.671(1), c=14.431(4)$	
0.5	$a=5.670(1), c=14.392(4)$	+3.30, 15.41
0.6	$a=5.660(1), c=14.350(4)$	+3.27, 15.29
1	$a = 5.66, c = 14.27$	+3.25, 15.24

3.4.2.b) ^{19}F NMR

In earlier works, ^{19}F solid state NMR technique was used to confirm the incorporation of F only in the [BaOX] layers in the $\text{Ba}_6\text{Co}_6\text{Cl}_{1-y}\text{F}_y\text{O}_{16-\delta}$, Fig.3-16 (b). The single isotropic resonances validate the structural hypothesis of the statistic occupation of F/Cl on one single site ([BaOX] layers). Note also that the large number of spinning sidebands noted with * indicate F – Co_{para} magnetic interactions. The rather broad peaks are due to this paramagnetic effect and may also denote the possible off-centring of F around its ideal position. At least, to our opinion F presence in [BaO₃] layers is refuted, since it would probably lead to strongly different chemical shifts.

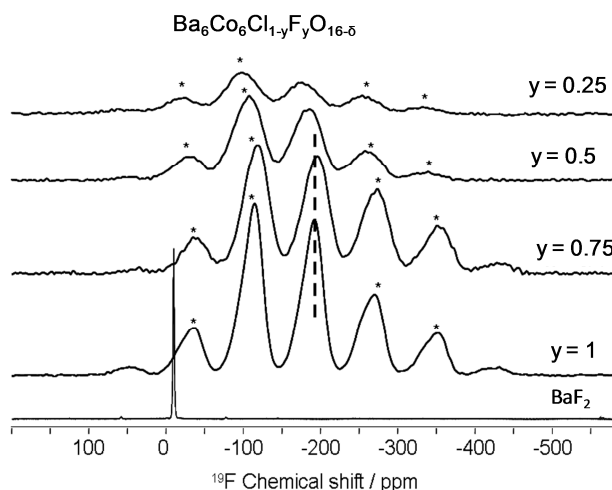


Fig.3-16: ^{19}F RMN spectra for the $\text{Ba}_6\text{Co}_6\text{Cl}_{1-y}\text{F}_y\text{O}_{16-\delta}$

3.4.2.c) Magnetic properties

The members of this series are AFM similarly to all the compounds described so far, with relative low Néel temperatures (between 125K – 150K) (Table 3-8). The $M = f(\mu_0 H)$ at 5K show no opening for $y = 0.2$, and 0.8 suggesting a well-respected AFM ordering below T_N (Fig.3-17, (a)). The effective magnetic moments values are given in Table 3-8. We have two sets of magnetic characterizations (Fig.3-17, (b) and (c)), the first one recorded under $H = 1000$ Oe using a VSM (IEMN), the second one under $H = 10000$ Oe using the extraction method (Maglab EXA 9T, UCCS). The more recent set of data (at 0.1T) was collected in order to

avoid any erroneous conclusions from the high-field data set. Indeed we have seen in the trimeric case that the $M(\mu_0H)$ plots are not systematically linear (\rightarrow change between the low-field and high-field regimes). However both datasets are in good agreement, as expected from the linear $M(\mu_0H)$ plots systematically observed at low temperature and shown in (Fig.3-17, (a)).

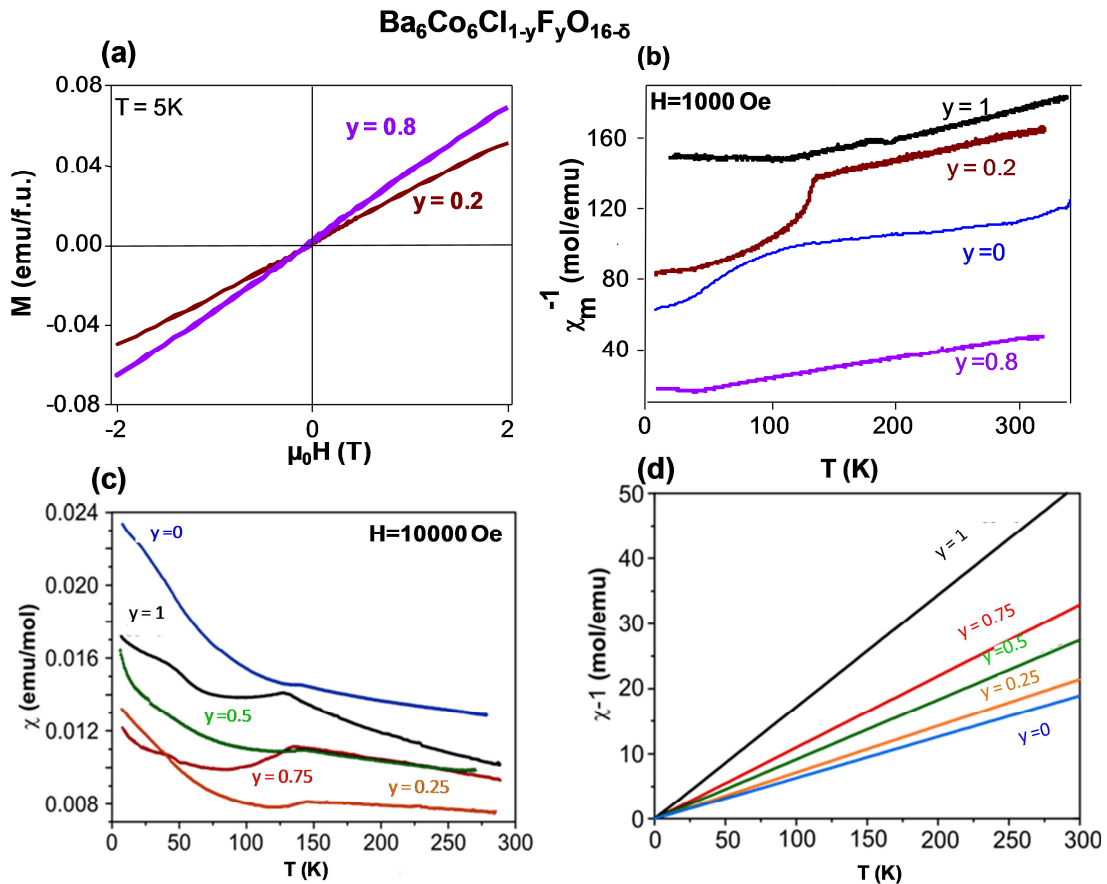


Fig.3-17: (a) $M(\mu_0H)$ at $T=5K$ for $y = 0.8$ and $y = 0.2$; (b) $\chi^{-1}(T)$ at $H=1000$ Oe (VSM (IEMN)) for $y = 1, 0.8, 0.2,$ and 0 ; (c) $\chi(T)$ at $H=10000$ Oe (Maglab EXA 9T, UCCS) for $y = 1, 0.75, 0.5, 0.25, 0$; (d) $\chi^{-1}(T)$ at $H=10000$ Oe corrected from θ_{CW} showing an increase of the slope with y value

If on one hand, no clear change can be deduced from the $\chi(T)$ plots ((Fig.3-17, (c))), on the other hand, the linear dependence of the effective magnetic moments with the F/Cl ratio (Fig.3-17, (d)) is more instructive. In this figure, for an easier direct comparison of the idealized plots, $\chi^{-1}(T)$ are corrected from the Curie-Weiss temperature. It pictures a strong dependence of μ_{eff} as a function of y , see Table 3-8 since the slope of the lines evolves with the substitution ratio (progressive

passage from $\mu_{\text{eff}}=11.2$ ($y=0$) to 6.8 ($y=1$)). Concerning the electronic configuration of the different compounds, the only clear assignment concerns $\text{Co}^{3+}_{\text{HS}}$ in the tetrahedra, while in the tetrameric units the distribution is more or less confusing, similarly to what was observed in the trimeric case. Even if several models can be proposed an overview of all the related systems do not lead to an unified charge distribution model and once again, we could conclude that tetramers have a tendency for LS configurations within a strongly delocalized mixed Co^{3+} - Co^{4+} valence. However, the progressive passage from $\mu_{\text{eff}}=11.2$ ($y=0$) to 6.8 ($y=1$) questions about a particular phenomenon. We recall that such evolution was not observed for mixed Cl/F trimeric compounds. To explain this evolution, by analogy of effect of high pressure on spin transition (*Vanko2006, Langsdorf2007*), we propose a model of chemical pressure.

Table 3-8: Susceptibility and neutrons diffraction information for $\text{Ba}_6\text{Co}_6\text{Cl}_{1-y}\text{F}_y\text{O}_{13.5}$

y	Magnetic susceptibility			Neutron diffraction		
	μ_{eff} ($\mu\text{B}/\text{f.u.}$) (H(Oe))	θ_{CW} (K) (H(Oe))	T_{N} (K)	MCo1 ($\text{Oh}_{\text{marginal}}$)	MCo2 ($\text{Oh}_{\text{central}}$)	MCo3 Td
0	11.26 (10^4) /11.04 (10^3)	-986(10^4) /-970(10^3)	135	0	0	2.99(7)
0.2	10.22 (10^3)	-766 (10^3)	134			
0.25	10.15 (10^4)	-760 (10^4)	142			
0.5	9.18 (10^4)	-866 (10^4)	140			
0.75	8.54 (10^4)	-670 (10^4)	132			
0.8	8.38 (10^3)	-710 (10^3)	130			
1	6.82 (10^4) /6.85 (10^3)	-311 (10^4) /-329(10^3)	126	0	0	2.5(7)

- A possible chemical pressure effect:

As already pointed out, we can deduce that the evolution of μ_{eff} mainly concern the octahedral sites with a tendency to go from a mixed HS/LS configurations ($y=0$) to LS configurations ($y=1$) in the trimeric units. Note that the weak change of mean Co oxidation ($\text{Co}^{+3.37}$ for $y=0$ while $\text{Co}^{+3.25}$ for $y=1$) can also contribute to the lowering of μ_{eff} , but this effect is too low to fully justify this change from only $\text{Co}^{3+}/\text{Co}^{4+}$ redistribution. We propose therefore a scheme based on indirect

chemical pressure effect, see Fig.3-18. According to our model, F^- within $[BaOX]$ layers would create a more closed-contact between the terminal octahedral sites (4.67\AA) and the Ba (Ba1) at their vertices, will push on them, increasing the pressure seen by these marginal octahedra. For largest Cl species in the layer, the largest hexagonal interleave (4.84\AA), allows a structural relaxation of the terminal octahedral Co-O bonds and thus a lowest internal pressure. We propose that this pressure effect would be responsible of local HS-configurations in presence of Cl.

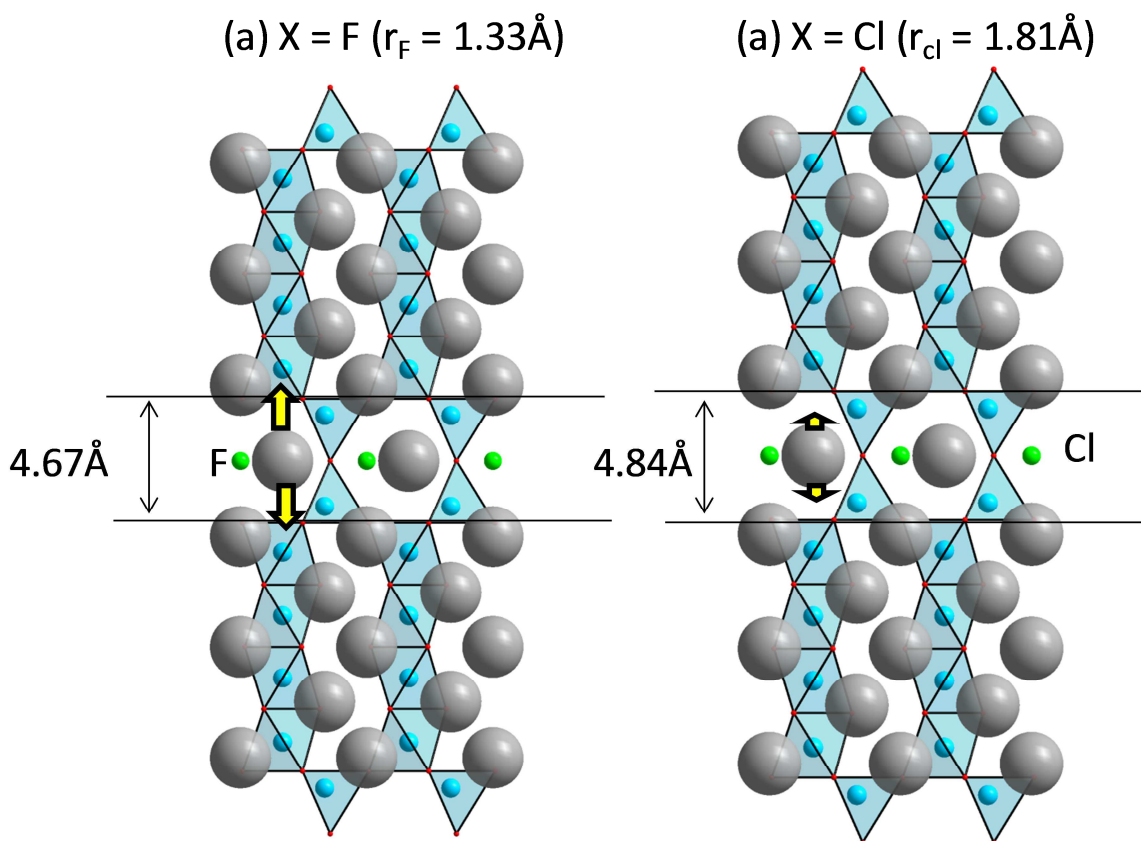


Fig.3-18: Mechanism of possible chemical pressure proposed as responsible for the monotone evolution of magnetic susceptibility with F/Cl ratio in $Ba_6Co_6Cl_{1-y}F_yO_{13-\delta}$

A quantification appears rather ambitious, but this effect would be inversely proportional to the c parameter, considering that the c -elongation relaxes the blocks interface at both sides of the h - $[BaOX]$ interface. This same effect was not observed for the trimeric compound. To explain this fact, we can argue that, probably the compressibility of the tetramers is much more efficient than the compressibility of the trimers. Also, in the tetrameric compounds the magnetic structure of the end-

members (Cl/y=0 and F/y=1) did not show any local ordered moments on the octahedral sites (see Table 2), contrarily to the weak moments for the trimers (see section 3.4.1.e) , Page 135). This could denote a greater chemical pressure effect effective for the full $\text{Ba}_6\text{Co}_6\text{Cl}_{1-y}\text{F}_y\text{O}_{13-\delta}$ solid solutions, and even more great at the F-rich side.

3.4.2.d) Transport properties:

The DC-resistivity of several terms of the solid solution was measured by the 4-probes method in the “Materials and method” section. All compounds are semi-conductors and similarly to the observations on the trimeric Cl–F solid solution, a decrease of the resistivity with the increase of y (F) is observed (Fig. 3-19, (a)). Then the latter explanation of the influence of the unit-cell shrinking towards a better conductivity (improved orbital overlapping) is still a predominant feature. However, in this system the evolution from one compound to another is less pronounced for instance around RT all compounds show in resistivity of the same order of magnitude. Here measurements of the Seebeck coefficient for the y=0 term, $\text{Ba}_6\text{Co}_6\text{ClO}_{16-\delta}$ show a positive sign of the thermoelectric power which involve a p-type conductivity (Kauffmann2007c, (Fig. 3-19, (b))).

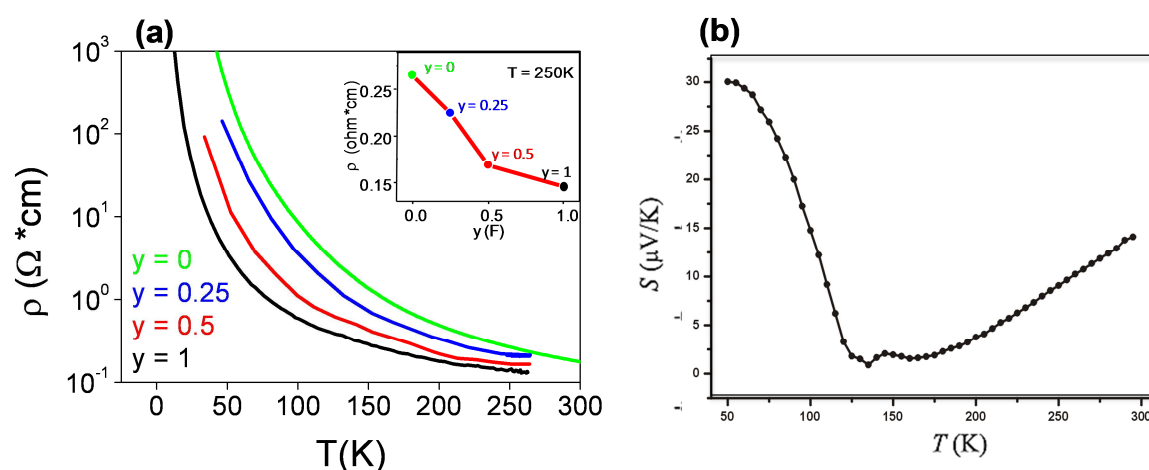


Fig.3-19: (a) Resistivity evolution for $\text{Ba}_6\text{Co}_6\text{Cl}_{1-y}\text{F}_y\text{O}_{16-\delta}$ solid solutions (logarithmic scale); (b) Seebeck coefficient thermal evolution for $\text{Ba}_6\text{Co}_6\text{ClO}_{16-\delta}$ from (Kauffmann2007c)

Two conclusions follow:

- The trimeric (10H) system (more reduced) shows an electronic conductivity (the charge carriers are the electrons (*Wang2009*)), while tetrameric compounds (more oxidized) show a hole-conductivity. Then, despite the strong structural similarities, these two system-types are to be considered differently at two distinct areas of an electronic phase diagrams.
- For both samples the conductivity is higher for smaller unit-cell volumes which involve better orbital overlappings. But the reduction observed with increasing y , increases the carrier concentration for the trimeric n-type system, while it decreases it in the p-type tetrameric system. This feature could explain the smallest evolution of $\sigma(y)$ in the latter, since the volume evolution and carrier concentration play against each others, Fig. 3-20. One more time, the redox effect plays an important role in the understanding of the complex behavior of these compounds.

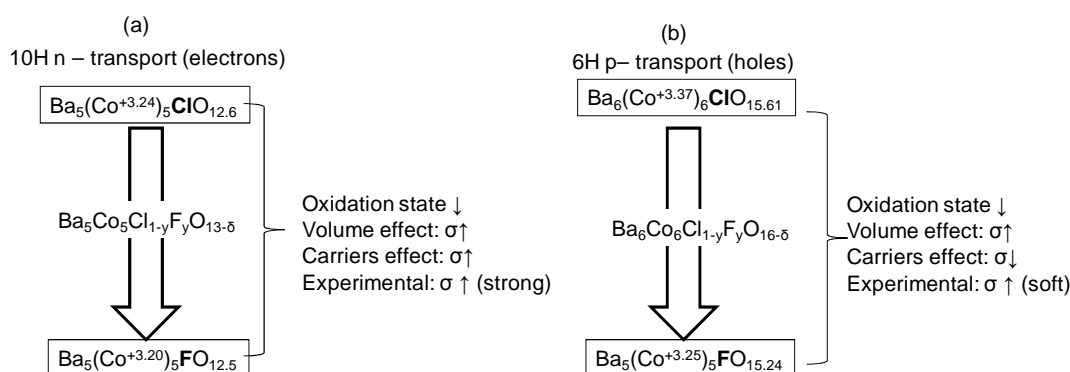


Fig.3-20: Schematic representation of transport properties modification in (a) 10H- $Ba_5Co_5Cl_{1-y}F_yO_{13-\delta}$ ($y = 0-1$) polytypes and (b) 6H- $Ba_6Co_6Cl_{1-y}F_yO_{16-\delta}$ polytypes

3.4.2.e) Conclusion in few points:

- The cell evolution parameters for $Ba_6Co_6Cl_{1-y}F_yO_{16-\delta}$ solid solution (as for $Ba_5Co_5Cl_{1-y}F_yO_{13-\delta}$) respect the expected behaviour, c parameter decreasing with the introduction of F in the structure.

- While, in the $Ba_6Co_6Cl_{1-y}F_yO_{16-\delta}$ solid solution case, **the linear evolution of the μ_{eff} can be attributed to the increase of the compressibility of the**

octahedral-tetramer with the shrinking of the c parameter (chemical pressure effect), in the $\text{Ba}_5\text{Co}_5\text{Cl}_{1-y}\text{F}_y\text{O}_{13-\delta}$ case, the non – linear dependency is not well understood.

• In $\text{Ba}_6\text{Co}_6\text{Cl}_{1-y}\text{F}_y\text{O}_{16-\delta}$ solid solution (more oxidized) a p –type conductivity (charge carriers are holes) is measured. The reduction observed as Cl is replaced by F implies thus an increase of the holes concentration and as outcome, the resistivity is still controlled by the unit cell volume but decreases less efficiently with the F/Cl ratio. Contrarily, in the $\text{Ba}_5\text{Co}_5\text{Cl}_{1-y}\text{F}_y\text{O}_{13-\delta}$ case (more reduced), the transport is n–type (carriers are electrons) and, in consequence, the reduction observed from Cl to F is decreasing the number of n- carriers determining the drastic decrease of the transport.

3.4.3. $\text{Ba}_5(\text{Co}, \text{Pt})_5\text{BrO}_{13-\delta}$

In this section, a new term of the $\text{Ba}_{n+2}\text{M}_{n+2}\text{XO}_{3n+4}$ (M=Co, Pt) series, namely the 10H (n=3, trimer) with X=Br, will be introduced. The synthesis is given in section 3. 3. (Page 123). The structure is similar to the 10H structure of $\text{Ba}_5\text{Co}_5\text{ClO}_{13}$ or $\text{Ba}_5\text{Co}_5\text{FO}_{13}$. However the incorporation of large Br- anions ($r= 1.96\text{\AA}$, (Shanon1976)) in the hexagonal [BaOX] layers is at the basis of strong atomic shifts, that will be discussed. Our analysis results from crystallographic characterisation by single crystal XRD. It is noteworthy that until the evidence of this new compound, two series of halides were distinguished (Fig.3-21):

a) F and Cl that likely integrate the [BaOX] layers individually or concomitantly, as intensively discussed in the two previous sections (Fig.3-21, (a))

b) Br- which has been exclusively located in double $[\text{Ba}_2\text{O}_2\text{Br}]$ spacers after the preparation of Br-containing related compounds (Kauffmann2007b, Kauffmann2007c): 14H- $\text{Ba}_7\text{Co}_6\text{BrO}_{17-\delta}$ and 18R- $\text{Ba}_6\text{Co}_5\text{BrO}_{14-\delta}$ (Fig.3-21, (c)).

Particularly, one should mention that our attempts to prepare mixed Br/F and Br/Cl compounds systematically led to Br-only and F/Cl-only phase segregation. For instance, the sample formulated $\text{Ba}_6\text{Co}_6\text{Cl}_{1-y}\text{Br}_y\text{O}_{16-\delta}$ lead to a mixture of the 6H- $\text{Ba}_6\text{Co}_6\text{ClO}_{16-\delta}$ and 14H- $\text{Ba}_7\text{Co}_6\text{BrO}_{17-\delta}$ for $y = 0.1$, with no deviation of the c -lattice parameters. It is such that, if possible, the 6H-cobalt polytype could incorporate less than 10% of Br.

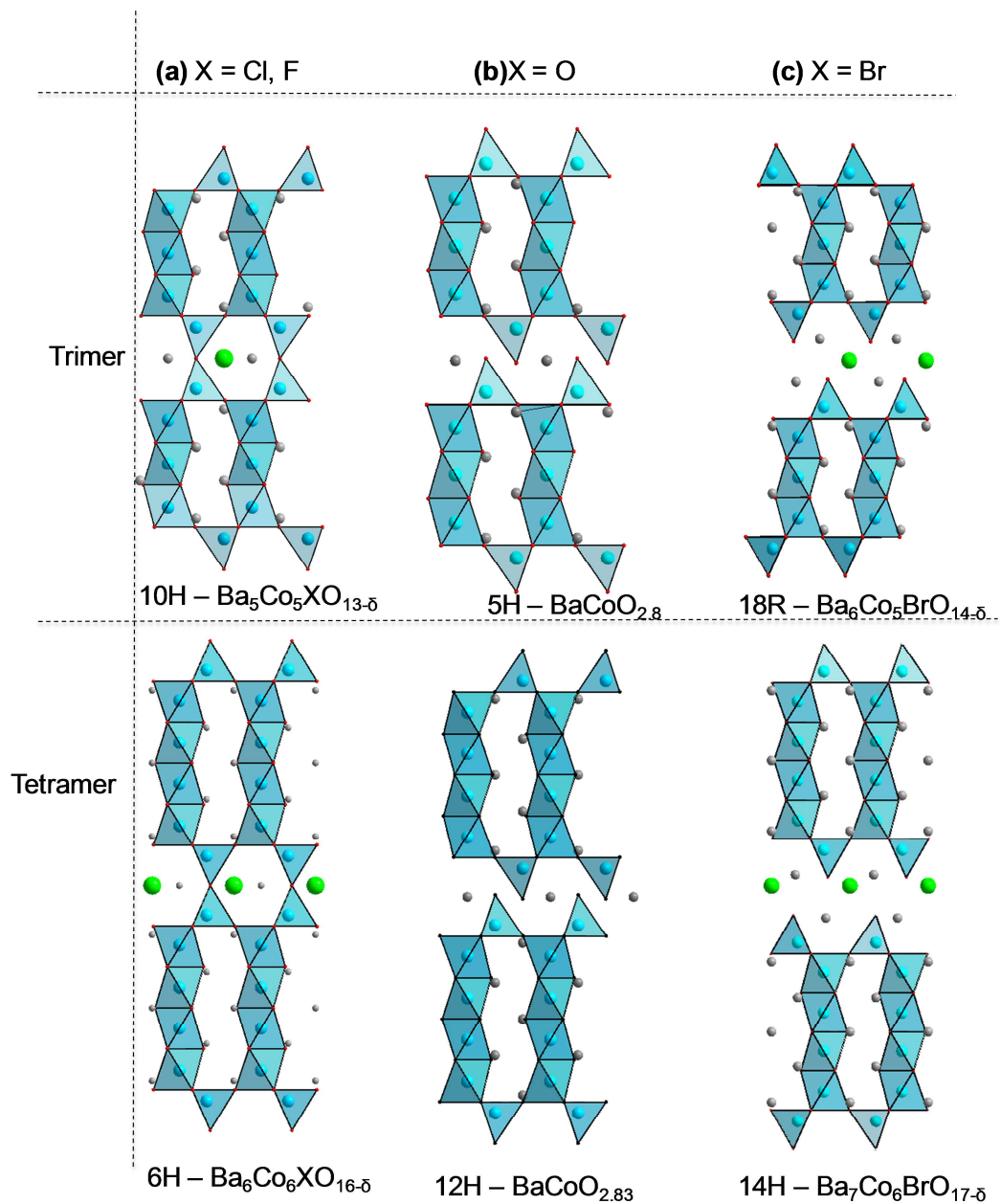


Fig.3-21: The two series of halides observed until now and they relation with the 5H and 12H-BaCoO_{3.5} oxides

3.4.3.a) Structural analysis by X – ray diffraction

Black crystals were obtained by the procedure described in section 3. 3. (Page 123). One suitable crystal was collected following a strategy based on ψ and ω scans (see 3. 6. Supplementary information). The spots were indexed with respect of the $P6_3/mmc$ hexagonal symmetry ($a=5.727(1)$ Å and $c=24.922(3)$ Å). The symmetry is the same than for the trimer Cl or F compounds, but with a larger cell (compared to $a=5.66$ Å both for Cl as for F trimers, and $c=24.3$ Å for Cl, 23.7 Å for F). The structure was solved and refined using JANA 2006 package (*Petricek2006*). It is formed by face sharing octahedral trimers and corner sharing tetrahedra corresponding to the trimer structures already intensively discussed. As evoked, this is somehow interesting, since up to now, all attempts to synthesize bromine compounds lead to disconnected trimeric or tetrameric blocks with $[Ba_2O_2Br]$ layers or $Ba_2Co_4BrO_7$ compounds with a central CdI_2 layer presented later in this manuscript (see section 3.5.1. (Page 159)).

In order to match a correct refinement we considered mixed Pt–Co sites. Here platinum comes from the platinum crucible used for synthesis. Note that, in this series, other examples of Pt introduction after reaction with the crucible have been reported in the past for $X = Cl$ trimeric compounds with Fe and Co, namely $Ba_5(Fe, Pt)_5ClO_{13}$ and $Ba_5(Co, Pt)_5ClO_{13}$ series (*Tancret2004*). In the current case the refined formula is $Ba_5Co_4Pt_1BrO_{13.5}$. We emphasize that all attempts to synthesize the pure powder corresponding to this compound, by the introduction of the Pt as reactant, lead to failures regarding either the Pt incorporation in the compound, nor the obtaining of 10H polytypes.

a. Cationic and charge distribution

The cationic distribution refined from single crystals X – ray data based on the different atomic numbers Z of Co and Pt lead to the following distribution: 27%Pt/73%Co for the marginal octahedra, 47%Pt/53%Co in the central octahedron, and 100%Co in the tetrahedra (Fig.3-22). Similar cationic distribution was observed for $Ba_5Co_{3.92}Pt_{1.08}ClO_{13}$ and $Ba_5Co_{4.028}Pt_{0.972}ClO_{13}$ (*Tancret2004*) given in Table 3-9.

Table 3-9: Refined cationic distribution of the title compound compared with Co – Pt halides from the literature (Tancret2004):

compound	(Oh_{marginal})	(Oh_{central})	(Td)
$Ba_5Co_4Pt_1BrO_{13-\delta}$	27%Pt/73%Co	47%Pt/53%Co	100%Co
$Ba_5Co_{4.028}Pt_{0.972}ClO_{13}$	25%Pt/75%Co	48%Pt/51%	100%Co
$Ba_5Co_{3.92}Pt_{1.08}ClO_{13}$	22%Pt/78%Co	65%Pt/35%Co	100%Co

Note that the Pt^{4+} location in the octahedra is fully compatible with a mixed M^{3+}/M^{4+} mixed occupancy in the linear units, while the hypothesis of terminal tetrahedra with Co^{3+} remain valid. Based on these observations, we can propose the following formula: $Ba^{2+}_5 [(Co^{3+})_2](Td) [(0.73Co^{3+}/0.27Pt^{4+})_2](Oh_{\text{marginal}})[(0.53Co^{3+}/0.47Pt^{4+})](Oh_{\text{central}}) Br^- O^{2-}_{12.505}$

b. Metal – Metal and Metal – Oxygen distances

The refined M – M and M – O distances for $Ba_5(Co,Pt)_5BrO_{13-\delta}$ are given in Fig.3-22 as well as those of $Ba_5Co_5ClO_{13-\delta}$ and $Ba_5Co_5FO_{13-\delta}$, given for comparison.

Octahedral sites: in the title compound, the most affected intermetallic distance is between $M(Oh_{\text{central}})$ and $M(Oh_{\text{marginal}})$ (2.59 Å for Br, 2.50 Å for Cl, and 2.49 Å for F) (Fig.3-22). This larger distance can be attributed to the Pt insertion in the central (47%) and marginal (23%) sites, the ionic radius for Pt^{4+} in coordination VI being 0.625Å compared to 0.545Å for Co^{3+}_{LS} and 0.61Å Co^{3+}_{HS} in the same coordination (Shannon1976). A similar effect is observed for M – O distances (Fig.3-22), with (Pt/Co)-O distances close to 1.97 Å, as already observed for other mixed Co/Pt compounds (ex $M2-O2= 1.981(4)$ Å in $Ba_5Co_{3.92}Pt_{1.08}ClO_{13}$, Tancret2004).

Tetrahedral site: Since the single crystal refinement clearly ruled out the presence of Pt in this position, the modification of the Co – Co and Co – O distances in the dimers can be attributed to a pure steric effect related to the introduction in the [BaOX] layer of a larger anion (r_{Cl} in a VI configuration 1.81Å compared to $r_{Br}=1.96$ Å in the same configuration, (Shannon1976)). Clearly, this effect mainly involves the Co3-O3 distance along c due to the dilatation of the hexagonal-interleave.

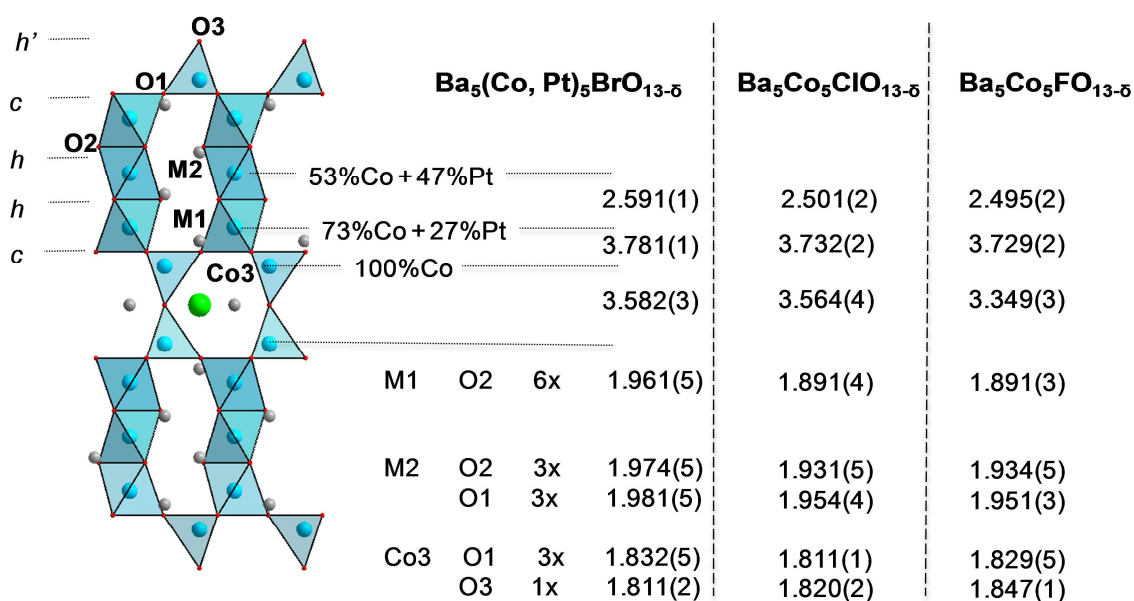


Fig.3-22 : Metal – metal and metal - oxygen distances in $Ba_5(Co, Pt)_5BrO_{13-\delta}$, $Ba_5Co_5ClO_{13-\delta}$ and $Ba_5Co_5FO_{13-\delta}$. The structure, atoms labeling and the description of the structure in terms of c, h and h' layers is recalled.

- Distortion of the Co_2O_7 units; towards an ideal structure

The structural characteristic of the trimeric cobalt oxo - halides in function of X nature are given in Fig.3-23. We have seen that in the F case, on one part, the small anionic radius of F will allow a larger off – centring of the O3 in the [BaOX] layer. In the 0.5F/0.5Cl and 1Cl cases (given as example in Fig.3-23), a larger mean anionic size increases the Co-O-Co angle of the tetrahedral dimers (reducing the off-centring of O3). A new increase of the halogen anionic radius in the h' – [BaOX] layer should lead to an ideal structure with Co-O-Co angle of 180°. In the Br case, this angle is 163° which represents the most regular Co_2O_7 units ever displayed in these series, most probably due to the large Br- anions.

- Halides environment - Ba5 pyramid

The large Br anion force the vertical displacement of the Ba1 positioned at the vertices of the XBa_5 bipyramid ($d_{Ba1-F}=2.66\text{Å}$, $d_{Ba1-Cl}=2.94\text{Å}$ and $d_{Ba1-Br}=3.04\text{Å}$, Fig.3-23). We think that only greatest M-O distances within the octahedra (i.e. the effect of Pt incorporation in the octahedra) can accommodate such a displacement of this barium atom out of its ideal [BaO₃] layer. One should

recall here that, despite numerous attempts, it has not been possible to incorporate Br in the Co-only 6H and 10H-polytypes, all attempts leading to stabilisation of disconnected oligomers (Kauffmann2007b, Kauffmann2007c).

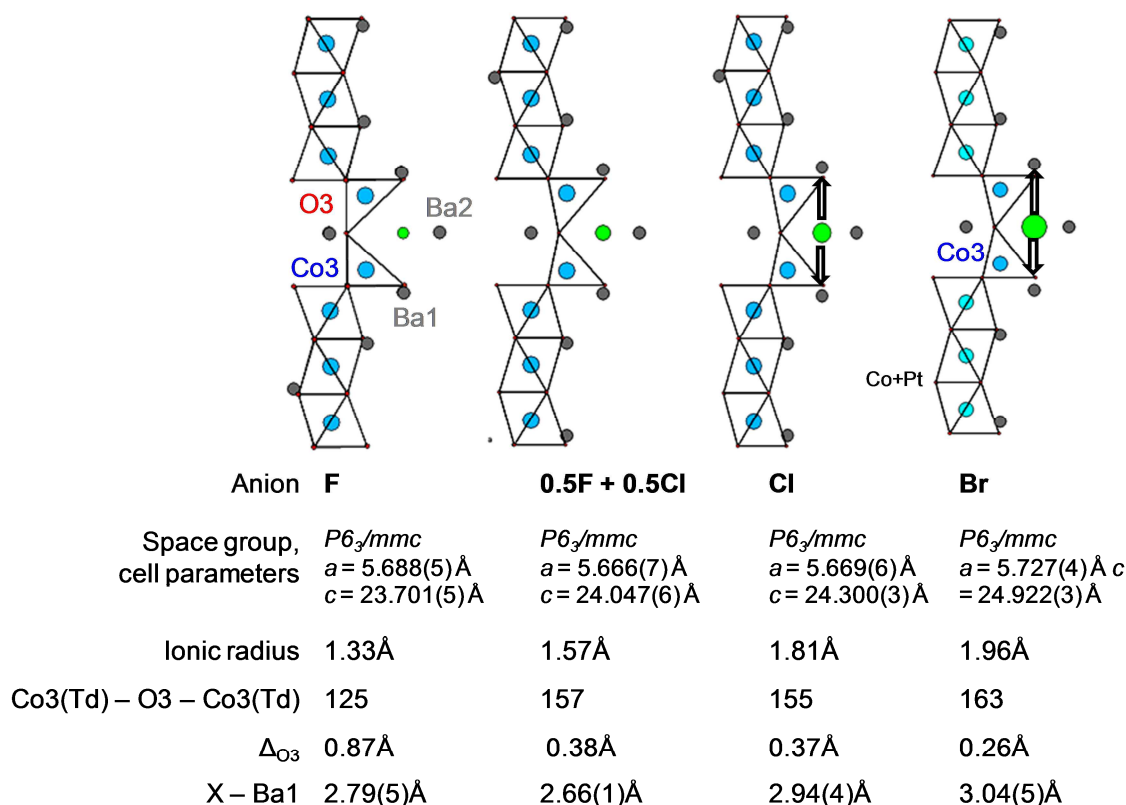


Fig.3-23: Summary of main structural characteristics regarding tetrahedral dimers distortion of the F, Cl/F (as example is given $y = 0.5$), Cl and Br trimer structures.

3.4.3.b) Conclusion in few points:

- The originality of $Ba_5Pt_1Co_4BrO_{13-\delta}$ compound lies in the unique presence of Br anions in the h' - [BaOX] layer. This original layer for Br is probably made possible by the concomitant incorporation of Pt in mixed octahedral Co/Pt sites.
- The large anionic radius of the Br reduce the tetrahedral dimer distortion by reducing the off – centring of the oxygen in the h' - [BaOX] layer.
 - As expected for platinum, the presence of Pt^{4+} was detected only in mixed octahedral sites while the tetrahedra are solely occupied by Co
 - The charge distribution proposed considering only Co^{3+} by analogy to $Ba_6Mn_2Co_4ClO_{16-\delta}$ is:



3. 5. Compounds with carbonate groups

3.5.1. Case of carbonate groups as inter – block separators

We have introduced the potentialities offered by the disconnection between structural units for magnetic specificities such as metamagnetic properties. A series of compounds with formula $Ba_2Co_4XO_7$ ($X = Cl, Br$) suitable for this concept were isolated and characterized by Kauffmann *et al* (Kauffmann2007). During our syntheses we also obtained crystals of these compounds which have been more accurately re-characterized. The structure and magnetic properties were reinvestigated and the new results will be presented in this section.

In 2006, Sun *et al* have reported the existence of a barium cobaltite series corresponding to the $[BaCoO_3]_n[BaCo_8O_{11}]$ intergrowth-family, in which $Ba_2Co_9O_{14}$ (Sun2006, Ehora2007a) and $Ba_3Co_{10}O_{17}$ (David2011) correspond to the $n = 1$ and $n=2$ terms, respectively. The compound $Ba_6(Co,Ga)_{13}O_{26}$ (Pelloquin2007) corresponds to the $n= 5$ term, but Ga-doped. As evidenced by their general formula, the structures can be described as intergrowth between perovskite blocks and the original $[BaCo_8O_{11}]$ unit which contain central $[CoO_2]$ layers (CdI_2 -type) and terminal CoO_6 octahedra and CoO_4 tetrahedra. The $n = 1, 2$ and 5 terms are shown on the (Fig.3-24, (a), (b), (c)). The CoO_2 layers could be at the origin of interesting properties since they are also present, for example, in the misfit layered cobaltites series $[Ti_{1-x}Sr_{2+x-y}Co_yO_3][CoO_2]_z$ (Maignan2002) and seem to be responsible for the very interesting high thermopower and low resistivity properties, explaining the interest of this type of compounds.

In 2007, Kauffmann *et al* (Kauffmann2007b) reported the synthesis and structural characterization of the two isostructural oxy-halides cobaltites (Fig.3-24, (d)) presented in this chapter, which adopt hexagonal $18R$ structures. These structures, closely related to those observed by Sun *et al*, can be described by the stacking along $[001]$ of fluorite-type double layers $[Ba_2Cl_2]^{2+}$ or $[Ba_2Br_2]^{2+}$ and blocks $[Ba_2Co_8O_{14}]^{2-}$ also built up from CdI_2 -type oxide layers (Fig.3-24, (d)).

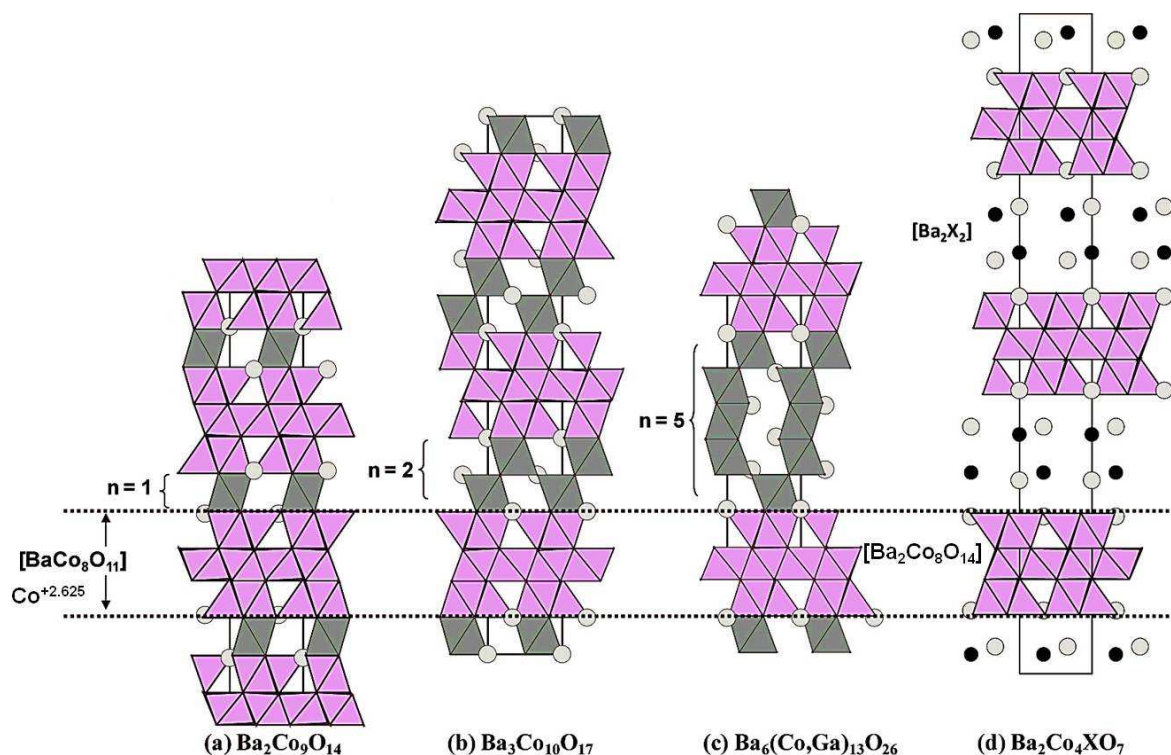


Fig.3-24: Barium cobaltite series corresponding to the $[BaCoO_3]_n[BaCo_8O_{11}]$ intergrowth-family (a) $Ba_2Co_9O_{14}$ (Sun2006, Ehora2007a), (b) $Ba_3Co_{10}O_{17}$ (David2011), (c) $Ba_6(Co,Ga)_{13}O_{26}$ (Pelloquin2007). The correspondence between the $[BaCo_8O_{11}]$ blocks from these compounds (with Co oxidation degree) and $[Ba_2Co_8O_{14}]$ form $Ba_2Co_4XO_7$ ($X = Br, Cl$) (d) (Kauffmann2007b) is also given.

Fig.3-24 displays the similitude between $[Ba_2Co_8O_{14}]^{2-}$ and $[BaCo_8O_{11}]$ blocks of the full-series. In the previous analysis of these two compounds, some disorder was observed in the layers between the structural blocks. In order to explore the real nature of this disorder, and since the presence of carbonates groups was already reported in the literature in the interleaves between the blocks in others hexagonal perovskites (even after a high temperature treatment) (Boulahya2002, Bréard2004), we used an Attenuated Total Reflectance (ATR) InfraRed Spectrometer on one Cl - sample that has allowed us to evidence the CO_3^{2-} group characteristic vibrational-bands. Using this information, the structural disorder observed by MEM was clearly related to the presence of such groups in the interleaves. Note that the results for only a Cl sample will be presented, but the

conclusions must be extended for the Br compounds also, since the disorder reported in Br compound seems similar to what is observed for the Cl one.

3.5.1.a) Carbonate presence investigation by infrared spectroscopy

ATR-IR spectroscopy was used (see Materials and method section) on grinded single crystals (XRD-checked) obtained as described in section 3. 3. , (Page 123). According to the literature (*Bréard2004*), the absorption band at 852 cm^{-1} corresponds to the characteristic $\pi(\text{CO}_3)$ bonding and indicates that the CO_3 groups are actually present in the heart of the crystallites (Fig.3-25). The band observed around 1450cm^{-1} corresponds to the $\nu_{\text{antisymmetric}}$ bonding, while the very small one observed at 1100 cm^{-1} to the $\nu_{\text{symmetric}}$ bonding.

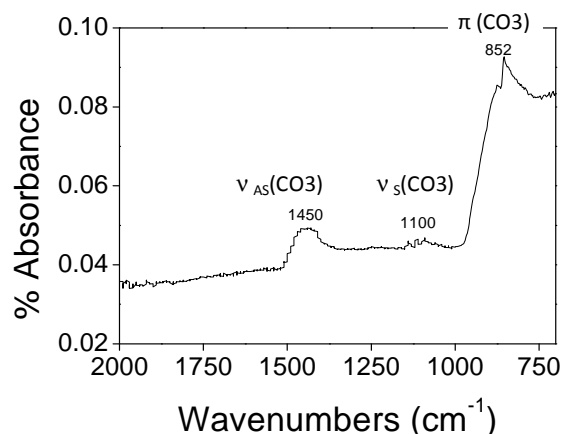


Fig.3-25: Infrared spectroscopy between 2000 and 1000 cm^{-1} showing the presence of $(\text{CO}_3)^{2-}$ groups

3.5.1.b) Structural analysis by single crystal XRD and MEM

A suitable crystal from a $\text{Ba}_2\text{Co}_4\text{ClO}_7$ preparation obtained as described in section 3. 3. , (Page 123) was mounted on a fiber glass and aligned on a XRD Bruker X8 Apex2 CCD4K diffractometer. The collection of intensities was performed at room temperature (λ -Mo K_α radiation) at a completeness of 99% up to $2\theta = 97.52^\circ$ following a strategy based on ω and ϕ scans. Intensities were corrected from absorption effects using a semi-empirical method based on redundancy. The intensities were indexed in the $R\bar{3}m$ space group with $a = 5.729(2)\text{ \AA}$ and

$c = 45.099(1)$ Å. The structure was solved by the direct methods, and least-squares refined with the JANA2006 Software package (Petricek2006).

The structure was previously described by *Kauffmann et al* as perovskite-related material with an 18-layers $[O_4]$, $[BaO_3]$ and $[BaX]$ ($X = Cl$ or Br) stacking along the c -axis. In the stacking sequence, two $[O_4]$ layers are sandwiched by two $[BaO_3]$ layers, leading to the creation of octahedral and tetrahedral sites where the cobalt atoms are located, blocks formulated $[Ba_2Co_8O_{14}]$, as previously discussed. In terms of the separation between the blocks, these were reported to be separated by double disordered fluorite-type $(Ba_2X_2)^{2+}$ layers. In this latter investigation, the maximum entropy based electron density maps around Cl atom attest the presence of a high density zone atom showing clearly the presence of $(CO_3)^{2-}$ groups. In the Fig.3-26, (a) we show the disordered layer (half of the double-layers) below the Co-O blocks and the corresponding MEM electronic density.

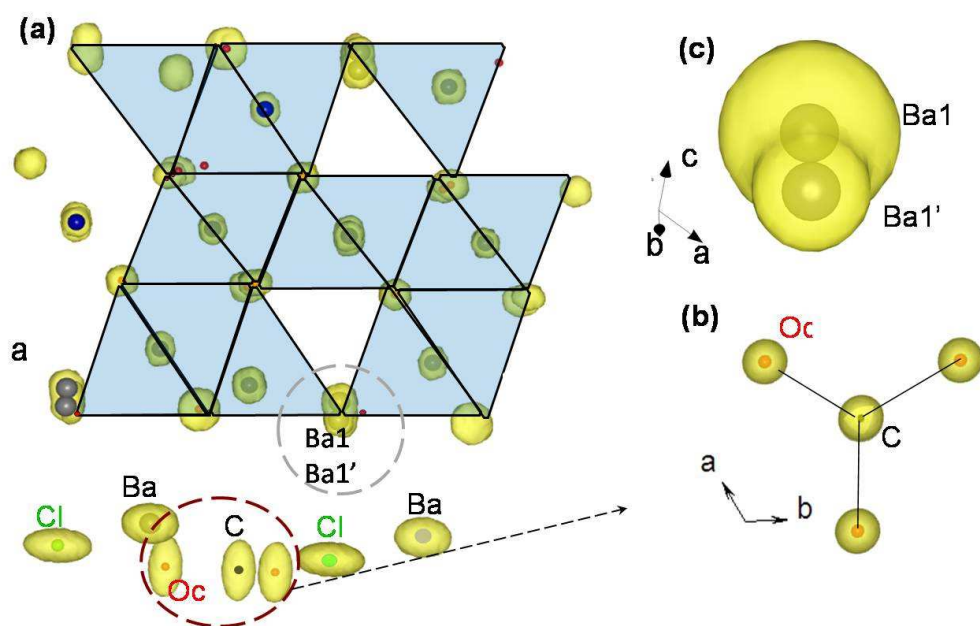


Fig.3-26 : (a) MEM map for $Ba_2Co_4(Cl, CO_3)O_7$ -compound, (b) MEM around Ba1 split and (CO_3) group.

It clearly evidences the location of $(CO_3)^{2-}$ anions (Fig.3-26, (b)). This disorder was then introduced in the refinement. The carbonate introduction seems to be highly significant since the R decrease from 4.43% to 3.47%. Note that, at the introduction of $(CO_3)^{2-}$ group in the refinement, several constraints must be imposed

as $ai[Oc] = 3 \times ai[C]$, otherwise said, for each C we have three O and $z[C] = z[Oc]$ (the C and its oxygens are at the same level, *i.e.* $(CO_3)^{2-}$ group is imposed to be planar. The refined formula is $Ba_2Cl_{0.87}(CO_3)_{0.13}Co_4O_7$. The electron density maps show also a zone of electron density at 0.31\AA from Ba1 corresponding to the split of this atom (Fig.3-26, (c)). This split can be correlated to the presence (or absence) of Cl^- anion above. Then a constraint was imposed that the Ba1/Ba1' ratio to be the same to the refined $87\%Cl/13\%(CO_3)^{2-}$ ratio. In conclusion, when the $(CO_3)^{2-}$ group is present, a 0.31\AA displacement of the Ba is observed. The corresponding C – O bonds lengths are 1.45\AA (1.43\AA for a C – O single bond) and the O – O distances are 2.17\AA .

3.5.1.c) Disorder rationalisation

From the disordered model presented in Fig.3-27 (a), several local scenarii can be proposed such as shown on Fig.3-27 (b) and (c) (carbonate and the associated Cl and Ba/Ba' occupancies), (d) (local absence of $(CO_3)^{2-}$).

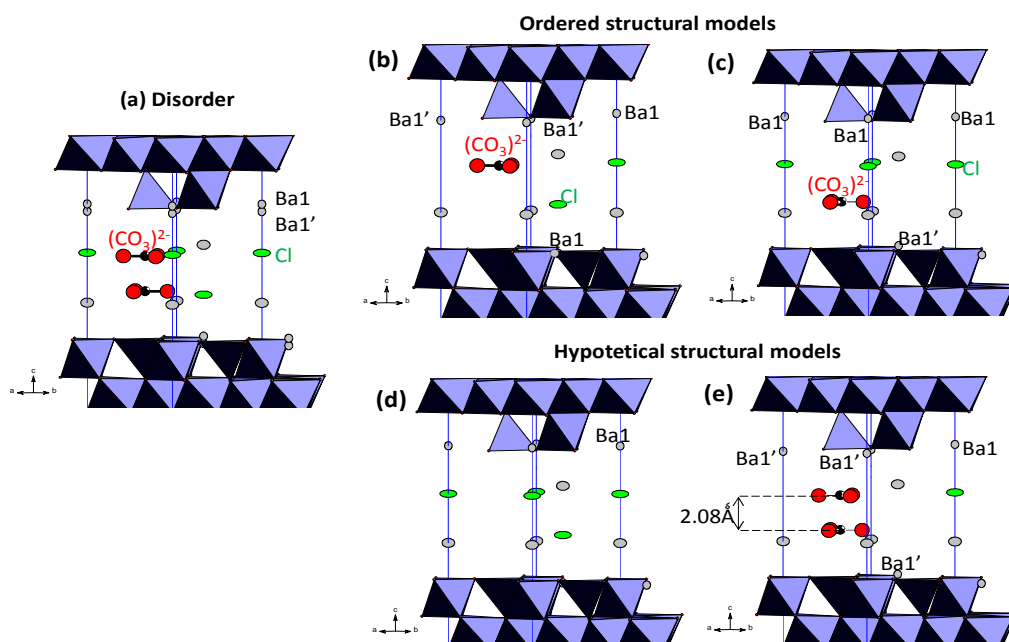


Fig.3-27. (a) Disorder observed in $Ba_2Co_4(Cl,CO_3)O_7$ compound. Rationalization of the disorder using hypothetical ordered structural models with carbonate ether in the first inter – block half – layer (b), ether in the second one (c). The corresponding split of the Ba1 is also given. The hypothetical limit members are given in (d) (local carbonate absence) and (e) with carbonate present in each of the two half – layers.

The Fig.3-27 (e) shows a hypothetical model with two superposed $(\text{CO}_3)^{2-}$ groups. This model cannot be fully refuted but appears unlikely in consideration of the short C – C distance of 2.08 Å along c, inappropriate for a non-bonding between the two C atoms.

3.5.1.d) Compound formulation and Co average charge

To formulate such kind of extended-defect structures, we set the limit members:

- in absence of any carbonates the crystal formula correspond to $\text{Ba}_2\text{Co}_4\text{ClO}_7$.
- in order to respect correct carbon-carbon distances, the maximal $(\text{CO}_3)^{2-}$ content would correspond to one-half-layer filled with $(\text{CO}_3)^{2-}$ groups while the superposed other half would be $(\text{CO}_3)^{2-}$ free. Then the formula is $\text{Ba}_2\text{Co}_4\text{Cl}_{0.5}(\text{CO}_3)_{0.5}\text{O}_7$. It corresponds also to the general assumption that if a Cl is present, a $(\text{CO}_3)^{2-}$ group cannot be simultaneously present, (this leading to the general $\text{Ba}_2\text{Co}_4\text{Cl}_{1-y}(\text{CO}_3)_y\text{O}_7$ formulation). The actual formula is refined to **$\text{Ba}_2\text{Cl}_{0.87}(\text{CO}_3)_{0.13}\text{Co}_4\text{O}_7$** .

The stacking is performed between $A^{\alpha+}B^{\alpha-}$, where A is $[\text{Ba}_2\text{Cl}_{2-2x}(\text{CO}_3)_{2x}]$ and B is $[\text{Ba}_2\text{Co}_8\text{O}_{14}]$. Since the refined number of $(\text{CO}_3)^{2-}$ is 0.13, the calculated $\alpha+$ charge is then +0.87. Consequently, the $[\text{Ba}_2\text{Co}_8\text{O}_{14}]$ balancing charge is -0.87 leading to mixed valence state of $\text{Co}^{+2.782}$. A small difference from the mean $\text{Co}^{+2.625}$ charge deduced from a $\text{Co}^{2+}/\text{Co}^{3+}$ charge ordered model in the similar blocks of $\text{Ba}_2\text{Co}_9\text{O}_{14}$ and $\text{Ba}_3\text{Co}_{10}\text{O}_{17}$ (Sun2006, Ehora2007a) can be observed permitting us to consider similar charge ordering.

3.5.1.e) Magnetic properties:

The magnetic structures of $\text{Ba}_2\text{Co}_9\text{O}_{14}$ and $\text{Ba}_3\text{Co}_{10}\text{O}_{17}$ are shown on the Fig.3-28 (a) and (b) respectively. Typically in both compounds the $[\text{BaCo}_8\text{O}_{11}]$ blocks show ordered $-\text{Co}^{2+}_{\text{HS}} (S=3/2)$ and $\text{Co}^{3+}_{\text{LS}} (S=0)$ such that individual blocks behave as ferrimagnets with a net moment of $\sim 3.8\mu\text{B}$ per $[\text{BaCo}_8\text{O}_{11}]$ sub-unit. Here we do not consider the magnetism of the perovskite connectors that are shown on grey on the Fig.3-28. Then in the compounds concerned here, the same disconnected blocks

could be considered as formed of interactions between such 2D-macrospins ($\sim 1.9\mu_B$ per $Ba_2Co_4(Cl,CO_3)O_7$), assuming a similar magnetic ordering within the blocks

Paramagnetic domain: This work was performed on a large single crystal ($m = 1.2\text{mg}$) in collaboration with Alain Pautrat from the CRISMAT. If one assumes a distribution of only magnetic HS Co^{2+} (1.5 per formula unit) in the blocks surrounded by diamagnetic LS Co^{3+} (2.5 per formula unit) as in the related compounds, the theoretical spin-only $\mu_{eff} = 2 \sqrt{S(S+1)} = 4.8 \mu_B/\text{f.u.}$ It is in relatively good agreement with the value μ_{eff} value fitted from a Curie-Weiss law between 300 and 100K considering a diamagnetic contribution ($\chi = \chi_{dia} + \frac{C}{T - \theta_{CW}}$) ($\mu_{eff} = 5.44\mu_B/\text{f.u.}$, $\theta_{CW} = 41\text{K}$, $\chi_{dia} = -0.00345\text{emu/mol}$), (Fig.3-29, (a), (b)). The positive θ_{CW} comforts predominant ferromagnetic exchanges.

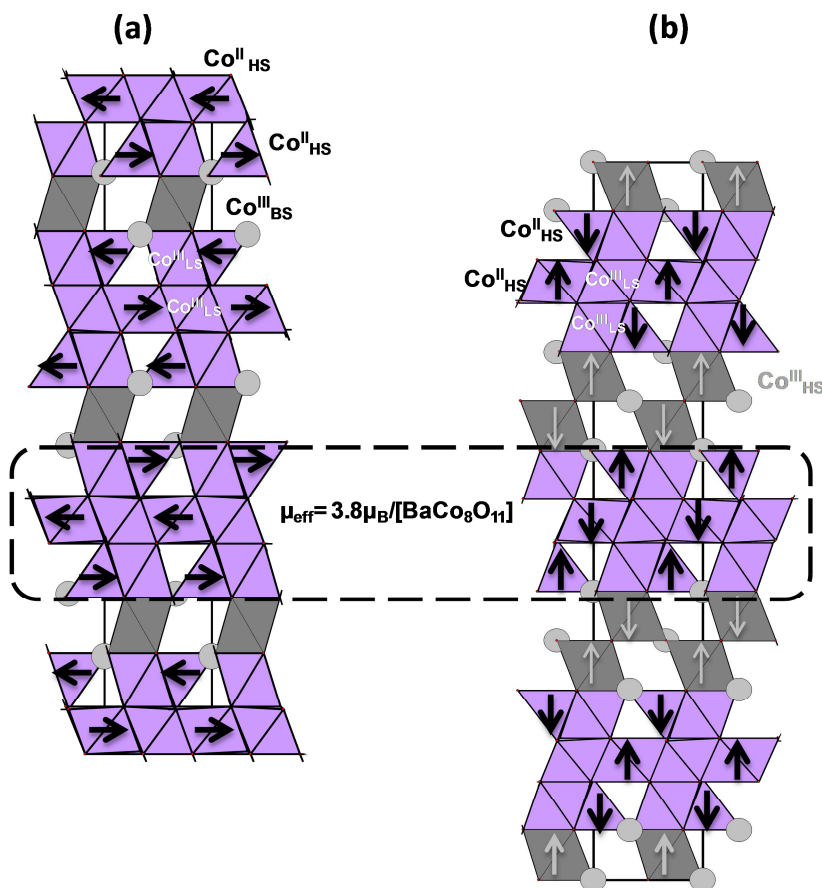


Fig.3-28: Magnetic structure of (a) $Ba_2Co_9O_{14}$ and (b) $Ba_3Co_{10}O_{17}$. The grey blocks – interconnectors are not to be considered here. The μ_{eff} / structural unit is also given.

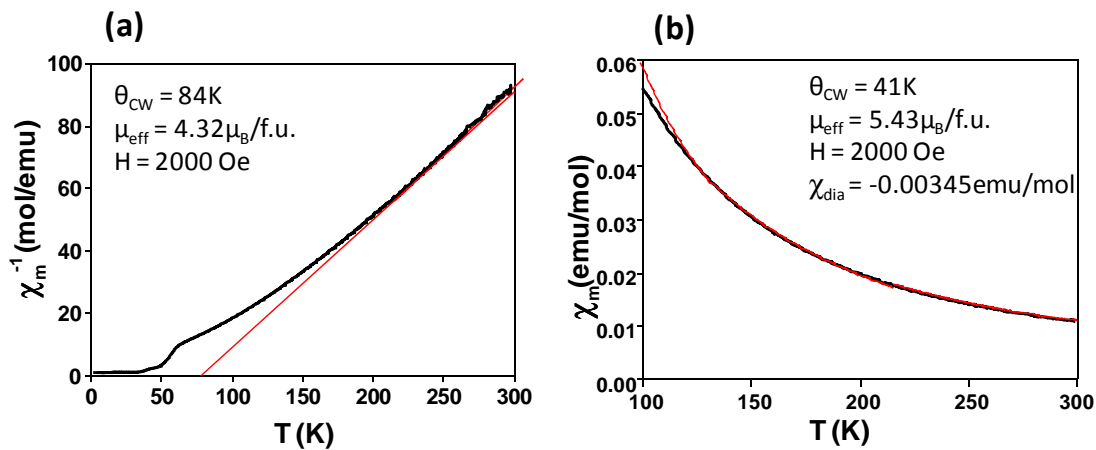


Fig.3-29: (a) $\chi_m^{-1}(T)$ at 2000 Oe and (b) $\chi_m(T)$ at same field with fitting considering a diamagnetic contribution of -0.00345 emu/mol

Magnetic ordering between blocks: the ZFC/FC cycles at $H=1000$ Oe and 30000 Oe are shown on the Fig.3-30, (a) and (b) respectively, and show typical ZFC/FC divergence for a ferromagnetic-related system. However two points should be noted:

- Two transitions occurs at 55K ($=T_c$) and 45K ($=T_t$) as evidenced from measurements in AC-field Fig.3-30, (c) and should be related to the competition between intra block couplings and inter-block couplings. Below T_c the blocks get individually ordered. Below T_t the inter-block ordering occurs.
- At high field (30000 Oe), the FC curve shows at T_2 a peak very similar to a Néel transition (AFM ordering?).

The magnetization plots at several temperatures are shown on the Fig.3-30, (d). Clearly above 45 K, the magnetization shows a FM behavior with important remanent magnetization and almost no coercitif champ. This could be assigned to individual ferromagnetic blocks that are more or less aligned on the external field. Below 45 K the curvature of $M(\mu_0H)$ show that AFM exchanges start to interplay with the FM alignment of the blocks. This behavior appears complex and is still under investigation but at this point we expect the following a scenario:

-Below 55K individual blocks order ferrimagnetically, in the same way as for $\text{Ba}_2\text{Co}_9\text{O}_{14}$ and $\text{Ba}_3\text{Co}_{10}\text{O}_{17}$ (Fig.3-28). At this point we can see the influence of an external field which tend to align the 2D-units parallel and one can reach a remanant moment up to $0.4\mu\text{B}/\text{f.u.}$ while the theoretical expected value is $\sim 1.9\mu\text{B}/\text{Ba}_2\text{Co}_4(\text{Cl},\text{CO}_3)\text{O}_7$ -see above).

- At T_t , despite a strong spatial separation the magnetic 2D-units tend to order antiferromagnetically as observed for the two related compounds. It is evidenced by the curvature on $M(\mu_0H)$ below 45K which results from the competition between AFM exchanges and FM-alignment under magnetic field. Fig.3-31 (a) illustrates this behavior. At 2K $M(\mu_0H)$ gives a plateau until 10T and suddenly the effect of the field predominates. It reaches a moment of $2.5 \mu_B/f.u.$ greater than the expected one based on the ideal $n=1$ and $n=2$ models.

- Finally it is noteworthy that all the measurements described here have been performed with $H//c$. $M(\mu_0H)$ at 2K for $H//(a,b)$ is shown on the Fig.3-31 (b), and evidences a pure AFM behavior with moments aligned parallel to the c-axis.

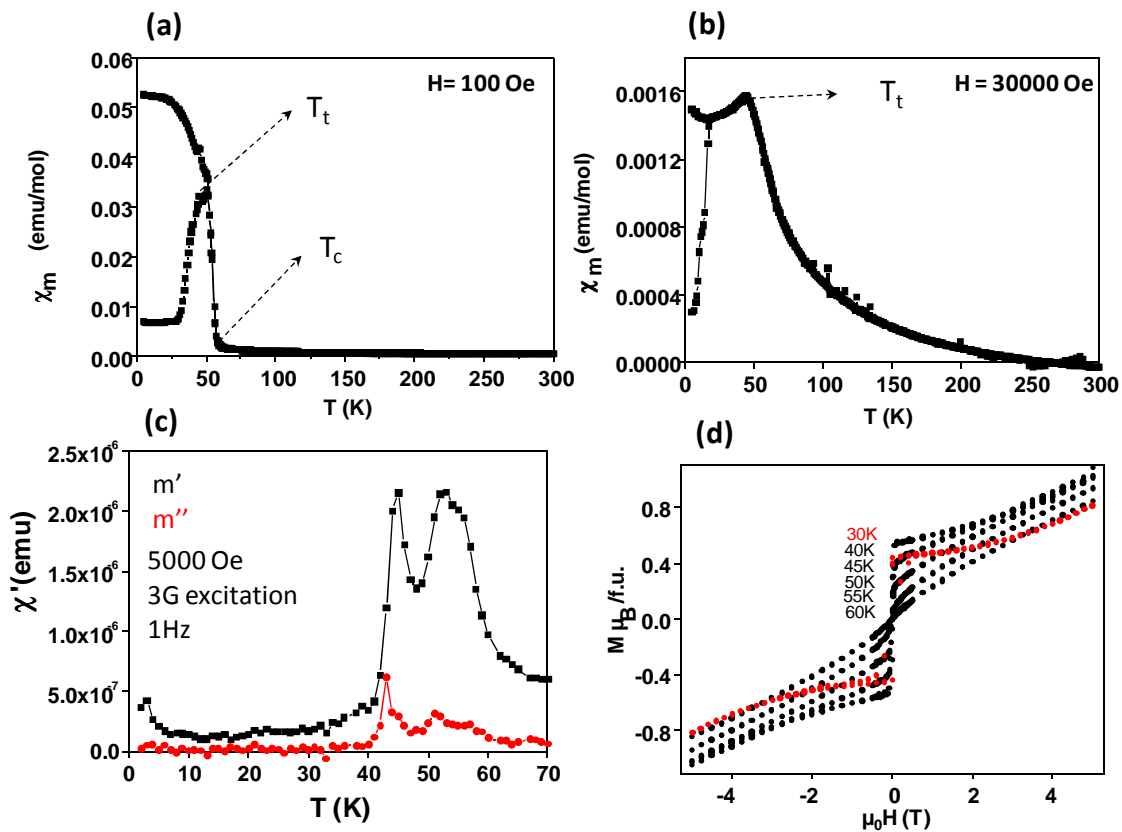


Fig.3-30: (a) ZFC and FC curves at $H = 100$ Oe showing two transitions at T_t and T_c respectively; (b) ZFC and FC $\chi_m(T)$ at $H = 30000$ Oe showing a transition at T_t ; (c) AC-field susceptibility measurements using a 5000 Oe field, 3G excitation and 1Hz as frequency; (d) Magnetization plots at 30K- 60K.

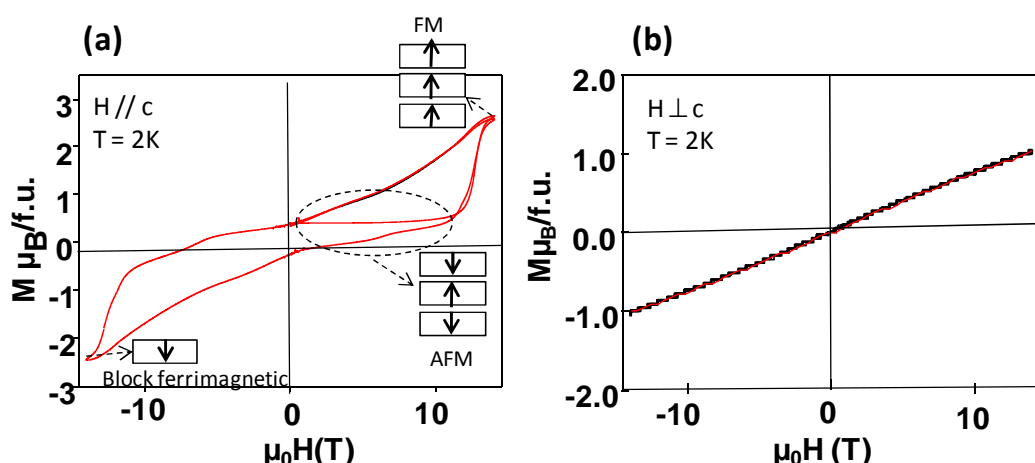


Fig.3-31: (a) $M(\mu_0H)$ at 2K with $H//c$ showing a plateau until 10T; (b) $M(\mu_0H)$ at 2K with $H\perp c$ showing an along c axis orientation of the magnetic moments.

3.5.2. Carbonate insertion possibility in 2H-BaCoO₃ compounds; evidence of a new family of 2H-Ba(Co, CO₃)O₃ compounds

Since this section is dedicated to novel 1D compound that we prepared accidentally, it is worth recalling the main features of the parent 2H-BaCoO₃ compound. It has been extensively studied because of its magnetic properties attributed based on Co⁴⁺ transition metals. The properties of this compound were investigated from both theoretical and experimental points of view (*Pardo2004a and b*) due to the competition between intra-chains (FM) and inter-chains (AFM frustration) exchanges. It crystallizes in the $P6_3/mmc$ space group with $a = 5.63 \text{ \AA}$ and $c = 4.76 \text{ \AA}$ (*Taguchi1977*). The structure of 2H-BaCoO₃ is one dimensional formed by parallel chains of face – sharing CoO₆ octahedra (Co⁴⁺) separated by Ba²⁺ cations. It corresponds to the ideal 2H-ABX₃ hexagonal structure as 2H-BaNiO₃ (*Lander1951*) and 2H-BaMnO₃, (*Cussen2000*).

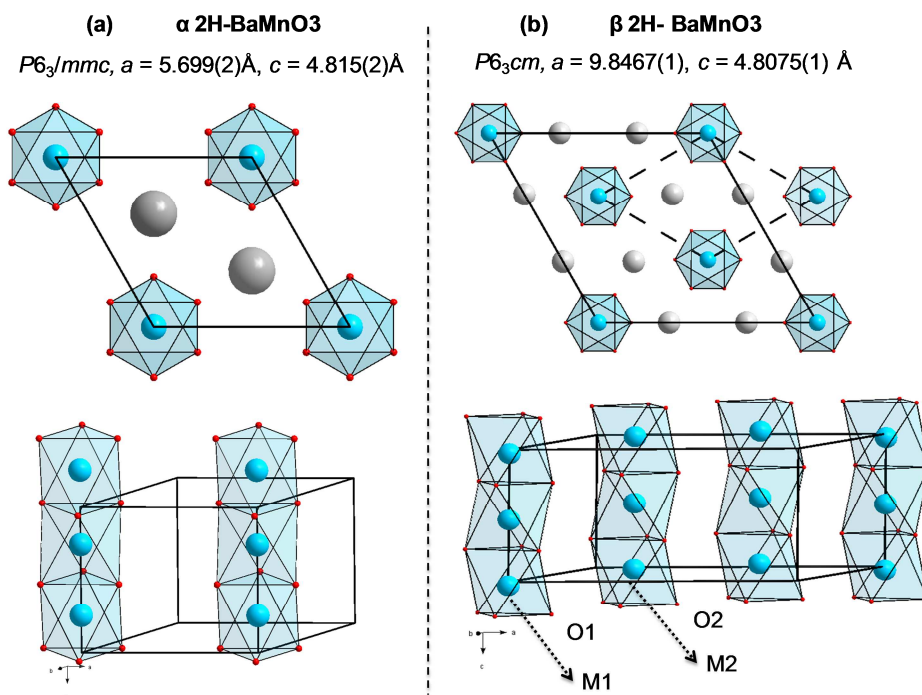


Fig. 3-32: α 2H-BaMnO₃ (a) and its low temperature (80 K) phase (b)

Neutron diffraction investigation of this least compound (2H-BaMnO₃, $a = 5.699(2)\text{\AA}$, $c = 4.815(2)\text{\AA}$, space group $P6_3/mmc$, called hereafter α phase, Fig. 3-32(a)) highlighted a low temperature phase transition at 80 K into a new symmetry ($\rightarrow a = 9.8467(1)$, $c = 4.8075(1)\text{\AA}$, space group $P6_3cm$, called hereafter β phase) due to a shift of half of the chains along c by $\Delta d = 0.41\text{\AA}$ (Cussen2000) (Fig. 3-32 (b)). It results in the non-equivalence between Co1 and Co2 atoms and leads to the hexagonal supercell $\sqrt{3}$. In contradiction with 2H-BaMnO₃, no $\alpha \rightarrow \beta$ low temperature phase transition was reported for BaCoO₃.

The synthesis methods of the compounds investigated in this section are given in the beginning of this chapter (section 3.3, (Page 123)). A short recall is given below:

- we have prepared 2H - BaCo₃ (**sample A**) in NaOH flux from an oxo-chloride precursor without the use of HT and HP of oxygen.
- the second compounds (**sample B**, obtained during the attempts to prepare Ba₇Mn₅Ca₂O₁₉, Floros2000) leads to a new form of BaCoO₃.

The XRD patterns of the two samples are given in Fig.3-33. Sample A was indexed in the 2H – BaCoO₃ cell ($P6_3/mmc$ space group with $a = 5.63\text{\AA}$ and $c = 4.76$

Å, α form), the sample B shows an additional peak at $\approx 10^\circ$ in 2θ , leading to a cell similar to what was observed for β 2H-BaMnO₃ (Fig. 3-32, (b)).

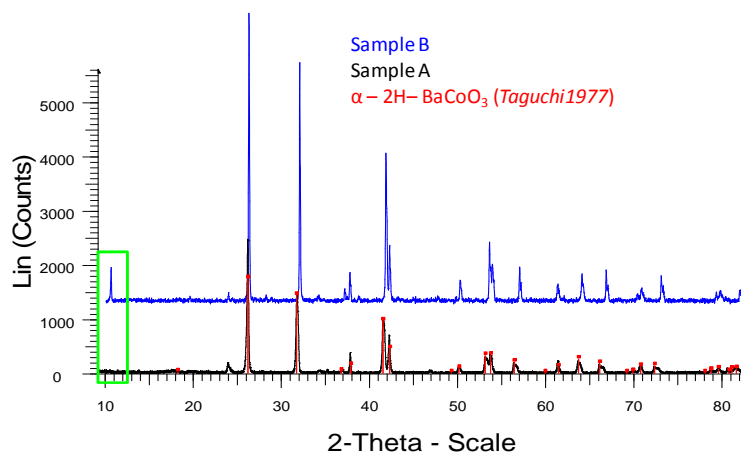


Fig.3-33: (a) X – ray diffraction patterns of sample A in black corresponding to α - 2H - BaCoO₃ (Taguchi1977) (in red) and sample B in blue.

3.5.2.a) Evidence of the $(\text{CO}_3)^{2-}$ entities presence in the hypothetical β - 2H-BaCoO₃

Energy Dispersive Spectroscopy (EDS) and selected area electron diffraction (SAED) analysis were also performed in order to verify the real composition of the two samples (sample A – oxo-chloride precursor in NaOH, sample B – CaCO₃ powder precursor) and the unit cell corresponding to the two samples. The results are summarily given below:

- 1) For **A sample** (X – ray indexation corresponding to α 2H-BaCoO₃), six crystals were tested leading to an average ratio between Ba/Co/Cl of 1/1.1/0.026. The very small amount of Cl can be interpreted as a surface-dopant since the washing procedure can be incomplete. The reconstruction of the reciprocal space (SAED) confirm the $a = 5.8 \text{ \AA}$ and $c = 4.8 \text{ \AA}$ parameters (Fig.3-34, (a)). Still, for some crystals, long streaks appear along c indicating a disorder.
- 2) For the **B sample** (X – ray indexation corresponding to an hypothetical β 2H-BaCoO₃), an inhomogeneity of the preparation was evidenced by EDS and SAED. Then, different compositions and electron diffraction patterns (EDP) were observed between crystals. Indeed, the Fig.3-34 shows three different (010) EDP for three crystals from the same B sample. The indexation of the majority of crystals (Fig.3-34 (b)) correspond to a hypothetical β cell ($a = 9.68$ and $c = 4.77 \text{ \AA}$), but some

crystals show superstructure with double (Fig.3-34 (c)) or triple (Fig.3-34 (d)) c parameters. Note that the intensities of these extra – spots are relatively small, explaining way they were not detected by powder XRD.

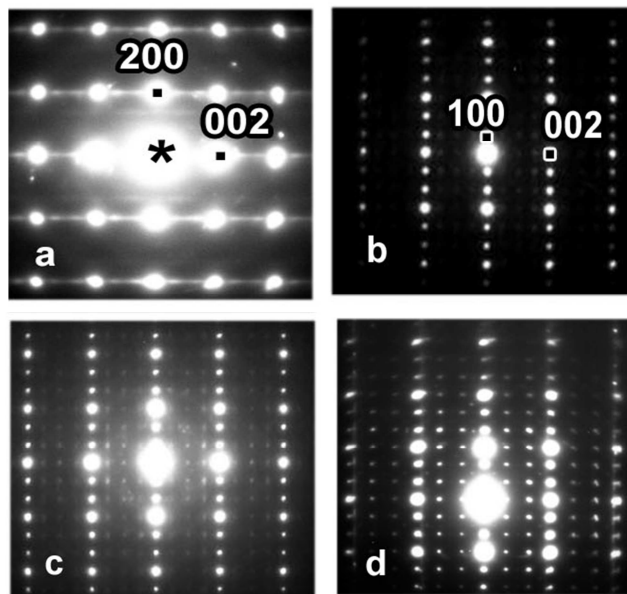


Fig.3-34: [010] electron diffraction a) for α 2H-BaCoO₃. (b), (c), (d) for different crystals of the β – 2H BaCoO₃ preparation.

The mean observations of EDS and SAED for this B sample can be summarized as follows:

- The majority of crystals lead to a Ba/Co ratio 3/2 with EDP given in figure Fig.3-34 (b) and indexation cell: $a = 9.68 \text{ \AA}$ and $c = 4.77 \text{ \AA}$
- For two crystals, a Ba/Co = 3/1 ratio was found (EDP in Fig.3-34 (c), with the lattice parameters $a = 9.7 \text{ \AA}$, $c = 2 \times 4.8 \text{ \AA}$. Note that these elemental ratios change to 3:2 after a long acquisition exposition-time whereas the EDP remains the same. It can be explained by an evolution of the phase that will be commented later (see section 3.5.2.c) , (Page 176).
- Few checked crystals (about twenty of the tested ones) lead to an average Ba/Co ratio of 1.8/1 with the corresponding lattice parameters $a = 9.7 \text{ \AA}$, $c = 3 \times 4.8 \text{ \AA}$. The EDP is shown on the Fig.3-34 (d)). There have not been investigated yet.

Some crystals, (only a few and with a bad crystallinity, explaining way they have not been observed by X-ray diffraction) exhibit only Ba, only Co or only Ca, corresponding, probably, to simple Ba, Co and Ca oxides.

In fact, these deviations from the ideal Ba/Co = 1/1 are likely explained by a possible substitution of cobalt-octahedra by carbonate groups. Indeed, the literature reports the compound $\text{Ba}_3\text{Co}_2(\text{CO}_3)_{0.6}\text{O}_6$ (Boulahya2002), with cell parameters $a=9.683(1)\text{\AA}$ and $c=9.5180(8)\text{\AA}$ and P space group. The structure of this compound is given in Fig.3-35 (a) and it is closely related to the ideal 2H one, but with one central column filled by CoO_6 octahedra and the other filled by carbonate groups (Fig.3-38, (c)). To confirm this hypothesis, Infrared Spectroscopy was performed on the sample B. The resulting spectrum is given in Fig.3-35 (b) and is in agreement with the presence of carbonate groups.

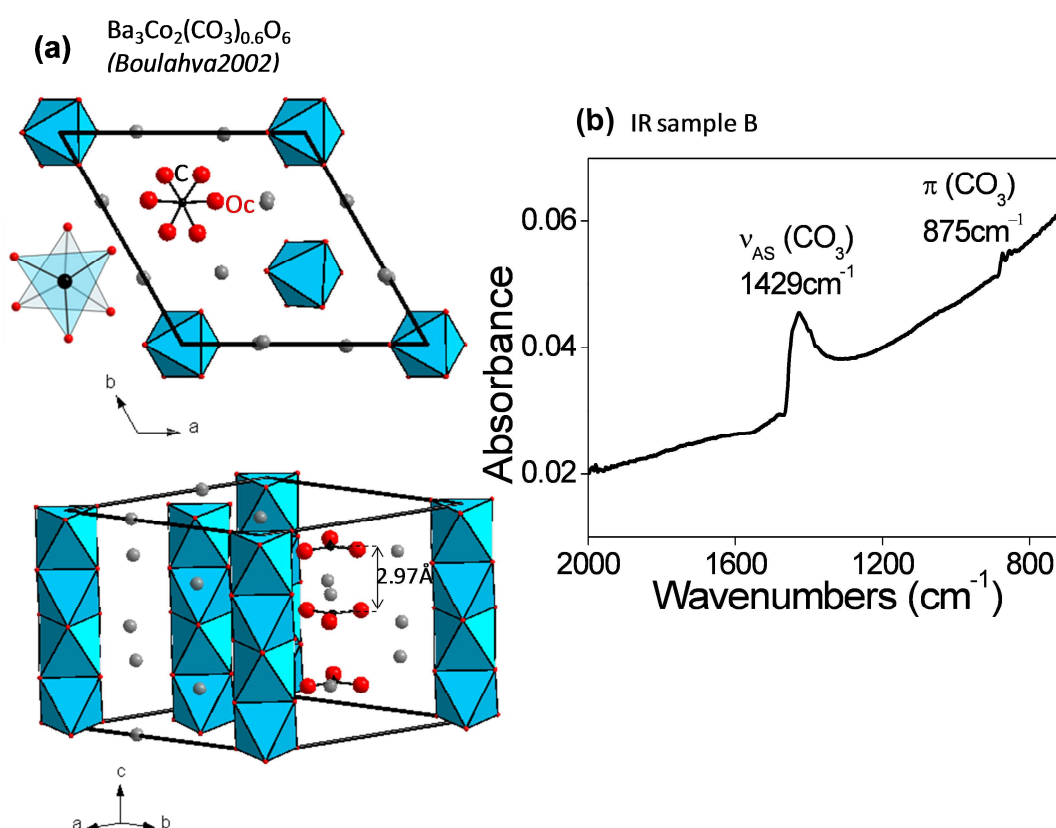


Fig.3-35: (a) Different views of $\text{Ba}_3\text{Co}_2(\text{CO}_3)_{0.6}\text{O}_6$ (Boulahya2002) compound. The distance between two carbonate groups is also given (2.97\AA). The carbonate groups are in staggered conformations; (b) Infra – red spectrum for B sample showing two of the specific absorption bands for CO_3 groups

3.5.2.b) Structural models for sample B

As a general procedure for the three models presented below, the refinement has been performed using JANA 2006 software. We have used five terms of Legendre polynoms in order to describe the background and for the asymmetry correction, the Simpson method was applied. The profile was refined using a Pseudo–Voigt function. The atomic parameters and thermal parameters were refined in the final stage.

1) Model $\text{Ba}_3\text{Co}_2(\text{CO}_3)_{0.6}\text{O}_6$: In a first step, the data corresponding to the title structure (*Boulahya2002*) was considered, Fig.3-35 (a). It was rapidly categorically rejected due to unrealistic R values and differences.

2) Model β 2H–BaCoO₃: Despite the mismatching stoichiometry (experimental Ba/Co = 3/2 for the majority of the crystals), we have tested also the structure corresponding to β 2H–BaMnO₃. The refined structure is given in Fig. 3-36 (a). The profile was refined in the non –centrosymmetric space group with $a = 9.68(1)\text{\AA}$ and $c = 4.77(4)\text{\AA}$ (*Cussen2000*). Due to the absence of a centre of symmetry, an atom position had to be fixed in order to define an origin and the Co cation occupying the 2a site, position $(0, 0, z)$ was therefore fixed at $z = 0$.

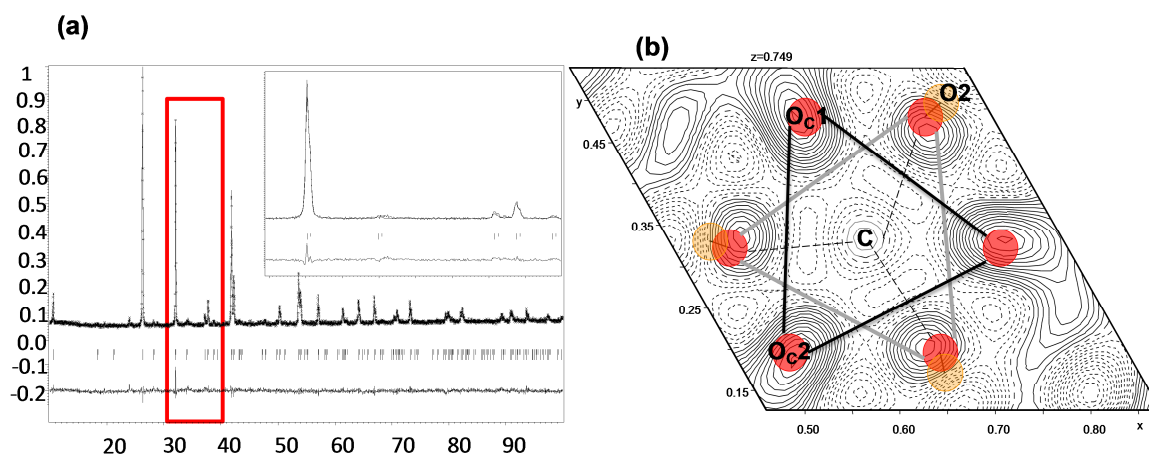


Fig. 3-36: (a) Rietveld using the β 2H–BaMnO₃ structural model ($R = 6.72\%$). In the insert is given a zoom between $30 - 40^\circ 2\theta$; (b) Fourier difference map in the O2 atoms plan (given in orange) (octahedra basal plan) showing densities that could be attributed to carbonate groups in intercalated configurations.

The rather good accordance between the theoretical and experimental diffractogram is expressed by the agreement factor $R = 6.80\%$ (Rwp). However, the difference Fourier maps show residual densities on the basal plane of the O2 faces of the deficient Co2 octahedron (one of the two columns) which could be related to the presence of carbonate group (Fig. 3-36 (b)). Then the central peak is assigned to C, while the surrounding ones (more or less superposed to the O3 face) are assigned to oxygen of CO₃ groups. Two configurations of carbonate groups seem to be present.

3) Disordered CO₃ model. Thus, the occupancies of Co2 atom was refined (Fig. 3-32). The refinement dropped to 50%, confirmed by a decrease of the R factors from $R = 6.80\%$ to 6.24% (for Co1, the refinement of the occupancies converged close to full occupancy). The refined Ba/Co ratio is then 3/2 in good agreement with the EDS results. The introduction of one carbonate group force the removal of at least two Co atoms in order to respect a sufficient distance between the remaining cobalt and the introduced (CO₃)²⁻ (note the constraint imposed of the z of the two carbonates configurations to be equal, *i.e.* planar carbonate).

Table 3-10: Rietveld refinement information for an ideal octahedra dimers/one (CO₃) model:

Atom	Ox.	Wyck.	S.O.F.	x/a	y/b	z/c	U [Å ²]
Ba		6c		0.3254(5)	0.3254(5)	0.237(3)	0.047(2)
Co1		2a		0	0	0.026(8)	0.018(3)
Co2		4b	0.5	2/3	1/3	0.945(7)	0.018(3)
O1		6c		0	0.125(3)	0.334(7)	0.025(6)
O2		12d	0.75	0.67460	0.49679	0.24156	0.025(6)
Oc1		12d	0.125	0.81019	0.32702	0.72000	0.025(6)
Oc2		12d	0.125	0.51435	0.33394	0.72000	0.025(6)
C1		4b	0.25	2/3	1/3	0.72000	0.025(6)

We have tried to refine the two carbonate configurations (considering equal ratio) given in Table 3-10, but the refinement would not converge. This is to be expected because we reach here the limits of Rietveld refinement on XRD powder data. At this point, the occupancies and atomic positions have been fixed in order to correspond to the ideal model shown in Fig. 3-37, (a)), according to information given in Table 3-10. The R value was 6.15%. However, the Fourier difference from Fig.

3-36 (b)) is showing non-equals ratio for the two configurations and the refinement seems to lead in the same direction.

4) Ideal CO₃ ordering: The ideal hypothetical model mentioned above corresponds to the presence of one Co atom out of two in the carbonated columns (double multiplicity) while the other column (simple multiplicity) remains unchanged. It corresponds to the alternation of octahedral Co(2)₂O₉ dimers with one (CO₃) (Fig. 3-37, (a)). In this case, the calculated formula is Ba₃Co₂(CO₃)_{0.5}O_{7.5}.

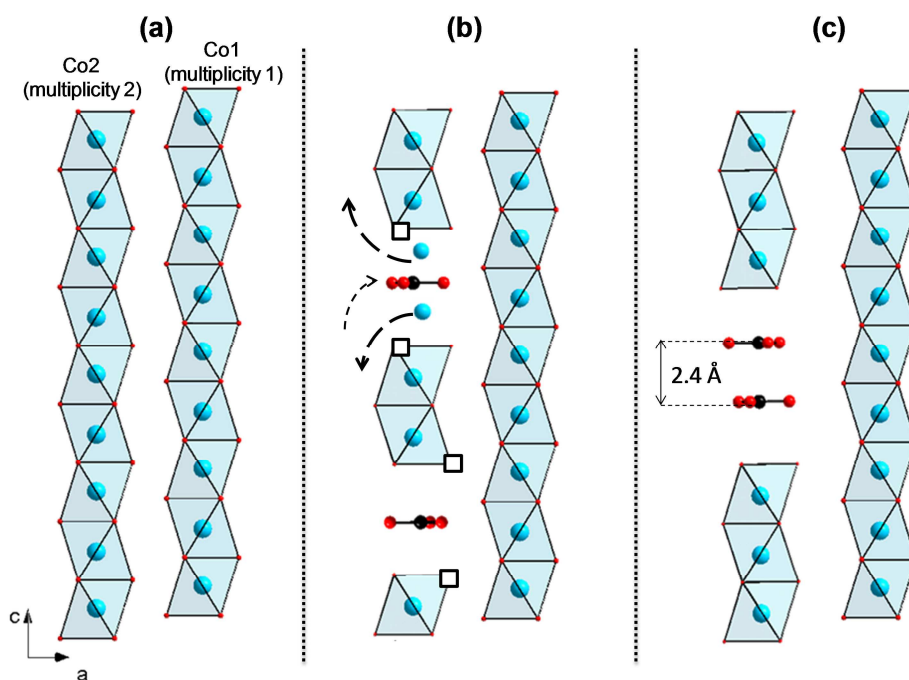


Fig. 3-37: Ideal (CO₃) ordering structural models for the B sample and the correspondence with infinite octahedral chains – introduction of one carbonate group force the removal of two Co atoms; (a) octahedral dimers with one carbonate group. Oxygen vacancies can be correlated with the presence of carbonates groups; octahedral trimers separated by two carbonates groups – unlikely due to the short C – C distance compared to Boulahya2002

However, this formula yields an unlikely Co⁵⁺ valence state. For a mixed Co^{3/4+} valence, we should consider deficient oxygen sites on the borders of the Co₂O₉ units which are favoured by the neighbourhood of a carbonate group in the column. Such effect was already observed for Ba₃(Ru_{1.69}Co_{0.31})(Na_{0.95}Ru_{0.05})O_{8.69} (Quarez2003a). Then the mean substitution scheme corresponds to BaCo_{1-2x}C_xO_{3-2x} or BaCo_{1-2x}(CO₃)_xO_{3-5x} with x = 0.16 in our case from EDS measurements, and a substitution arising in particular columns (Fig. 3-37, (a)).

Other particular sequence between carbonates and cobalt cations (e.g. octahedral trimers separated by two carbonates groups, Fig. 3-37, (b)) can be imagined but are unlikely because of the short C – C distance of 2.4Å compared to 2.97Å in Ba₃Co₂(CO₃)_{0.6}O₆ (Fig.3-35, (a)).

3.5.2.c) Superstructure investigation by Precession Electron Diffraction (PED)

An interesting point of view that was neglected up to now is the observation by SAED of superstructure with a doubling or tripling of the c parameter, compared to the β - 2H-BaCoO₃ (Fig.3-34 (c)). Only a few crystallites of this double cell with Ba /Co = 3 were observed preventing a structural analysis by Rietveld method. To overcome this problem, Precession Electron Diffraction data were collected to attempt an electron diffraction structure determination based on the approach proposed by Kolb *et al* (Mugnaioli2009). This technique is beyond the scope of this thesis, but in summary, 111 non – oriented PED patterns were collected (from a tilt angle of -60° to +51°) on a Tecnai MET , operating at 200kV ($\lambda = 0.0251\text{\AA}$) with a precession angle of 1°. This series of diffraction images were processed using the PETS software (Process Electron Tilt series given by courtesy of Dr. Lukas Palatinus from the Academy of Science of Czech Republic. After peaks hunting (*i.e.* the search of diffraction peaks in each image), microscope parameters refinement (*i.e.* the adjustment of the angle, omega, between the projection of the tilt axis on the pattern and the horizontal axis that depends on the camera length and on the exact focusing conditions), and clustering of centres (*i.e.* the use of centres of the clusters of equivalent measured reflections instead of individual peak position, raw peak list being usually too noisy to be used for direct indexing), the indexing procedure was done manually in Jana 2006 (Petricek2006) leading to a “classical” orientation matrix UB. After the full integration procedure implemented in PETS, the intensities were imported in Jana 2006, with the cell parameters refined in the indexing plug-in of Jana 2006. The structure was solved by direct method using the 2011 version of Sir (Altomare1997) adapted for electron diffraction data.

However, despite the use of Precession (which is known to reduce the dynamical effect due to multiple diffraction) and the use of “not – oriented” patterns (which are also less affected by multiple diffraction and then more kinematical), it is very difficult to obtain low agreement for electron data, since all available software

are done for kinematical diffraction, and not for dynamical. It was however possible to obtain using Jana 2006 a structural model which is coherent from chemical point of view, (see later), with R factors around 27%. The cell parameters are $a=9.789(1)$ Å, $c=9.679(1)$ Å, S.G. $P\bar{6}2m$. The main characteristic of this structure is that two strings of Co octahedra of the β – phase are now replaced by strings of carbonate groups. Because of the limitations imposed by the quality of the data, some soft constraints have been imposed on the C-O distances (3.26Å), beside the constraint imposed on the carbonate atoms co-planarity. The Rietveld information are given in Table 3-11. The refined formula is $Ba_3Co(CO_3)_{1.5}O_3$.

Table 3-11: Rietveld refinement information for $Ba_3Co(CO_3)_{1.5}O_3$ from PED data:

Atom	Wyck.	Occ.	x	y	z	U [Å ²]
Ba1	3f		0	0.3193(12)	0	0.0089(7)
Ba2	3g		0.3096(12)	0	1/2	0.0089(7)
Ba3	6i		0.3348(5)	0.3348(5)	0.2564(6)	0.0089(7)
Co1	2e		0	0	0.126(2)	0.0044(13)
Co2	2e		0	0	0.374(2)	0.0044(13)
O1	6i		0	0.145(2)	0.261(3)	0.0070(18)
O2	3g		-0.176(4)	0	1/2	0.0070(18)
O3	3f		0.157(4)	0.157(4)	0	0.0070(18)
Oc1	6k		0.455(2)	-0.1966(15)	1/2	0.0070(18)
Oc2	12l		0.2007(12)	0.5400(14)	-0.1898(15)	0.0070(18)
C1	2d		1/3	2/3	1/2	0.0070(18)
C2	4h		1/3	2/3	-0.1898(15)	0.0070(18)

It is very interesting to compare the different members of this family:

- 2H-BaMO₃ = strings of faces sharing CoO₆ octahedra running along c, (M = Co and Mn) (Fig.3-38, (a))
- For M = Mn, a new form at low temperature it has been evidenced, with two non-equivalent strings of octahedra (Cussen2000), Fig.3-38, (b)
- Deriving from this form, we propose a new structure formulated $Ba_3Co_2(CO_3)_{1.5}O_{7.5}$, but for M = Co this time, in which a disorder between carbonate groups and CoO₆ octahedra is observed in the two non-equivalent strings Fig.3-38, (c)

- A greater order is achieved for the last member of this family $\text{Ba}_3\text{Co}(\text{CO}_3)_{1.5}\text{O}_3$ evidenced using PED data, with, instead of two face sharing octahedra chains, string of carbonate entities (Fig.3-38, (e)).

Concerning the Ba/Co ratio evolution mentioned previously (from 3 to 1.5) for long time EDS acquisition without change of the EDP, a transition from the new form (Ba/Co = 3) (Fig.3-38 (e)) to $\text{Ba}_3\text{Co}_2(\text{CO}_3)_{0.6}\text{O}_6$ phase (Ba/Co = 1.5) (Fig.3-38 (c)) could be envisaged due to some CO_3 departure in the microscope atmosphere. Indeed the [010] EDP of these two structures are similar, whereas the Ba/Co are different (Ba/Co=3 and Ba/Co=1.5 for respectively the new $\text{Ba}_3\text{Co}(\text{CO}_3)_{1.5}\text{O}_3$ and $\text{Ba}_3\text{Co}_2(\text{CO}_3)_{0.6}\text{O}_6$ phases.

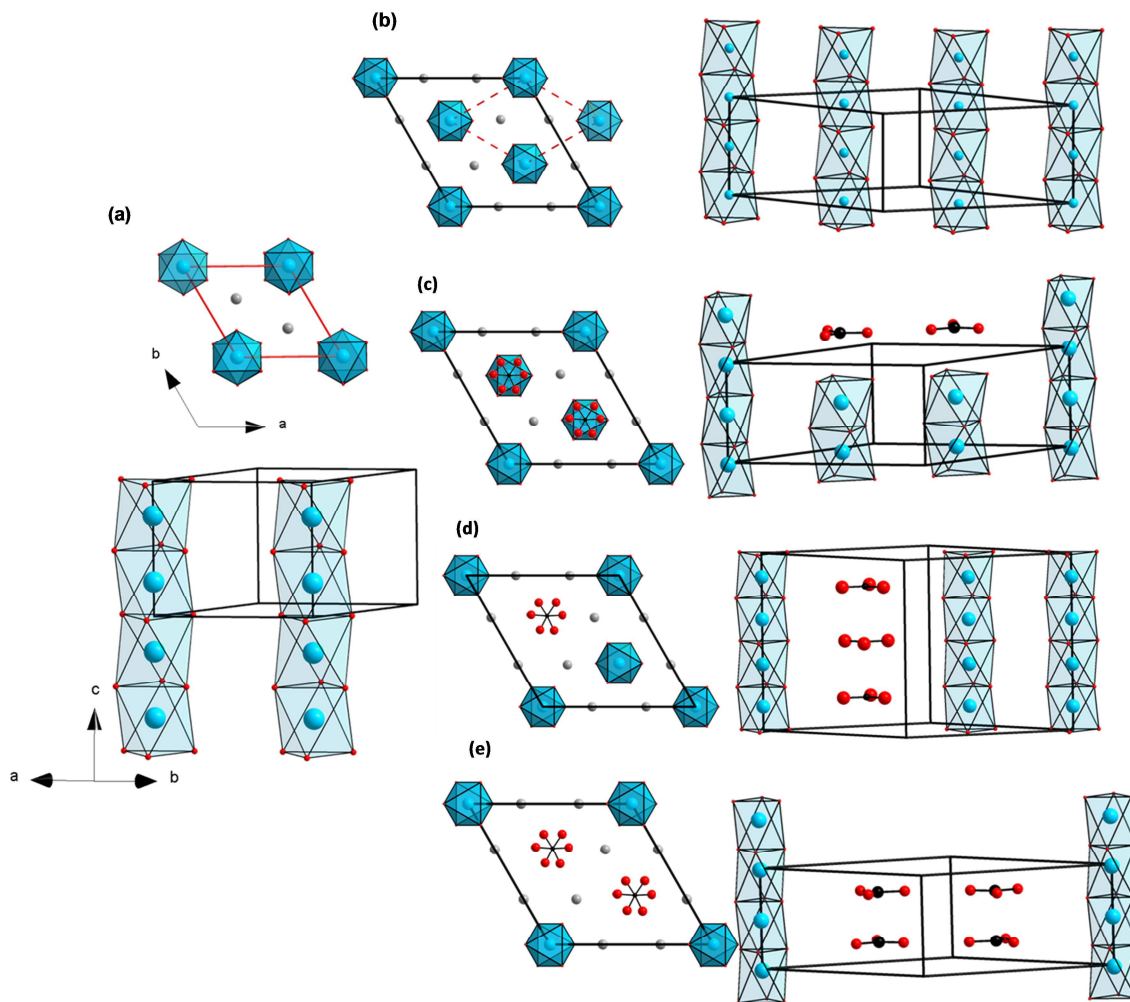


Fig.3-38: (a) $2H\text{-BaMO}_3$ ($M = \text{Mn}, \text{Co}, \text{Ni}$), (b) $\beta 2H\text{-BaMO}_3$ ($M = \text{Co}, \text{Mn}, \text{Ni}$); (c) $\text{Ba}_2\text{Co}_3(\text{CO}_3)_{0.6}\text{O}_6$ (Boulahya2002); (d) an ideal ordered structure proposed for the B sample; (e) $\text{Ba}_3\text{Co}(\text{CO}_3)_{1.5}\text{O}_3$ new form evidenced using PED data.

Supplementary information

3. 6. Supplementary information

Annexes 1: Atomic positions, site occupancies and anisotropic displacement parameters from Rietveld refinement on ND data for $y = 0.8$, $y = 0.5$ and $y = 0.2$ terms of the $Ba_5Co_5Cl_{1-y}F_yO_{13.5}$ solid solution:

Atom	Wyck	Occ.	x	y	z	Uiso (Å ²)
Ba1	2b	1	0	0	1/4	0.0218(1)
						0.0192(1)
						0.0199(1)
Ba2	4f	1	1/3	2/3	0.36428(1)	0.0084(4)
						0.36625(1)
						0.36938(1)
Ba3	4f	1	1/3	2/3	0.96015(1)	0.0084(4)
						0.96004(1)
						0.95945(1)
Co1	4e	1	0	0	0.6045(2)	0.0018(5)
						0.6040(2)
						0.6036(2)
Co2	2a	1	0	0	0	0.0018(5)
						0.0034(5)
						0.0017(5)
Co3	4f	1	1/3	2/3	0.8200(2)	0.0018(5)
						0.8227(2)
						0.8218(2)
F1/Cl1	2c	0.740(9)/0.186(9) 0.407(2)/0.500(2) 0.365(9)/0.620(9)	1/3	2/3	1/4	0.0800(2)
						0.0422(9)
						0.0271(8)
O1	12k	0.969(6)	0.3168(8)	0.1584(4)	0.34873(8)	0.01013(2)
						0.962(6)
						0.974(5)
O2	12k	0.975(5)	0.7028(6)	0.8514(3)	0.44855(8)	0.01013(2)
						0.989(5)
						0.983(5)
O3	6h	0.333(9)	0.3816(1)	0.7632(2)	0.44923(8)	0.00858(2)
						0.332(6)
						0.330(7)
					3/4	0.00763(2)
						0.7048(6)
						0.7030(6)
						0.00763(2)
						0.7412(4)
						0.7382(4)
						0.042(3)
						0.023(3)
						0.027(3)

Annexes 2: Single crystals XRD information for $Ba_5Co_5Cl_{0.2}F_{0.8}O_{13.5}$:

Crystal data	
Crystal symmetry	hexagonal
Space group	$P6_3/mmc$
Unit cell (Å and °)	$a = b = 5.6983(2)$
	$c = 24.1061(1)$
	$\alpha = \beta = 90$
	$\gamma = 120$
Volume (Å ³)	677.87(4)
Z	2
Mw , Calculated density (g/cm ³)	1219.9,6.6942
F(000)	1059
Data collection	
Equipment	Bruker X8
Radiation MoK α (Å)	0.71073
Scan mode	ω/φ - scan
Recorded angular range θ (°)	1.69 – 37.46
Recording reciprocal space	$-9 \leq h \leq 9$
	$-9 \leq k \leq 9$
	$-40 \leq l \leq 40$
Number of measured reflections	30175
Number of independent reflections	754
Number of independent reflections [$I > 3\sigma(I)$]	543
μ (mm ⁻¹) ($\lambda = \text{MoK}\alpha$)	10.36
Absorption correction	Multiscan (Sadabs)
Transmission Tmin/Tmax	0.5849(9)
R merging factor (%)	7.4
Refinement parameters	
Software, refinement type	Jana 2006, L.S. on F
Number of refined parameters	37
R_1 (F) all, [$I > 3\sigma(I)$] (%)	4.77/6.97
wR_1 (F) all, [$I > 3\sigma(I)$] (%)	5.31/5.59
Goodness of fit	2.80
Max / Min $\Delta\rho$ e/Å ³	3.53/-5.33

Annexes 3: Anisotropic displacement parameters, in Å² from single crystals X – ray diffraction for Ba₅Co₅Cl_{0.2}F_{0.8}O_{13.5}:

Atom	U ₁₁	U ₂₂	U ₃₃	U ₁₂	U ₁₃	U ₂₃
Ba1	0.0230(3)	0.0230(3)	0.0212(6)	0.01152(1)	0	0
Ba2	0.0112(2)	0.0112(2)	0.0383(5)	0.00559(1)	0	0
Ba3	0.0142(2)	0.0142(2)	0.0196(4)	0.00709(1)	0	0
Co1	0.0116(4)	0.0116(4)	0.0153(7)	0.0058(2)	0	0
Co2	0.0089(4)	0.0089(4)	0.0167(8)	0.0044(2)	0	0
Co3	0.0066(5)	0.0066(5)	0.0112(1)	0.0033(2)	0	0
F1	0.035(5)	0.035(5)	0.029(6)	0.017(3)	0	0
Cl1	0.035(5)	0.035(5)	0.029(6)	0.017(3)	0	0
O1	0.010(2)	0.0149(2)	0.026(3)	0.0048(1)	0.005(2)	0.0027(1)
O2	0.017(3)	0.022(2)	0.013(3)	0.0086(1)	0.002(2)	0.0009(1)
O3	0.03(1)	0.018(12)	0.033(2)	0.009(6)	0	0

Annexes 4: Atomic parameters from single crystals XRD for Ba₅Co₅Cl_{0.2}F_{0.8}O_{13.5}:

Atom	Wyck.	Occ.	x/a	y/b	z/c
Ba1	2b		0	0	1/4
Ba2	4f		1/3	2/3	0.36723(4)
Ba3	4f		1/3	2/3	0.95752(4)
Co1	4e		0	0	0.60583(8)
Co2	4f		1/3	2/3	0.82037(8)
Co3	2a		0	0	0
F1	2c	0.8	1/3	2/3	1/4
Cl1	2c	0.2	1/3	2/3	1/4
O1	12k		0.3254(8)	0.1627(4)	0.3494(2)
O2	12k		0.7051(8)	0.8525(4)	0.4505(2)
O3	6h	0.3333	0.409(2)	0.817(5)	3/4

Annexes 6: Single crystals XRD information for $Ba_5Co_4Pt_1BrO_{13-\delta}$:

Crystal data	
Crystal symmetry	hexagonal
Space group	$P6_3/mmc$
Unit cell (Å and °)	$a = b = 5.7274(1)$
	$c = 24.9223(3)$
	$\alpha = \beta = 90$
	$\gamma = 120$
Volume (Å ³)	708.00(4)
Z	2
Mw / Calculated density (g/cm ³)	1464.3/6.8667
F(000)	1211
Data collection	
Equipment	Bruker X8
Radiation MoK α (Å)	0.71073
Scan mode	ω/φ - scan
Recorded angular range θ (°)	3.27 – 40.98
Recording reciprocal space	$-9 \leq h \leq 10$
	$-9 \leq k \leq 5$
	$-44 \leq l \leq 44$
Number of measured reflections	20477
Number of independent reflections	884
Number of independent reflections [$I > 3\sigma(I)$]	829
μ (mm ⁻¹) ($\lambda = MoK\alpha$)	32.07
Absorption correction	Multiscan (Sadabs)
Transmission Tmin/Tmax	0.5264(3)
R merging factor (%)	5.9
Refinement parameters	
Software, refinement type	Jana 2006, L.S. on F
Number of refined parameters	29
R_1 (F) all, [$I > 3\sigma(I)$] (%)	5.9/6.26
$wR_1(F)$ all, [$I > 3\sigma(I)$] (%)	7.05/7.1
Goodness of fit	5.27
Max / Min $\Delta\rho$ e/Å ³	11.75/-8.28

Annexes 7: Atomic parameters from single crystal XRD refinement for $Ba_5Co_4Pt_1BrO_{13-\delta}$:

Atom	Wyck.	Site	Occ.	x	y	z	U(Å ²)
Ba1	4f	3m.		2/3	1/3	0.1279(3)	-
Ba2	4f	3m.		1/3	2/3	0.0404(3)	-
Ba3	2b	-6m2		0	0	1/4	-
Co1/ Pt1	2a	-3m.	0.528(1)/0.472(1)	0	0	0	-
Co2 /Pt2	4e	3m.	0.731(2)/0.269(2)	0	0	0.1042(4)	-
Co3	4f	3m.		1/3	-1/3	0.1781(7)	-
Br1	2d	-6m2		2/3	1/3	1/4	-
O1	12k	.m.		0.1610(6)	-0.1610(6)	0.1513(3)	0.0125(1)
O2	12k	.m.		0.1484(5)	0.2968(10)	0.5518(2)	0.0052(9)
O3	6h	-6m2		0.360(4)	-0.360(4)	1/4	0.053(9)

Annexes 7: Anisotropic displacement parameters in Å² for $Ba_5Co_4Pt_1BrO_{13-\delta}$ from single crystal XRD refinement:

Atom	U ₁₁	U ₂₂	U ₃₃	U ₁₂	U ₁₃	U ₂₃
Ba1	0.0044(2)	0.0044(2)	0.0095(3)	0.0022(1)	0	0
Ba2	0.0044(2)	0.0044(2)	0.0131(4)	0.0022(1)	0	0
Ba3	0.0201(4)	0.0201(4)	0.0081(5)	0.0101(2)	0	0
Co1	0.0013(4)	0.0013(4)	0.0059(4)	0.0006(2)	0	0
Pt1	0.0013(4)	0.0013(4)	0.0059(4)	0.0006(2)	0	0
Co2	0.0017(3)	0.0017(3)	0.0083(5)	0.0008(2)	0	0
Pt2	0.0017(3)	0.0017(3)	0.0083(5)	0.0008(2)	0	0
Br1	0.0302(8)	0.0302(8)	0.0188(1)	0.0151(4)	0	0
Co3	0.0046(4)	0.0046(4)	0.0056(7)	0.0023(2)	0	0

Annexes 8: Single crystals XRD information for $Ba_2Cl_{0.87}(CO_3)_{0.13}Co_4O_7$:

Crystal data	
Crystal symmetry	Trigonal
Space group	$R\bar{3}m$
Unit cell (Å and °)	$a = 5.7288(2)$ $c = 45.0990(15)$
Volume (Å ³)	1281.81(8)
Z	6
Mw , Calculated density (g/cm ³)	663.3, 5.155
F(000)	1773
Data collection	
Equipment	Bruker X8
Radiation MoK α (Å)	0.71073
Scan mode	ω/ϕ - scan
Recorded angular range θ (°)	4.07 – 48.76
Recording reciprocal space	$-12 \leq h \leq 11$ $-9 \leq k \leq 11$ $-95 \leq l \leq 93$
Number of measured reflections	21070
Number of independent reflections	2700
Number of independent reflections [$I > 3\sigma(I)$]	2509
μ (mm ⁻¹) ($\lambda = MoK\alpha$)	16.91
Absorption correction	Multiscan (Sadabs)
Transmission Tmin/Tmax	0.5548(2)
R merging factor (%)	4.0
Refinement parameters	
Software, refinement type	Jana 2006, L.S. on F
Number of refined parameters	42
R_1 (F) all, [$I > 3\sigma(I)$] (%)	7.9/7.55
wR_1 (F) all, [$I > 3\sigma(I)$] (%)	12.43/12.49
Goodness of fit	4.19
Max / Min $\Delta\rho$ e/Å ⁻³	9.86 / -6.62

Annexes 9: Atomic parameters for $Ba_2Cl_{0.87}(CO_3)_{0.13}Co_4O_7$ from single crystal XRD refinement:

Atom	Wyck.	Site	Occ.	x/a	y/b	z/c	U [Å ²]
Ba1a	6c	3m	0.865	0	0	0.42954(2)	0.0078(1)
Ba1b	6c	3m	0.135	0	0	0.42271(9)	0.0078(1)
Ba2	6c	3m		1/3	2/3	0.37383(1)	
Co3	9d	.2/m		1/2	0	1/2	
Co4	3b	-3m		1	0	1/2	
Co5	6c	3m		1/3	-1/3	0.44804(2)	
Co6	6c	3m		2/3	1/3	0.43455(2)	
Cl7	6c	3m	0.865	0	0	0.36235(6)	
O8	18h	.m		0.4887(3)	0.5113(3)	0.42322(7)	
O9	6c	3m		2/3	1/3	0.47811(9)	
O10	18h	.m		0.6395(6)	-0.1803(3)	0.47619(5)	
C	6c	3m	0.135	2/3	1.33333	0.3564(4)	0.010(3)
O	18h	.m	0.135	0.394(5)	1.197(2)	0.3564(4)	0.010(3)

Annexes 8: Anisotropic displacement parameters in Å² for $Ba_2Cl_{0.87}(CO_3)_{0.13}Co_4O_7$ from single crystal XRD refinement:

Atom	U ₁₁	U ₂₂	U ₃₃	U ₁₂	U ₁₃	U ₂₃
Ba2	0.0247(2)	0.0247(2)	0.0129(2)	0.0124(1)	0	0
Co3	0.0037(2)	0.0038(2)	0.0048(2)	0.0019(1)	0.00010(7)	0.00021(2)
Co4	0.0052(3)	0.0052(3)	0.0103(4)	0.0026(1)	0	0
Co5	0.0042(2)	0.0042(2)	0.0070(2)	0.0021(1)	0	0
Co6	0.0063(2)	0.0063(2)	0.0081(3)	0.0031(1)	0	0
Cl7	0.0456(1)	0.0456(1)	0.0128(8)	0.0228(7)	0	0
O8	0.0097(9)	0.0097(9)	0.0123(9)	0.0078(9)	0.0002(4)	0.0002(4)
O9	0.0066(9)	0.0066(9)	0.0034(1)	0.0033(5)	0	0
O10	0.0072(9)	0.0051(6)	0.0057(7)	0.0036(4)	0.0008(6)	0.0004(3)

Conclusions

Conclusions

The main objective of this work was the study of cationic and anionic substitution possibilities in $\text{BaCoX}_{0.2-x}\text{O}_{3-\delta}$ systems and to establish the influence of the different substitutions on the structural, magnetic and electric properties.

The rules that guide the substitution in these systems were established based on bibliographic observations of similar compounds in the first chapter. As a general statement, in $\text{BaMO}_{3-\delta}$ systems, with $M = \text{Fe}, \text{Co}, \text{Mn}$, the decrease of oxygen content leads to the increase of cubic type layers, passing from the so called hexagonal perovskites to the cubic ones. This, in our opinion, leads to the conclusion that, in these systems, the agglomeration of vacancies is made in the cubic layers and then, the most reduced compounds are the cubic ones.

Based on these observations, the substitutions were performed for $X = \text{Cl}$ and $X = \text{F}$. The syntheses are presented in the second chapter of the manuscript. Then, the obtained doped compounds serve to the creation of two phase diagrams discussed in the second chapter also. The structural characterization of each line of the diagrams is given in the second part of the second chapter. The most important observations are given in few points below:

- 1) **Fe substitution** stabilizes only **10H** structural polytypes. The redox titrations show a progressive reduction with the increase of Fe ratio. Neutrons diffraction show that **Fe is mostly concentrated in the marginal octahedra and in the tetrahedra**, keeping his affinity for polyhedra cubic – neighboring, while **Co is observed to be in the central polyhedra** in majority.
- 2) **Mn-substitution**. In majority stabilize oxidized structural polytypes (**6H** or long face sharing string of 6 octahedra-8H discussed latter), even if the **synthesis are not reproducible**. The **oxygen vacancies are once again located in majority in the cubic layers**. Mn is concentrated in the centrals octahedra, while the **tetrahedra are Co – occupied**.
- 3) **8H-new polytype**. A new structural polytype whose structure is form by chains of **6 face sharing octahedra** terminated by connected tetrahedra is presented. The single-crystal XRD refinement leads to the **$\text{Ba}_8\text{Co}_2\text{Mn}_6\text{ClO}_{21}$** formula in good agreement with the elemental analysis. Based on DFT calculation and observations

from previous chapter, a **Mn octahedra/Co tetrahedra cationic distribution** was proposed.

4) Mn-Fe substitutions. The predominant structural type depends on the Mn ratio ($10H \rightarrow 6H \rightarrow 2H$) and the mean overall oxidation degrees increase as the Mn ratio increases. However, a **poor miscibility of Mn in the 10H-Fe polytype** estimated about $y = 0.13$ is suggested. HRTEM observations show that the deficient polytypes can create **fully disordered intergrowths** between the 10H, 6H and 2H forms.

5) Ternary substitution. This short section resumes the investigations on the ternary substitutions. This area was not fully investigated, the compounds permitting us only to create the central areas of the phase diagrams.

Finally, some mixed compounds were investigated from magnetic and electric point of view. The introduction of Fe does **not modify the observed strongly AFM connection between corner-sharing tetrahedral Co-O-Co**, while a small Fe ratio is **sufficient to turn the tetrahedral/octahedral FM exchanges** (in the Co-compound) **into AFM ones**. Another interesting point about $Ba_5Co_{5-y}Fe_yXO_{13-\delta}$ solutions concerns the **high TN** observed after introduction of Fe.

The first part of the last chapter is dedicated to the study of anionic Cl/F substitutions in the two structural types (10H and 6H). The principal conclusions regarding the two structural polytypes are listed below.

- The cell parameters evolution is in good agreement with the introduction of a larger anion in the [BaOX] layer (**increase of only the c parameter**)
- From titration results, the **Cl/F mixed compounds are progressively oxidized towards the Cl-rich zone**.
- The magnetic structure was investigated only for one term of the trimeric Cl/F solid solution, showing similar results then for the parents compounds (10H or 6H)
- While, in the **(6H)** $Ba_6Co_6Cl_{1-y}F_yO_{16-\delta}$ solid solution case, the **evolution of the effective magnetic moment** can be attributed to the increase of the compressibility of the octahedral-tetramer with the shrinking of the c parameter (chemical pressure effect), in the **(10H)** $Ba_5Co_5Cl_{1-y}F_yO_{13-\delta}$ case, the **non – monotone dependency is not well understand**.
- In **6H-** $Ba_6Co_6Cl_{1-y}F_yO_{16-\delta}$ solid solution (more oxidized) a **p – type conductivity** (charge carriers = holes) is measured. The reduction observed as Cl is replaced

by F implies an increase of the holes concentration, opposing to the decrease of the resistivity with F/Cl ratio. The resistivity is still controlled by the unit cell volume, decreasing with the F/Cl ratio but less efficiently than in the case of **10H-Ba₅Co₅Cl_{1-y}F_yO_{13-δ}** (more reduced). Here, the **transport is n – type** (carriers are electrons) and, in consequence, the reduction observed from Cl to F is decreasing the number of n- carriers determining the decrease of the transport. This added to the cell shrinking as Cl is replaced by F will lead to the more efficiently decrease of the resistivity with F/Cl.

For 10H compounds an important distortion of the tetrahedra observed in the F-rich area for the 10H compounds (due to off-centring of the oxygen corners of the [BaOX] layers) is at the origin of the magnetocrystalline anisotropy change for the pure F compound in which moments are aligned in the (a,b) plane while for others F/Cl ratio, the magnetic anisotropy involves moment aligned along c. This distortion is re-examined in the case of a Br 10H compound (Pt doped) where the introduction of a very large anion will reduce the off-centring. Also for the same 10H F/Cl mixed compounds, a slight displacement of F out of its ideal position is observed using MEM investigations while Cl remains located on the 3-fold axis.

The second part of the last chapter is dedicated to the re-investigation of previously studied compounds where a structural disorder was observed. Particularly, the presence of carbonate groups in Ba₂Co₄(X,CO₃)O₇ (X = Cl, Br) compounds was evidenced by infrared analysis and observed by MEM on single crystals. Also, some single crystal magnetic investigations are given: an along c axis magnetic moments orientation is observed, while, at low temperature, the compound is ferrimagnetic until 55K where, despite a strong spatial separation, the magnetic 2D-units tend to order antiferromagnetically.

Finally, a new family of compounds is evidenced. It corresponds to 2H-Ba(Co,CO₃)O_{3.δ} formulation and the general structural characteristics can be described as columns of faces sharing octahedra alternating with strings of carbonates groups or mixed octahedra/carbonate strings. Indeed, beside the classic 2H-BaCoO₃, we evidenced two new phases, one in which there is a disorder between carbonate groups and CoO₆ octahedra and another phase with, instead of two face sharing CoO₆ octahedra, strings of carbonate entities.

Bibliography

A.

- Abbas1983 Y. Abbas, F. Mostafa, M. Fayek, *Acta Cryst B*, **1983**, 39, 1
- Adkin2006 J. J. Adkin, M. A Hayward, *J. Solid State Chem.* **2006**, 179, 70
- Adkin2007 J. J. Adkin and M. A. Hayward, *Chem. Mater.*, **2007**, 19, 755
- Altomare1997 A. Altomare, M. C. Burla, M. Camalli, G. Cascarano, C. Giacovazzo, A. Guagliardi, A. G. G. Moliterni, G. Polidori, R. Spagna, *SIR97, A Package for Crystal Structure Solution by Direct Methods and Refinement*, **1997**, Italy.
- Ardenne1939 M. Von Ardenne, *Das Elektronen-Rastermikroskop. Theoretische Grundlagen*, *Zeitschrift für Physik*, **1939**, 108, 553

B.

- Battle1988 P. D. Battle, T. C. Gibb, C. W. Jones, *JSSC*. **1988**, 74, 60
- Bednorz1986, J.G. Bednorz, et al, *Z. Phys. B*, **1986**, 64, 189.
- Berry2008 F.J. Berry, P.R. Slater, *J. Phys.: Condens. Matter*, **2008**, 20, 215207
- Bhalla2000 A. S. Bhalla, R. Guo, R. Roy, *Mat. Res. Innovat.*, **2000**, 4, 3
- Bish1989 D.L. Bish, J.E. Post, *Modern Powder Diffraction. Reviews in Mineralogy*, 1989. 20. Mineralogical Society of America
- Bland1961 J. A. Bland, *Acta Cryst.*, **1961**, 14, 875
- Boulahya2005 K. Boulahya, M. Parras, J. M. Gonzalez-Calbet, U. Amador, J. L. Martinez, V. Tissen and M. T. Fernandez-Diaz, *Phys. Rev.B*, **2005**, 71, 144402
- Boulahya2002a K. Boulahya, M. Parras, J.M. Gonzales – Calbet, A. Vega, *J.S.S.C.*, **2000**, 151, 77
- Boulahya2002 K. Boulahya, U. Amador, M. Parras, J.M. Gonzales – Calbet, *Chem Mater*, **2000**, 12, 966
- Bréard2004 Y. Bréard, C. Michel, M. Hervieu, N. Nguyen, A. Ducouret, V. Hardy, A. Maignan, B. Raveau, *Chem. Mater.*, **2004**,

16,2895

C.

- CampanaBAAN* C.F. Campana, *Bruker Analytical Application Note*
- Chamberland1970* B.L. Chamberland, A.W. Sleight, J.F. Weiher, *JSSC*, **1970**, 1, 506.
- Chamberland1985* B.L. Chamberland, M.P. Herrerofernandez, T.A. Hewston, *JSSC*. **1985**, 59, 111
- Colthup1990* N .Colthup, L. Daly, S. Wilberley, *Introduction to Infrared and Raman Spectroscopy*, **1990**, Academic Press, New York,
- Cussen2000* E.J. Cussen, P.D. Battle, *Chem. Mater.*, **2000**, 12, 831
- Czaya1971* R. Czaya, *Acta Crysta. B* ,**1971**, 27, 848
- D.**
- Dann1992* S.E. Dann, M.T. Weller, D.B. Currie, *JSSC*, **1992**,97, 179
- Dann1993* S. E. Dann, M. T. Weller, D. B. Currie, M. F. Thomas, A. D. Alrawwas, *J. Mater. Chem.* **1993**, 3, 1231
- Darriet1989* J. Darriet, L. Elcoro, A. El Abed, E. Gaudin, J.M. Perez - Mato, *Chem. Mater.*, **1989**, 14, 3349
- Darriet1995* J. Darriet, A.M. Subramanyam, *Chem Mater*, 1995,5, 543
- David2011* R. David, A. Pautrat, H. Kabbour, M. Sturza, S. Curelea, G. André, D. Pelloquin, O. Mentré, *Chem Matt*, **2011**, dx.doi.org/10.1021/cm202106t
- Delattre2002* J.L. Delattre, A.M. Stacy, V.G. jr. Young, G.-J. Long, R. Hermann, F. Grandjean, *Inorg. Chem.*, **2002**, 41 (11), 2834

- Delattre2004* J.L. Delattre, A.M. Stacy, T. Siegrist, *JSSC*, **2004**, 177, 928
- Dudarev1998* S.L. Dudarev, G.A. Botton, S.Y. Savrasov, C. Humphreys, A.P. Sutton, *Phys. Rev. B*, **1998**, 57, 1505.
- E.**
- Ehora2007* G. Ehora, C. Renard, S. Daviero-Minaud, and O. Mentré, *Chem. Mater.*, **2007**, 19, 12, 2924
- Ehora2007a* G. Ehora, S. Daviero-Minaud, M. Colmont, G. André, O. Mentré, *Chem. Mater.*, **2007**, 19, 2180
- Ehora2007b* G. Ehora, « Nouveaux oxides à valence mixte: transfer de la chimie à l'électrochimie du solide », **2007**, thesis,
- Elwell1980* D.Elwell, "High-Temperature Solution Growth", Ed. Pergamon Press : New York, **1980**, 12, 432
- Erchak1946* M. Erchak, I. Fankuchen, R. Ward, *J. Am Chem Soc.* , **1946**, 68, 2085
- F.**
- Fauth2002* F. Fauth, E. Suard, V. Caignaert, I. Mirebeau, *Phys. Rev.*, **2002**, B66, 184421
- Floros2000* N. Floros, C. Michel, M. Hervieu, B. Raveau, *Chem. Matter.*, **2000**, 12, 3197
- Floros2002* N. Floros, C. Michel, M. Hervieu , B. Raveau, *JSSC*, **2002**, 168, 11
- Forbes 2006* T. B. Forbes, *Engineering System Dynamics*, **2006**, 43, CRC Press
- G.**
- Goldschmidt1926* Goldschmidt, V. M. *Naturwissenschaften*, **1926**, 14, 477
- Gomez2001* M.I. Gomez, G. Lucotti, J.A. de Moran, P.J. Aymonino, S. Pagola, P.W. Stephens, R.E. Carbonio, *JSSC*, **2001**, 160, 17

- Gonzales –Calbet1990* J.M. Gonzales – Calbet, M. Parras, M.J. Vallet – Regi, J.C. Grenier, *JSSC*, **1990**, 86, 149
- Gonzales –Calbet1993* J.M. Gonzales – Calbet, M. Parras, J.M. Alonso, M.J. Vallet – Regi, *SSC*, **1993**, 106, 99
- Gonzales-Calbet1993b* M. Parras, J.M. Gonzales – Calbet, J.M. Alonso, , M.J. Vallet – Regi, *SSC*, **1995**, 113, 78
- Gonzales –Calbet1994* J.M. Gonzales – Calbet, M. Parras, J.M. Alonso, M.J. Vallet – Regi, *SSC*, **1994**, 111, 202
- Gonzales-Calbet1995a* M. Parras, J.M. Alonso, J.M. Gonzales – Calbet, M.J. Vallet – Regi, *SSC*, **1995**, 117, 21
- Goodenough1963* J. B. Goodenough, *Wiley – Interscience*, 1963, New – York
- Grey1998* I.E. Grey, C. Li, L.M.D.Cranswick, R.S Roth, T.A.Vanderah, *JSSC*, **1998**, 135, 312
- Grenier1989* J.C. Grenier, A. Wattiaux, M. Pouchard, P. Hazgenmuller, M. Parras, M. Vallet – Regi, J.M. Gonzalez – Calbert, M.A. Alario – Franco, *JSSC*, **1989**, 80, 6
- H.**
- Hall1977* M.M. Hall, *J. Apl. Cryst.*, **1977**, 10, 66
- Hardy1962* A. Hardy, *Acta. Crysta.*, **1962**, 15, 179
- Hardy2004* V. Hardy, M. R. Lees, O. A. Petrenko, D. M. K. Paul, D. Flahaut, S.Hebert, and A. Maignan, *Phys. Rev.B* , **2004**, 70, 64424
- Hébert2007* S. Hébert, V. Pralong, D. Pelloquin, A. Maignan, *JMMM*, **2007**, 316, 394
- Hector2001* A. L. Hector, J. A. Hutchings, R. L. Needs, M. F. Thomas and T. Weller, *Chem. Mater.*, **2001**, 11, 527
- Helmot1993* R. von Helmot, J. Wecker, B. Holzapfel, L. Schultz, K. Sam-Wer, *Phys. Rev. Lett.*, **1993**, 71, 2331
- Hill1976* R.M. Hill, *Phys. Stat. Sol.* , **1976**, 34, 601
- Hong1997* S.T. Hong, A.W. Sleight, *JSSC*, **1997**, 128, 251
- Hu2004* Z. Hu, H. Wu, M.W. Haverkort, H. H. Hseih, H. J. Lin, T. Lorentz, J. Baier, A. Reichl, I. Bonn, C. Felser, A. Tanaka, C.T. Chen, L.H. Tjeng, *Phys. Rev. B*, **2004**, 92, 207402

- Huang2008* D. Huang, Q. Xu, F. Zhang, W. Chen, H. Liu, J. Zhou, *J. of Wuhan University of Technology-Mater. Sci. Ed*, **2008**, 23, 8
- I**
- Ibberson2002* R. M. Ibberson, W. I.F. David, *Neutron powder diffraction*, **2002**, IUCr – Oxford, 5
- Iorgulescu2010* M. Iorgulescu, H. Kabbour, N. Tancret, O. Mentré, P. Roussel, *Chem. Commun.*, **2010**, 46, 5271
- J.**
- Jacobson1976* A.J. Jacobson, *Acta Crysta. B*, **1976**, 32, 1087
- Jacobson1980* A. Jacobson, J. L. Hutchison, *JSSC.*, **1980**, 35, 334
- Jost1977* K.H. Jost, B. Ziemer, R. Seydel, *Acta Crysta. B*, **1977**, 33, 1696
- K.**
- Karvonen2008* L. Karvonen, H. Yamauchi, M. Karppinen, *Chem. Mater.* **2008**, 20, 7143
- Kauffmann2006* M. Kauffmann, O. Mentré, A. Legris, N. Tancret, F. Abraham and P. Roussel, *Chem. Phys. Lett.*, **2006**, 432, 88
- Kauffmann2007a* M. Kauffmann, N. Tancret, F. Abraham, P. Roussel, *SSS*, **2007**, 9, 885
- Kauffmann2007b* M. Kauffmann, P. Roussel, *Acta Crysta. B*, **2007**, 63, 589
- Kauffmann2007c* M. Kauffmann, « *Structure, dimensionnalité et magnétisme de nouvelles halogéno-cobaltites* », **2007**, thesis
- Kauffmann2008* M. Kauffmann, O. Mentré, A. Legris, S. Hebert, A. Pautrat, P. Roussel, *Chem. Mater.*, **2008**, 20, 1741
- Katz1964* L. Katz, R. Ward, *Inorg. Chem.* **1964**, 3, 205.
- Kenneth2004* L. K. Kenneth, *Electromagnetic Compatibility Handbook*. 2004, CRC Press, 13.
- Korotin2006* M.A. Korotin, S. Ezhov, I.V. Solovyev, V. I. Anisimov, D.I. Khomskii, G.A. Sawatzky, *Phys. Rev. B*, **1996**, 54(8), 5309
- Kresse2004.* G. Kresse, J. Furthmuller, *Vienna Ab-initio Simulation Package (VASP)*, 2004, Institut für Materialphysik, Vienna.
- Kresse1999* G. Kresse and D. Joubert, *Phys. Rev. B*, **1999**, 59, 1758

- Kuroda1981* K. Kuroda, N. Ishizawa, N. Mizutani, M. Kato, *JSSC*, **1981**, 38, 297
- Kuphaldt2006* T.R. Kuphaldt, *Lessons in electrical circuits*, **2006**, 1 - DC, 282
- L.**
- Lander1951* J.J. Lander, *Acta Crysta.*, **1951**, 4, 148
- Leib1985* W. Leib, H. Mueller, *Buschbaum, Zeitschrift fuer Anorganische und Allgemeine Chemie*, **1985**, 521, 56
- Leslie – Pelecki1996* D.L. Leslie – Pelecki, R.D. Riecke, *Chem Matter*, **1996**, 8, 1770
- Lengesdorf2007* R. Lengesdorf, J.P. Rueff, G. Vanko, T. Lorenz, L.H. Tjeng, M.M. Abd-Elmeguid, *Phys. Rev. B*, **2007**, 75, 181401
- Liu1993a* G. Liu, J. E. Greedan, W. H. Gong, *JSSC*. **1993**, 105,78
- Liu1993b* G. Liu, J. E. Greedan, *JSSC*. **1993**, 103, 228
- Lovesey1984*, S. W. Lovesey, *Theory of Neutron Scattering from Condensed Matter*, **1984**, 1
- Lucchini1973* E. Lucchini, S. Meriani, D. Minichelli, *Acta Crysta. B.*, **1973**. 29, 1217
- M.**
- Maignan2000* A. Maignan, C. Michel, A. C. Masset, C. Martin, B. Raveau, *Europ. Phys. Jour. B*, **2000**, 15, 657
- Maignan2002* A. Maignan, L. Wang, S. Hébert, D. Pelloquin, B. Raveau, *Chem. Mater.* , **2002**, 14, 1231.
- Malinofsky1954* W. W. Malinofsky, H. Kedesdy, *J.AC.S.*, **1954**,76, 3090
- Mansfield1991* R. Mansfield, « *Hopping transport in solids* », **1991**, Pollak M. and Shklovskii B.I., Amsterdam,
- Mattausch1971* H. Mattausch, H .Muller-Buschbaum, *Z. Anorg. Allg. Chem.* **1971**, 386, 1
- Mattausch1974* H. Mattausch, H. Muller-Buschbaum, *Z. Anorg. Allg. Chem.* **1974**, 407, 129
- Meyer1978* G.M. Meyer, R.J. Nelmes, J. Hutton, *Ferroelectrics*, **1978**, 21, 461
- Mentré2008* O. Mentré, M. Kauffmann, G. Ehora, S. Daviero-Minaud, F.

- Abraham, P. Roussel, SSS, **2008**, 10, 471
- Mentré2010* O. Mentré, H. Kabbour, G. Ehora, S. Daviero-Minaud, G. Tricot and M. Whangbo, *JACS*, **2010**, 132(13), 4865
- Miranda2007* L. Miranda, J. Ramirez-Castellanos, A. Varela, J. Gonzalez-Calbet, M. Parras, M. Hernando, M. T. Fernandez-Diaz, M. Garcia Hernandez, *Chem. Mater.* **2007**, 19, 1503.
- Miranda2007a* L. Miranda, J. Ramírez-Castellanos, M. Hernando, A. Varela, J. M. González-Calbet, M. Parras, *Eur. J. Inorg. Chem.*, **2007**, 2129
- Miranda2008* L. Miranda, A. Feteira, D. C. Sinclair, M. G. Hernández, K. Boulahya, M. Hernando, A. Varela, J. M. González-Calbet, M. Parras, *Chem. Mater.* 2008, 20, 2818
- Miranda2009* L. Miranda, D C Sinclair, M Hernando, A Varela, A Wattiaux, K Boulahya, J. M. Gonzalez-Calbet, M. Parras, *Chem. Mater.*, **2009**, 21, 5272
- Mizusaki1983* J. Mizusaki, T. Sasamoto, W.R. Cannon, H.K. Bowen, , *J. Am. Ceram. Soc.*, **1983**, 66, 247
- Mizusaki1989* J. Mizusaki, J. Tabuchi, T. Matasuura, S. Yamauchi, K. Fueki, *J. Electrochem. Soc.*, **1989**, 136, 2082
- Mugnaioli2009* E. Mugnaioli, T. Gorelik, U. Kolb, *Ultramicroscopy*, **2009**, 109, 758
- Momma2008* K. Momma, F. Izumi : *J. Appl. Crystallogr.*, 2008, 41, 653
- Muller-Buschbaum1990* H. Muller – Buschbaum, M. Scheikowski, *Z. Anorg. Allg. Chem.*, **1990**, 591, 174
- Müller2006* P. Müller, “*Crystal Structure Refinement: A Crystallographer's Guide to SHELXL*”, **2006**, IUCr/Oxford
- N.**
- Negas1971* T. Negas, R. S. Roth, *JSSC*. **1971**, 3, 323
- P.**
- Pardo2004a* V. Pardo, P. Blaha, M. Iglesias, K. Schwartz, D. Baldomir, J.

- E. Arias, *Phys. Rev. B*, **2004**, 70, 1444422
- Pardo2004b* V. Pardo, J. Rivas, D. Baldomir, P. Blaha, M. Iglesias, K. Schwartz, J. E. Arias, *Phys. Rev. B*, **2004**, 70, 212404
- Pardo2007* V. Pardo, P. Blaha, R. Laskowski, D. Baldomir, J. Castro, K. Schwarz, J. E. Arias, *Phys. Rev. B*, **2007**, 76, 165120
- Parras1995*, M. Parras, A. Varela, H. Seehofer, J.M. Gonzalez- Calbert, *JSSC*, **1995**, 120, 327
- Pelloquin2007* D.Pelloquin, O.Perez, G.Martinet, S.Hebert, A.Maignan, *Chem. Mater.*, **2007**, 19, 2658.
- Perdew1992* J. P. Perdew and Y. Wang, *Phys. Rev. B*, 1992, 45, 13244
- Petricek2006* V. Petricek, M. Dusek and L. Palatinus, *JANA2006*, **2006**, Institute of Physics, Academy of Sciences, Praha, Czech Republic,
- Phuc2003* N. X. Phuc, L. V. Bau, N. V. Khiem, L. H. Son and D. N. H. Nam, *Phys. B: Condens. Matter*, **2003**, 327, 177.
- Poepelmeier1982* K. R. Poepelmeier, M. E.Leonowicz, J. C Scanlon, J.M. Longo, W. B. Yelon, *JSSC*, **1982**, 45, 71.
- Potoff1973* A. D. Potoff, B. L. Chamberland, L Katz, *JSSC*,**1973**, 8, 234
- Purcell1984*, E. M. Purcell, *Electricity and Magnetism*,1984, Berkeley Physics Course, 2
- Putnis1992* A. Putnis, *Introduction to Mineral Sciences*; Cambridge, **1992**, UK: Cambridge University Press,3, 41
- Q.**
- Quarez2003* E. Quarez, F. Abraham, O. Mentré, *JSSC*, **2003**, 176, 137
- Quarez2003a* E. Quarez, M. Huve, F. Abraham, O. Mentré, *SSC*, **2003**, 5, 951
- R.**
- Radaeli2002* P.G. Radaeli, S.W. Cheong, *Phys.Rev.*,2002, B66, 094408
- Ramirez1997*, P. Ramirez, *J. Phys. Condens. Matter*, **1997**, 9, 8171
- Raveau1998* B. Raveau, A. Maignan, C. Martin, M. Hervieu, *Chem. Mater.*, 1998, 10, 2641,

- Raveau2001 B. Raveau, M. Hervieu, A. Maignan, C. Martin, *J. Mater. Chem.*, **2001**, 11, 29.
- Rietveld1967 H.M. Rietveld, *Acta Cryst.*, **1967**, 22, 151
- Rietveld1969 H.M. Rietveld; *J. Appl. Cryst.*, **1969**, 2, 65
- RodriguezCarvajal1990 J. Rodriguez - Carvajal, « *FULLPROF: A program for Rietveld refinement and pattern matching analysis* », 1990, Abstract - the XV Congress of the IUCr, Toulouse, France,
- Roussel2008 P. Roussel, *Modélisation des phénomènes ordre – désordre dans les solides : apport des diffractions X et neutronique*, **2008**, public HDR
- Ruddlesden1957 S. N. Ruddlesden, P. Popper, *Acta Cryst.* **1957**, 10, 538
- S.**
- Shannon1976 R.D. Shannon, *Acta Cryst. A*, **1976**, 32, 751
- Shamshi, DOI: H. M. Shamshi, A.M. Shaheer, K. Shim, O.B. Yang, *Journal of Nanoscale Research Letters* Vol. 5 Issue 4 DOI: 10.1007/s11671-010-9547-8 10.1007/s11671-010-9547-8
- Sheldrick2008 G.M. Sheldrick, *Acta Cryst. A.*, **2008**, 64, 112
- Shpanchenko1990 R. V. Shpanchenko, E.V. Antipov, L.N. Lykova, L.M. Kovba, *Vestn. Mosk. Univ. Ser. 2: Khim*, **1990**, 31, 555
- Shull1995 C. Shull, *Rev. Mod. Phys.* , **1995**, 67, 753
- Spitsbergen1960 U. Spitsbergen, *Acta Cryst.*, **1960**, 13, 197
- Stanjek2004 H. Stanjek , W. Häusler, *Basics of X-ray Diffraction*, **2004**, Hyperfine interaction, 154, 107
- Strauss1951 S.W. Strauss, I. Fankuchen, R. Ward, *JACS*, **1951**, 73, 5084
- Sturza2010 M. Sturza, S. Daviero-Minaud, H. Kabbour, O. Gardoll, O. Mentré, *Chem Mater.*, **2010**, 22, 6726
- Sturza2011 M. Sturza, H. Kabbour, S. Daviero-Minaud, D.Filimonov, K. Pokholok, N. Tiercelin, F. Porcher, L. Aldon, O. Mentré, *JACS*, **2011**, 133, 10901
- Sturza2011b M. Sturza, « *Oxyfluorures de fer de type pérovskite: influence du sous – réseau anionique sur les structures et les propriétés physicochimiques* », **2011**, thesis

- Sun2006 J. Sun, M. Yang, G. Li, T. Yang, F. Liao, Y. Wang, M. Xiong, J. Lin, *Inorg. Chem.*, **2006**, 45, 9151.
- T.**
- Taguchi1977 H. Taguchi, Y. Takeda, F. Kanamaru, M. Shimida, M. Koizume, *Acta Cryst. B.*, **1977**, 33, 1299
- Takeda1976 Y. Takeda, F. Kanamura, M. Shimada, M. Koizumi, *Acta Cryst. B*, **1976**, 32, 2464
- Takeda1978 Y. Takeda, S. Naka, M. Takano, T. Shinjo, T. Takada and M. Shimada, *Bull. Inst. Chem. Res. Jpn.*, **1978**, 13, 61.
- Takizawa1996 H. Takizawa, H. Steinfink, *JSSC*, **1996**, 121, 133
- Tancret2005 N. Tancret, P. Roussel, F. Abraham, *JSSC.*, **2005**, 178, 3066
- Tancret2004 N. Tancret, P. Roussel, F. Abraham, *JSSC*, **2004**, 177, 1023
- Thomas1885 C. Thomas, *Physico – chemical constants*, **1885**, 1, D.Sc. (Lond), F.C.S.
- Toulemonde2010 O. Toulemonde, P. Roussel, O. Isnard, G. Andre', O. Mentre', *Chem Mater*, **2010**, 22, 3807
- U.**
- Vanko2006 G. Vanko, J.P. Rueff, A. Mattila, Z. Nemeth, A. Shukla, *Phys. Rev. B*, **2006**, 73, 024424
- Y.**
- Yamaura2000 K. Yamaura, R.J. Cava, *SSC*, **2000**, 115, 301
- Z.**
- Zanne1972 M. Zanne, A. Courtiois, C. Gleitzer, *Bul. Soc. Chim. F.*, **1972**, 12, 4470
- Zanne1971 M. Zanne, C. Gleitzer, *Bull. Soc. Chim. Fr.*, **1971**, 1567.
- W.**
- Wang2009 H. Wang, J. Yang, Z. Zhang, C. Dong, M. Fang, *Phys Lett A*, **2009**, 373 4092
- Wittry1958 D.B. Wittry, *Electron Probe Microanalyzer*, **1958**, Washington, DC, U.S.

Materials and methods

1. Powder synthesis:

The majority of the compounds presented in this manuscript were synthesised by the solid state reaction. The precursors used were oxides or carbonates with purity > 99%, carefully weighed in the proportion respecting the expected ratio, well ground in an agate mortar and introduced in an alumina crucible. The reaction mixture was then heated at the synthesis temperature in air using a tubular furnace. Depending on compounds, intermediate regrinding or several steps of synthesis at different heating temperatures (section Chapter 1. , Page 60), were required. Furnaces under different gas pressure (oxygen, nitrogen for inert atmosphere, 2%H₂ argon for reductive atmosphere) were used. The products obtained are presented like fine black powders.

2. Single crystals synthesis:

The crystals were obtained using the flux method (Elwell1980). The reactant with the lower melting point and water soluble was used as flux, in our case BaCl₂·2H₂O (melting point 963 °C) and BaBr₂ (melting point 880 °C) (Thomas1885). The method is particularly suitable for crystals needing to be free from thermal strain and it takes place in a crucible made of low-reactivity metal (platinum in our case). The flux–compound is introduced in a large excess in order to obtain a melted environment for dissolving all the others reactants. The reaction mixture is then slowly cooled to room temperature. The crystals of the flux-compound are washed on filter with hot water. The solubility of BaCl₂, for example, in water is 35.8g/100mL at 20°C and 59.4 g/100 mL at 100 °C. The presence of the BaCl₂ in the filtrate can be verified using a drop of sulphuric acid, when the following reaction takes place and a white barium sulphate precipitate is formed: $\text{BaCl}_2 + \text{H}_2\text{SO}_4 \rightarrow \text{BaSO}_4 + 2\text{HCl}$. The absence of the precipitate shows that all the excess of BaCl₂ was washed.

3. Electron probe microanalysis (EPMA):

Generalities: EPMA works by bombarding a micro-volume of a sample with a focused electron beam (typical energy = 5-30 keV) and collecting the X-ray photons thereby emitted by the various elemental species (Wittry1958). Because the wavelengths of these X-rays are characteristic of the emitting species, the sample composition can be easily identified by recording WDS spectra (Wavelength Dispersive Spectroscopy). WDS spectrometers are based on the Bragg's law and use various moveable, shaped monocrystals as monochromators. EPMA is a fully qualitative and quantitative method of non-destructive elemental analysis of micron-sized volumes at the surface of materials, with sensitivity at the level of ppm. Routine quantification to 1% reproducibility is obtained over several days. It is the most precise and accurate micro-analysis technique available and all elements from B to U and above can be analyzed. EPMA is fully compatible with routine analysis sessions, with easy and direct interpretation of the results. EPMA instruments are equipped with a complete kit of built-in microscopy tools that allow simultaneous X-ray (WDS and EDS), SEM and BSE imaging, plus sophisticated visible light optics. The schematic cut-away diagram of a typical microprobe analyzer is given in Figure 1, (a).

Instrumentation: Cameca SX100 electron probe microanalyser (EPMA) was used for elemental analysis in the case of $\text{Ba}_8\text{Mn}_6\text{Co}_2\text{ClO}_{22}$ compound (section 2.2.3.d) (Page 75), (Figure 1, (b)). Quantifications of the elements present in the samples were carried out at 15 kV and 15 nA with a spot size of 20 mm. A PET (Pentaerythritol) crystal was used to detect the Cl and Ba $\text{K}\alpha$ X-rays, a LiF crystal to detect Co and Mn $\text{K}\alpha$ X-rays, and a PC2 (multilayer crystal) to detect the Oxygen $\text{K}\alpha$ X-rays. Standards used for quantification were made of pure BaCl_2 , Co_3O_4 , MnO_2 powder pressed into small pellets.

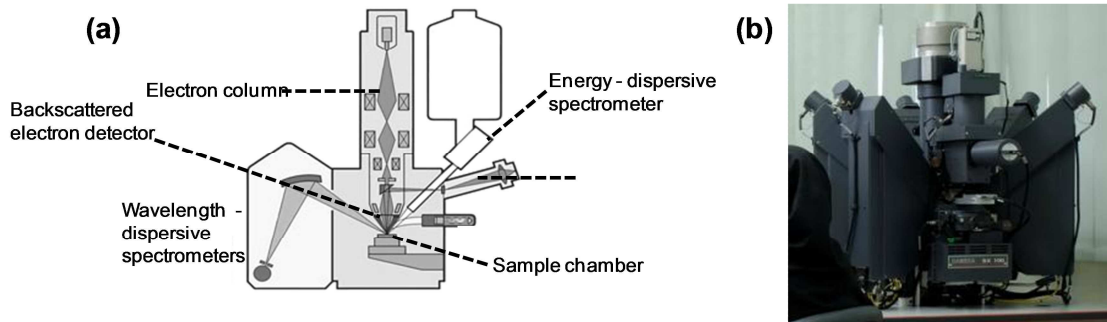


Figure 1: (a) Schematic cut-away diagram of a typical EPMA; (b) Cameca SX100 electron probe microanalyser

4. Scanning electron microscopy (SEM) and energy dispersive X-ray spectroscopy (EDS):

Generalities: The scanning electron microscope (SEM) uses a focused beam of high-energy electrons to generate a variety of signals at the surface of solid specimens. The signals reveal information about the sample including external morphology (texture), chemical composition, and crystalline structure and orientation of materials making up the sample. In most applications, data are collected over a selected area of the surface of the sample, and a 2-dimensional image is generated that displays spatial variations in these properties. Areas ranging from approximately 1 cm to 5 microns in width can be imaged in a scanning mode using conventional SEM techniques (magnification ranging from 20X to approximately 30,000X, spatial resolution of 50 to 100 nm). The SEM is also capable of performing analyses of selected point locations on the sample; this approach is especially useful in qualitatively or semi-quantitatively determining chemical compositions.

The design and function of the SEM is very similar to the EPMA and considerable overlap in capabilities exists between the two instruments (Ardenne1939). In a typical SEM, an electron beam is emitted from an electron gun fitted with a tungsten filament cathode (schema form Figure 2, (a)). Tungsten is normally used in thermionic electron guns because it has the highest melting point and lowest vapor pressure of all metals, thereby allowing it to be heated for electron emission, and because of its low cost. Other types of electron emitters include

lanthanum hexaboride (LaB₆) cathodes, which can be used in a standard tungsten filament SEM if the vacuum system is upgraded and field emission guns (FEG), which may be of the cold-cathode type using tungsten single crystal emitters or the thermally-assisted Schottky type, using emitters of zirconium oxide. The electron beam, which typically has an energy ranging from 0.5 keV to 40 keV, is focused by one or two condenser lenses to a spot about 0.4 nm to 5 nm in diameter. The beam passes through pairs of scanning coils or pairs of deflector plates in the electron column, typically in the final lens, which deflect the beam in the x and y axes so that it scans over a rectangular area of the sample surface. When the primary electron beam interacts with the sample, the electrons lose energy by repeated random scattering and absorption within a teardrop-shaped volume of the specimen known as the interaction volume, which extends from less than 100 nm to around 5 μm into the surface. The size of the interaction volume depends on the electron's landing energy, the atomic number of the specimen and the specimen's density. The energy exchange between the electron beam and the sample results in the reflection of high-energy electrons by elastic scattering, emission of secondary electrons by inelastic scattering and the emission of electromagnetic radiation, each of which can be detected by specialized detectors. The beam current absorbed by the specimen can also be detected and used to create images of the distribution of specimen current. Electronic amplifiers of various types are used to amplify the signals which are displayed as variations in brightness on a cathode ray tube. The raster scanning of the CRT display is synchronized with that of the beam on the specimen in the microscope, and the resulting image is therefore a distribution map of the intensity of the signal being emitted from the scanned area of the specimen. The image may be captured by photography from a high resolution cathode ray tube, but in modern machines is digitally captured and displayed on a computer monitor and saved to a computer's hard disk.

Instrumentation: The scanning electron microscope used in the work presented in this manuscript is Hitachi S4700 equipped with an EDS microanalyzer and with field emission guns (FEG) (Figure 2, (b)).

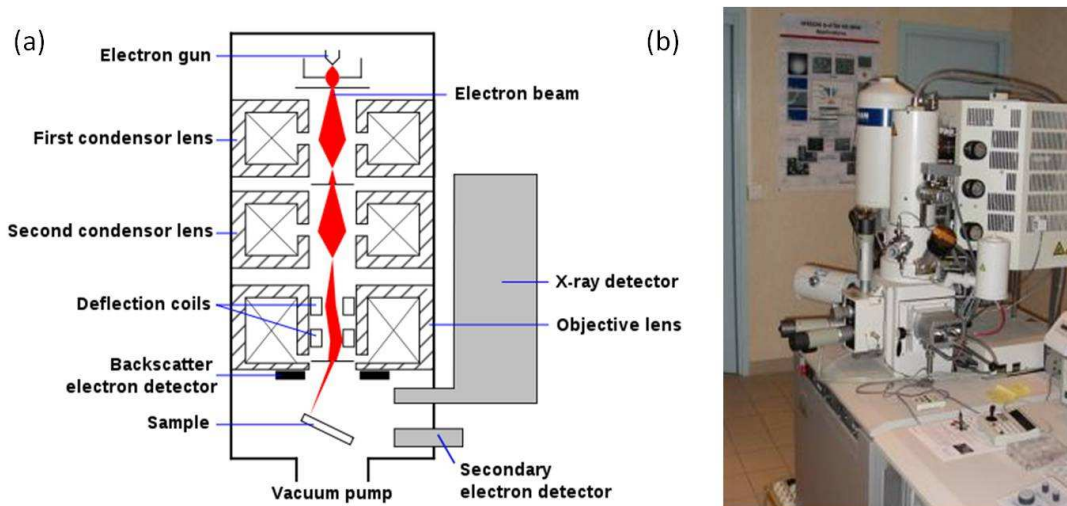


Figure 2: (a) Schema for SEM machine and (b) Hitachi S4700

5. Transmission electron microscopy (TEM):

Transmission electron microscopy (TEM) is a microscopy technique whereby a beam of electrons is transmitted through an ultra-thin specimen, interacting with the specimen as it passes through. An image is formed from the interaction of the electrons transmitted through the specimen; the image is magnified and focused onto an imaging device, such as a fluorescent screen, on a layer of photographic film, or to be detected by a sensor such as a CCD camera. The schema is given in Figure 3 (I). TEM is capable of imaging at a significantly higher resolution than light microscopes, owing to the small de Broglie wavelength of electrons. This enables the instrument's user to examine fine detail — even as small as a single column of atoms — which is ten of thousands times smaller than the smallest resolvable object in a light microscope. TEM forms a major analysis method in a range of scientific fields, in both physical and biological sciences. TEMs find application in cancer research, virology, materials science as well as pollution, nanotechnology, and semiconductor research. At smaller magnifications TEM image contrast is due to absorption of electrons in the material, due to the thickness and composition of the material. At higher magnifications complex wave interactions modulate the intensity of the image, requiring expert analysis of observed images. Alternate modes of use allow for the TEM to observe modulations in chemical identity, crystal orientation, electronic structure and sample induced electron phase

shift as well as the regular absorption based imaging. A TEM image of Pr_6O_{11} (ShamshiDOI: 10.1007/s11671-010-9547-8) is given in Figure 3 (II) (a). In this work, the transmission electron microanalyser used is FEI Tecnai G 220.

6. High-resolution transmission electron microscopy (HRTEM):

High-resolution transmission electron microscopy (HRTEM) is an imaging mode of the (TEM) that allows the imaging of the crystallographic structure of a sample at an atomic scale. Because of its high resolution, it is an invaluable tool to study nanoscale properties of crystalline material such as semiconductors and metals. At present, the highest resolution realized is 0.8 \AA (0.08 nm).

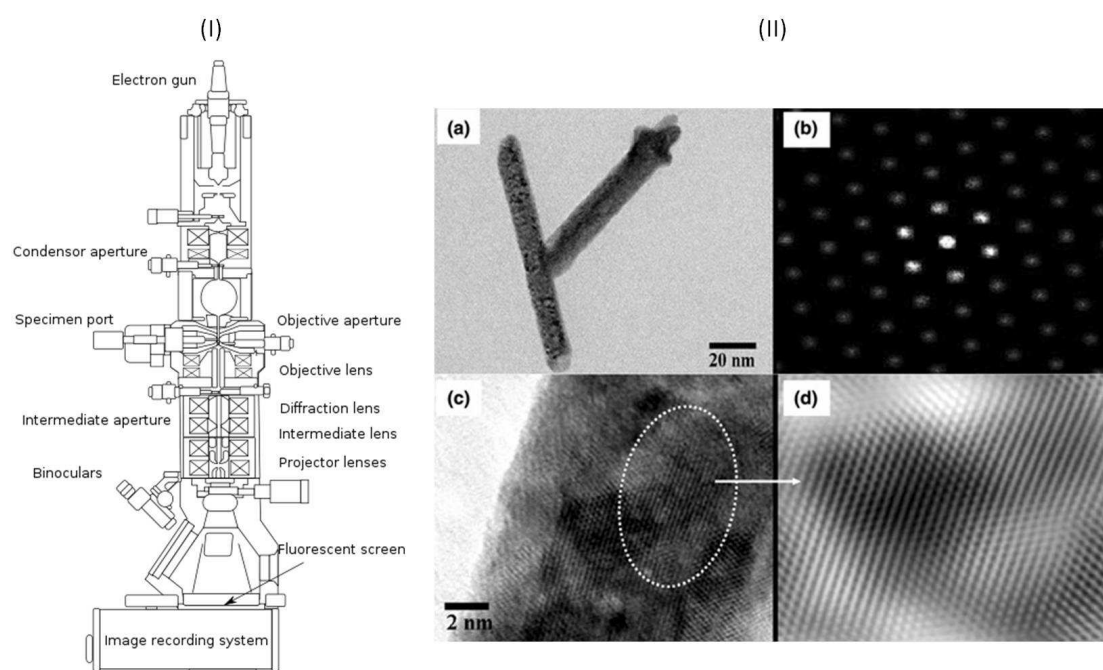


Figure 3: (I) Schema of transmission electron microanalyser and (II) (a) TEM image, (b) SAED image; (c) HRTEM and (d) FFT of HRTEM image for Pr_6O_{11}

Ongoing research and development will soon push the resolution of HRTEM to 0.5 \AA . At these small scales, individual atoms and crystalline defects can be imaged. Since all crystal structures are 3-dimensional, it may be necessary to combine several views of the crystal, taken from different angles, into a 3D map. This technique is called electron crystallography. One of the difficulties with HRTEM is that image formation relies on phase-contrast. In phase-contrast imaging, contrast is not necessarily intuitively interpretable as the image is influenced by strong aberrations

of the imaging lenses in the microscope. One major aberration is caused by focus and astigmatism, which often can be estimated from the Fourier transform of the HRTEM image. The HRTEM image and Fast Fourier transform (FFT) image of Pr_6O_{11} is given in Figure 3, (II), (c) and (d).

7. Selected area electron diffraction (SAED):

Selected area (electron) diffraction (abbreviated as SAD or SAED), is a crystallographic experimental technique that can be performed inside a transmission electron microscope (TEM). In a TEM, a thin crystalline specimen is subjected to a parallel beam of high-energy electrons. As TEM specimens are typically ~100 nm thick, and the electrons typically have energy of 100-400 kiloelectron volts, the electrons pass through the sample easily. In this case, electrons are treated as wave-like, rather than particle-like. Because the wavelength of high-energy electrons is a few thousandths of a nanometer, and the spacing between atoms in a solid is about a hundred times larger, the atoms act as a diffraction grating to the electrons, which are diffracted. That is, some fraction of them will be scattered to particular angles, determined by the crystal structure of the sample, while others continue to pass through the sample without deflection. As a result, the image on the screen of the TEM will be a series of spots—the selected area diffraction pattern, SADP, each spot corresponding to a satisfied diffraction condition of the sample's crystal structure. If the sample is tilted, the same crystal will stay under illumination, but different diffraction conditions will be activated, and different diffraction spots will appear or disappear. The SAED image of Pr_6O_{11} is given in Figure 3 (II), (b).

8. Infrared spectroscopy:

Infrared spectroscopy (IR spectroscopy) deals with the infrared region of the electromagnetic spectrum, light with a longer wavelength and lower frequency than visible light. It covers a range of techniques, mostly based on absorption spectroscopy. As with all spectroscopic techniques, it can be used to identify and study chemicals (*Colthup1990*). The infrared portion of the electromagnetic spectrum is usually divided into three regions; the near-, mid- and far- infrared, named for their relation to the visible spectrum. The higher energy near-IR, approximately 14000–

4000 cm^{-1} (0.8–2.5 μm wavelength) can excite overtone or harmonic vibrations. The mid-infrared, approximately 4000–400 cm^{-1} (2.5–25 μm) may be used to study the fundamental vibrations and associated rotational-vibrational structure. The far-infrared, approximately 400–10 cm^{-1} (25–1000 μm), lying adjacent to the microwave region, has low energy and may be used for rotational spectroscopy (*Colthup 1990*). The names and classifications of these sub-regions are conventions, and are only based on the relative molecular or electromagnetic properties. The infrared spectrum of a sample is recorded by passing a beam of infrared light through the sample. When the frequency of the IR is the same as the vibrational frequency of a bond, absorption occurs. Examination of the transmitted light reveals how much energy was absorbed at each wavelength. This can be done with a monochromatic beam usually created by an Interferometer, but also may have a monochromator before the Infrared detector, which changes in wavelength over time. Analysis of these absorption characteristics reveals details about the molecular structure of the sample.

9. Thermo – gravimetric analysis (TGA):

The eventual phase transformation, oxygen loss and oxygen gain were analysed by thermo – gravimetric analysis (TGA). Thermogravimetric analysis or thermal gravimetric analysis (TGA) is a type of testing performed on samples that determines changes in weight, in relation to changes in temperature. Such analysis relies on a high degree of precision in three measurements: weight, temperature, and temperature change. As many weight loss curves look similar, the weight loss curve may require transformation before results may be interpreted. A derivative weight loss curve can identify the point where weight loss is most apparent. Again, interpretation is limited without further modifications and deconvolution of the overlapping peaks. Analysis is carried out by raising the temperature of the sample gradually and plotting weight (percentage) against temperature. The temperature in many testing methods routinely reaches 1000°C or greater. After the data are obtained, curve smoothing and other operations may be done to find the exact points of inflection. The method consists in measuring the weight modification of the sample with the temperature. The residuals gases evolved in the heating process can be analysed by coupled TGA – MS (mass spectroscopy). For the analysis of the oxygen loss or oxygen gain, the samples were heated at high temperatures (900 – 1000°C)

and then cooled to room temperature, with a second reheating to verify if the samples will lose even more oxygen with the second reheating. A typical thermogravimetric analyser is given in Figure 4



Figure 4: Thermogravimetric analyzer

10. **Maximum entropy method (MEM):**

The target of a diffraction experiment is to provide information about the structure of the compound studied. The information concerning the average order (long distance) are contained in the Bragg peaks, while the information regarding the local order (short distance) are contained in the diffuse scattering situated between the Bragg spots and this is the one to permit the disorder affecting the crystalline periodicity. In the same time, the Bragg peaks are also affected by the disorder. In conclusion, the information given by the Bragg peaks is not related only to the crystalline order, but also to the disorder phenomena. These phenomena have mostly a low intensity and can be described only by a much elaborated image. A method to describe these phenomena is the Fourier maps but some limits are attributed to this method (difficult to use when the data set is not complete). In this case (incomplete data set), another complementary method is MEM. This method permits the reconstruction of the most probable electronic (or nuclear) density (*Roussel2008*). In this work, the software used for the visualization of the most probable electronic (or nuclear) density is Vesta (*Momma2008*).

11. Iodometric titration:

Method description and installation: The iodometric titration method was first used by (Karvonen2008) and it was modified in order to be applicable to our compounds. 0.3 g of KI were dissolved in an HCl solution 9.25% and the resulted solution was kept under N₂ for 30 min. 0.02 grams of compound were dropped into the solution using a glass sample holder in order to reduce at maximum the errors due to the powder loss and agitated under N₂ until complete dissolution of the black powder. At this step, the colour of the solution will change to yellow – orange as the +3 and +4 cations (M = Co, Fe, Mn)) react with I⁻ from KI after the reactions given in Figure 5 (a) forming I₂.

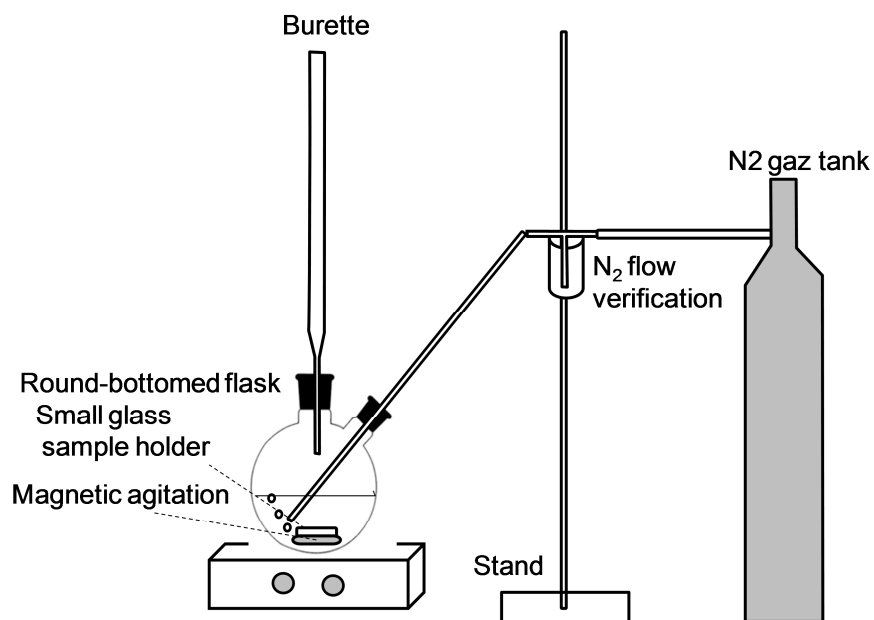


Figure 5: Iodometric titration installation.

The I₂ form is at this step titrated using a 0.02 M solution of Na₂S₂O₃. Close to the equilibrium, the solution changes from orange to light yellow and 2 – 3 drops from a starch solution are added in order to highlights the change of the coloration. The coloration of the solution will change again to violet due to the formation of a purple complex between the starch solution and I₂ left unreacted in the solution. The end of the titration is indicated by the change of the coloration of the solution from violet to colourless as all the I₂ from *the starch* + I₂ violet complex is

consumed by $\text{Na}_2\text{S}_2\text{O}_3$ after the reaction from Figure 6 (a). The special condition of titration (elimination of the O_2 from the solution due to the instability of M^{+4} (especially Co^{+4})) requires a special red – ox titration installation. This installation is presented in Figure 5.

Standard oxido - reduction potentials and the Gamma rule: The condition for oxido – reduction process to take place is to respect the Gamma rule. This is summarized in Figure 6 (b). The standard oxido - reduction potentials and the Gamma rule applied in the case of the ionic species presents in solution (in gray) for both Co – Fe and Co – Mn mixed compounds is given in Figure 7 (a) and (b) respectively. As seen in the schema from Figure 7, the presence of Cl^- does not affect our titration due to his reducer character. The formation of species as $(\text{ClO}_4)^-$, $(\text{ClO}_3)^-$, $(\text{ClO}_2)^-$, $(\text{ClO})^-$ from the reaction of Cl^- with H_2O or H^+ is unlikely for the same reason ($\text{Cl}^- = \text{reducer}$). In Figure 7, in the cases of M^{+4} reductions to M^{+2} or M^{+3} , the values of oxido - reduction potentials have not yet been determined and now evidence is given in the tables of standard oxido - reduction potentials, but, by assimilation to others cases, the values of these potentials should be bigger than for +3 cations.

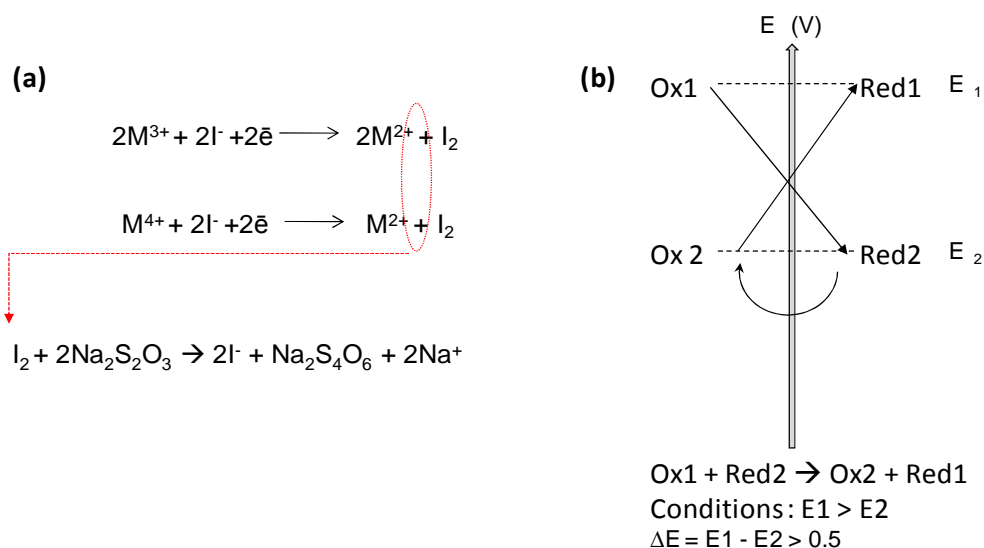


Figure 6: (a) Schema of oxido – reduction process implied in the iodometric titration of the compounds presented in this manuscript ($M = \text{Co}, \text{Fe}, \text{Mn}$); (b) schema of Gamma rule

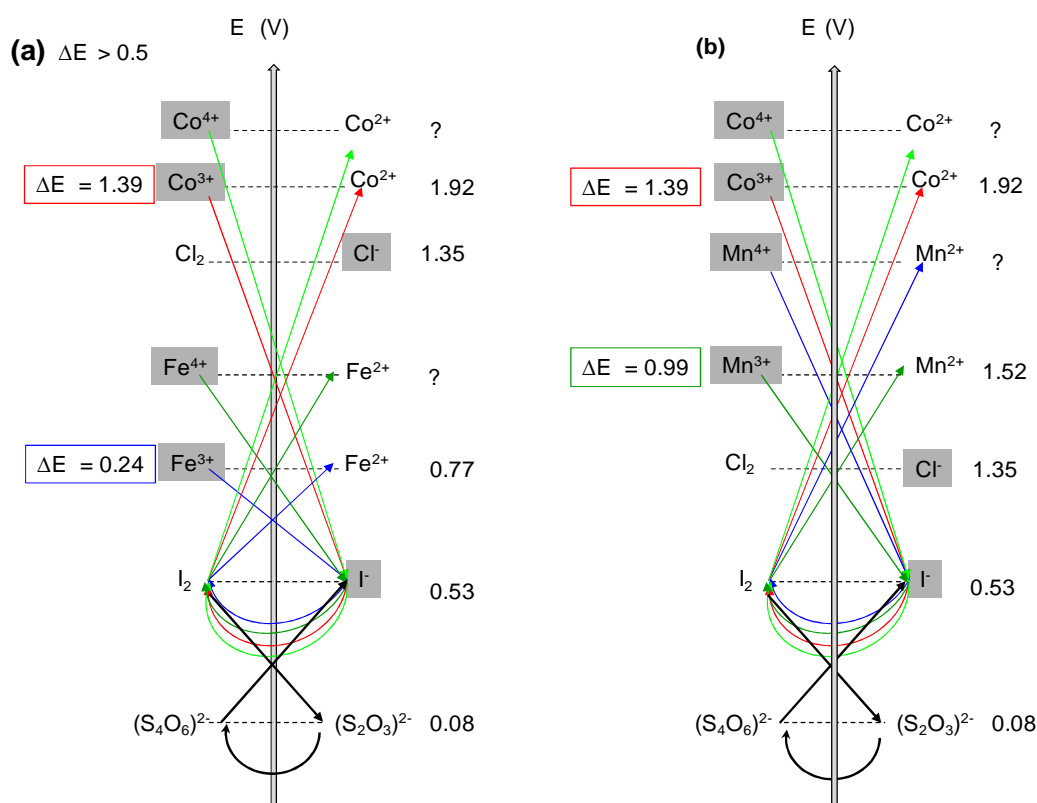


Figure 7: Standard oxido – reduction potentials (V) and Gamma rule for the ionic species present in solution (given in gray) in the case of mixed Co – Fe compounds (a) and Co – Mn compounds (b). The question marks show the oxido - reduction potentials that have not yet been determined.

Case of Co compounds and Co – Mn compounds: The case of Co compounds was the most simple since the difference between the oxido- reduction potentials for $\text{Co}^{3+}/\text{Co}^{2+}$ reaction with I_2/I^- is very big ($\Delta E = E(\text{Co}^{3+}/\text{Co}^{2+}) - E(\text{I}_2/\text{I}^-) = 1.39\text{V}$). The Gamma rule in this case is given in red in both (a) and (b) schema from Figure 7. In the same way, the iodometric titration of Co – Mn compounds is working very well due to big $\Delta E = 0.99\text{V}$ in the Mn case (Figure 7, (b)).

Case of mixed Co – Fe compounds : It was the most difficult case due to the very small ΔE in this case (0.24 V) comparing to the minimal allowed value (0.5 V), (Figure 7, (a)) in order that reaction takes place (Gamma rule). So the possibility of the reduction of Fe species present in solution was tested on compounds like Fe_2O_3 and also on compounds where the average oxidation degrees were determined by neutron diffraction or others complementary techniques. The method seems to work for Fe also and the results obtained were in good accordance with the

expectations. Since for the Co – Fe and Co – Mn mixed compounds, the iodometric titration is working well, no problem can be expected in the case of mixed Fe – Mn compounds.

Average oxidation degree and oxygen content calculation: Knowing the concentration and the volume of titrate used (C_T and V_T), we can calculate the number of moles of M that were titrated: $n(M_{\text{titrated}}) = C_T * V_T$. Using the weighed mass of the compound and the molecular weight W , we can also calculate the number of moles of the transitional metal in the compound: $n(M_{\text{total}}) = (m * \text{number of M}) / W$. If the $n(M_{\text{titrated}}) > n(M_{\text{total}})$, the difference is: $n(M_{\text{titrated}}) - n(M_{\text{total}}) = n(M^{+4})$. The valence will be calculated using the formula: $[n(M^{+3}) \times 3] + [n(M^{+4}) \times 4] / n(M_{\text{total}})$.

12. X-ray diffraction

Fundamental Principles of X-ray Diffraction (XRD): X-ray diffraction (XRD) is a rapid analytical technique primarily used for phase identification of a crystalline material and can provide information on unit cell dimensions. The analyzed material is finely ground, homogenized, and average bulk composition is determined. Max von Laue, in 1912, discovered that crystalline substances act as three-dimensional diffraction gratings for X-ray wavelengths similar to the spacing of planes in a crystal lattice. X-ray diffraction is now a common technique for the study of crystal structures and atomic spacing. X-ray diffraction is based on constructive interference of monochromatic X-rays and a crystalline sample (Putnis1992). These X-rays are generated by a cathode ray tube, filtered to produce monochromatic radiation, collimated to concentrate, and directed toward the sample. The interaction of the incident rays with the sample produces constructive interference (and a diffracted ray) when conditions satisfy Bragg's Law ($n\lambda = 2d \sin \theta$). This law relates the wavelength of electromagnetic radiation to the diffraction angle and the lattice spacing in a crystalline sample. These diffracted X-rays are then detected, processed and counted. By scanning the sample through a range of 2θ angles, all possible diffraction directions of the lattice should be attained due to the random orientation of the powdered material. Conversion of the diffraction peaks to d-spacing allows identification of the mineral because each mineral has a set of unique d-spacing (Stanjek2004). Typically, this is achieved by comparison of d-spacing with standard

reference patterns. All diffraction methods are based on generation of X-rays in an X-ray tube. These X-rays are directed to the sample, and the diffracted rays are collected. A key component of all diffraction is the angle between the incident and diffracted rays. Powder and single crystal diffraction vary in instrumentation beyond this.

X-ray powder diffraction instrumentation: X-ray diffractometers consist of three basic elements: an X-ray tube, a sample holder, and an X-ray detector. X-rays are generated in a cathode ray tube by heating a filament to produce electrons, accelerating the electrons toward a target by applying a voltage, and bombarding the target material with electrons. When electrons have sufficient energy to dislodge inner shell electrons of the target material, characteristic X-ray spectra are produced. These spectra consist of several components, the most common being $K\alpha$ and $K\beta$. $K\alpha$ consists, in part, of $K\alpha_1$ and $K\alpha_2$. $K\alpha_1$ has a slightly shorter wavelength and twice the intensity as $K\alpha_2$. The specific wavelengths are characteristic of the target material (Cu, Fe, Mo, Cr). Filtering, by foils or crystal monochromators, is required to produce monochromatic X-rays needed for diffraction. $K\alpha_1$ and $K\alpha_2$ are sufficiently close in wavelength such that a weighted average of the two is used (*Bish 1989*). Copper is the most common target material for diffraction, with $CuK\alpha$ radiation = 1.5418Å but Mo is also used ($MoK\alpha$ radiation = 0.7107Å). These X-rays are collimated and directed onto the sample. As the sample and detector are rotated, the intensity of the reflected X-rays is recorded. When the geometry of the incident X-rays impinging the sample satisfies the Bragg Equation, constructive interference occurs and a peak in intensity occurs. A detector records and processes this X-ray signal and converts the signal to a count rate which is then output to a device such as a printer or computer monitor. Diffractometers can be operated both in transmission and in reflection configurations. The reflection one is more common. The powder sample is filled in a small disc like container and its surface carefully flattened. The disc is put on one axis of the diffractometer and tilted by an angle θ while a detector (scintillation counter) rotates around it on an arm at twice this angle. This configuration is known under the name Bragg-Brentano. Another configuration is the theta-theta configuration in which the sample is stationary while the X-ray tube and the detector are rotated around it. The angle formed between the tube and the detector is 2θ . This configuration is most convenient for loose powders. The availability of position sensitive detectors and CCD's (bidimensional cooled camera detector) is making this

type of equipment more and more obsolete. In this work, two different powder diffractometers were used.

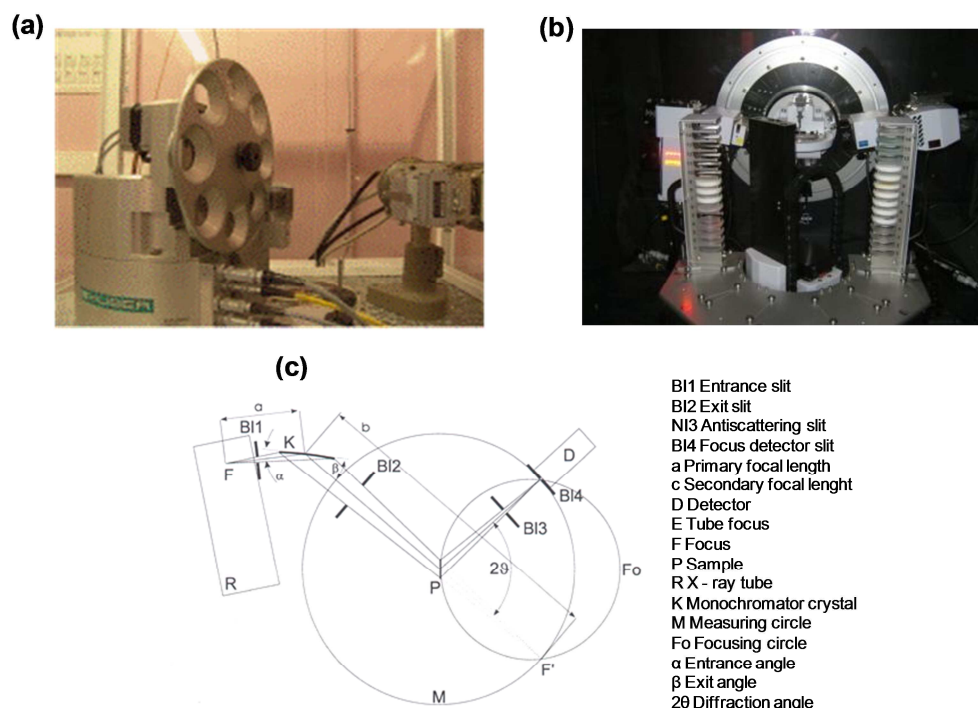


Figure 8: Different X – ray powder diffractometers used for powder structural investigation; (a) RX Huber G670 diffractometer and (b) D8 Advance (Bruker-AXS) and (c) the schematic diagram from Bruker AXS manual for D8 Advance diffractometer

A short description of the diffractometers used is given below. The X – ray diffractograms were recorded between 4 and 90° 2 θ , for a simple identification and for the refinement of the unit cell parameters, but for the structural refinement, a bigger angular domain was needed (4 – 120° 2 θ).

- RX Huber G670 diffractometer with Guinier geometry (Figure 8, (a)) equipped with front-monochromator using $\text{CuK}_{\alpha 1}$ radiation ($\lambda = 1.54056\text{\AA}$) with 8 samples using transmission.
- D8 Advance (Bruker-AXS) (Figure 8, (b)) using a rapid Lynxeye detector and an auto sampler with 90 positions working in transmission as well as in reflection geometry. Is using $\text{CuK}_{\alpha 1}$ and $\text{CuK}_{\alpha 2}$ radiation ($\lambda_1 = 1.54056\text{\AA}$ and $\lambda_2 = 1.54439\text{\AA}$ with a ratio equal to 0.5). It enables a quick switch between the para-focusing Bragg-Brentano geometry to parallel beam geometry without realignment of the system.

X-ray single crystals diffraction instrumentation: Molybdenum is the most common target material for single-crystal diffraction, with MoK α radiation = 0.7107Å. These X-rays are collimated and directed onto the sample. When the geometry of the incident X-rays impinging the sample satisfies the Bragg Equation, constructive interference occurs. A detector records and processes this X-ray signal and converts the signal to a count rate which is then output to a device such as a printer or computer monitor. Single-crystal diffractometers use either 3- or 4-circle goniometers (*CampanaBAAN*). These circles refer to the four angles (2θ , χ , φ , and Ω) ((Figure 9, (a)) that define the relationship between the crystal lattice, the incident ray and detector. Samples are mounted on thin glass fibers which are attached to brass pins and mounted onto goniometer heads. Adjustment of the X, Y and Z orthogonal directions allows centering of the crystal within the X-ray beam. X-rays leave the collimator and are directed at the crystal. Rays are either transmitted through the crystal, reflected off the surface, or diffracted by the crystal lattice. A beam stop is located directly opposite the collimator to block transmitted rays and prevent burn-out of the detector. Reflected rays are not picked up by the detector due to the angles involved. Diffracted rays at the correct orientation for the configuration are then collected by the detector. Modern single-crystal diffractometers use CCD (charge-coupled device) technology to transform the X-ray photons into an electrical signal which are then sent to a computer for processing. In the work presented here, an X8 (Bruker-AXS) single crystal diffractometer (Figure 9, (b)) ($\lambda_1 = 0.71073 \text{ \AA}$ and a MoK α radiation selected by a graphite monochromator) with 4 circles and equipped with a bi - dimensional CDD 4K detector allowing the resolution of the crystalline structures at R.T. and at low temperature (to reduce the atoms vibration and observe the eventual structure transformation) by the usage of a N₂ cooling system. The temperature can reach 100K. The most suitable crystal is selected from the mixture using a needle and washed from the powder and from the small crystals stuck on the surface using special grease. The crystal is then mounted on a glass fiber and aligned on the diffractometer. The first step is to test the quality of the crystal and to discover the cell parameters and the symmetry. If the crystal is suitable, the next step is the long acquisition of the crystal intensities. This process can take several hours and it consists generally in rotating the crystal using the 4 circles well being bombarded with X-rays, producing a diffraction pattern of regularly spaced spots known as reflections. After the collection is finished, the intensities from all the photos

are harvested, corrected from absorption (using a mathematical model included in SADABS program or the crystal faces absorption) and integrated. The next step is the structure solving using one of the following methods: direct method, Patterson method and the extend method. Usual, the direct method is used to solve a structure using as software Sir (included in Jana, *Altomare1997*), Shell X (*Müller2006*, *Sheldrick2008*). The structural refinement is similar to the one performed on powder data and will be discussed later.

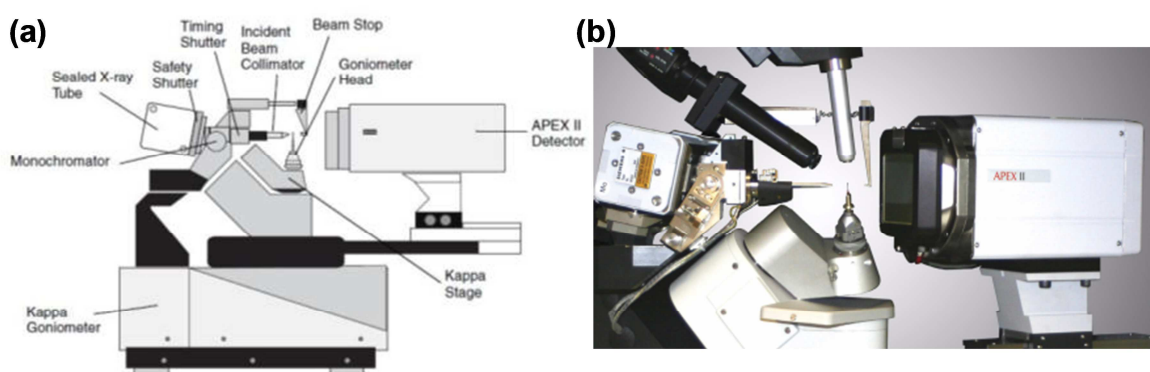
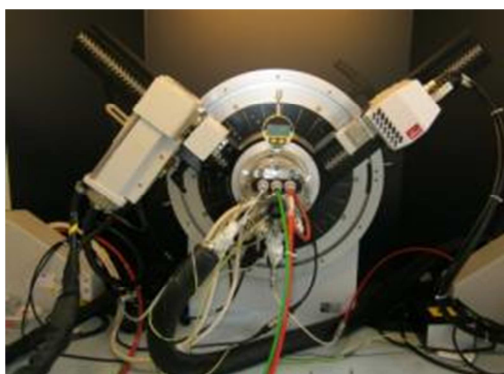


Figure 9: (a) X8 (Bruker-AXS) single crystal diffractometer schema; (b) X8 (Bruker-AXS) single crystal diffractometer

D8 Advance - XRK900 (Bruker-AXS)



D8 Advance – HTK1200N (Bruker-AXS)

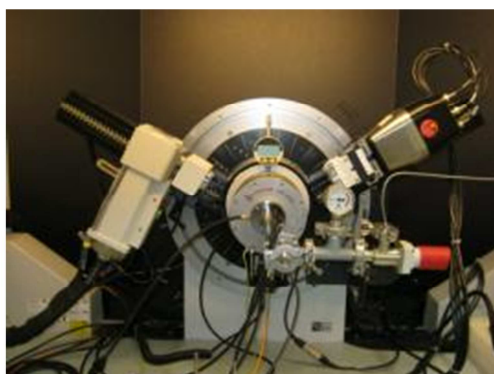


Figure 10: High temperature X – ray diffractometers

High temperature X – ray diffraction: Some compounds were investigated by high temperature X – ray diffraction. The diffractometers used are:

- D8 Advance - XRK900 (Bruker-AXS): Diffractometer dedicated to the study of polycrystalline samples at high temperature (1000°C) and under gas flow (vacuum, various gases). It is equipped with a Lynxeye rapid sensor type and an Anton Paar XRK900 reactive room (Figure 10).
- D8 Advance – HTK1200N (Bruker-AXS) for the study of the polycrystalline samples at high temperature (1200°C) and under atmosphere (vacuum, inert gas). It is equipped with a rapid detector type Vantec and an Anton Paar HTK1200N chamber (Figure 10).

13. Neutron diffraction

The transitional metals (Fe, Mn, Co) and the anions used in this work are not distinguishable by X - rays (close Z). Furthermore, the interaction of the X – ray with the magnetic spins is null. For these reasons, room temperature and low temperature neutron diffraction investigations were used.

Fundamental Principles of neutron diffraction: The technique is similar to X-ray diffraction but due to the different scattering properties of neutrons versus x-rays complementary information can be obtained. Neutrons are particles found in the atomic nucleus of almost all atoms, but they are bounded. The technique requires free neutrons and these normally do not occur in nature, because they have limited life-time. In a nuclear reactor, however, neutrons can be set free through nuclear decay particularly when fission occurs. All quantum particles can exhibit wave phenomena typically associate with light or sound. Diffraction is one of these phenomena; it occurs when waves encounter obstacles whose size is comparable with the wavelength. If the wavelength of a quantum particle is short enough, atoms or their nuclei can serve as diffraction obstacles. When a beam of neutrons emanating from a reactor is slowed down and selected properly by their speed, their wavelength lies near one angstrom (0.1 nanometer), the typical separation between atoms in a solid material. Such a beam can then be used to perform a diffraction experiment. Impinging on a crystalline sample it will scatter under a limited number of well-defined angles according to the same Bragg's law that describes X-ray diffraction (*Shull1995*)

Nuclear scattering: Neutrons interact with matter differently than X-rays. X-rays interact primarily with the electron cloud surrounding each atom. The

contribution to the diffracted X-ray intensity is therefore larger for atoms with a high atomic number (Z) than it is for atoms with a small Z . On the other hand, neutrons interact directly with the nucleus of the atom, and the contribution to the diffracted intensity is different for each isotope; for example, regular hydrogen and deuterium contribute differently. It is also often the case that light (low Z) atoms contribute strongly to the diffracted intensity even in the presence of large Z atoms. The scattering length varies from isotope to isotope rather than linearly with the atomic number. An element like vanadium is a strong scatterer of X-rays, but its nuclei hardly scatter neutrons, which is why it often used as a container material. Non-magnetic neutron diffraction is directly sensitive to the positions of the nuclei of the atoms (*Ibberson2002*). A major difference with X-rays is that the scattering is mostly due to the tiny nuclei of the atoms. That means that there is no need for an to describe the shape of the electron cloud of the atom and the scattering power of an atom does not fall off with the scattering angle as it does for X-rays. Therefore can show strong well defined diffraction peaks even at high angles, particularly if the experiment is done at low temperatures. Many neutron sources are equipped with liquid helium cooling systems that allow to collect data at temperatures down to 4.2 K for magnetic investigations. The superb high angle (i.e. high resolution) information means that the data can give very precise values for the atomic positions in the structure. On the other hand, Fourier maps (and to a lesser extent difference Fourier maps) derived from neutron data suffer from series termination errors, sometimes so much that the results are meaningless (*Lovesey1984*).

Magnetic scattering: Although neutrons are uncharged, they carry a spin, and therefore interact with magnetic moments, including those arising from the electron cloud around an atom. Neutron diffraction can therefore reveal the microscopic of a material. Magnetic scattering does require an atomic form factor as it is caused by the much larger electron cloud around the tiny nucleus. The intensity of the magnetic contribution to the diffraction peaks will therefore dwindle towards higher angles (*Lovesey1984*).

Neutron diffraction instrumentation: A neutron diffraction measurement requires a neutron source (i.e. a nuclear reactor) or spallation source), a sample (the material to be studied), and a detector. Samples sizes are large compared to those used in X-ray diffraction. The technique is therefore mostly performed as powder diffraction. At a research reactor other components such as crystal monochromators

or filters may be needed to select the desired neutron wavelength. Some parts of the setup may also be movable. At a spallation source the time of flight technique is used to sort the energies of the incident neutrons (Higher energy neutrons are faster), so no monochromator is needed, but rather a series of aperture elements synchronized to filter neutron pulses with the desired wavelength.

Long R.T. ($4 - 120^\circ 2\theta$) neutron diffractograms were collected using “thermal neutrons” 2 axis (20 detectors) high resolution powder diffractometer (R.T. 3T2) with $\lambda = 1.225\text{\AA}$ incident wavelength, at the Laboratoire Léon Brillouin (LLB – France) (Figure 11, (a)). The schema of the diffractometer is given in Figure 11, (b). 3T2 is a two - axis diffractometer using a thermal beam tube ($30\times 80\text{nm}^2$), a vertically focusing Ge (335) monochromator and a 50^3 He detector (2.4° apart). The angular range is $5 < 2\theta < 120^\circ 2\theta$ and the typical acquisition time is between 12 and 24h. Depending on the collimation and on the relative flux, different Cagliotti profile parameters are obtained.

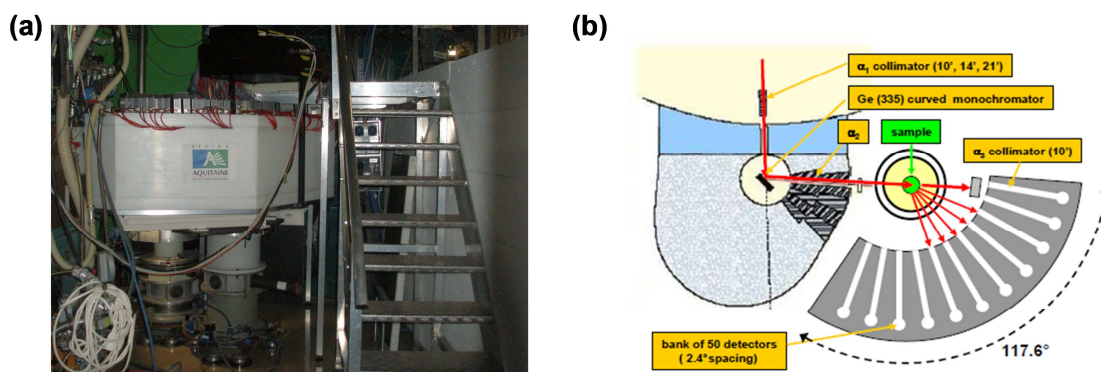


Figure 11: (a) photo of 3T2 neutrons diffractometer; (b) schema of 3T2 neutrons diffractometer

Low temperature neutron diffractograms were collected using the LLB “cold neutrons” 2 axis high flux powder diffractometer (G4.1) for magnetic structure. The diffractograms were recorded from 4 to 90° in 2θ , from 1.5K to R.T. using the $\lambda = 2.4226\text{\AA}$ wavelength at the same Laboratoire Léon Brillouin (LLB – France). G 4-1 is a two-axis powder diffractometer equipped with a vertical focusing pyrolytic graphite monochromator and an 800-cells multidetector covering an $80^\circ - 2\theta$ range (step 0.1° between 2 cells). The most frequently used wavelength is 2.43\AA but can occasionally vary between 2.43 and 5.5\AA . The accessible 2θ diffusion angle covers the range $3^\circ - 105^\circ$, in that range it is possible to perform diagrams with 0.02° step

(2 θ). The instrumental resolution of the spectrometer being minimal at low 2 θ diffusion angle (2 θ < 60°), G 4-1 is particularly well adapted for magnetic structure determination. The high acquisition rate of the multidetector allows to perform diffraction studies (structural or magnetic) as a function of external parameters (temperature, pressure...) and to follow in situ kinetic reactions or phase transitions; the minimal acquisition time is of the order of one minute. With longer acquisition time (a few hours) it becomes possible to detect and quantify minority phases present in a multiphase compound, generally down to 0.1% (weight percentage). A photo is given of the diffractometer and the schema are given in Figure 12.

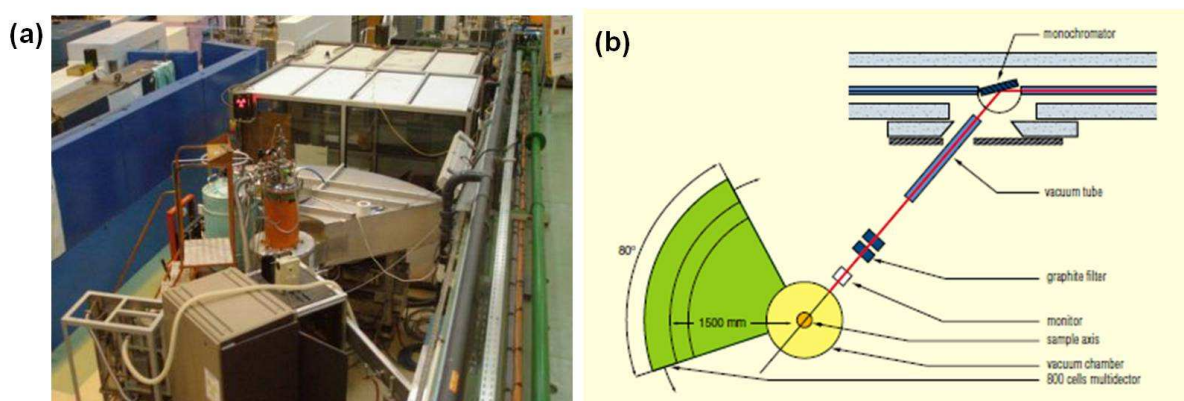


Figure 12: (a) Photo of G4-1 diffractometer and (b) Principe schema of the G4 – 1

14. Lattice parameters, atomic and magnetic structure refinement

Lattice parameters refinement (pattern matching): The cell parameters refinement was performed using either FullProf program (Rodriguez-Carvajal1990), either Jana (Petricek2006) software. Both of them are based on mathematical calculation using an approximate value of the cell parameters, the space group, the reflections read in the input file and a background line given by the user to calculate a theoretical pattern. To match the experimental and theoretical profiles, the least squares method is used. In order to describe the angular dependence of the peak full-width at half-maximum (H), the formula of Caglioti is used: $H^2 = U \tan^2\theta + V \tan \theta + W$, with U, V and W refined in the process. The cell parameters, the 2-theta zero point and the shape of the peaks were refined.

In order to describe the shape of the peaks, two types of profiles were used in the work presented in this manuscript:

- Pseudo – Voigt type of profile (*Hall1977*) where the ratio between the Lorentzian and the Gaussian form of peaks is refined. (Shape, Lorentz/Gauss = 0.5)
- Thomson profile (for neutron diffraction) where the percentage of Lorentzian and Gaussian are refined.

Structure refinement (Rietveld): In a powder case, the structure solving is more difficult than in the case of single crystals. For unknown compounds, the cell parameters and the space group can be identified using Trevor, DicVol, ... included in FullProf software. Similar compounds (with same space group and cell parameters) can afterwards be found in the literature and the similar structure can be modified to fit to the chemical composition of the compound in question. For structure refinement, the pattern matching input file (described anterior) is used. The atomic positions and thermal parameters are introduced in the refinement and a new theoretical pattern is calculated using the anterior refined profile and the structural information for describing the intensities of the peaks. The same least squares method is used to refine the atomic position and thermal parameters of the atoms. In the case of mixed site occupation, the cationic or anionic distribution is calculated by the refinement of the occupancies of the atoms in the site, constraining the sum of the occupancies for the atoms present in the same site to be equal to site total occupation. The anionic vacancies are also calculated by the refinement of the sites occupation (*Rietveld1967*).

Magnetic structure refinement: After a pattern matching for the profile modulation and the nuclear structure refinement, a secondary magnetic phase was introduced in the refinement. The magnetic phase was considered to be in P -1 space group and the magnetic moments values were refined at different temperatures. In the case of the compounds with magnetic coupling at R.T., the magnetic peaks were declared excluded areas for profile modulation and the nuclear structure refinement and the refinement of the structure was repeated after the magnetic structure refinement (*Rietveld1969*).

15. Magnetic properties

Classification of the magnetic materials: The magnetic susceptibility is the quantitative measure of the extent to which a material may be magnetized in relation to a given applied magnetic field. The magnetic susceptibility of a material, commonly symbolized by χ_m , is equal to the ratio of the magnetization M within the material to the applied magnetic field strength H , or $\chi_m = M/H$ (Purcell 1984). This ratio, strictly speaking, is the volume susceptibility, because magnetization essentially involves a certain measure of magnetism (dipole moment) per unit volume.

The magnetic materials classification is given below

Diamagnetic materials, such as bismuth, when placed in an external magnetic field, partly expel the external field from within themselves and, if shaped like a rod, line up at right angles to a non-uniform magnetic field. Diamagnetic materials are characterized by constant, small negative susceptibilities, only slightly affected by changes in temperature.

Paramagnetism results from the electron spin of unpaired electrons. An electron has a magnetic dipole moment—which is to say that it behaves like a tiny bar magnet—and so when a group of electrons is placed in a magnetic field, the dipole moments tend to line up with the field. The effect augments the net magnetization in the direction of the applied field. Like diamagnetism, paramagnetism is weak and exists only in the presence of an applied field, but since the effect enhances the applied field, the sign of the paramagnetic susceptibility is always positive. The susceptibility of a paramagnetic substance is on the order of 10^{-4} to 10^{-6} emu/cm³. Paramagnetic materials, such as platinum, increase a magnetic field in which they are placed because their atoms have small magnetic dipole moments that partly line up with the external field. Paramagnetic materials have constant, small positive susceptibilities, less than 1/1000 at room temperature, which means that the enhancement of the magnetic field caused by the alignment of magnetic dipoles is relatively small compared with the applied field. Paramagnetic susceptibility is inversely proportional to the value of the absolute temperature. Temperature increases cause greater thermal vibration of atoms, which interferes with alignment of magnetic dipoles.

Ferromagnetism also exists because of the magnetic properties of the electron. Unlike paramagnetism, however, ferromagnetism can occur even if no

external field is applied. The magnetic dipole moments of the atoms spontaneously line up with one another because it is energetically favorable for them to do so. A remanent magnetization can be retained. Complete alignment of the dipole moments would take place only at a temperature of absolute zero (0 K, or -273.15° C). Above absolute zero, thermal motions begin to disorder the magnetic moments. At a temperature called the Curie temperature, which varies from material to material, the thermally induced disorder overcomes the alignment, and the ferromagnetic properties of the substance disappear. The susceptibility of ferromagnetic materials is large and positive. It is on the order of $10 - 10^4$ emu/cm³. Only a few materials—iron, cobalt, and nickel—are ferromagnetic in the strict sense of the word and have a strong residual magnetization. In general usage, particularly in engineering, the term ferromagnetic is frequently applied to any material that is appreciably magnetic. Ferromagnetic materials, such as iron and cobalt, do not have constant susceptibilities; the magnetization is not usually proportional to the applied field strength. Measured ferromagnetic susceptibilities have relatively large positive values, sometimes in excess of 1000. Thus, within ferromagnetic materials, the magnetization may be more than 1000 times larger than the external magnetizing field, because such materials are composed of highly magnetized clusters of atomic magnets (ferromagnetic domains) that are more easily lined up by the external field.

Antiferromagnetism occurs when the dipole moments of the atoms in a material assume an antiparallel arrangement in the absence of an applied field. The result is that the sample has no net magnetization. The strength of the susceptibility is comparable to that of paramagnetic materials. Above a temperature called the Néel temperature, thermal motions destroy the antiparallel arrangement, and the material then becomes paramagnetic. Spin-canted (anti)ferromagnetism is a special condition which occurs when antiparallel magnetic moments are deflected from the antiferromagnetic plane, resulting in a weak net magnetism. Hematite (α -Fe₂O₃) is such a material. Also, all the materials presented in this manuscript are antiferromagnetic materials.

Ferrimagnetism is an antiparallel alignment of atomic dipole moments which does yield an appreciable net magnetization resulting from unequal moments of the magnetic sub-lattices. Remanent magnetization is detectable (see below). Above the Curie temperature the substance becomes paramagnetic. Magnetite (Fe₃O₄), which is the most magnetic common mineral, is a ferrimagnetic substance.

Superparamagnetism occurs in materials having grains so small (about 100 angstroms) that any cooperative alignment of dipole moments is overcome by thermal energy.

Magnetic susceptibility determination: In order to determine the magnetic susceptibility of the compounds presented in this work, a Vibration Sample Magnetometer (VSM) was used (Figure 13). The compounds were pressed into bars, densified with an isostatic press and heated at the temperature of synthesis in order to increase the compactness up to 80% (ratio between the theoretic and experimental densities). The sample is then placed inside a uniform magnetic field to magnetize the sample. The sample is then physically vibrated sinusoidally, typically through the use of a piezoelectric material.



Figure 13: Vibrating sample magnetometer

Commercial systems use linear actuators of some form, and historically the development of these systems was done using modified audio speakers, though this approach was dropped due to the interference through the in-phase magnetic noise produced, as the magnetic flux through a nearby pickup coil varies sinusoidally. The induced voltage in the pickup coil is proportional to the sample's magnetic moment, but does not depend on the strength of the applied magnetic field. In a typical setup, the induced voltage is measured through the use of a lock-in amplifier using the piezoelectric signal as its reference signal. By measuring in the field of an external electromagnet, it is possible to obtain the hysteresis curve of a material.

16. 4 four-terminal sensing low temperature electrical resistivity determination

Generalities: The electrical resistance of an electrical element measures its opposition to the passage of an electric current; the inverse quantity is electrical conductance, measuring how easily electricity flows along a certain path. Electrical resistance shares some conceptual parallels with the mechanical notion of friction. The SI unit of electrical resistance is the ohm (Ω), while electrical conductance is measured in Siemens (S). An object of uniform cross section has a resistance proportional to its resistivity and length and inversely proportional to its cross-sectional area. All materials show some resistance, except for superconductors, which have a resistance of zero under a specific temperature. The resistance of an object is defined as the ratio of voltage across it to current through it: $R = V / I$ (R = resistance, V = voltage, I = current intensity). For a wide variety of materials and conditions, the electrical resistance R is constant for a given temperature; it does not depend on the amount of current through or the potential difference (voltage) across the object. Such materials are called ohmic materials. For objects made of ohmic materials, the definition of the resistance, with R being a constant for that resistor, is known as Ohm's law. In the case of a nonlinear conductor (not obeying Ohm's law), this ratio can change as current or voltage changes; the inverse slope of a chord to an I-V curve is sometimes referred to as a "chordal resistance" or "static resistance" (*Forbes2006, Kenneth200*). The resistance of a given resistor or conductor grows with the length of conductor and specific resistivity of the material, and decreases for larger cross-sectional area. The resistance R and conductance G of a conductor of uniform cross section, therefore, can be computed as $R = \rho \frac{l}{A}$ where l is the length of the conductor, measured in meters, A is the cross-section area of the conductor measured in square meters [m^2], and ρ (rho) is the electrical resistivity (also called specific electrical resistance) of the material, measured in ohm*meters ($\Omega \cdot m$). Resistivity is a measure of the material's ability to oppose electric current.

Instrumentation: An instrument for measuring resistance is called an ohmmeter. Simple ohmmeters cannot measure low resistances accurately because the resistance of their measuring leads causes a voltage drop that interferes with the

measurement, so more accurate devices use four-terminal sensing. Four-terminal sensing (4T sensing), 4-wire sensing, or 4-point probes method is an electrical impedance measuring technique that uses separate pairs of current-carrying and voltage-sensing electrodes to make more accurate measurements than traditional two-terminal (2T) sensing (Figure 14). The key advantage of four-terminal sensing is that the separation of current and voltage electrodes eliminates the impedance contribution of the wiring and contact resistances. (Kuphaldt2006). The materials were pressed into bars and densified with an isostatic press and heated at the temperature of synthesis in order to increase the compactness up to 80% (ratio between the theoretical and experimental densities). Then the contacts were glued using special carbon glue and heated for 2h at 100°C in order to dry the glue.

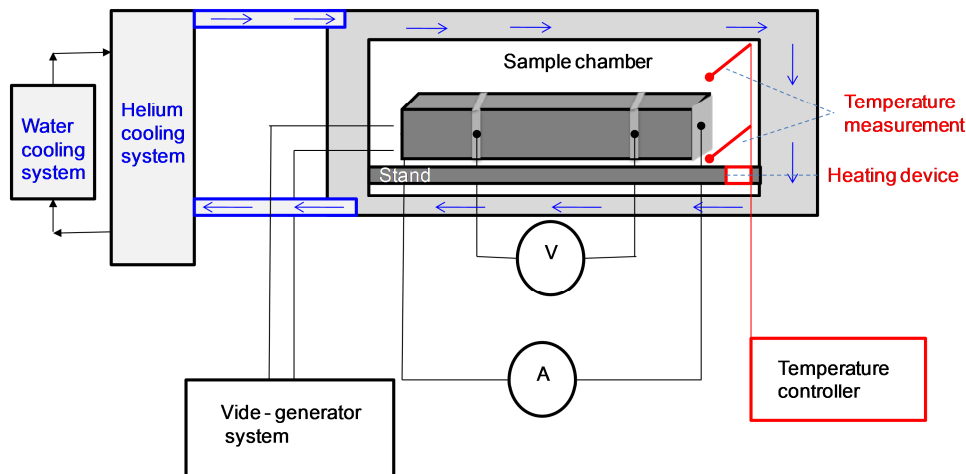


Figure 14: Schematic representation of 4 – terminal resistivity measurement installation

Then, the sample is introduced in the sample chamber and hermetically closed. The sample chamber is equipped one inner mantle and one exterior mantle. In the sample chamber, 10^{-4} vacuum is produced using one primary and one secondary vacuum pump. Between the interior and exterior mantels is pumped helium in order to cool the sample chamber. The helium cooling system is also cooled using a water cooling system ($T = 9K$). Two thermocouples serve for the temperature measurement, one at the sample level and one close to the heating device linked to an ITC503 temperature controller. The resistivity is measured using a multimeter Model 2000.

Résumé:

Ce travail a consisté en la synthèse, l'étude structurale et les caractérisations physico-chimiques de systèmes dérivés des polytypes 6H et 10H des perovskites hexagonales de formule $BaMX_{0.2-x}O_{3-\delta}$ ($M=Co, Fe, Mn; X=F, Cl, Br$). En premier lieu, la compréhension des polytypes stables en fonction de la substitution sur les sites M et X disponibles dans la structure a été entreprise via des analyses de la sous-stœchiométrie du réseau anionique. Il apparaît que la réduction du métal s'accompagne de la stabilisation de polytypes incluant des oligomères triples d'octaèdres reliés par les faces, tandis qu'une oxydation aura tendance à stabiliser des structures à sous-unités plus longues, de type tétramériques, hexamériques (composé inédit mis en évidence pendant ce travail) ou autres. Nous avons ainsi pu distinguer les effets privilégiés des métaux : cobalt (redox versatile dépendant des conditions de synthèse), fer (effet réducteur) et manganèse (effet oxydant) par des analyses structurales fines. Bien sûr les interactions métal-métal modulables influent sur les propriétés électroniques et magnétiques de ces solides. A ces effets redox, s'ajoutent des effets stériques, qui varient suivant la nature de l'anion X, conduisant à une sous-stœchiométrie sur l'halogène et à une délocalisation spatiale variable dépendant du rayon ionique. Cet effet a été analysé en détail dans les systèmes chimiques 6H- $Ba_6Co_6(Cl_{1-y}F_y)O_{16-\delta}$ et 10H- $Ba_5Co_5(Cl_{1-y}F_y)O_{13-\delta}$ en prenant soin de systématiser la compréhension des relations structures-redox-propriétés. Finalement l'ensemble du travail réalisé sur ces phases conduit à un certain nombre de composés inédits éventuellement associés à des structures originales (cas de nH- $Ba_8Mn_6Co_2ClO_{22-\delta}$) ou inattendue (cas du composé 10H- $Ba_5Co_4Pt_1BrO_{13-\delta}$, exemple rare de feuillet [BaOBr] dans les pérovskites hexagonales). En essence, il apparaît après notre étude qu'une généralisation du comportement structural de ces composés peut être proposée, à la base d'une anticipation plausible des propriétés physico-chimiques dans ce système chimique particulièrement complexe. Finalement, l'insertion, non volontaire dans un premier temps, de groupements carbonates $(CO_3)^{2-}$ dans différents types structuraux a également été étudiée. Notamment, dans des structures de type 2H- $BaCoO_3$, elle a conduit à une série de composés montrant une mise en ordre originale des colonnes d'octaèdres de cobalt et des groupements carbonates.

Abstract:

This work concerns the synthesis, structural study and physico-chemical characterization of structural systems derived from the 6H and 10H hexagonal perovskites polytypes, formulated $BaMX_{0.2-x}O_{3-\delta}$ ($M = Co, Fe, Mn, X = F, Cl, Br$). First, the understanding of the stable structural types depending on the substitution on the M and X sites available in the structure, was undertaken through analysis of the sub-stoichiometry of the anionic network. It appears that the reduction of the metal is accompanied by the stabilization of polytypes including oligomers of three face-sharing octahedra, while oxidation will tend to stabilize structures with longer sub-units, tetrameric or hexameric type (new compound revealed during this work) and others. We have been able to distinguish trends of particular metals by detailed structural analysis, e.g. cobalt (versatile redox - depending on the synthesis conditions), iron (reducing effect) and manganese (oxidizing effect). Of course the flexible metal-metal interactions affect the electronic and magnetic properties of these solids. In addition to the redox changes, steric effects appear, depending on the nature of the X anion, leading to a sub-stoichiometry of the halogen and variable ionic radius-dependent spatial delocalization. This effect has been analyzed in detail in 6H- $Ba_6Co_6(Cl_{1-y}F_y)O_{16-\delta}$ and 10H- $Ba_5Co_5(Cl_{1-y}F_y)O_{13-\delta}$ chemical systems, by taking care of the systematic understanding of the relationship structures properties. Finally, the work on these phases led to a number of novel compounds, sometimes associated with original structures (8H- $Ba_8Mn_6Co_2ClO_{22-\delta}$ case) or unexpected (case of compound 10H - $Ba_5Co_4Pt_1BrO_{13-\delta}$, rare example of a [BaOBr] layer in the hexagonal perovskite). In essence, it appears from our study that a generalization of the structural behaviour of these compounds can be proposed, based on a plausible anticipation of physico-chemical properties in this particularly complex chemical system. Finally, the insertion, non-voluntary at first, of carbonates $((CO_3)^{2-})$ groups in different structural types, was also studied. Particularly, in the 2H- $BaCoO_3$ structural types, it led to a series of compounds showing an original ordering of cobalt octahedra columns and carbonate groups.